

**SYNTHESIS OF COBALT VANADIUM OXIDE/REDUCED
GRAPHENE OXIDE COMPOSITE ELECTRODE FOR
SUPERCAPACITOR APPLICATION**

A THESIS SUBMITTED TO
**D. Y. PATIL EDUCATION SOCIETY (DEEMED TO BE UNIVERSITY),
KOLHAPUR**



FOR THE DEGREE OF
DOCTOR OF PHILOSOPHY
IN
PHYSICS

UNDER THE FACULTY OF
INTERDISCIPLINARY STUDIES
BY

Mr. SAMBHAJI SHIVAJI KUMBHAR

M. Sc.

UNDER THE SUPERVISION OF

Dr. UMAKANT MAHADEV PATIL

M. Sc., Ph. D.

ASSOCIATE PROFESSOR,

CENTRE FOR INTERDISCIPLINARY RESEARCH,

D. Y. PATIL EDUCATION SOCIETY (DEEMED TO BE UNIVERSITY),

KOLHAPUR- 416 006, MAHARASHTRA, (INDIA)

2024

DECLARATION

I am **Sambhaji S. Kumbhar**, hereby declare that the thesis entitled “**SYNTHESIS OF COBALT VANADIUM OXIDE/REDUCED GRAPHENE OXIDE COMPOSITE ELECTRODE FOR SUPERCAPACITOR APPLICATION**” submitted for the degree of **Doctor of Philosophy (Ph.D.) in Physics**, Faculty of Interdisciplinary Studies, under the guidance of **Dr. Umakant M. Patil**, Centre for Interdisciplinary Research (CIR), D. Y. Patil Education Society (Deemed to be University), Kolhapur is completed and written by me, has not before made the basis for the award of any other higher education institute in India or any other country to the best of my knowledge and belief the thesis contains no material previously published or written by another person except where due reference is made. Further, I declare that I have not violated any of the provisions under the Copyright and Piracy/Cyber/IPR Act amended from time to time.

Place: Kolhapur

Research Student

Date: / /2024

Mr. Sambhaji Shivaji Kumbhar

CERTIFICATE OF GUIDE

This is to certify that the thesis entitled “**SYNTHESIS OF COBALT VANADIUM OXIDE/REDUCED GRAPHENE OXIDE COMPOSITE ELECTRODE FOR SUPERCAPACITOR APPLICATION**” which is being submitted herewith for the award of the Degree of **Doctor of Philosophy (Ph.D.) in Physics**, Faculty of Interdisciplinary Studies, under the guidance of Dr. Umakant M. Patil, Centre for Interdisciplinary Research (CIR), D. Y. Patil Education Society (Deemed to be University), Kolhapur, is the result of the original research work completed by **Mr. Sambhaji Shivaji Kumbhar** under my supervision and guidance and to the best of my knowledge and belief the work embodied in this thesis has not formed earlier the basis for the award of any degree or similar title of this or any other university or examining body.

Place: Kolhapur

Research Guide

Date: / /2024

Dr. Umakant Mahadev Patil

**Associate Professor,
D. Y. Patil Education (Deemed to
be University), Kolhapur-416006.**

Forwarded through,

Prof. C. D. Lokhande

**Dean and Research Director,
Centre for Interdisciplinary Research
D. Y. Patil Education (Deemed to be University),
Kolhapur-416006.**

ACKNOWLEDGEMENT

This journey has been a beautiful odyssey, an exploration of expanding the horizons of knowledge, uncovering strengths and weaknesses, and fostering mental and emotional resilience. The remarkable individuals I encountered along the path have greatly enhanced its beauty and richness. I would like to seize this moment to express my profound gratitude to those persons who enriched this journey with their presence.

*Upon completing my Ph.D. thesis, I extend my sincere gratitude to my mentor, **Dr. Umakant M. Patil**, an Associate Professor at the Centre for Interdisciplinary Research (CIR), D. Y. Patil Education Society (Deemed to be University), Kolhapur. His unwavering support throughout my Ph.D. studies and related research, coupled with his motivation and profound knowledge, have been invaluable. I am grateful not only for his guidance in the realm of research but also for instilling in me a deep passion for science, thereby illuminating the path of my life. With his assistance, I was able to overcome personal and scientific obstacles in writing scientific papers, including this Ph.D. thesis. This work could not have been accomplished without his inspiring mentorship and constant encouragement during my research tenure. Also, I sincerely acknowledge the wholehearted assistance, valuable discussions, guidelines, and suggestions provided by **Prof. C. D. Lokhande**, Dean and Research Director at the Centre for Interdisciplinary Research (CIR). His fruitful discussions and helpful guidance on time management greatly contributed to the progress of my Ph.D.*

*I extend my sincere thanks to Vice-Chancellor **Prof. R. K. Mudgal**, former IQAC Director **Dr. S. Sharma**, and Registrar **Dr. V. V. Bhosale** for their inspiration and support. I also express gratitude to **Dr. Jayavanat Gunjekar**, **Dr. Sharad Patil**, **Dr. Vishwajeet Khot**, and **Dr. Pravin Pawar** for their assistance in analyzing the results with their empathy and cooperative mindset. Additionally, I acknowledge the contributions of **Dr. Rahul Salunkhe (IIT Jammu)**, **Dr. Vinayak Parale (Yonsei University, Korea)**, and **Dr. Nilesh Tarwal (Shivaji University, Kolhapur)** for providing important sample characterization data throughout my research endeavor.*

In addition, I acknowledge the funding support from Mahatma Jyotiba Phule Research & Training Institute (MAHAJYOTI), Government of Maharashtra State for Mahatma Jyotiba Phule Senior Research Fellowship (MJPSRF-2021) sanctioned to me.

*I would like to special thanks to my colleague, **Ms. Shraddha Bhosale**, for her assistance and support in my research endeavors. I would like to express sincere thanks to my mentors and seniors, **Dr. Ajinkya M. More, Dr. Pranv Katkar, Dr. Sachin Pujari, Dr. Shivaji Ubale, Dr. Suraj Khalate, Dr. Shrikant Sadavar, Dr. Navanath Padalkar, Dr. Rohini Shinde, Dr. Vikas Mane, Dr. Satish Jadhav, Dr. Prity Bagwade, Mr. Vikas Magdum, Mr. Yogesh Chitare, and Ms. Shirin Kulkarni** for their insightful guidance, scientific discussions, and valuable suggestions on the present work.*

*To my dear friends **Rushiraj Bhosale, Vinod Patil, and Rutuja Gambhir**, I extend my heartfelt gratitude for always being there for me in every situation and for your unwavering support and assistance. I would like to acknowledge my colleagues and juniors at the Centre for Interdisciplinary Research, **Sambhaji Khot, Satish Phalke, Manohar Lad, Shahabaj Mujawar, Anuja Vibhute, Ajinkya Bagade, Sumita Patil, Kuldip Belekar, Rakesh Mohite, Ganesh Jadhav, Dhanashri Phadatare, Suhasini Yadav, Shivprasad Jadhav, Anil Sutar, Arti Patil, Prashant Sawant, Shweta Talekar, Shraddha Pawar, Jyoti Thorat, Sohel Shaikh, Sagar Patil, and Dilip Patil** for their wonderful collaboration. I want to thank them for their support and valuable suggestions during research work.*

I am also thankful to all teaching and non-teaching staff of the Centre for Interdisciplinary Research for their cooperation.

*I hereby express my deepest appreciation and regards to my beloved parents (**Aji, Aai, and Bhau**), Brothers (**Sayaji and Samadhan**), sister (**Shital**) and uncle and aunty (**Nana and Mau**), all of the family members who despite their hard times and sufferings, continuously supported and encouraged me to complete my research.*

~Sambhaji

Place: Kolhapur

SUMMARY OF RESEARCH WORK

Granted (05)/Published (01) Indian Patents

- 1) Chemical method for growing a cobalt vanadium oxide thin film on solid substrate, Dr. U. M. Patil, **Mr. S. S. Kumbhar**, Ms. S. B. Bhosale, Mr. V. V. Patil, Prof. C. D. Lokhande, Dr. P. R. Deshmukh, (Patent No: 459219).
- 2) Cobalt vanadium oxide, preparation method for the same, and supercapacitor comprising the same, Dr. U. M. Patil, **Mr. S. S. Kumbhar**, Ms. S. B. Bhosale, Mr. V. V. Patil, Prof. C. D. Lokhande, Dr. R. R. Salunkhe, (Patent No: 529322).
- 3) Nickel cobalt phosphate thin-film electrodes: chemical method for preparation of the same, application for supercapacitor and electrocatalysis using the same, Dr. U. M. Patil, Mr. V. V. Patil, **Mr. S. S. Kumbhar**, Ms. S. B. Bhosale, Prof. C. D. Lokhande, (Patent No: 432303).
- 4) A chemical synthesis process of manganese ferrite thin films on conducting substrates for energy storage, Dr. V. S. Jamadade, Mr. R. P. Bhosale, Mr. S. B. Ubale, **Mr. S. S. Kumbhar**, Prof. C. D. Lokhande, (Patent No: 415578).
- 5) A method of preparation of lanthanum strontium tungsten oxide composite electrode for supercapacitor application, Prof. A. P. Torane, Mr. A. Mr. R. P. Bhosale, Dr. S. B. Ubale, **Mr. S. S. Kumbhar**, Prof. C. D. Lokhande, Prof. B. T. Jadhav, (Patent No: 471088).
- 6) Nickel vanadate thin film on conducting substrate, preparation method for the same and supercapacitor comprising the same, Dr. J. L. Gunjekar, Ms. S. B. Bhosale, Dr. U. M. Patil, **Mr. S. S. Kumbhar**, Mr. V. V. Patil, Prof. C. D. Lokhande, (Application No: 202221020652).

Papers Accepted at International Journals (12)

- 1) **S. S. Kumbhar**, S. B. Bhosale, S. S. Pujari, V. V. Patil, N. Kumar, R. R. Salunkhe, C. D. Lokhande, U. M. Patil*, Growth dynamics-dependent chemical approach to accomplish nanostructured cobalt vanadium oxide thin film electrodes with controlled surface area for high-performance solid-state hybrid supercapacitor devices, Energy Technology, 11 (2023) 2300400 (**I.F- 3.6**).
- 2) **S. S. Kumbhar**, S. B. Bhosale, S. S. Patil, A. Ransing, V. G. Parale, C. D. Lokhande, H.H. Park* and U. M. Patil*, Chemical synthesis of binder-free

nanosheet-like cobalt vanadium oxide thin film electrodes for hybrid supercapacitor devices, Sustainable Energy & Fuels, (2024) (**I. F. 5**).

- 3) S. B. Bhosale, **S. S. Kumbhar**, S. S. Patil, A. Ransing, V. G. Parale, C. D. Lokhande, J. L. Gunjekar, H. Park, U. M. Patil*, Harnessing morphological alteration from microflowers to nanoparticles and cations synergy (Co:Ni) in binder-free cobalt nickel vanadate thin film cathodes synthesized via SILAR method for hybrid supercapacitor devices, Journal of Colloid and Interface Science, 666 (2024) 101-117 (**I.F- 9.4**).
- 4) S. A. Khalate, S. A. Kadam, Y. R. Ma, **S. S. Kumbhar**, S. B. Bhosale, V. V. Patil, V. G. Parale, S. B. Kulkarni, C. D. Lokhande, H. Park, U. M. Patil*, Impact of Co:Fe cations composition in amorphous and mesoporous cobalt iron phosphate electrocatalysts synthesized by SILAR method on durable electrochemical water splitting, International Journal of Hydrogen Energy, 61 (2024) 162–172 (**I.F- 8.1**).
- 5) R. P. Bhosale, **S. S. Kumbhar**, P. P. Bagwade, C. D. Lokhande, V. S. Jamdade*, Chemical synthesis of manganese ferrite thin films for energy storage application, Journal of Materials Science: Materials in Electronics, 35 (2024) 5, (**I.F- 2.8**).
- 6) R. P. Bhosale, **S. S. Kumbhar**, S. B. Bhosale, R. R. Salunkhe, V. A. Kadam, S. P. Pardhi, S. S. Gholap, C. D. Lokhande, V. S. Jamdade*, Morphology modulation of MnFe_2O_4 thin film electrode for enhanced performance of hybrid supercapacitor, Journal of Energy Storage, 86 (2024) 111146 (**I.F- 8.9**).
- 7) S. B. Bhosale, **S. S. Kumbhar**, S. S. Pujari, V. V. Patil, N. Kumar, R. R. Salunkhe, C. D. Lokhande, J. L. Gunjekar, U. M. Patil*, Development of binder-free, amorphous nickel vanadate cathodes by SILAR method for hybrid supercapacitors: Exploiting surface area by monitoring growth rate, Journal of Energy Storage, 72 (2023) 108417-108432 (**I.F- 8.9**).
- 8) V. V. Patil, S. S. Pujari, S. B. Bhosale, **S. S. Kumbhar**, V. G. Parale, C. D. Lokhande, J. L. Gunjekar, M. G. Mali, D. S. Mhamane, H. Park, U. M. Patil*, SILAR synthesized binder-free, hydrous cobalt phosphate thin film electrocatalysts for OER application: annealing effect on the electrocatalytic activity, International Journal of Energy Research, 2023 (2023) 1-17 (**I.F- 4.3**).
- 9) G. Kadam, S. Patil, B. Patil, S. Kumbhar, **S. Kumbhar**, S. Madake, L. Kadam, Y. Ma, S. Kadam, R. Nimat*, Dielectric behavior and phase transition of

La₂Mo₂O₉ thin films synthesized by spray pyrolysis technique, Journal of Materials Science: Materials in Electronics, 34 (2023) 387 (**I.F-2.8**).

- 10) S. S. Pujari, S. A. Kadam, Y. R. Ma, S. B. Jadhav, **S. S. Kumbhar**, S. B. Bhosale, J. L. Gunjekar, C. D. Lokhande, U. M. Patil*, Hydrothermally synthesized nickel copper phosphate thin film cathodes for high-performance hybrid supercapacitor devices, Journal of Energy Storage, 52 (2022) 105037 (**I.F-8.9**).
- 11) S. S. Pujari, S. A. Kadam, Y. R. Ma, S. B. Jadhav, **S. S. Kumbhar**, S. B. Bhosale, V. V. Patil, J. L. Gunjekar, C. D. Lokhande, U. M. Patil*, A binder-free facile synthetic approach for amorphous, hydrous nickel copper phosphate thin film electrode preparation and its application as a highly stable cathode for hybrid asymmetric supercapacitors, Sustainable Energy & Fuels, 6 (2022), 5608 (**I.F- 5**).
- 12) V. V. Patil, S. S. Pujari, S. B. Bhosale, **S. S. Kumbhar**, V. G. Parale, J. L. Gunjekar, H. Park, C. D. Lokhande, M. G. Mali, D. S. Mhamane, U. M. Patil*, Hydrous and amorphous cobalt phosphate thin-film electrodes synthesized by the SILAR method for high-performing flexible hybrid energy storage devices, Energy & Fuels, 36 (2022) 12791 (**I.F- 5.2**).

Book Chapter (01)

- 1) **S. S. Kumbhar**, S. J. Marje, V. V. Patil, S. B. Bhosale, S. S. Pujari, J. L. Gunjekar, C. D. Lokhande, U. M. Patil, 1D, 2D and 3D structured chalcogenides for supercapacitor applications, Chemically deposited nanocrystalline metal chalcogenide based carbon composite for versatile applications, Springer Nature, ISBN-13:9783031234002.

Presented/Attended, National/International Conferences, Workshops and Seminar (06)

- 1) Poster presentation at the National Conference on “Recent Trends in Functional Materials and Their Applications (RTFMA-2024) held at Shardabai Pawar Mahila Arts, Commerce & Science College Shardanagar, Malegoan, Baramati, from 13th to 14th March 2024.
- 2) Poster presentation at the “International Conference on Nanotechnology Addressing the Convergence of Materials Science, Biotechnology, and

Medical Science (IC-NACMBM-2024)” held at D. Y. Patil Education Society, Kolhapur, from 12th -14th February 2024.

- 3) Poster presentation in the International Conference on “Advanced Materials Synthesis, Characterisation and Application-2023 (AMSCA-2023)” held at Savitribai Phule Pune University, Pune, from 21st to 24th November 2023.
- 4) Attended DST-STUTI funded one-week training programme on “Hands-on Training on Sophisticated Instruments for Materials Science” organized by Bundelkhand University, Jhansi, from 14th to 20th September 2022.
- 5) Attended national seminar on “Emerging Nano Materials for Renewable Energy” organized by Sanjay Ghodawat University, Kolhapur, held on 26th December 2022.
- 6) Attended workshop & hands-on training on XRD organized by SAIF-CFC under STRIDE programme in the Shivaji University, Kolhapur held from 11th to 12th November 2021.

CONTENTS

Chapter No.	Chapter Name	Page No.
1	General Introduction and Literature Survey	1-36
2	Theoretical Background of CBS and SILAR Methods, and Characterization Techniques	37-66
3	Preparation of Cobalt Vanadium Oxide/Reduced Graphene Oxide Composite Electrodes by CBS Method and their Characterization and Supercapacitive Performance	67-118
4	Preparation of Cobalt Vanadium Oxide/Reduced Graphene Oxide Composite Electrodes by SILAR Method and their Characterization and Supercapacitive Performance	119-158
5	Fabrication of Hybrid Supercapacitor Devices and Performance Evaluation	159-178
6	Summary and Conclusions	179-186
7	80_Recommendation	187-188

List of Abbreviations

AC	Activated Carbon	LIBs	Lithium-Ion Batteries
AEESDs	Electrochemical Energy Storage Devices	MIBs	Metal Ion Batteries
AHSD	Aqueous Hybrid Supercapacitor Device	MOF	Metal-Organic Framework
ASD	Asymmetric Supercapacitor Device	MTMOs	Mixed Transition Metal Oxides
C	Capacitance	NEC	Nippon Electric Company
CBS	Chemical Bath Synthesis	NF	Nickel Foam
CNTs	Carbon Nanotubes	PD	Power Density
CNFs	Carbon Nanofibers	PPy	Polypyrrole
CPE	Constant Phase Element	R_s	Solution Resistance
CV	Cyclic Voltammetry	R_{ct}	Charge Transfer Resistance
CVO	Cobalt Vanadium Oxide	SAED	Selected Area Electron Diffraction
CVD	Chemical Vapor Deposition	SCs	Supercapacitors
DC	Direct Current	SE	Specific Energy
DDW	Double Distilled Water	SHSD	Solid-State Hybrid Supercapacitor Device
ED	Energy Density	SILAR	Successive Ionic Layer Adsorption and Reaction
EDLC	Electrochemical Double-Layer Capacitor	SOHIO	Standard Oil Company of Ohio
EDS	Energy-Dispersive X-ray Spectroscopy	SP	Specific Power
EDTA	Ethylenediaminetetraacetic Acid	S_p	Solubility Product
EIS	Electrochemical Impedance Spectroscopy	SSA	Specific Surface Area
FE-SEM	Field Emission Scanning Electron Microscopy	SS	Stainless Steel
FT-IR	Fourier Transform Infrared	TGA	Thermogravimetric Analysis
GCD	Galvanostatic Charge-Discharge	TMHs	Transition Metal Hydroxides
HNC	Hollow Nanocube	TMOs	Transition Metal Oxides
HR-TEM	High-Resolution Transmission Electron Microscopy	W	Warburg Impedance
HSCs	Hybrid Supercapacitors	XPS	X-ray Photoelectron Spectroscopy
HSD	Hybrid Supercapacitor Device	XRD	X-ray Diffraction
I_p	Ionic Product		
KE	Kinetic Energy		
LASER	Light Amplification by Stimulated Emission of Radiation		

List of Figures

Figure No.	Figure Name	Page No.
Chapter-1: General Introduction and Literature Survey		
1.1	Illustrative representation of SC operational process and associated parameters.	7
1.2	Schematic representation of charge storage mechanism of EDLC.	10
1.3	Schematic representation of charge storage mechanism of pseudocapacitor.	10
1.4	Various structures and phases of CVO.	15
1.5	Schematic illustration of preparation of rGO.	18
Chapter-2: Theoretical Background of CBS and SILAR Methods, and Characterization Techniques		
2.1	Utilizations associated with thin film materials-based devices.	38
2.2	Processes on a solid surface that lead to heterogeneous nucleation.	42
2.3	Particle growth via the processes of aggregation and coalescence.	43
2.4	Schematic illustration of SILAR thin film deposition method.	48
2.5	Schematic illustration of substrate surface featuring various forms of nucleation sites.	50
2.6	Schematic of thin film growth mechanisms.	51
2.7	Schematic diagram of (a) half-cell electrochemical (three-electrode) system and (b) full-cell (two-electrode) systems.	59
2.8	The CV curve of the single electrode with reversible redox reaction.	60
2.9	Plot of GCD curve.	62
2.10	(a) Nyquist plot without Warburg and inset its Randles circuit and (b) Nyquist plot with Warburg and inset its Randles circuit.	65
Chapter-3: Preparation of Cobalt Vanadium Oxide/Reduced Graphene Oxide Composite Electrodes by CBS Method and their Characterization and Supercapacitive Performance		

3.1	Schematic representation of precursors ratio variation of C-CV thin films by chemical bath synthesis method.	70
3.2	Bar diagram of loading mass of CVO on SS substrate.	73
3.3	XRD patterns of precursors molar concentration ratio variation of C-CV series thin films on SS substrate.	74
3.4	FT-IR spectra of C-CV thin films series (C-CV1, C-CV2, C-CV3, C-CV4, and C-CV5).	75
3.5	(a) XPS full survey spectra and the corresponding (b) Co 2p, (c) V 2p, and (d) O 1s of the sample C-CV4.	76
3.6	FE-SEM images and histograms of C-CV series thin films: (a1-a4) C-CV1, (b1-b4) C-CV2, (c1-c4) C-CV3, (d1-d4) C-CV4, and (e1-e4) C-CV5 at different magnifications of X1,000, X10,000, and X40,000.	78
3.7	Schematic illustration of morphological changes of C-CV series samples.	79
3.8	EDS mapping of (a-d) C-CV1, (e-h) C-CV2, (i-l) C-CV3, (m-p) C-CV4, and (q-t) C-CV5.	80
3.9	(a-e) EDS spectra of C-CV series samples.	81
3.10	N ₂ adsorption-desorption isotherms and inset pore size distribution of samples (a) C-CV1, (b) C-CV2, (c) C-CV3, (d) C-CV4, and (e) C-CV5.	82
3.11	(a) At 50 mV s ⁻¹ scan rate comparative CV curves, (b-f) CV curves of C-CV series electrodes at different scan rates (2-50 mV s ⁻¹).	84
3.12	(a) The plot of log (peak current) vs the log (scan rate) for C-CV series electrodes, (b) the plot of the total charge against the reciprocal of the square root of scan rate for C-CV series electrodes, and (c) comparative plot of surface and diffusive charge contribution to C-CV series electrodes, and (d-h) charge contribution of C-CV series samples at different scan rates.	86
3.13	(a) Comparative GCD curves of C-CV series electrodes at 1 A g ⁻¹ current density, (b-f) GCD curves at different current densities from 1 to 5 A g ⁻¹ of C-CV series electrodes, (g) the bar diagram of Cs at 1 A g ⁻¹ current density of C-CV series electrodes, (h) bar diagram of Cs vs current density, and (i) bar diagram of specific capacity vs current density (1-5 A g ⁻¹) of C-CV series.	88
3.14	(a) Nyquist plots of C-CV series electrodes and (b) cyclic stability of C-CV4 electrode.	89
3.15	(a-f) Synthesis procedure of GO by Modified Hummer's method.	92

3.16	XRD patterns of GO and rGO.	93
3.17	Raman spectrum of rGO.	94
3.18	CV curves of rGO electrode at different scan rates.	95
3.19	GCD curves of rGO electrode at 2-6 A g ⁻¹ current densities.	96
3.20	Nyquist plot of rGO, inset fitted circuit, and magnified view of a semicircle at higher frequency.	97
3.21	Schematic illustration of the preparation of C-CVR series electrodes by CBS method.	98
3.22	The plot of loading mass of C-CVR series on unit area of SS substrate.	99
3.23	XRD patterns of rGO, pristine C-CVR0, and C-CVR1 to C-CVR4 composite material samples.	100
3.24	FT-IR spectra of pristine C-CVR0 and C-CVR1 to C-CVR4 samples.	102
3.25	Raman spectra of rGO and C-CVR0 to C-CVR4 samples.	103
3.26	XPS spectra of pristine C-CVR0 and C-CVR3 samples and the corresponding (a) survey, (b) Co 2p, (c) V 2p, (d) O 1s, and (e) C 1s of the samples C-CVR3 and rGO.	105
3.27	TGA plot of C-CVR series samples.	106
3.28	FE-SEM images and histograms of (a1-a4) C-CVR0, (b1-b4) C-CVR1, (c1-c4) C-CVR2, (d1-d4) C-CVR3, and (e1-e4) C-CVR4 samples.	107
3.29	EDS mapping of (a1-a5) C-CVR0, (b1-b5) C-CVR1, (c1-c5) C-CVR2, (d1-d5) C-CVR3, and (e1-e5) C-CVR4.	108
3.30	EDS spectra of C-CVR series samples.	109
3.31	(a-d) HR-TEM images of C-CVR3 sample, (e) HR-TEM lattice fringes with line profile showing ($\bar{1}31$) hkl plane of CVO/rGO composite material, and (f-j) Co, V, O, and C elemental mapping of C-CVR3.	110
3.32	Adsorption-desorption isotherms of SSA and inset pore size distribution of samples (a) C-CVR0, (b) C-CVR1, (c) C-CVR2, (d) C-CVR3, and (e) C-CVR4.	111
3.33	(a) At 20 mV s ⁻¹ scan rate comparative CV curves of pristine C-CVR0 and C-CVR1 to C-CVR4 composite electrodes, (b-f) CV curves of pristine C-CVR0, and C-CVR1 to C-CVR4 composite electrodes at different scan rates (2-50 mV s ⁻¹).	112
3.34	(a) Plot of log (scan rate, mV s ⁻¹) vs log (current density, A ⁻¹) for C-CVR series electrodes, (b) the plot of the total charge against the reciprocal of the square root of potential scan rate for C-CVR series electrodes, and (c-g)	113

	plots of surface and diffusive charge contribution of C-CVR series at different scan rate.	
3.35	(a) The comparative GCD curves of C-CVR series electrodes at fixed current density (1 A g^{-1}), (b-f) the GCD curves of C-CVR0, C-CVR1, C-CVR2, C-CVR3, and C-CVR4 electrodes at different current densities from $1\text{-}5 \text{ A g}^{-1}$, (g) plot of C_s vs current density, and (h) plot of specific capacity vs current density.	115
3.36	(a) Nyquist plot of C-CVR series electrodes, and (b) cyclic stability of C-CVR3 electrode.	116
Chapter-4: Preparation of Cobalt Vanadium Oxide/Reduced Graphene Oxide Composite Electrodes by SILAR Method and their Characterization and Supercapacitive Performance		
4.1	Schematic representation of dip time variation of S-CV series thin films by SILAR method.	121
4.2	Plot of loading mass of S-CV on SS substrate.	123
4.3	(a) XRD patterns of S-CV series thin films with dip time variation (S-CV1, S-CV2, and S-CV3).	124
4.4	FT-IR spectra of S-CV series materials (S-CV1, S-CV2, and S-CV3).	125
4.5	(a) XPS full survey spectra and the corresponding (b) Co 2p, (c) V 2p, and (d) O 1s of the sample S-CV2.	126
4.6	FE-SEM and histogram images of S-CV series samples: (a1-a4) S-CV1, (b1-b4) S-CV2, and (c1-c4) S-CV3 at different magnifications.	127
4.7	EDS mapping of CVO thin film samples (a-d) S-CV1, (e-h) S-CV2, (i-l) S-CV3, and (m) EDS spectrum of S-CV2 thin film.	128
4.8	Adsorption-desorption isotherms and inset pore size distribution of samples (a) S-CV1, (b) S-CV2, and (c) S-CV3.	130
4.9	(a) At 20 mV s^{-1} scan rate, comparative CV curves of S-CV series electrodes, CV curves of (b) S-CV1, (c) S-CV2, and (d) S-CV3 at different scan rates.	131
4.10	Plot of \log (current density, A g^{-1}) versus \log (scan rate, mV s^{-1}) for electrode (a) S-CV1, (b) S-CV2, and (c) S-CV3, (d) the plot of total charge against the reciprocal of the square root of scan rate for S-CV series electrodes, (e) comparative plot of surface and diffusive charge contribution at fixed scan rate (S-CV1, S-CV2, and S-CV3), and (f-h) plots of surface and diffusive charge	133

	contribution of S-CV series at different scan rate.	
4.11	(a) The comparative GCD curves of S-CV series electrodes at fixed current density, (b-d) the GCD curves of S-CV series electrodes at different current densities from 1-5 A g ⁻¹ , (e) plot of Cs vs current density, and (f) plot of specific capacity vs current density.	134
4.12	(a) Nyquist plots of S-CV series electrodes, and (b) cyclic stability of S-CV2 electrode.	135
4.13	(a) Schematic representation of SILAR synthesis of CVO/rGO composite and (b) photographs of S-CVR series thin films.	138
4.14	Bar diagram of loading mass on 1x1 cm ² SS substrate.	139
4.15	XRD patterns of rGO, S-CVR series samples.	141
4.16	FT-IR spectra of S-CVR series samples.	142
4.17	Raman spectra of rGO, S-CVR series samples.	143
4.18	XPS spectra of pristine S-CVR0 and S-CVR2 samples and the corresponding (a) survey, (b) Co 2p, (c) V 2p, (d) O 1s, and (e) C 1s of the samples S-CVR2 and rGO.	144
4.19	TGA plot of S-CVR series samples.	145
4.20	FE-SEM images and histograms of (a1-a4) S-CVR0, (b1-b4) S-CVR1, (c1-c4) S-CVR2, and (d1-d4) S-CVR3 thin films.	146
4.21	EDS mapping of CVO/rGO series samples.	147
4.22	EDS spectra of CVO/rGO composite series samples.	148
4.23	(a-d) HR-TEM images of S-CVR2 sample, (e) HR-TEM lattice fringes with line profile showing (002) hkl plane of CVO/rGO composite material, (f) SAED pattern, and (g-k) Co, V, O, and C elemental mapping of S-CVR2.	149
4.24	Adsorption-desorption isotherms and inset BJH plots of (a) S-CVR0, (b) S-CVR1, (c) S-CVR2, and (d) S-CVR3 samples.	150
4.25	(a) At 20 mV s ⁻¹ scan rate comparative CV curves of S-CVR series electrodes, (b-e) CV curves of S-CVR0, S-CVR1, S-CVR2, and S-CVR3 electrodes at different scan rates (2-50 mV s ⁻¹).	151
4.26	(a) Plot of log (current density, A g ⁻¹) versus log (scan rate, mV s ⁻¹) for S-CVR series electrodes, (b) the plot of total charge against the reciprocal of the square root of potential scan rate for S-CVR series electrodes, (c) comparative plot of surface and diffusive charge contribution at fixed scan rate (S-CVR series), and (d-g) plots of surface and diffusive charge contribution of S-	152

	CVR series at different scan rate.	
4.27	(a) The comparative GCD curves of S-CVR series electrodes at fixed current density (1 A g^{-1}), (b-e) the GCD curves of S-CVR0, S-CVR1, S-CVR2, and S-CVR3 electrodes at different current densities from $1\text{-}5 \text{ A g}^{-1}$, (f) bar diagram of C_s vs current density, and (g) bar diagram of specific capacity vs current density.	154
4.28	(a) Nyquist plot of S-CVR series electrodes, and (b) cyclic stability of S-CVR2 electrode.	155
Chapter-5: Fabrication of Hybrid Supercapacitor Devices and Performance Evaluation		
5.1	Schematic representation of C-AHSD.	161
5.2	Comparative CV curves plot of rGO and C-CVR3 electrode at 50 mV s^{-1} scan rate.	162
5.3	(a) Voltage variation in CV curves of C-AHSD at fixed scan rate (50 mV s^{-1}), and (b) CV curves of C-AHSD at different scan rates in optimal voltage 0 to 1.6 V.	163
5.4	(a) Voltage window variation GCD curves of C-AHSD at fixed current density (2.3 A g^{-1}), (b) GCD curves of C-AHSD at different current densities (1.6 to 2.6 A g^{-1}), (c) bar diagram of C_s vs current density, and (d) Ragone plot of C-AHSD.	163
5.5	(a) Nyquist plot of C-AHSD and (b) Plot of capacitance retention and Coulombic efficiency vs cycle number.	164
5.6	Photographs of $4 \times 4 \text{ cm}^2$ electrodes of rGO, C-CVR3, and fabricated leakproof device.	165
5.7	(a) CV curves of voltage variation (C-SHSD) at fixed scan rate (50 mV s^{-1}) and (b) CV curves at different scan rates 5 to 100 mV s^{-1} at optimal voltage range (0 to 1.6 V).	166
5.8	The GCD curves of C-SHSD (a) variation of voltage window (0 to 1.2-1.6 V) and (b) at different current densities from 1.4 A g^{-1} to 2.6 A g^{-1} .	167
5.9	(a) Bar diagram of C_s vs current density and (b) Ragone plot of C-SHSD.	167
5.10	(a) The Nyquist plot of C-SHSD (inset: fitted equivalent circuit) and (b) the capacitive retention and Coulombic efficiency vs cycle number plot of C-SHSD.	168
5.11	(a-c) C-CVR3//PVA-KOH//rGO C-SHSD practical demonstration photographs.	169
5.12	Comparative CV curves of rGO and S-CVR2 at 20 mV s^{-1} scan rate.	170

5.13	(a) Voltage variation in CV curves of S-AHSD at fixed scan rate 50 mV s ⁻¹ , and (b) CV curves of S-AHSD at different scan rates in the voltage range of 0 to 1.6 V.	171
5.14	(a) Voltage variation GCD curves of S-AHSD at fixed current density, (b) GCD curves of S-AHSD at different current densities (0.5 to 1.1 A g ⁻¹), (c) plot of Cs vs current density, and (d) Ragone plot of S-CVR2//KOH//rGO S-AHSD.	171
5.15	(a) The Nyquist plot of S-AHSD (inset: fitted equivalent circuit) and (b) plot of the capacitive retention and Coulombic efficiency vs cycle number.	172
5.16	Photographs of 4x4 cm ² electrodes of rGO, S-CVR2, and fabricated S-CVR2//PVA-KOH//rGO S-SHSD.	173
5.17	(a) Voltage variation CV curves of S-SHSD at fixed scan rate (50 mV s ⁻¹), and (b) CV curves of S-SHSD at different scan rates in the optimal voltage of 0 to 1.6 V.	173
5.18	(a) The GCD curves of S-SHSD, (b) bar diagram of Cs vs current density, and (c) Ragone plot of S-SHSD.	174
5.19	(a) Nyquist plot of S-SHSD and (b) plot of capacitive retention and Coulombic efficiency vs cycle number.	175
5.20	Photographs of glowing LED using S-SHSDs.	175
Chapter-6: Summary and Conclusions		
6.1	(a-c) C-SHSD practical demonstration photographs.	183
6.2	(a-c) Photographs of S-SHSDs (S-CVR2//PVA-KOH//rGO) practical demonstration.	184
6.3	(a) FE-SEM image of C-CVR3, (b) bar diagram of Cs vs current density for C-CVR3 electrode, (c) FE-SEM image of S-CVR2, and (d) bar diagram of Cs vs current density for S-CVR2 electrode.	185

List of Tables and Charts

Table 1.1	A comparative structural, morphological, and three-electrode system electrochemical analysis of the CVO and their composite materials literature survey.	22
Table 1.2	Literature study of CVO and their composite hybrid, symmetric, and asymmetric SC devices.	29
Table 2.1	Common electrical components.	63
Table 3.1	Preparative parameters for the synthesis of C-CV series thin film electrodes.	71

Table 3.2	EIS circuit fitted values of C-CV series electrodes.	89
Table 3.3	EIS circuit fitted values of rGO electrode.	97
Table 3.4	Preparative parameters for the synthesis of C-CVR series electrodes.	98
Table 3.5	EIS circuit fitted values of C-CVR series electrodes.	116
Table 4.1	Preparative parameters for the synthesis of S-CV series thin film electrodes.	122
Table 4.2	EIS circuit fitted values of S-CV series electrodes.	136
Table 4.3	Preparative parameters for the synthesis of S-CVR series electrodes.	139
Table 4.4	EIS circuit fitted values of S-CVR series electrodes.	155
Table 6.1	HSC devices electrochemical performance.	186
Chart 1.1	Categorization of SCs based on charge storage mechanism of electrodes.	8
Chart 2.1	Categorization of approaches for thin film preparation.	39

CHAPTER-1

General Introduction and Literature Survey

CHAPTER-1

General Introduction and Literature Survey

Sr. No.	Title		Page No.
1.1	General Introduction		1
	1.1.1	Essentiality of Supercapacitor	1
	1.1.2	Overview and Present Perspectives of Supercapacitors	3
	1.1.3	Fundamental and Working Concept of Supercapacitors	6
1.2	Categorization of Supercapacitors		8
	1.2.1	Electric Double Layer Capacitor (EDLC)	9
	1.2.2	Pseudocapacitors	10
		1.2.2.1 Intrinsic Pseudocapacitor	11
		1.2.2.2 Intercalation Pseudocapacitor	11
		1.2.2.3 Extrinsic Pseudocapacitor	12
	1.2.3	Hybrid Supercapacitors	12
1.3	Materials for Supercapacitors		13
	1.3.1	Transition Metal Oxides for Supercapacitor	13
	1.3.2	Introduction of Cobalt Vanadium Oxide	13
	1.3.3	Introduction of Reduced Graphene Oxide	16
1.4	Literature on Cobalt Vanadium Oxides and their Composite Materials		19
1.5	Literature on Supercapacitor Devices of Cobalt Vanadium Oxides and their Composite Materials		26
1.6	Orientation and Purpose of Thesis		32
1.7	References		34

1.1 General Introduction

1.1.1 Essentiality of Supercapacitor

The need to investigate substitute and maintainable devices of energy conversion and storage with suitable energy density (ED) and power density (PD), paired with affordable and environmentally benign materials, has been driven by growing concern over environmental contamination and the depletion of fossil fuels [1]. Developing secure, clean, and environmentally friendly renewable energy sources is required to address environmental contamination and the depletion of fossil fuels issues. Sources of renewable energy may be able to tackle this issue quickly and for no cost, giving them a unique development potential. Electric energy can be produced by transforming natural sources of energy like the sun, tides, and winds into renewable and sustainable resources. The major issue with renewable energy is its unpredictable availability. So, many researchers are working to prepare and improve the effectiveness of energy storage devices (ESDs) using a range of power sources to produce clean and green energy.

Several appliances require electrical ESDs, including hybrid cars, computers, solar cells, mobile phones, etc. Electric equipments are widely employed in household and industrial settings and plays a significant role in our daily lives. Also, depending on the situation, electrical energy can easily be turned into mechanical energy, heat, and light. Electricity is difficult to always have on hand in the needed form, though. Thus, a robust ESD that can hold a lot of energy is required. To satisfy the energy requirements of contemporary society, massive power generation is the genuine need for storing energy. Energy moves incredibly quickly and has no expiration date when it is flowing as electricity. Energy-consuming equipment is immediately used after being prepared from a source of energy and the remaining energy is lost. So, storing energy is essential for use at a later use [2, 3]. To replace harmful fossil fuels, research is now focused on preparing green ESDs to address the significant variability in wind and solar power production, which complicates grid connection and the supply of consistent power. This highlights the significance of ESDs that work by integrating batteries into electrical networks so that green sources of energy may be added with ease [4, 5]. Renewable energy is stored in batteries, which supply the grids as needed, improving the smoothness and predictability of the power supply. Moreover, ESDs can be used to obtain

electricity from renewable sources in places without access to the grid. In the battery, energy is stored chemically within the electrode through an electrochemical reaction that takes place in the electrode material due to the movement of ions from the electrolyte. This stored energy is released when a load is applied across the battery. In the battery's charge storage reaction, an electrolyte acts as an ion carrier. Due to their rising demand in various applications, batteries' storage capacity has recently improved thanks to proper standards. Until now, there is not yet a solution for the issues with batteries, such as their short lifespan and poor PD. So, in the current environment, it is necessary to design a device with unique characteristics like high PD, ED, and long cycle life [6].

Moreover, a capacitor is a different energy-storing device that primarily acts as a filter in electrical circuits and electric energy stores in the range of micro-Farad (μF). In capacitors, two conducting plates are separated by an insulating substance called a dielectric. When the potential is applied between two plates, one acquires a positive charge, and the other a negative charge; whenever a potential is removed, the charges dissipate through load [7]. In an electronic circuit, it is essential for two different reasons. By doing so, one is charging/discharging the electricity, resulting in some beneficial effects on that circuit. For example, it smooths the circuits of power sources, and microcomputers enabled backup circuits and the current flow for a charging-discharging duration controlled through timer circuits. The capacity to halt the circuit's direct current (DC) supply is another purpose for the capacitor. When only a single frequency's manifestation is required, it is advantageous to delete or erase other frequencies. The drawback of a capacitor is that it can only hold a small amount of electrical energy, which means that it is useless for high-energy applications [8]. Capacitors and batteries are incapable of meeting the enormous energy requirements of today's high-power equipments, together with their need for rapid delivery. The only source of high power now available for portable devices and hybrid cars is electrochemical energy systems. Due to their clean, affordable, and environmentally friendly character, electrochemical ESDs are more advantageous than burning fuel methods and are crucial from an environmental standpoint. The creation of high-performance, lightweight, flexible, and affordable ESDs is essential to meet future energy needs. Researchers have been motivated by this circumstance to look into

more advanced ESDs, like sodium-ion batteries, supercapacitors (SCs), and lithium-ion batteries (LIBs). Recently, SCs have been prepared to meet the primary needs of ordinary capacitors and batteries.

The LIBs and the SCs, both of which are used in electrochemical systems for storing energy, are two of the most appealing next-generation technologies. The primary features to examine the behaviour of electrochemical ESDs for storing energy, especially in practical implementations, are ED and PD, cycle longevity, specific capacitance (Cs), affordability, and security tolerance. SCs have several noteworthy characteristics, such as a power delivery capacity of up to 10 kW kg^{-1} , a long cycle lifetime ($>100,000$ cycles), and quick charge-discharge processes (in a few seconds) [9, 10]. Also, it connects the power/energy gap between conventional dielectric capacitors and batteries, with a broad spectrum of uses along with portable electronics and backup for memory systems, hybrid electric cars, energy management, and mass-scale power. The precise output of energy and power refers to conventional modern batteries and SCs, respectively. SCs use electrode materials with a large specific surface area (SSA) and thin electrolyte dielectric layers to obtain higher Cs values than regular capacitors. Hence, they can store both high PD (compared with batteries) and high ED (in comparison to capacitors). Because of this, they are appropriate for applications that need a lot of energy in a short period with better cycle stability.

1.1.2 Overview and Present Perspectives of Supercapacitors

In 1957, 'General Electric Company' discovered the practical application of double-layer capacitors for electrolytic capacitors by using porous carbon electrodes [11]. This event marked the beginning of the history of SCs. At the time of its discovery, the capacitor displayed an unexpectedly high capacitance (C). The actual charge storage mechanism of the SC was still unknown, despite the belief that energy was kept within the carbon pores. Despite its high C, the device was not made available in the market due to its impractical design. Moreover, the battery market was already established, and the device required both electrodes to be immersed in an electrolyte vessel, making it less commercially viable. The Standard Oil Company of Ohio (SOHIO) used high-surface-area carbon compounds in tetra-alkyl ammonium electrolytes in 1966, which led to substantial advancements in ESDs [12]. Despite the breakthrough, SOHIO was unable to bring their invention to

the market. In 1978, Nippon Electric Company (NEC) obtained a license from SOHIO and successfully marketed the SCs as a power backup source for preserving computer memory and powering a range of consumer devices. In 1975, B. E. Conway introduced a new approach to the mechanism of charge storage, this relied on rapid and reversible redox reactions happening near the surface of the electrode material. Subsequently, the first pseudocapacitor was prepared using ruthenium dioxide (RuO_2) film electrodes [13-15]. It is important to note that a SC is also referred to as a pseudocapacitor.

Currently, the capacitors that are commercially accessible in the market consist of activated carbonaceous material with an enlarged SSA and highly redox-active RuO_2 [16]. During the 1980s, several companies started manufacturing electrochemical capacitors. 'Panasonic', formerly known as 'Matsushita Electric Industrial Co.', was one of these companies, and it developed a new type of capacitor called the 'Gold Capacitor' [17]. The primary distinction between the devices produced by Panasonic and NEC was the type of electrolyte used. While NEC utilized an electrolyte (aqueous), Panasonic opted for a non-aqueous electrolyte. In 1987, ELNA began manufacturing a double-layer capacitor, which they named the 'Dyna capacitor' [18]. In 1982, 'PRI Ultracapacitors' created the first high-power double-layer capacitors, which utilized metal-oxide electrodes [19]. In 1990, the entire research community focused on developing SC devices with better performance. The emergence of SC devices piqued the interest of researchers, leading the 'United States Department of Energy' to commence the study on their potential application in hybrid electric vehicles. By 1992, Maxwell Laboratories had initiated a development program for ultracapacitors [18]. From the emergence of SCs until 1998, only four companies dominated the market: NEC-Token, Panasonic, Maxwell Technologies, and Elena Capacitors. Between 1999 and 2013, numerous suppliers offered SCs to meet the high global demand, which exceeded market growth estimates. By 2013, the carbon dielectric SC market was fiercely contested by 40 companies worldwide. As stated by Paomanok's investigation data, the utilization of electrochemical double-layer capacitor (EDLC) SCs had increased by 275%, while the number of vendors supplying the market had grown by 1000% [20]. This indicates a significant expansion in both supply and demand for SCs after 2013. The SC market is currently dominated by products

originating from Japan, the United States, and Russia. Each country's SC offerings possess distinct characteristics and advantages, including variances in capacity, power, price, and other factors. The SC market is anticipated to expand to USD 912 million by 2027, exhibiting a robust growth trajectory from USD 520 million in 2023. This represents a compound annual growth rate of 14.1% during the forecast period [21]. At present, a significant portion of the market is focused on symmetric SCs, where activated carbon (AC) is utilized as the preferred electrode material.

SCs, an emerging ESD, are poised to have a substantial impact on the future of ESDs. One key characteristic of SCs is their ability to store large amounts of energy, making them a crucial choice for various manufacturers [22]. Ongoing research advancements are boosting the popularity of SCs in global markets, particularly in rail transportation and automotive industries, where they are creating new opportunities such as grid energy storage, while the rising demand for hybrid vehicles, driven by stringent government carbon emission regulations, is further pushing the growth of the SC market. [23]. The changing landscape of consumer electronics, like sensors and cell phones, requires diverse power solutions to support their numerous functionalities. As a result, there is a growing industry interest in SCs, which offer advantages over batteries in terms of PD and durability. SCs possess the capability to provide substantial at high power energy levels and rapid charge-discharge rates, making them suitable for powering multifunctional electronic devices. However, the practicality of SCs in industrial applications is hindered by their relatively low ED. Currently, researchers are actively exploring different approaches to enhance the ED of SCs while maintaining their other desirable features, aiming to overcome this limitation. Over the past few decades, carbon-based materials have been commonly employed in commercial SCs. The utilization of carbon-based materials in commercial SCs has been restricted due to their limited Cs. However, recent studies indicate that pseudocapacitive transition metal oxides (TMOs) show immense promise as electrode materials for SCs. These materials offer advantages such as cost-effectiveness, lower resistance, and environmental friendliness, making them a more favorable option for future SC applications [24]. Moreover, the energy-storing capacity of SCs has been significantly enhanced through the reversible and rapid surface redox reactions of pseudocapacitive materials. However, the cycling

lifespan of these materials is limited due to the breakdown of the active material in the aqueous electrolyte during repeated use. As a result, there is a growing interest in exploring solid-state SCs, which employ solid polymer (gel-type) electrolytes. Solid-state SCs offer numerous advantages over their aqueous counterparts, including the mitigation of electrolyte leakage issues, improved flexibility, and ease of handling [25]. Additionally, ongoing research has been directed toward enhancing SCs through the utilization of diverse ionic liquid electrolytes. These electrolytes offer notable advantages as they are non-toxic and exhibit high thermal stability. Furthermore, SCs incorporating these ionic liquid electrolytes have the potential to operate within an extended voltage range, reaching up to 4-6 V [26]. The electrochemical performance of a SC depends not only on the electrode material but also on the electrolyte, separator, and current collector. Selecting the appropriate electrode material, which is both non-toxic and cost-effective, along with a compatible electrolyte, enhances the Cs and ED of the SC [27].

1.1.3 Fundamental and Working Concept of Supercapacitors

A capacitor consists of two metallic plates separated by a dielectric material. When a DC voltage is applied across the metallic plates, one plate becomes positively charged while the other becomes negatively charged. It reaches its maximum charge capacity, after which, upon disconnecting the DC voltage, both plates retain their respective charges for a period, effectively transforming the capacitor into a source of electrical energy. As the load is connected across the metallic plates, the capacitor undergoes a discharge process as current flows through the external load [28, 29]. The working principle of the capacitor is illustrated in Figure 1.1. The calculation of charge stored in a capacitor is determined by the formula:

$$Q = C \times V \quad (1.1)$$

Where, Q , C , and V are stored charge, capacitance, and voltage, respectively. However, it is important to note that the Farad is the unit of C . Using equation 1.1 alone may not be accurate or convenient as the actual C depends on factors such as the dimensions of the metal plates and the characteristics of the dielectric medium. The C of a capacitor can be determined using the equation (1.2).

$$C = \frac{\epsilon A}{d} \quad (1.2)$$

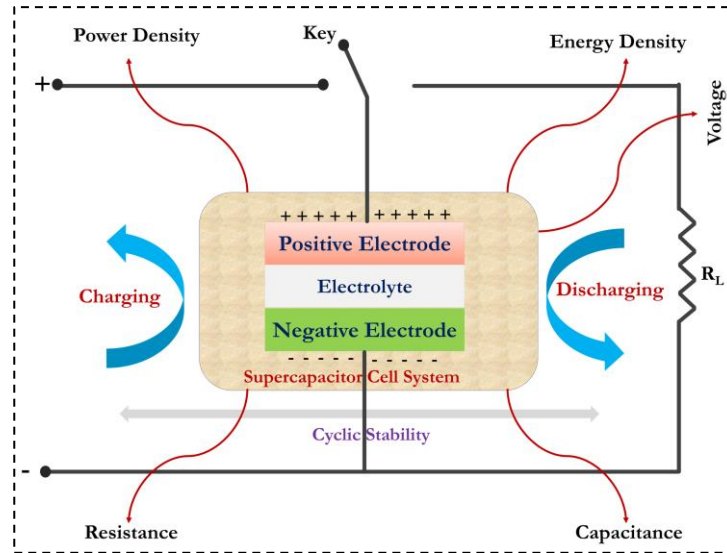


Figure 1.1 Illustrative representation of SC operational process and associated parameters.

In this equation, C represents capacitance, ϵ represents the permittivity of the dielectric, A corresponds to the surface area of each plate, and d refers to the distance between the two metal plates or thickness of the dielectric medium. Hence, the C is influenced by both the surface area and the distance between the metal plates, as well as the permittivity of the dielectric medium.

The working principle of a SC is similar to that of a capacitor. Typically, an SC consists of four main components: electrodes coated with electroactive materials, an electrolyte (either organic or aqueous), a current collector, and a separator. When the SC electrodes are immersed in the electrolyte, charges accumulate at the interface between the electrode and the electrolyte, creating an electrochemical double layer.

The calculation of the C_s from galvanostatic charge-discharge (GCD) for the SC is determined through the subsequent equation.

$$C_s = \frac{I \times \Delta t}{m \times \Delta V} \quad (1.3)$$

In this context, C_s represents the specific capacitance, I is the current density, t is the discharging time, V denotes the operational potential window of the SC, and m denotes the active material's mass.

The calculation for the ED and PD of the SC can be conducted in the following manner.

$$ED = \frac{1}{2} CV^2 \quad (1.4)$$

$$PD = \frac{ED}{\Delta t} \quad (1.5)$$

Where C, V, and t represent the capacitance, voltage window, and discharge time, respectively.

1.2 Categorization of Supercapacitors

The SCs are categorized based on their charge storage mechanism into three types: EDLCs, pseudocapacitors, and hybrid capacitors. Chart 1.1 illustrates the various types and subtypes of SCs.

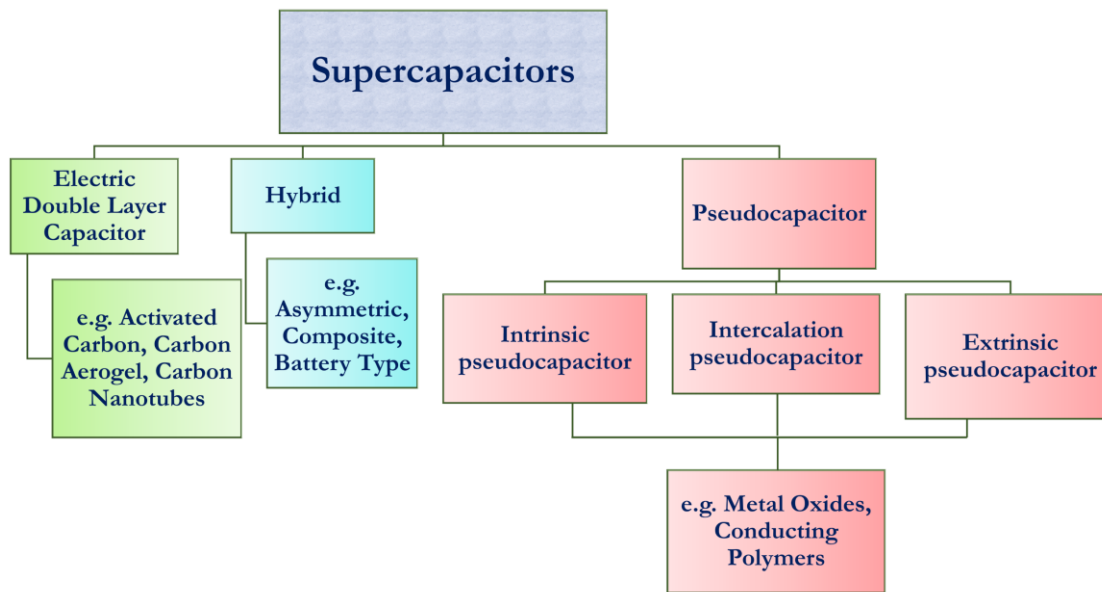


Chart 1.1 Categorization of SCs based on charge storage mechanism of electrodes.

In the process of charge storage in SCs, three distinct charge storage mechanisms are involved: faradic, non-faradic, and a combination of both, known as the hybrid process. In the case of EDLC-type SCs, charge storage occurs through non-faradic processes, specifically by forming an electrochemical double-layer that operates electrostatically. Conversely, in pseudocapacitor-type SCs, charge storage takes place through reversible faradic processes [30-32]. Pseudocapacitors employ a charge storage mechanism that involves the transfer of electrons. To facilitate this process, pseudocapacitive materials are required to have multiple oxidation states, enabling redox reactions. Therefore, materials such as TMOs, hydroxides, phosphides, sulfides, conducting polymers, phosphates, layer double hydroxides, and similar substances are suitable for use as electrodes in pseudocapacitors [33, 34]. Hybrid SCs (HSCs) incorporate both faradaic and non-faradaic charge storage

mechanisms. These HSCs are constructed using carbon-based materials combined with metal oxides, conducting polymers, or a combination of both. The selection of electrode materials is of utmost importance in SCs, as they significantly impact the electrochemical performance enhancement of the device.

1.2.1 Electric Double Layer Capacitor (EDLC)

The EDLC is the most prevalent and extensively researched type of SC. In EDLCs, the C is generated through the adsorption of both anions and cations at the interface between the electrode and electrolyte [35]. The capacity of EDLCs is significantly influenced by the surface characteristics of the electrode materials, such as the SSA and the distribution of pores. These surface properties determine the accessibility of electrolyte ions to the electrode, thereby playing a crucial role in the C of EDLCs. In the charging process, electrons flow from the negative electrode to the positive electrode through the external circuit, while anions migrate towards the positive electrode. In contrast, during the discharging process, the cations migrate towards the negative electrode while the electrons and ions change their direction of movement [36, 37]. The Helmholtz model is a simple approach to describe the double-layer C in this process, utilizing the equation (1.2) for a parallel plate capacitor.

In the equation (1.2), the double-layer C is determined by the permittivity (ϵ) of the dielectric that separates the charges, the surface area (A) of the electrode, and the thickness of the layer (d) of adsorbed ions over the surface. Carbon-based porous materials like AC [38, 39], carbon nanotubes (CNTs) [40, 41], xerogels [42, 43], carbon nanofibers (CNFs) [44, 45], carbide-derived carbons [46, 47], and graphene [48, 49], commonly exhibit EDLC characteristics due to their high SSA, electrochemical inertness, and conductivity. The charge and discharge process in EDLCs is attributed to purely non-Faradaic reactions, enabling them to respond promptly to changes in potential. Figure 1.2 demonstrates the charge storage mechanisms of EDLC-based materials.

The cyclic voltammetry (CV) curves of these materials exhibit a distinctive rectangular box shape, while the GCD profiles display a symmetrical triangular pattern. The limited ED values, particularly in terms of volumetric ED, pose a challenge to the practical implementation of carbon-based SCs. Hence research prioritizes the optimization of synthesis conditions to improve the performance-

enhancing factors of carbon-based SCs, including SSA, pore size distribution, and electrical conductivity [50].

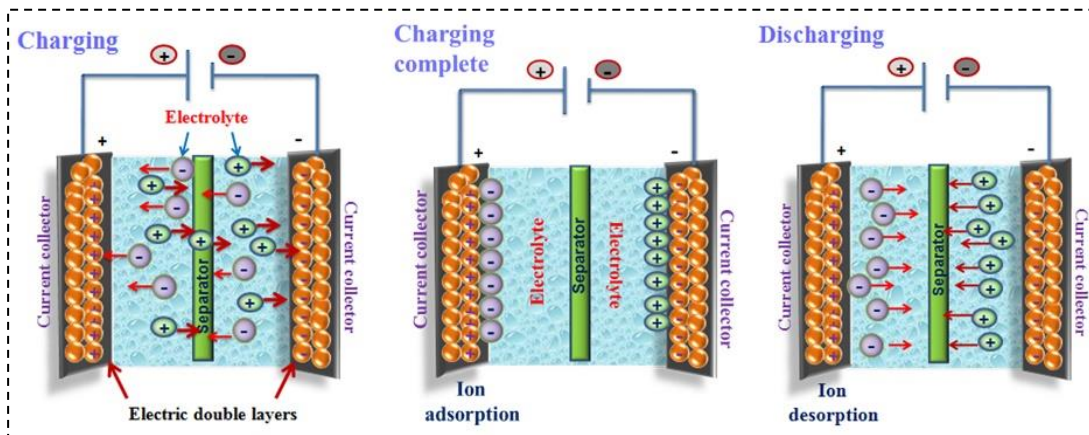


Figure 1.2 Schematic representation of charge storage mechanism of EDLC.

1.2.2 Pseudocapacitors

Pseudocapacitors exhibit rapid and reversible redox surface reactions facilitated by the movement of charges between the electrode and electrolyte. Charges can be stored through reversible faradaic reactions. Figure 1.3 illustrates the schematic representation of the charge storage mechanism in pseudocapacitors.

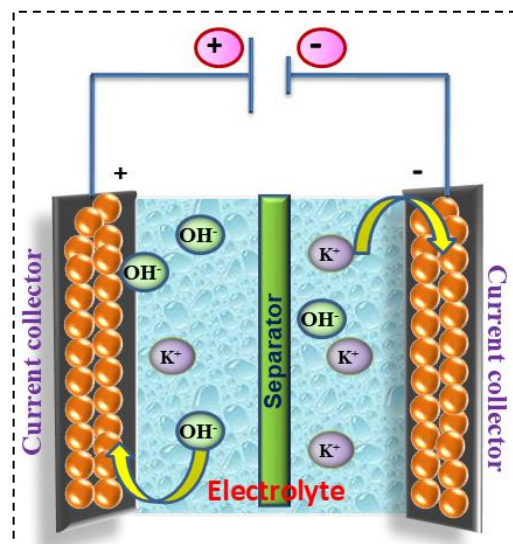


Figure 1.3 Schematic representation of charge storage mechanism of pseudocapacitor.

Pseudocapacitors have the potential to exhibit higher C and EDs compared to EDLCs because they utilize reversible faradaic processes in charge storage. The performance of pseudocapacitors relies heavily on the particle size, SSA, and conductivity of the active material since the reversible faradaic reactions primarily

occur at the electrode surface. Based on the charge storage mechanisms, pseudocapacitors can be categorized into three types: a) intrinsic pseudocapacitors, involving faradaic reactions on or near the material surface, b) intercalation-type pseudocapacitors, where the charge is stored within tunnels or layers of materials, and c) extrinsic pseudocapacitors, characterized by faradaic reactions occurring at the surface of nano-sized battery-like materials.

1.2.2.1 Intrinsic Pseudocapacitor

In various cases, RuO_2 has shown charge-discharge curves that are perfectly linear or approximately linear, without notable voltage plateaus. Additionally, its CV curves exhibit quasi-rectangular shapes with closely overlapped redox peaks [50]. With these characteristics, RuO_2 can be considered an intrinsic pseudocapacitive material. Irrespective of their crystalline structure, surface morphology, or particle size, intrinsic pseudocapacitive materials display the attributes of capacitive charge storage [51]. TMOs such as RuO_2 , MnO_2 , and IrO_2 exhibit inherent pseudocapacitive behavior, which sets them apart as high-performance electrodes in comparison to EDLC electrodes. Their ability to store charges through surface redox reactions contributes to their enhanced performance. While these materials have shown promising electrochemical performance, addressing challenges related to their long-term stability during cycling, cost, and limited availability is crucial [52].

1.2.2.2 Intercalation Pseudocapacitor

Intercalation pseudocapacitor materials store charges through the Faradaic intercalation of electrolyte ions without causing any disruption to the material's phase. Augustyn et al. [53] discovered a charge storage mechanism in Nb_2O_5 material, referred to as 'intercalation pseudocapacitors'. This mechanism involves the intercalation of ions and is unique to this particular material. One fascinating property of intercalation pseudocapacitors is that the electrode material remains in the same phase throughout the charge storage process [53]. In intercalation pseudocapacitors, the charge storage process involves not only the surface but also the bulk of the electrode material, utilizing both regions for the electrochemical reaction. Nb_2O_5 serves as a prime example of intercalation pseudocapacitance, illustrating the characteristic charge storage mechanism exhibited by this material.

1.2.2.3 Extrinsic Pseudocapacitor

In their unprocessed state, conventional battery materials exhibit distinct oxidation-reduction peaks in CV plots and display a voltage plateau in GCD curves, indicating characteristic behavior consistent with batteries. Nevertheless, when battery-type materials reduced to nanoscale dimensions, their GCD curves tend to become nearly linear, and they demonstrate enhanced performance at high rates while mitigating phase changes [52, 53]. As a result, these materials can be classified as extrinsic pseudocapacitor materials, displaying unique properties distinct from their bulk counterparts. The reduction in the size of battery materials from bulk to nanoscale leads to an increase in the dominance of surface-based ion storage mechanisms, which is primarily attributed to the shorter ion diffusion lengths in the nano-sized materials. Consequently, conventional battery-type materials exhibit characteristics resembling pseudocapacitive behavior. Nano-sized cobalt oxide, V_2O_5 , CeO_2 , and $LiCoO_2$ are among the examples of extrinsic pseudocapacitive materials [54, 55].

1.2.3 Hybrid Supercapacitors

The collaboration between EDLCs and pseudocapacitors has led to the development of a novel capacitor known as a hybrid capacitor. This type of capacitor accumulates charge by utilizing both faradic and non-faradic reaction mechanisms at the electrodes. EDLCs utilize carbon-based materials, which offer significantly larger SSAs and allow EDLCs to provide a higher charge accumulation. In addition, EDLCs exhibit relatively lower capacitive performance, which limits their EDs and restricts their broader application in SCs. Pseudocapacitors have higher EDs compared to EDLCs. However, they face limitations in terms of long life cycles, electrical conductivity, and PDs [56-60]. Researchers are actively engaged in the exploration of hybrid materials for SC electrodes. These materials aim to achieve a balance of higher Cs, enhanced ED, and increased PD while ensuring the cyclic stability of the device. Asymmetric hybrid capacitors are composed of both EDLC and pseudocapacitor electrodes within a single cell [61]. The hybrid electrode system involves the integration of carbon-based materials with metal oxides or conducting polymers. This combination allows for the synergistic utilization of both EDLC and pseudocapacitive charge storage mechanisms within a single electrode, resulting in enhanced performance. The presence of a high SSA

in carbon materials promotes stronger interactions between pseudocapacitive materials and the electrolyte. Meanwhile, the inclusion of faradaic reactions in composite electrodes enhances their capacity for storing charges. Consequently, the combination of carbon-based electrode materials with pseudocapacitive materials has gained significant importance due to the substantial increase in the electrochemical C of devices [62].

1.3 Materials for Supercapacitors

1.3.1 Transition Metal Oxides for Supercapacitor

TMO materials have been acknowledged as being among the most promising candidates for use as electrodes for ESDs, which is a result of their wide availability, environmental friendliness, simplicity of access, and other alluring qualities. Their diverse compositions and topologies, large SSAs, and impressive theoretical Cs are a few of these characteristics [63, 64]. These materials are also essential for making electrodes for electrochemical SCs. Through the control and modification of their flaws and surface interactions at a precise nanoscale level, they exhibit a noticeably increased C [65]. Although their ED has increased somewhat, these materials still have problems in real-world applications because of their poor electrical conductivity, unpredictable volume expansion, and slow ion diffusion in the bulk phase [66]. Exploring functional metal oxide compounds with better electrochemical characteristics is therefore urgently needed. The improvement of metal oxide materials includes several different features, such as their composition, the development of novel nanostructures, enhancements to conductivity, and control over oxygen vacancies. The physical and chemical properties of metal oxides have improved as a result of these aspects taken together. Their electrical conductivity, SSA, electroactive sites, and general chemical stability are all relevant here. Firstly, compared to separate metal oxides, a single crystal structure containing two unique cations instantaneously can produce a more significant number of electrons, and electrical conductivity is improved as a result.

1.3.2 Introduction of Cobalt Vanadium Oxide

Vanadium, an element with an atomic number of 23, belongs to the transition metal category and is situated in the 5B position on the periodic table. It is

characterized as a robust, steel-grey metal [67]. The valence electron layer has a structure of $3d^34s^2$, with the outermost layer containing a total of five valence electrons that are available for participating in bonding. Vanadium can exist in multiple oxidation states, specifically 5+, 4+, 3+, and 2+, offering the potential for impressive pseudocapacitance. Within the range of vanadium's valence states, 5+ exhibited the highest stability, while 2+ was susceptible to oxidation in the atmosphere [68]. Consequently, the extensively examined compounds derived from vanadium included V_yO_z , exemplified by V_2O_5 , V_2O_3 , V_2O_4 , etc [67]. The transition metals-based vanadium oxides ($M_xV_yO_z$, with M being Co, Ni, Zn, Cu, Fe, Mn), also known as binary metal oxides, belonged to the $A_xB_yO_z$ family. Here, A and B denote metal elements with low and high oxidation states, respectively. Both metallic elements A and B actively participated in the electrochemical energy storage process, as varying ratios of A and B could lead to the formation of $A_xB_yO_z$ compounds with diverse crystal structures like AB_2O_6 , ABO_4 , $A_2B_2O_7$, $A_3B_2O_8$, etc.

Among them, the cobalt vanadium oxide (CVO), a category of vanadium-derived compounds, exhibits notable chemical stability, resistance to high temperatures, and favorable crystallization properties. These attributes make them promising for applications in optical devices, LIBs, electrochemical SCs, and catalysts. CVO can manifest in diverse phases such as $Co_3V_2O_8$, $Co_2V_2O_7$, CoV_2O_6 , Co_2VO_4 , etc., as shown in Figure 1.4, each defined by unique structural arrangements and properties, and these phases may encompass differences in the composition, crystalline structure, and electronic configuration of the CVO material.

a) $Co_3V_2O_8$

The CVO in the phase of $Co_3V_2O_8$ crystallizes in the orthorhombic $Cmce$ space group with a 0 eV band gap. V^{5+} forms bonds with four O^{2-} atoms, creating VO_4 tetrahedra that share corners with nine CoO_6 octahedra. The angles between the corner-sharing octahedra range from 50-56°. V-O bond distances vary between 1.72-1.79 Å. Two distinct Co^{2+} sites exist: in the first, Co^{2+} bonds with six O^{2-} atoms to create CoO_6 octahedra that share corners with six equivalent VO_4 tetrahedra and edges with four CoO_6 octahedra, exhibiting Co-O bond distances ranging from 2.00-2.13 Å. In the second Co^{2+} site, Co^{2+} is bonded to six O^{2-} atoms, forming CoO_6 octahedra that share corners with six equivalent VO_4 tetrahedra and edges with

four equivalent CoO_6 octahedra. This site displays two shorter (2.04 Å) and four longer (2.08 Å) Co-O bond lengths. There are three different O^{2-} sites: the first involves O^{2-} in a distorted trigonal planar geometry bonded to one V^{5+} and two equivalent Co^{2+} atoms; the second has O^{2-} in a 3-coordinate geometry with one V^{5+} and two Co^{2+} atoms; and the third features O^{2-} in a rectangular see-saw-like geometry bonded to one V^{5+} and three Co^{2+} atoms [69, 70].

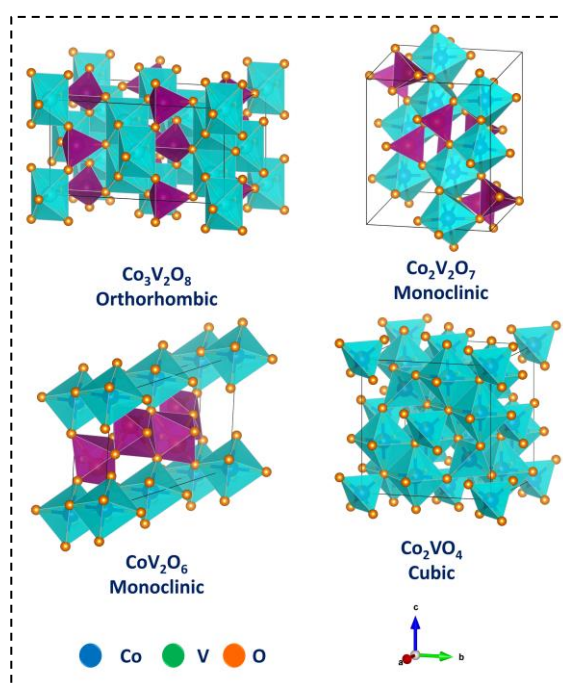


Figure 1.4 Various structures and phases of CVO.

b) $\text{Co}_2\text{V}_2\text{O}_7$

The phase of $\text{Co}_2\text{V}_2\text{O}_7$ has a monoclinic crystal structure in the $P2_1/c$ space group with a 1.83 eV band gap. It contains two different types of vanadium (V) sites. In the first V site, V is bonded to four oxygen (O) atoms, forming tetrahedra that share corners with six cobalt (Co) octahedra and one additional V tetrahedron. The angles between the shared octahedra vary from 38-62°, and the V-O bond distances range from 1.66-1.85 Å. In the second V site, V is bonded to four O atoms, creating tetrahedra that share corners with seven Co octahedra and one additional V tetrahedron. The angles between the shared octahedra range from 45-59°, and the V-O bond distance ranges from 1.71-1.84 Å. There are two distinct Co sites. In the first Co site, Co is bonded to six O atoms, forming octahedra that share corners with six V tetrahedra and edges with three Co octahedra. The Co-O bond distances range from 2.03-2.06 Å. In the second Co site, Co is bonded to six O atoms, forming octahedra that share corners with seven V tetrahedra and edges with two

equivalent Co octahedra. The Co-O bond distances range from 1.97-2.14 Å. There are seven different O sites, each with unique bonding arrangements to V and Co atoms [71].

c) CoV_2O_6

The phase of CoV_2O_6 adopts a monoclinic crystal structure within the C2 space group with a 1.91 eV band gap. V^{5+} is in a 5-coordinate arrangement, bonded to five O^{2-} atoms. The V-O bond distances range from 1.70 to 2.12 Å. Co^{2+} forms edge-sharing CoO_6 octahedra by bonding with six O^{2-} atoms, with Co-O bond distances spanning from 2.00 to 2.28 Å. Three distinct O^{2-} sites exist: in the first site, O^{2-} is in a 3-coordinate arrangement with three equivalent V^{5+} atoms; in the second site, O^{2-} is in a 2-coordinate arrangement with one V^{5+} and one Co^{2+} atom; and in the third site, O^{2-} is in a distorted trigonal planar arrangement with one V^{5+} and two equivalent Co^{2+} atoms [72].

d) Co_2VO_4

Phase Co_2VO_4 exhibits a spinel-derived structure and crystallizes in the monoclinic Cm space group with 0.03 eV band gap. The crystal structure comprises four distinct V^{3+} sites. In the first site, V^{3+} forms VO_4 tetrahedra by bonding with four O^{2-} atoms, sharing corners with three VO_6 octahedra, four equivalent CoO_6 octahedra, and five CoO_6 octahedra. The V-O bond lengths vary, with two shorter (1.85 Å) and two longer (1.88 Å) bonds. The second V^{3+} site involves V^{3+} bonding to six O^{2-} atoms, forming VO_6 octahedra that share corners with three VO_4 tetrahedra, three CoO_4 tetrahedra and edges with six CoO_6 octahedra. The V-O bond distances range from 1.90 to 2.15 Å. The third and fourth V^{3+} sites exhibit similar arrangements with variations in V-O bond distances. Additionally, there are eight distinct V^{4+} sites, each forming VO_6 octahedra with different CoO_4 tetrahedra arrangements. The Co^{3+} and Co^{2+} sites form CoO_6 octahedra with varying Co-O bond lengths. Thirty-six inequivalent O^{2-} sites participate in diverse bonding geometries with V and Co ions. The O^{2-} atoms contribute to the structural complexity by forming rectangular see-saw-like and distorted trigonal pyramidal geometries with the surrounding metal ions [73].

1.3.3 Introduction of Reduced Graphene Oxide

The identification of atomically thin graphene from graphite in 2004 by Novoselov et al. [74] ignited an exploration into the essential characteristics and possible uses of two-dimensional (2D) materials due to their distinct physical and chemical attributes. The phrase '2D material' denotes a category that experiences weak interlayer connections through van der Waals forces. These materials demonstrate diverse electrical properties, including both indirect and direct band gaps across the ultraviolet, visible, and infrared spectra. Additionally, they can manifest as metals, semimetals, or semiconductors. Among the array of 2D materials, graphene has emerged as a prominent figure in the realm of materials science. Characterized by its inherent atomic-thin structure, flexibility, elevated carrier mobility, extensive SSA, efficient thermal conductivity, and robust mechanical strength, graphene stands out as a promising contender for applications in energy generation and storage [75].

Graphene is recognized as the precursor to various graphitic configurations, encompassing three-dimensional (3D) stacked graphite, one-dimensional (1D) rolled CNTs and zero-dimensional (0D) buckyballs. While its potential spans a wide range of applications in electronic devices, as well as biological and chemical sensing, materials derived from graphene are remarkably esteemed and extensively investigated for their role in energy conversion and storage. Two primary techniques for the synthesis of graphene exist: the top-down and bottom-up approaches. In the top-down method, graphene materials are produced through mechanical or liquid phase exfoliation, involving the breakdown of graphite. The weak van der Waals force existing between the layers facilitates the separation of individual 2D layers from their bulk counterparts, rendering these exfoliation methods suitable for the synthesis of 2D materials. Mechanical exfoliation involves applying mechanical force, typically utilizing scotch tape, to peel highly oriented pyrolytic graphite.

However, the significant limitations of this method include its restricted yield and the small size of the resulting flakes. Consequently, the synthesis of graphene and other 2D materials through this process is mainly feasible at a basic laboratory scale. Despite notable advancements, the challenge persists in achieving cost-effective, high-quality graphene production on an industrial scale. There are two steps for the preparation of graphite to reduced graphene oxide (rGO). Firstly,

graphene oxide is derived from graphite flakes using the modified Hummers method. Further, GO was reduced by chemical method to produce rGO, as displayed in Figure 1.5.

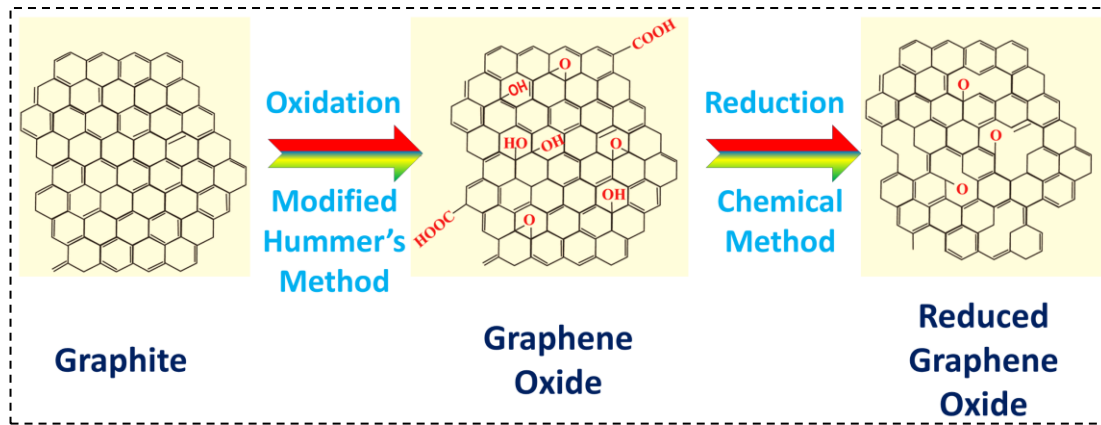


Figure 1.5 Schematic illustration of preparation of rGO.

a) Properties of Reduced Graphene Oxide

i) Electrical Property

The electrical characteristics of graphene, composed of 2D layers featuring single-atom-thick sp^2 carbon arrangements, are intricately tied to its π bond. This material exhibits excellent electrical conductivity, boosting high electron mobility at $25 \text{ m}^2 \text{ V}^{-1} \text{ S}^{-1}$ and an impressive electrical conductivity of 6500 S m^{-1} . To meet the demands of commercial applications, scientists have explored various approaches to improve the generation of electrically conducting rGO by selecting suitable reduction methods for GO. Stankovich et al. [76] employed a colloidal suspension of GO and subjected it to reduction using hydrazine hydrate. The resulting product exhibited a conductivity of $2 \times 10^2 \text{ S m}^{-1}$, representing a conductivity increase of five orders of magnitude compared to GO. The increased conductivity of rGO makes it a promising option for electrode materials in SC applications [77, 78].

ii) Mechanical Property

Graphene holds the record as the most robust material ever identified, surpassing steel by a factor of 200, boosting a tensile strength of 130 GPa. Additionally, it is an exceptionally lightweight material, weighing around 0.77 mg m^{-2} , and possesses Young's modulus of $1.0 \pm 0.1 \text{ TPa}$ (assuming a thickness of 0.335 nm). Graphene stands out as a prospective candidate for deployment in nanoelectromechanical systems or similar flexible devices owing to its remarkable attributes. The Young's modulus of rGO nanostructures is comparatively reduced

in contrast to graphene, attributable to the existence of numerous surface groups and defects resulting from oxidation or other treatment processes. Gomez et al. [79] produced monolayer rGO by subjecting GO to thermal annealing in a hydrogen atmosphere, yielding Young's modulus of 250 ± 150 TPa.

iii) Chemical Property

The usual modification of rGO nanosheets involves the introduction of functional groups containing oxygen and nitrogen. This modification enhances the wettability and conductivity of the nanosheets. In comparison to other carbon nanostructures like nanotubes and buckyballs, rGO exhibits the highest ratio of edgy carbon and dangling bonds. The presence of a curved and wrinkled surface, with carbon atoms at the edges, imparts a high degree of defects and augmented electrochemical activity to rGO nanosheets [80]. The rGO samples with a combination of a substantial SSA, microporosity, conductivity, and the presence of oxygen-containing functional groups are promising candidates for a range of electrochemical applications. The stability of rGO is notably pronounced in both acidic and basic environments, rendering it a fitting choice for utilization as an electrode in a diverse array of electrochemical devices, particularly in SCs [81].

1.4 Literature on Cobalt Vanadium Oxide and their Composite Materials

CVO has garnered significant interest among researchers because of its superior electrochemical performance, electrical conductivity, and C when compared to single-metal oxides [82]. These properties make it a promising candidate for use in SC as a positive electrode material. Various deposition methods have been compiled for the preparation of CVO materials for electrodes in SCs, including the solvothermal, hydrothermal, co-precipitation, ionothermal, electrospinning, etc. approaches. The documented electrochemical C results for electrodes based on CVOs have been consolidated and are presented in Table 1.1.

Fahimi et al. [83] synthesized hollow spheres of $\text{Co}_3\text{V}_2\text{O}_8$ through a two-step hydrothermal process. The resulting recorded Cs was 2376 F g^{-1} at a current density of 2 A g^{-1} . Yao group [84] prepared porous hexagonal nanoplatelets of cobalt vanadate by an environmentally friendly ionothermal method. The $\text{Co}_2\text{V}_2\text{O}_7$ material exhibited a Cs of 304 F g^{-1} at 1 A g^{-1} in a 2 M KOH electrolyte solution. Sun et al. [82] synthesized porous microflowers of $\text{Co}_2\text{V}_2\text{O}_7 \cdot 3.3\text{H}_2\text{O}$ and achieved Cs was

351 F g⁻¹ at a current density of 1 A g⁻¹, accompanied by impressive capacitive retention of 103% following 30,000 cycles. The Co₂V₂O₇ hexagonal nanosheets with cyclic stability retention of 272% after 100000 cycles were prepared by Wang et al. [85], which exhibited a Cs of 1834 F g⁻¹ at 1 A g⁻¹. Haung et al. [86] synthesized Co₃V₂O₈ thin nanosheets by hydrothermal approach, which exhibited a Cs of 1320 F g⁻¹ at 1 A g⁻¹ with 89.1% retention over 10000 cycles. The nanoroses of cobalt vanadate were prepared by Zhang et al. [87] using the solvothermal method and obtained Cs of 353.6 F g⁻¹ at the current density of 1 A g⁻¹. Nguyen et al. [88] synthesized nanosheet arrays of cobalt vanadate by chemical bath method on Ni foam (NF) substrate. The exhibited Cs of 878.9 F g⁻¹ with 95% capacitive retention after 5000 cycles. Arasi et al. [89] synthesized cobalt vanadate nanoparticles by chemical precipitation with exhibited Cs of 790 F g⁻¹ at 1 A g⁻¹. Thin nanoplates of Co₃V₂O₈ were prepared by Zhang et al. [90] using a hydrothermal approach and obtained Cs of 739 F g⁻¹ at 0.5 A g⁻¹. Teng et al. [91] prepared CoV₂O₆ micron blocks using a hydrothermal process, which exhibited Cs of 114.1 F g⁻¹ in 6 M KOH electrolyte. The nanosheets of CoV₂O₆.2H₂O prepared by Liu et al. [92], using a microwave irradiation process, reported a Cs of 363 F g⁻¹ at 0.5 A g⁻¹ with excellent retention of 99.8% over 80000 cycles. Li et al. [93] synthesized hollow nanocubes of Co₂VO₄ by hydrothermal method and obtained Cs of 427.6 F g⁻¹ at 1 A g⁻¹ with 89.3% retention after 10000 cycles. Isacfranklin et al. [94] prepared CVO nanoparticles by using a hydrothermal approach and reported a Cs of 285.6 F g⁻¹ at 0.5 mA g⁻¹.

Zhang et al. [95] synthesized nanorods of Co₃O₄/Co₃(VO₄)₂ by hydrothermal method and obtained a Cs of 847.2 F g⁻¹ at 1 A g⁻¹ with 99.3% retention over 5000 cycles. Lv et al. [96] prepared Co₃O₄/CoV_xO_y nanosheets by using the hydrothermal method and obtained Cs of 1162.2 F g⁻¹ at 1 A g⁻¹ with 82.6% capacitive retention after 5000 cycles. The Co₃V₂O₈@CuV₂O₆, using solution processing prepared by Sekhar et al. [97] and obtained an areal specific capacity of 188.70 μAh cm⁻² at 4 mA cm⁻². Zhou et al. [98] synthesized nanospheres of Co₃V₂O₈@Ti₃C₂T_x using the hydrothermal method and achieved areal Cs of 2960.5 mF cm⁻² at 8 mA cm⁻². Fahimi and Moradlou [99] prepared a Co₃V₂O₈/CNT composite and obtained a Cs of 1959.9 F g⁻¹ at 1 A g⁻¹. The nanoparticles of Co₃V₂O₈/CN_x were synthesized using a solvothermal approach by Mishra et al. [100] and obtained Cs of 1236 F g⁻¹ at 1 A

g^{-1} in 2 M KOH electrolyte. Also, it retained 87% over 4000 cycles. Hosseini and Shahrokhian [101] prepared $\text{Co}_3\text{V}_2\text{O}_8\text{-Ni}_3\text{V}_2\text{O}_8$ nanosheets by electrospinning method and obtained a Cs of 1731 F g^{-1} at 1 A g^{-1} . Devi et al. [102] synthesized $\text{Co}_3\text{V}_2\text{O}_8$ nanoparticles over rGO by hydrothermal method and obtained a specific capacity of 241.6 C g^{-1} at 0.5 A g^{-1} . The $\text{CoV}_2\text{O}_6/\text{CNTs}$ nanorods were prepared using ultrasound and subsequent annealing treatment by Lv et al. [103] and achieved a Cs of 226.3 F g^{-1} at 1 A g^{-1} with 88% retention over 9000 cycles. Low et al. [104] prepared Graphene/ $\text{Co}_3\text{V}_2\text{O}_8$ micropencils using a solvothermal approach and observed Cs of 528.1 F g^{-1} at 0.5 A g^{-1} . Maitra et al. [105] synthesized PPy/FeO@CVO nanocane arrays by hydrothermal route and obtained a Cs of 1202 F g^{-1} at 1 A g^{-1} with 96.5% retention over 3000 cycles.

Amiri et al. [106] prepared $\text{CuCo}_2\text{V}_2\text{O}_8$ hollow spheres via the self-templating method and reported a specific capacity of 799.8 C g^{-1} at 2 A g^{-1} with 96.5% retention over 7000 cycles. Lv et al. [107] synthesized $\text{NiCo}_z\text{V}_x\text{O}_y$ nanospheres by chemical precipitation method and achieved a Cs of 1449.3 F g^{-1} at 2 A g^{-1} . Sharma et al. [108] prepared S-doped $\text{Co}_3\text{V}_2\text{O}_8$ nanosheets using a hydrothermal approach and obtained a capacity of 410 mAh g^{-1} at 2 A g^{-1} with 94.2% capacitive retention after 4000 cycles.

Table 1.1: A comparative structural, morphological, and three-electrode system electrochemical analysis of the CVO and their composite materials literature survey.

Sr. No.	Material	Method	Morphology	Electrolyte	Specific capacitance (F g ⁻¹) at Current density	Stability cycles (capacitive retention%)	Ref.
1.	Co ₃ V ₂ O ₈	Hydrothermal	Hollow spheres	1 M KOH	2376 at 2 A g ⁻¹	10000 (97.4%)	[83]
2.	Co ₂ V ₂ O ₇	Ionothermal	Hexagonal nanoplates	2 M KOH	304.8 at 1 A g ⁻¹	100 (103%)	[84]
3.	Co ₂ V ₂ O ₇ ·3.3H ₂ O	Co-precipitation	Microflowers	2 M KOH	351 at 1 A g ⁻¹	30000 (103%)	[82]
4.	Co ₂ V ₂ O ₇	Hydrothermal	Hexagonal sheets	4 M KOH	1834 at 1 A g ⁻¹	100000 (272%)	[85]
5.	Co ₃ V ₂ O ₈	Hydrothermal	Nanosheets	6 M KOH	1320 at 1 A g ⁻¹	10000 (89.1%)	[86]
6.	Co ₃ V ₂ O ₈	Solvothermal	Rose-like	2 M KOH	353.6 at 1 A g ⁻¹	7000 (89.6%)	[87]

7.	$\text{Co}_3\text{V}_2\text{O}_8$	Chemical bath	Nanosheets	3 M KOH	878.9 at 1 A g ⁻¹	5000 (95%)	[88]
8.	$\text{Co}_3\text{V}_2\text{O}_8$	Chemical Precipitation	Nanoparticles	2 M KOH	790 at 1 A g ⁻¹	10000 (90.1%)	[89]
9.	$\text{Co}_3\text{V}_2\text{O}_8$	Hydrothermal	Nanoplates	3 M KOH	739 at 0.5 A g ⁻¹	2000 (95.3%)	[90]
10.	CoV_2O_6	Hydrothermal	Micron blocks	6 M KOH	114.1 at 1 A g ⁻¹	1000 (81.9%)	[91]
11.	$\text{CoV}_2\text{O}_6 \cdot 2\text{H}_2\text{O}$	Microwave irradiation	Nanosheets	6 M KOH	363 at 0.5 A g ⁻¹	80000 (99.8%)	[92]
12.	Co_2VO_4	Hydrothermal	Hollow nanocubes	3 M KOH	427.6 at 1 A g ⁻¹	10000 (89.3%)	[93]
13.	$\text{Co}_2\text{V}_2\text{O}_7$	Hydrothermal	Nanoparticles	-	285.6 at 0.5 mA g ⁻¹	4000 (83.6%)	[94]
14.	$\text{Co}_3\text{O}_4 / \text{Co}_3(\text{VO}_4)_2$	Hydrothermal	Nanorods	2 M KOH	847.2 at 1 A g ⁻¹	5000 (99.3%)	[95]
15.	$\text{Co}_3\text{O}_4 / \text{CoV}_x\text{O}_y$	Hydrothermal	Nanosheets	3 M KOH	1162.2 at 1 A g ⁻¹	5000 (82.6%)	[96]

16.	$\text{Co}_3\text{V}_2\text{O}_8@\text{CuV}_2\text{O}_6$	Solution-processing	Nanohexagons	1 M KOH	$188.70 \mu\text{Ah cm}^{-2}$ at 4 mA cm^{-2}	5000 (89.5%)	[97]
17.	$\text{Co}_3\text{V}_2\text{O}_8@\text{Ti}_3\text{C}_2\text{T}_x$	Hydrothermal	Nanospheres	1 M KOH	$2960.5 \text{ mF cm}^{-2}$ at 8 mA cm^{-2}	20000 (75.6%)	[98]
18.	$\text{Co}_3\text{V}_2\text{O}_8/\text{CNT}$	Hydrothermal	Nanospheres	1 M KOH	1959.9 at 1 A g^{-1}	-	[99]
19.	$\text{Co}_3\text{V}_2\text{O}_8/\text{CN}_x$	Solvothermal	Nanoparticles	2 M KOH	1236 at 1 A g^{-1}	4000 (87%)	[100]
20.	$\text{Co}_3\text{V}_2\text{O}_8\text{-Ni}_3\text{V}_2\text{O}_8$	Electrospinning	Nanosheets	3 M KOH	1731 at 1 A g^{-1}	2000 (83.7%)	[101]
21.	$\text{Co}_3\text{V}_2\text{O}_8\text{-RGO}$	Hydrothermal	Nanoparticles	6 M KOH	241.6 C g^{-1} at 0.5 A g^{-1}	-	[102]
22.	$\text{CoV}_2\text{O}_6/\text{CNTs}$	Ultrasound and Annealing Treatment	Nano rod-like	3 M KOH	226.3 at 1 A g^{-1}	9000 (88%)	[103]
23.	$\text{Graphene}/\text{Co}_3\text{V}_2\text{O}_8$	Solvothermal	Micropencils-like	2 M KOH	528.1 at 0.5 A g^{-1}	5000 (80%)	[104]
24.	$\text{PPy}/\text{FeO}@ \text{CVO}$	Hydrothermal	Grass-like nanocanes arrays	1 M KOH	1202 at 1 A g^{-1}	3000 (96.5%)	[105]

25.	$\text{CuCo}_2\text{V}_2\text{O}_8$	Self-templating	Hollow spheres	3 M KOH	799.8 C g^{-1} at 2 A g^{-1}	7000 (96.5%)	[106]
26.	$\text{NiCo}_z\text{V}_x\text{O}_y$	Chemical Precipitation	Nanospheres	3 M KOH	1449.3 at 2 A g^{-1}	2000 (66%)	[107]
27.	$\text{S-Co}_3\text{V}_2\text{O}_8$	Hydrothermal	Nanosheets	6 M KOH	410 mAh g^{-1} at 2 A g^{-1}	4000 (94.2%)	[108]

Note: PPy-Polypyrrole, CNT-Carbon Nanotube, CVO-Cobalt Vanadium Oxide.

1.5 Literature on Supercapacitor Devices of Cobalt Vanadium Oxide and their Composite Materials

A review of the literature on SC devices based on CVO and composite materials is tabulated and presented in Table 1.4. Fahimi et al. [83] fabricated a $\text{Co}_3\text{V}_2\text{O}_8//\text{AC}$ HSD device (HSD) and achieved a Cs of 165.3 F g^{-1} at 1 A g^{-1} current density. Also, HSD delivered ED of 59.2 Wh kg^{-1} with 250 W kg^{-1} PD. The $\text{Co}_3\text{V}_2\text{O}_8//\text{AC}$ has performed 10000 cycles with 97.3% capacitive retention. Yao et al. [84] made a $\text{Co}_2\text{V}_2\text{O}_7//\text{AC}$ asymmetric SC device (ASD) using Ni-foam substrate and obtained Cs of 73.8 F g^{-1} at 1 A g^{-1} . The fabrication of $\text{Co}_2\text{V}_2\text{O}_7 \cdot 3.3\text{H}_2\text{O}/\text{rGO}$ ASD was reported by Sun et al. [82] and achieved a Cs of 60.7 F g^{-1} at 1 A g^{-1} , which delivered ED of 19 Wh kg^{-1} with 375.8 W kg^{-1} of PD. Moreover, the capacitive retention of 96.4% over 10000 cycles was obtained for ASD. Wang et al. [85] fabricated HSD, the $\text{Co}_2\text{V}_2\text{O}_7$ was used as a cathode and rGO as an anode. The obtained Cs of 113 F g^{-1} at 1 A g^{-1} with ED of 35.2 Wh kg^{-1} at 1001 W kg^{-1} for HSD with capacitive retention achieved after 10000 cycles was 71.4%. Nguyen et al. [88] assembled $\text{Co}_3\text{V}_2\text{O}_8//\text{AC}$ ASD. The maximum Cs of 156 F g^{-1} at 1 A g^{-1} with 55.5 Wh kg^{-1} ED at 800 W kg^{-1} of PD. The retention of 82.1% was calculated after 10000 cycles for ASD. The $\text{CoV}_2\text{O}_6 \cdot 2\text{H}_2\text{O}/\text{AC}$ ASD was fabricated by Liu et al. [92] and obtained a Cs of 53 F g^{-1} at 0.5 A g^{-1} current density. The ASD achieved ED of 19 Wh kg^{-1} at 400 W kg^{-1} of PD with 78.6% capacitive retention after 35000 cycles. Li et al. [93] fabricated a $\text{CoVO-HNC}/\text{AC}$ device and obtained a Cs of 71.1 F g^{-1} at a current density of 1 A g^{-1} with ED of 25.2 Wh kg^{-1} at 801.2 W kg^{-1} of PD. The cyclic stability of $\text{CoVO-HNC}/\text{AC}$ was maintained up to 10000 cycles with 78% capacitive retention.

Zhang et al. [95] assembled $\text{Co}_3\text{O}_4/\text{Co}_3(\text{VO}_4)_2//\text{AC}$ ASD and obtained a Cs of 105 F g^{-1} at 0.5 A g^{-1} with ED of 38 Wh kg^{-1} at 275 W kg^{-1} of PD. The fabricated ASD retained a capacitance of 94.7% over 5000 cycles. Lv et al. [96] prepared $\text{Co}_3\text{O}_4/\text{CoV}_x\text{O}_y//\text{AC}$ ASD and achieved Cs of 73.3 F g^{-1} at 0.5 A g^{-1} with 26.1 Wh kg^{-1} of ED at PD of 400 W kg^{-1} . The capacitive retention of 83.4% after 5000 cycles was observed for ASD. The $\text{CuV-CoV}/\text{MOF}$ HSD was fabricated by Sekhar et al. [97] and obtained areal Cs of 307.7 mF cm^{-2} at 3 mA cm^{-2} current density. The HSD achieved ED of $0.092 \text{ mWh cm}^{-2}$ at PD of 24.40 mW cm^{-2} with 86.9% retention over 5000 cycles. Zhou et al. [98] fabricated $\text{Co}_3\text{V}_2\text{O}_8@\text{Ti}_3\text{C}_2\text{T}_x//\text{AC}$ ASD and obtained a Cs of

203.8 mF cm⁻² at 4 mA cm⁻² with 70.2 mW h cm⁻² of ED at 3.3 mW cm⁻² of PD. The capacitive retention of 87.1% over 10000 cycles was observed for ASD. Fahimi and Moradlou [99] prepared a Co₃V₂O₈/CNT//AC device and obtained Cs of 120.1 F g⁻¹ at 1 A g⁻¹ with 37.5 Wh kg⁻¹ at 660 W kg⁻¹ of PD.

Mishra et al. [100] assembled Co₃V₂O₈/CNx//AC ASD and obtained a Cs of 131 F g⁻¹ at a current density of 0.5 A g⁻¹ with 40.8 Wh kg⁻¹ of ED at 385.1 W kg⁻¹. The Co₃V₂O₈/CNx//AC retained a capacitance of 63.3% over 10000 cycles. Hosseini and Shahrokhian [101] prepared Co₃V₂O₈-Ni₃V₂O₈//TLs@PCNFs and achieved a Cs of 191 F g⁻¹ at 5 A g⁻¹ with 59.7 Wh kg⁻¹ of ED at 1970 W kg⁻¹ of PD and retention of 88.5% after 3000 cycles. The ASD of Co₃V₂O₈/RGO//RGO was fabricated by Devi et al. [102] and achieved a specific capacity of 127.6 C g⁻¹ at 0.5 A g⁻¹ with 28.3 Wh kg⁻¹ ED at PD of 400 W kg⁻¹ with retention of 98.6% after 10000 cycles. Lv et al. [103] assembled CoV₂O₆/CNTs//AC and achieved a Cs of 38.7 F g⁻¹ at 1 A g⁻¹ with 13.8 Wh kg⁻¹ at 800 W kg⁻¹. After 9000 cycles, a capacitive retention of 113.6% was observed for CoV₂O₆/CNTs//AC. Low et al. [104] fabricated a Graphene/Co₃V₂O₈//Graphene/Co₃V₂O₈ symmetric device and obtained ED of 73 Wh kg⁻¹ at PD of 4100 W kg⁻¹. Maitra et al. [105] prepared PPy/FeO@CVO//Graphene ASD and obtained a Cs of 140.5 F g⁻¹ at 1 A g⁻¹ with ED of 38.2 Wh kg⁻¹ at 700 W kg⁻¹. The PPy/FeO@CVO//Graphene device achieved a capacitive retention of 95% over 5000 cycles. The CuCo₂V₂O₈//AC was fabricated by Amiri et al. [106] and obtained a Cs of 175.9 F g⁻¹ at 840 mA cm⁻² with 62.5 Wh kg⁻¹ at 1928 W kg⁻¹ and reported the capacitive retention of 94% after 7000 cycles. Lv et al. [107] assembled NiCo₂V_xO_y//AC ASD and achieved a Cs of 126.5 F g⁻¹ at 1 A g⁻¹ with 45 Wh kg⁻¹ of ED at 800 W kg⁻¹ PD and capacitive retention of 91.4% was observed after 2000 cycles. Sharma et al. [108] fabricated ASD of S-Co₃V₂O₈//AC and obtained a specific capacity of 48.3 mAh g⁻¹ at 1 A g⁻¹ current density with 36.4 Wh kg⁻¹ ED at 740 W kg⁻¹ PD.

According to a survey of the literature, there is limited information on the chemical preparation of CVO and CVO/rGO composites, with a few reports available on the above-discussed methods. Hence, our target is to synthesize CVO and CVO/rGO composite through cost-effective chemical approaches, including successive ionic layer adsorption and reaction (SILAR) and chemical bath synthesis (CBS) methods. These methods appear to be favourable for preparing thin films of

CVO/rGO composite on stainless steel (SS) substrates. They are likely the most facile, cost-effective, and well-suited approaches for synthesizing large-area, thin film electrodes of CVO and its composites with rGO suitable for SC application.

Table 1.2: Literature study of CVO and their composite hybrid, symmetric, and asymmetric SC devices.

Sr. No.	Material	Substrate	Electrolyte	Specific capacitance (F g ⁻¹) at Current density	Energy density (Wh kg ⁻¹)	Power density (W kg ⁻¹)	Cycles (Capacitive retention)	Ref.
1.	Co ₃ V ₂ O ₈ //AC	NF	6 M KOH	165.3 at 1 A g ⁻¹	59.2	250	10000 (97.3%)	[83]
2.	Co ₂ V ₂ O ₇ //AC	NF	6 M KOH	73.8 at 1 A g ⁻¹	-	-	-	[84]
3.	Co ₂ V ₂ O ₇ ·3.3H ₂ O//rGO	NF	2 M KOH	60.7 at 1 A g ⁻¹	19	375.8	10000 (96.4%)	[82]
4.	Co ₂ V ₂ O ₇ //rGO	NF	4 M KOH	113 at 1 A g ⁻¹	35.2	1001	10000 (71.4%)	[85]
5.	Co ₃ V ₂ O ₈ //AC	NF	0.05 M K ₃ [Fe(CN) ₆]	156 at 1 A g ⁻¹	55.5	800	10000 (82.1%)	[88]
6.	Co ₃ V ₂ O ₈ //AC	NF	6 M KOH	-	22.3	649.1	-	[91]

7.	CoV ₂ O ₆ .2H ₂ O//AC	NF	6 M KOH	53 at 0.5 A g ⁻¹	19	400	35000 (78.6%)	[92]
8.	CoVO-HNC//AC	NF	3 M KOH	71.1 at 1 A g ⁻¹	25.2	801.2	10000 (78%)	[93]
9.	Co ₃ O ₄ /Co ₃ (VO ₄) ₂ //AC	NF	2 M KOH	105 at 0.5 A g ⁻¹	38	275	5000 (94.7%)	[95]
10.	Co ₃ O ₄ /CoV _x O _y //AC	NF	3 M KOH	73.3 at 0.5 A g ⁻¹	26.1	400	5000 (83.4%)	[96]
11.	CuV-CoV//MOF	Cu foam	1 M KOH	307.7 mF cm ⁻² at 3 mA cm ⁻²	0.092 mWh cm ⁻²	24.40 mW cm ⁻²	5000 (86.9%)	[97]
12.	Co ₃ V ₂ O ₈ @Ti ₃ C ₂ T _x //AC	NF	1 M KOH	203.8 mF cm ⁻² at 4 mA cm ⁻²	70.2 mW h cm ⁻²	3.3 mW cm ⁻²	10000 (87.1%)	[98]
13.	Co ₃ V ₂ O ₈ /CNT//AC	NF	1 M H ₂ SO ₄	120.1 at 1 A g ⁻¹	37.5	660	3000 (95.2%)	[99]
14.	Co ₃ V ₂ O ₈ /CN _x //AC	NF	2 M KOH	131 at 0.5 A g ⁻¹	40.8	385.1	10000 (63.3%)	[100]
15.	Co ₃ V ₂ O ₈ -Ni ₃ V ₂ O ₈ // TLs@PCNFs	Electrospun porous CNFs	3 M KOH	191 at 5 A g ⁻¹	59.7	1970	3000 (88.5%)	[101]

16.	Co ₃ V ₂ O ₈ /RGO//RGO	NF	6 M KOH	127.6 C g ⁻¹ at 0.5 A g ⁻¹	28.3	400	10000 (98.6%)	[102]
17.	CoV ₂ O ₆ /CNTs//AC	NF	3 M KOH	38.7 at 1 A g ⁻¹	13.8	800	9000 (113.6%)	[103]
18.	Graphene/Co ₃ V ₂ O ₈ // Graphene/Co ₃ V ₂ O ₈	Al foil	2 M KOH	-	73	4100	-	[104]
19.	PPy/FeO@CVO//Grap -hene	NF	1 M KOH	140.5 at 1 A g ⁻¹	38.2	700	5000 (95%)	[105]
20.	CuCo ₂ V ₂ O ₈ // AC	NF	3 M KOH	175.9 at 840 mA cm ⁻²	62.5	1928	7000 (94%)	[106]
21.	NiCo ₂ V _x O _y //AC	NF	3 M KOH	126.5 at 1 A g ⁻¹	45	800	2000 (91.4%)	[107]
22.	S-Co ₃ V ₂ O ₈ //AC	NF	6 M KOH	48.3 mAh g ⁻¹ at 1 A g ⁻¹	36.4	740	4000 (98%)	[108]

Note: AC-Activated Carbon, HNC-Hollow Nanocube, MOF-Metal Organic Framework, CNT-Carbon Nanotube, TLs@PCNFs-Thin Layers@Porous Carbon Nanofibers, PPy-Polypyrrole.

1.6 Orientation and Purpose of Thesis

Recent studies on SCs provide insight into cutting-edge ESDs used in laptops, power backup systems, portable gadgets, hybrid electric cars, and other uses. As a result, SCs are becoming more widely acknowledged as a flexible alternative to traditional batteries. Also, they have increased ED and PD, longer lifespans, and faster charge-discharge rates with many other advantages. It is crucial to minimize resistance because supplying pulse power requires a quick response. Because of this, researchers are placing a strong emphasis on investigating and preparing active electrode materials that satisfy these particular requirements.

Since mixed TMOs (MTMOs) offer a range of oxidation states that allow for reversible redox reactions, they have been developed as electrode materials having Faradaic characteristics. Among TMOs, CVO is a promising electroactive MTMO material, because of its remarkable charge storage capabilities, affordability, and low toxicity. However, only modest progress has been made in the use of CVO and CVO/rGO composite materials for supercapacitive applications. The rGO is beneficial for composite with CVO material due to its distinctive characteristics, including favorable electrochemical durability, extensive SSA, robust structural integrity, exceptional electrical conductivity, and superior mechanical attributes. In the synthesis of these electrode materials, it is crucial to employ a simple, cost-effective, chemical approach to control the expenses associated with SC device production. The objectives of the thesis are as follows,

- 1) To prepare CVO/rGO composite electrodes by using CBS and SILAR methods.
- 2) To characterize prepared CVO/rGO composite electrodes by different characterization techniques.
- 3) To study the supercapacitive performance of CVO/rGO composite electrodes and utilization of HSD fabrication.

Among various deposition approaches, SILAR and CBS methods offer several advantages. Chemical processes result in thin films that are devoid of pinholes, exhibit strong adhesion, and display uniform deposition. The nucleation and growth processes in chemical synthesis play a pivotal role in generating nanocrystalline materials. Moreover, these approaches are commonly applied for large-scale production, which proves advantageous in the context of device

manufacturing. The examination of existing literature clarifies the feasibility of synthesizing a novel category of CVO/rGO composite electrode material. It suggests that HSDs can be fabricated using flexible SS substrates and polymer gel electrolytes. Simple chemical methods allow for the preparation of various morphologies of CVO; it can serve as an effective electrode material in the SCs. So, the primary objective is to synthesize thin films of CVO through uncomplicated chemical methods and characterize these films using diverse physicochemical analysis. An optimization of preparative parameters such as pH, concentration, solution temperature, and deposition time is undertaken. SILAR and CBS methods, as simple chemical approaches, have the potential to yield binder-free, additive-less thin film electrodes by enhancing the interfacial connection between the active material and SS substrates. Also, the use of low-temperature deposition methods can help restrict corrosion and oxidation of metallic substrates.

Additionally, meticulously examined CVO/rGO composite thin films, characterized by their strong adhesion and uniformity, undergo thorough analysis for phase identification, structural interpretation, surface composition, and microstructural aspects. Phase confirmation of the material is achieved through X-ray diffraction (XRD), while Fourier-transform infrared (FT-IR) spectroscopy analysis is employed to study chemical bonding in the prepared material. Raman spectroscopy is employed to identify molecules and examine chemical bonding as well as intramolecular interactions. Thermogravimetric analysis (TGA) measures temperature and weight changes during decomposition reactions, aiding in the quantitative analysis of composites.

The morphological assessment of the electrode material is conducted using field emission scanning electron microscopy (FE-SEM) and high resolution transmission electron microscopy (HR-TEM). Elemental composition confirmation is carried out through energy-dispersive X-ray spectroscopy (EDS), and the X-ray photoelectron spectroscopy (XPS) technique is applied to identify oxidation states, ascertain chemical composition, and confirm material formation. Electrochemical capacitive performances of the electrodes are explored via CV, GCD, and electrochemical impedance spectroscopy (EIS) using an electrochemical workstation. The supercapacitive performance of CVO/rGO composite thin film electrodes and HSC devices are assessed based on various electrochemical

parameters such as potential window, Cs, specific power (SP), specific energy (SE), and cyclic stability.

1.7 References

- [1] M. Guo, J. Balamurugan, X. Li, N. Kim, J. Lee, *Small*, 13, (2017), 1701275, 1-12.
- [2] H. Ibrahim, A. Ilinca, J. Perron, *Renew. Sust. Energ. Rev.*, 12, (2008), 1221-1250.
- [3] H. Lund, *Energy*, 32, (2007), 912-919.
- [4] Q. Hassan, S. Algburi, A. Sameen, H. Salman, M. Jaszczur, *Results Eng.*, 20, (2023), 101621, 1-25.
- [5] N. Kittner, F. Lill, D. Kammen, *Nat. Energy*, 2, (2017), 17125, 1-6.
- [6] R. Yadlapalli, R. Alla, R. Kandipati, A. Kotapati, *J. Energy Storage*, 49, (2022), 104194, 1-21.
- [7] C. Ao, Y. Jiang, L. Zhang, C. Yan, J. Ma, C. Liu, Y. Jiang, W. Zhang, S. Soh, *J. Mater. Chem. A*, 10, (2022), 19572-19605.
- [8] M. Jayalakshmi and K. Balasubramanian, *Int. J. Electrochem. Sci.*, 3, (2008), 1196-1217.
- [9] G. Yu, L. Hu, N. Liu, H. Wang, M. Vosgueritchian, Y. Yang, Y. Cui, Z. Bao, *Nano Lett.*, 11, (2011), 4438-4442.
- [10] D. Chen, Q. Wang, R. Wang, G. Shen, *J. Mater. Chem. A*, 3, (2015), 10158-10173.
- [11] P. Saini, *Indian J. Pure Appl. Phys.*, 61, (2023), 268-290.
- [12] E. Miller, Y. Hua, F. Tezel, *J. Energy Storage*, 20, (2018), 30-40.
- [13] M. Mohan, N. Shetti, T. Aminabhavi, *J. Energy Storage*, 58, (2023), 106321, 1-19.
- [14] C. Meng, P. Das, X. Shi, Q. Fu, K. Müllen, Z. Wu, *Small*, 1, (2021), 2000076, 1-15.
- [15] N. Wu, X. Bai, D. Pan, B. Dong, R. Wei, N. Naik, R. Patil, Z. Guo, *Adv. Funct. Mater.*, 8, (2021), 2001710, 1-17.
- [16] C. Hu, K. Chang, M. Lin, Y. Wu, *Nano Lett.*, 6, (2006), 2690-2695.
- [17] M. Akin, X. Zhou, *Int. J. Energy Res.*, 46, (2022), 10389-10452.
- [18] A. Khorate and A. Kadam, *J. Energy Storage*, 52, (2022), 104887, 1-25.
- [19] G. Bullard, H. Sierra-Alcazar, H. Lee, J. Morris, *IEEE Trans. Magn.*, 25, (1989), 102-106.
- [20] <https://www.ttiinc.com/content/ttiinc/en/resources/marketeye/categories/passives/me-zogbi-20130403.html>.
- [21] <https://www.marketsandmarkets.com/Market-Reports/supercapacitor-market-37140453.html>.
- [22] S. Kim, S. Kim, K. Jung, J. Kim, J. Jang, *Nano Energy*, 24, (2016), 17-24.
- [23] A. Castaings, W. Lhomme, R. Trigui, A. Bouscayrol, *Appl. Energy*, 163, (2016), 190-200.
- [24] C. Lokhande, D. Dubal, O. Joo, *Curr. Appl. Phys.*, 11, (2011), 255-270.
- [25] H. Pang, X. Li, Q. Zhao, H. Xue, W. Lai, Z. Hu, W. Huang, *Nano Energy*, 35, (2017), 138-145.
- [26] L. Miao, H. Duan, M. Liu, W. Lu, D. Zhu, T. Chen, L. Li, L. Gan, *J. Chem. Eng.*, 317, (2017), 651-659.
- [27] C. Guan, X. Qian, X. Wang, Y. Cao, Q. Zhang, A. Li, J. Wang, *Nanotechnology*, 26, (2015), 1-7.
- [28] C. Zhou, Y. Zhang, Y. Li, J. Liu, *Nano Lett.*, 13, (2013), 2078-2085.
- [29] W. Lu, R. Hartman, L. Qu, L. Dai, *J. Phys. Chem. Lett.*, 2, (2011), 655-660.
- [30] T. Chen and L. Dai, *Mater. Today*, 16, (2013), 272-280.
- [31] W. Wang and S. Wu, *Surf. Sci.*, 396, (2017), 1360-1367.
- [32] X. Li, Y. Zhao, Y. Bai, X. Zhao, R. Wang, Y. Huang, Q. Liang, Z. Huang, *Electrochim. Acta*, 230, (2017), 445-453.
- [33] M. Mastragostino, C. Arbizzani, F. Soavi, *Solid State Ion.*, 148, (2002), 493-498.
- [34] S. Gowda, A. Reddy, X. Zhan, P. Ajayan, *Nano Lett.*, 11, (2011), 3329-3333.
- [35] J. Long, D. Bélanger, T. Brousse, W. Sugimoto, M. Sassin, O. Crosnier, *MRS Bull.*, 36, (2011), 513-522.
- [36] G. Wang, L. Zhang, J. Zhang, *Chem. Soc. Rev.*, 41, (2012), 797-828.
- [37] F. Shi, L. Li, X. Wang, C. Gu, J. Tu, *RSC Adv.*, 4, (2014), 41910-41921.
- [38] C. Cougnon, E. Lebègue, G. Pognon, *J. Power Sources*, 274, (2015), 551-559.
- [39] F. Ma, S. Ding, H. Ren, Y. Liu, *RSC Adv.*, 9, (2019), 2474-2483.
- [40] D. Dubal, N. Chodankar, Z. Caban-Huertas, F. Wolfart, M. Vidotti, R. Holze, C. Lokhande, P. Gomez-Romero, *J. Power Sources*, 308, (2016), 158-165.
- [41] X. Fan, Z. Peng, Y. Yang, H. Zhou, X. Guo, *J. Mater. Chem. A*, 3, (2015), 10077-10084.
- [42] Y. Chang, C. Wu, P. Wu, *J. Power Sources*, 223, (2013), 147-154.
- [43] X. Lu, J. Shen, H. Ma, B. Yan, Z. Li, M. Shi, M. Ye, *J. Power Sources*, 201, (2012), 340-346.

-
- [44] W. Li, F. Zhang, Y. Dou, Z. Wu, H. Liu, X. Qian, D. Gu, Y. Xia, B. Tu, D. Zhao, *Adv. Energy Mater.*, 1, (2011), 382-386.
- [45] K. Jost, D. Stenger, C. Perez, J. McDonough, K. Lian, Y. Gogotsi, G. Dion, *Energy Environ. Sci.*, 6, (2013), 2698-2705.
- [46] M. Oschatz, L. Borchardt, K. Pinkert, S. Thieme, M. Lohe, C. Hoffmann, M. Benusch, F. Wisser, C. Ziegler, L. Giebeler, M. Rummeli, J. Eckert, A. Eychmüller, S. Kaskel, *Adv. Energy Mater.*, 4, (2014), 1300645, 1-9.
- [47] K. Pinkert, M. Oschatz, L. Borchardt, M. Klose, M. Zier, W. Nickel, L. Giebeler, S. Oswald, S. Kaskel, J. Eckert, *ACS Appl. Mater. Interfaces*, 6, (2014), 2922-2928.
- [48] L. Zhang, X. Zhao, H. Ji, M. Stoller, L. Lai, S. Murali, S. McDonnell, B. Cleveger, R. Wallace, R. Ruoff, *Energy Environ. Sci.*, 5, (2012), 9618-9625.
- [49] B. Nagar, D. Dubal, L. Pires, A. Merkoci, P. Gomez-Romero, *ChemSusChem*, 11, (2018), 1849-1856.
- [50] N. Chodankar, H. Pham, A. Nanjundan, J. Fernando, K. Jayaramulu, D. Golberg, Y. Han, D. Dubal, *Small*, 16, (2020), 2002806, 1-35.
- [51] J. Liu, J. Wang, C. Xu, H. Jiang, C. Li, L. Zhang, J. Lin, Z. X. Shen, *Adv. Sci. (Weinh.)*, 5, (2018), 1700322, 1-19.
- [52] P. Simon, Y. Gogotsi, B. Dunn, *Science*, 343, (2014), 1210-1211.
- [53] V. Augustyn, P. Simon, B. Dunn, *Energy Environ. Sci.*, 7, (2014), 1597-1614.
- [54] J. Brog, A. Crochet, J. doux, M. Clift, B. Baichette, S. Maharajan, H. Barosova, P. Brodard, M. Spodaryk, A. Züttel, B. Rutishauser, N. Kwon, K. Fromm, J. Nanobiotechnol., 15, (2017), 1-23.
- [55] H. Li, M. Yu, F. Wang, P. Liu, Y. Liang, J. Xiao, C. Wang, Y. Tong, G. Yang, *Nat. Commun.*, 4, (2013), 1-7.
- [56] X. Zhao, L. Zhang, S. Murali, M. D. Stoller, Q. Zhang, Y. Zhu, R. S. Ruoff, *ACS Nano*, 6, (2012), 5404-5412.
- [57] C. Hsieh, W. Lee, C. Lee, H. Teng, *J. Phys. Chem. C*, 118, (2014), 15146-15153.
- [58] T. Chen and Y. Elabd, *Electrochim. Acta*, 229, (2017), 65-72.
- [59] T. Nguyen, M. Boudard, M. Carmezim, M. Montemor, *Energy J.*, 126, (2017), 208-216.
- [60] W. Shaheen, M. Warsi, M. Shahid, M. Khan, M. Asgharb, Z. Ali, M. Sarfraz, H. Anwar, M. Nadeem, I. Shakir, *Electrochim. Acta*, 219, (2016), 330-338.
- [61] H. Jung, N. Venugopal, B. Scrosati, Y. Sun, *J. Power Sources*, 221, (2013), 266-271.
- [62] J. Liu, J. Essner, J. Li, *Chem. Mater.*, 22, (2010), 5022-5030.
- [63] G. Wang, L. Zhang, J. Zhang, *Chem. Soc. Rev.*, 41, (2012), 797-828.
- [64] Q. Lu, J. Chen, J. Xiao, *Angew. Chem.*, 52, (2013), 1882-1889.
- [65] Z. Yu, L. Tetard, L. Zhaia, J. Thomas, *Energy Environ. Sci.*, 8, (2015), 702-730.
- [66] C. An, Y. Zhang, H. Guo, Y. Wang, *Nanoscale Adv.*, 1, (2019), 4644-4658.
- [67] D. Rehder, *Dalton Trans.*, 42, (2013), 11749-11761.
- [68] Y. Yan, B. Li, W. Guo, H. Pang, H. Xue, *J. Power Sources*, 329, (2016), 148-169.
- [69] E. Sauerbrei, R. Faggiani, C. Calvo, *Acta. Crystallogr. B. Struct.*, 29, (1973), 2304-2306.
- [70] H. Fuess, E. Bertaut, R. Pauthenet, A. Durif, *Acta. Crystallogr. B.*, 26, (1970), 2036-2046.
- [71] E. Sauerbrei, R. Faggiani, C. Calvo, *Acta. Crystallogr. B.*, 30, (1974), 2907-2909.
- [72] B. Toennies, H. Buschbaum, *Z. Anorg. Allg. Chem.*, 508, (1984), 7-11.
- [73] C. Mu, J. Mao, J. Guo, Q. Guo, Z. Li, W. Qin, Z. Hu, K. Davey, T. Ling, S. Qiao, *Adv. Mater.*, 32, (2020), 1907168, 1-8.
- [74] K. Novoselov, A. Geim, S. Morozov, D. Jiang, Y. Zhang, S. Dubonos, I. Grigorieva, A. Firsov, *Science*, 306, (2004), 666-669.
- [75] F. Ahmad, M. Zahid, H. Jamil, M. Khan, S. Atiq, M. Bibi, K. Shahbaz, M. Adnan, M. Danish, F. Rasheed, H. Tahseen, M. Shabbir, M. Bilal, A. Samreen, *J. Energy Storage*, 72, (2023), 108731, 1-17.
- [76] S. Stankovich, D. Dikin, G. Dommett, K. Kohlhaas, E. Zimney, E. Stach, R. Piner, S. Nguyen, R. Ruoff, *Nature*, 442, (2006), 282-286.
- [77] D. Voiry, J. Yang, J. Kupferberg, R. Fullon, C. Lee, H. Jeong, H. Shin, M. Chhowalla, *Science*, 353, (2016), 1413-1416.
- [78] E. Jaafar, M. Kashif, S. Sahari, Z. Ngain, *Mater. Sci. Forum*, 917, (2018), 112-116.
- [79] E. Gómez, N. Guarnizo, J. Perea, A. López, J. Prías-Barragán, *ACS Omega*, 7, (2022), 3872-3880.
- [80] Z. Yin, S. Sun, T. Salim, S. Wu, X. Huang, Q. He, Y. Lam, H. Zhang, *ACS Nano*, 4, (2010), 5263-5268.
- [81] B. Lesiak, G. Trykowski, J. Tóth, S. Biniak, L. Kövér, N. Rangam, L. Stobinski, A. Malolepszy, *J. Mater. Sci.*, 56, (2020), 3738-3754.
-

- [82] H. Sun, X. Chen, H. Chai, Y. Wang, D. Jia, Y. Cao, A. Liu, *Appl. Surf. Sci.*, 469, (2019), 118-124.
- [83] Z. Fahimi, O. Moradlou, A. Sabbah, K. Chen, L. Chen, M. Qorbani, *J. Chem. Eng.*, 436, (2022), 135225, 1-12.
- [84] G. Yao, N. Zhang, Y. Zhang, T. Zhou, *J. Alloys Compd.*, 892, (2021), 162205, 1-9.
- [85] H. Wang, H. Zhang, D. Zhang, J. Chen, S. Zhang, S. Zhang, J. Yu, Q. Wu, Q. Li, *Appl. Mater. Interfaces*, 14, (2022), 8106-8114.
- [86] B. Huang, W. Wang, T. Pu, J. Li, C. Zhao, L. Xie, L. Chen, *J. Chem. Eng.*, 375, (2019), 121969, 1-11.
- [87] J. Zhang, B. Yuan, S. Cui, N. Zhang, J. Wei, X. Wang, D. Zhang, R. Zhang, Q. Huo, *Dalton Trans.*, 46, (2017), 3295-3302.
- [88] V. Nguyen, F. Sari, J. Ting, *RSC Adv.*, 12, (2022), 29170-29176.
- [89] S. Arasi, R. Ranjithkumar, P. Devendran, M. Krishnakumar, A. Arivarasan, *J. Energy Storage*, 41, (2021), 102986, 1-8.
- [90] Y. Zhang, Y. Liu, J. Chen, Q. Guo, T. Wang, H. Pang, *Sci. Rep.*, 4, (2014), 5687, 1-5.
- [91] Y. Teng, Y. Li, D. Yu, Y. Meng, Y. Wu, X. Zhao, X. Liu, *ChemistrySelect*, 4, (2019), 956-962.
- [92] S. Liu, S. Sarwar, H. Zhang, Q. Guo, J. Luo, X. Zhang, *Electrochim. Acta*, 364, (2020), 137320, 1-15.
- [93] C. Li, D. Ma, Q. Zhu, *Nanomaterials*, 12, (2022), 848, 1-15.
- [94] M. Isacfranklin, C. Deepika, G. Ravi, R. Yuvakkumar, D. Velauthapillai, B. Saravanakumar, *Ceram. Int.*, 46, (2020), 28206-28210.
- [95] W. Zhang, L. Kong, X. Ma, Y. Luo, L. Kang, *J. Power Sources*, 269, (2014), 61-68.
- [96] X. Lv, W. Huang, J. Tang, L. Tang, Q. Shi, *Electrochim. Acta*, 380, (2021), 138248, 1-10.
- [97] S. Sekhar, B. Ramulu, D. Narsimulu, S. Arbaz, J. Yu, *Small*, 16, (2020), 2003983, 1-15.
- [98] J. Zhou, B. Liu, L. Zhang, Q. Li, C. Xu, H. Liu, *J. Mater. Chem. A*, 10, (2022), 24896-24904.
- [99] Z. Fahimi and O. Moradlou, *J. Energy Storage*, 50, (2022), 104697, 1-11.
- [100] R. Mishra, P. Panda, S. Barman, *New J. Chem.*, 45, (2021), 5897-5906.
- [101] H. Hosseini, S. Shahrokhian, *J. Chem. Eng.*, 341, (2018), 10-26.
- [102] P. Devi, M. Srivastava, N. Kim, J. Lee, D. Mishra, *Compos. B.*, 227, (2021), 109384, 1-14.
- [103] X. Lv, W. Huang, Q. Shi, L. Tang, J. Tang, *J. Mater. Sci.: Mater. Electron.*, 31, (2020), 2388-2397.
- [104] W. Low, C. Siong, C. Chia, S. Lim, P. Khiew, *J. Sci-Adv. Mater. Dev.*, 4, (2019), 515-523.
- [105] A. Maitra, A. Das, S. Karan, S. Paria, R. Bera, B. Khatua, *Ind. Eng. Chem. Res.*, 56, (2017), 2444-2457.
- [106] M. Amiri, S. Davarani, S. Kaverlavani, S. Moosavifard, M. Shamsipur, *Appl. Surf. Sci.*, 527, (2020), 146855, 1-8.
- [107] X. Lv, W. Huang, Q. Shi, L. Tang, J. Tang, *J. Power Sources*, 492, (2021), 229623, 1-10.
- [108] G. Sharma, P. Gupta, S. Sharma, R. Pala, S. Sivakumar, *Appl. Energy Mater.*, 4, (2021), 4758-4771.

CHAPTER-2

Theoretical Background of CBS and SILAR Methods, and Characterization Techniques

CHAPTER-2

Theoretical Background of CBS and SILAR Methods, and Characterization Techniques

Sr. No.	Title		Page No.
2.1	Introduction		37
2.2	Chemical Bath Synthesis (CBS) Method		40
	2.2.1	Theoretical Background of CBS Method	40
	2.2.2	Basic Principle of CBS Method	40
	2.2.3	Theoretical Background of Nucleation and Growth	41
	2.2.4	Preparative Parameters of CBS Method	44
	2.2.5	Advantages of CBS Method	45
2.3	Successive Ionic Layer Adsorption and Reaction (SILAR) Method		46
	2.3.1	Theoretical Background of SILAR Method	46
	2.3.2	Mechanism of SILAR Method	47
	2.3.3	Introduction to Nucleation and Film Growth in SILAR Method	50
	2.3.4	Effect of Preparative Parameters	52
	2.3.5	Advantages of SILAR Method	54
2.4	Physicochemical Characterization Techniques		54
	2.4.1	X-Ray Diffraction (XRD)	55
	2.4.2	Fourier Transform-Infrared (FT-IR) Spectroscopy	55
	2.4.3	Field Emission-Scanning Electron Microscopy (FE-SEM) and Energy Dispersive X-ray Electron (EDS) Spectroscopy	56
	2.4.4	X-Ray Photoelectron Spectroscopy (XPS)	56
	2.4.5	Thermogravimetric Analysis (TGA)	56
	2.4.6	Brunauer-Emmett-Teller (BET) and Barrett-Joyner-Halenda (BJH)	57
	2.4.7	Raman Spectroscopy	57

	2.4.8	High Resolution Transmission Electron Microscopy	57
2.5		Electrochemical Characterization Techniques	58
	2.5.1	Cyclic Voltammetry (CV)	60
	2.5.2	Galvanostatic Charge-Discharge (GCD)	61
	2.5.3	Electrochemical Impedance Spectroscopy (EIS)	63
2.6		References	65

2.1 Introduction

The growing demand for thin film and its applications has elevated thin film science to a prominent field of global research, generating new opportunities for the development of innovative processes, materials, and technologies. As a result, considerable attention has been devoted to the development of advanced materials in the form of thin films to improve the performance of the current ESDs. Back in 1838, the initial production of thin solid films was accomplished through the utilization of the electrolysis technique. Over the past few decades, organic and inorganic materials have been successfully prepared in the form of thin films and employed for diverse applications [1-3]. As the term suggests, a 'thin film' refers to a material that possesses a thin structure characterized by a maximum 2D order or periodicity. The thickness of such material's thin film typically ranges from nanometers to micrometers, encompassing both liquid and solid systems. Thin layers of material can be applied onto various types of substrates, including conducting and non-conducting ones, using various deposition methods that involve the atom-by-atom or ion-by-ion processes. These deposition methods can be attributed to either purely physical or chemical processes. The scientific attraction to 2D solid materials and the numerous advantages offered by thin films have generated significant interest and attention in the area of science and technology studies. The extensive focus on thin film research is driven by its transformative impact on various fields, including electronics, optics, ESDs like SCs, sensors, and magnetism, as depicted in Figure 2.1 [4-7].

Nanomaterials are exhibited in thin film form, which enhances the electrochemical capacitive performance due to their ability to acquire desirable properties at both the bulk and surface levels. This unique characteristic contributes to the improved electrochemical behavior observed for these thin film electrodes. The advantages of nanomaterials in ESDs have predominantly focused on the benefits associated with reduced charge transfer length and high surface area. Moreover, nanocrystalline thin film materials offer a diverse range of advantages, which include a significantly larger SSA, lower thermal conductivity, higher electrical conductivity, improved diffusivity, enhanced strength, and a higher thermal expansion coefficient when compared to conventional materials in bulk form [8].

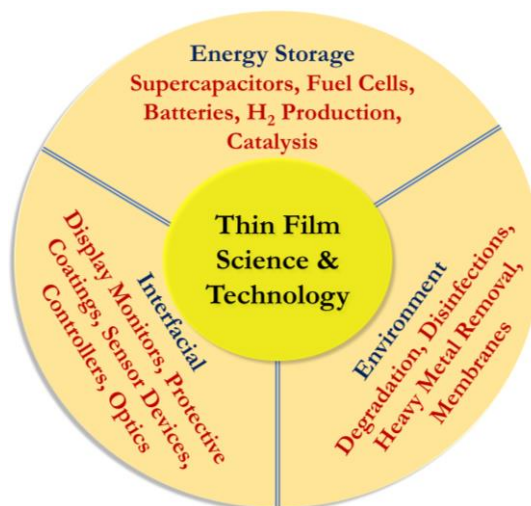


Figure 2.1 Utilizations associated with thin film materials-based devices.

Furthermore, the synthesis method employed for thin film preparation plays a crucial role in achieving the desired properties and versatility of the electrode. There are two primary branches of thin film preparation methods used for synthesizing nanomaterials in thin film form. These methods can broadly be classified as physical and chemical approaches. The physical methods, such as sputtering and vacuum evaporation, involve the transfer of the deposition material into the gaseous phase through the process of evaporation [9, 10]. Then, the material is condensed and deposited onto a substrate. Chart 2.1 provides a comprehensive classification of various thin film preparation methods.

The chemical methods of thin film deposition involve both gas and liquid phases. The gas-phase chemical methods involve a wide range of methods, including chemical vapor deposition (CVD), light amplification by stimulated emission of radiation (LASER), CVD, photochemical vapor deposition, plasma-enhanced CVD, and metal organo-CVD. These methods utilize different chemical evaporation and condensation processes to enable the growth of thin films. The chemical methods in the liquid phase encompass various approaches such as SILAR, CBS, hydrothermal, electrodeposition, anodization, sol-gel, spray pyrolysis, etc. These approaches involve chemical processes performed in liquid media to ease the preparation of thin films. The physical methods suffer from certain limitations, including the need for vacuum conditions, higher deposition temperatures, the requirement of sophisticated instrumentations, material wastage, and a limited area of deposition.

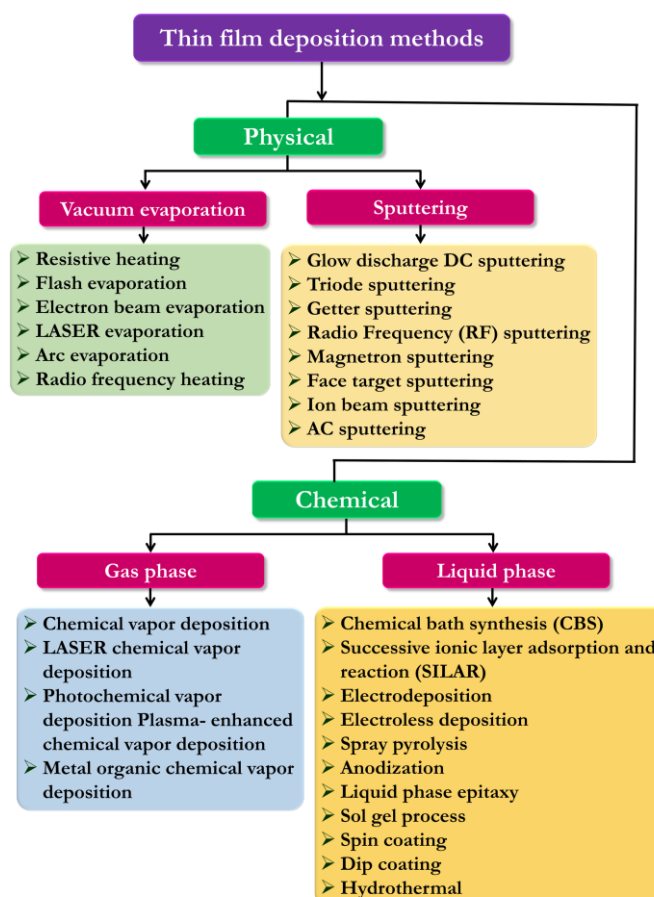


Chart 2.1 Categorization of approaches for thin film preparation.

On the other hand, chemical-based methods offer some advantages, such as simplicity, cost-effectiveness, and efficiency for large-area preparation of various materials in thin film form. The chemical methods allow for easy control of preparative parameters such as pH of the chemical bath, deposition time, reactant concentration, and temperature. In contrast, the physical methods may lead to oxidation and corrosion of metallic substrates, which can be reduced by utilizing low-temperature chemical deposition methods. Additionally, the chemical methods enable the production of adherent and uniformly deposited thin films. Consequently, these chemical methods have extensive applications in the preparation of nanostructured materials for various applications. This chapter delves into the theoretical basics of two widely used methods for thin film preparation: CBS and SILAR. This chapter explores the principles behind these methods and their application in achieving thin film formation. Additionally, various characterization techniques used for structural analysis, morphological assessment, and electrochemical analysis are discussed. These characterization

techniques play a crucial role in understanding the properties and performance of the thin films synthesized using CBS and SILAR methods for SC application.

2.2 Chemical Bath Synthesis (CBS) Method

2.2.1 Theoretical Background of CBS Method

Chemical synthesis methods for thin film formation rely on thermodynamic equilibrium and kinetic approaches. Specifically, the CBS method predominantly follows the thermodynamic approach. The synthesis process within this approach involves three main steps: (i) the generation of supersaturation, (ii) nucleation, and (iii) subsequent growth. When it comes to preparing nanomaterials, the CBS method has gained substantial popularity. The CBS method involves preparing nanomaterial by initiating nucleation from a liquid phase [11]. The significance of the CBS method in material preparation is underscored by its ability to deliver reproducible results, its convenience and user-friendly nature, the capability to prepare with high yield, and its potential for commercial-scale production [12].

The CBS method for material preparation only necessitates simple and readily available equipment such as a hot plate and a stirrer. The cost-effective CBS method allows for the preparation of nanomaterials with precise control over their size, shape, and composition. The properties of prepared materials are dependent on the preparative parameters, which can be effortlessly managed in the CBS method. Mane and Lokhande [13] have extensively elucidated the process of thin film formation using the cost-effective CBS method in their review article. Furthermore, the literature contains numerous other review articles that provide comprehensive coverage of the chemical methods utilized in thin film preparation [14].

2.2.2 Basic Principle of CBS Method

The fundamental principle of the CBS method for thin film preparation lies in the controlled precipitation of the desired compound in the solution. Essentially, the process of forming nanomaterials through controlled precipitation involves three essential steps: (i) the formation, (ii) the transportation, and (iii) the condensation of species [9, 10]. When a sparingly soluble salt AB is added to the solvent, it results in the formation of a saturated solution. This solution contains both A^+ and B^- ions, as well as undissolved solid AB. At this point, an

equilibrium is established between the solid phase and the ions present in the solution.



According to the law of mass action, the equilibrium condition is governed by the concentration of the reactants and products involved in a chemical reaction.

$$K = \frac{C_A^+ \cdot C_B^-}{C_{AB(s)}} \quad (2.2)$$

In this context, C_A^+ , C_B^- , and C_{AB} represent the concentrations of A^+ ions, B^- ions, and the AB compound, respectively, in the solution. The concentration of the pure solid phase remains constant and is represented by $C_{AB(s)}$, which is a fixed value denoted as K' .

$$K = \frac{C_A^+ \cdot C_B^-}{K'} \quad (2.3)$$

$$KK' = C_A^+ \cdot C_B^- \quad (2.4)$$

By considering the constancy of K and K' and their product denoted as K_s , the above equation can be expressed as;

$$K_s = C_A^+ \cdot C_B^- \quad (2.5)$$

The solubility product (S_P) is represented by K_s , while the product of $C_A^+ \cdot C_B^-$ is referred to as the ionic product (I_P). When the solution reaches a saturated state, the I_P is equal to the S_P of the ions in the solution. However, if the I_P exceeds the S_P , indicated by the ratio $I_P/S_P = S > 1$, the solution becomes supersaturated, resulting in precipitation. This precipitation leads to the formation of nuclei both in the solution (homogeneous) and on the surface of the solids (heterogeneous) [15]. In the CBS method at a supersaturated state, homogenous and heterogenous reactions occur, leading to the formation of nuclei and subsequent growth. To enable the nucleation and growth of material, it is essential to attain a supersaturation state in the solution.

2.2.3 Theoretical Background of Nucleation and Growth

During chemical deposition, nanomaterials are synthesized on a solid surface through reactions taking place within a solution. The preparation of the

nanomaterials involves various stages, which include nucleation, aggregation, coalescence, and particle growth [11].

a) Nucleation

There are two distinct types of nucleation based on the deposition mechanism: homogeneous and heterogeneous nucleation. Homogeneous nucleation takes place when the concentration of anions and cations surpasses the S_p . On the other hand, heterogeneous nucleation occurs when individual ions or subcritical embryos adhere to the solid surface. The schematic representation of the adsorption process of ions or subcritical embryos onto a solid surface is depicted in Figure 2.2. Typically, the energy needed to form an interface between an individual ion and the solid surface is lower than the energy required for the interface between ions. Consequently, heterogeneous nucleation is the preferred mechanism for the formation of a thin layer of material on the solid surface.

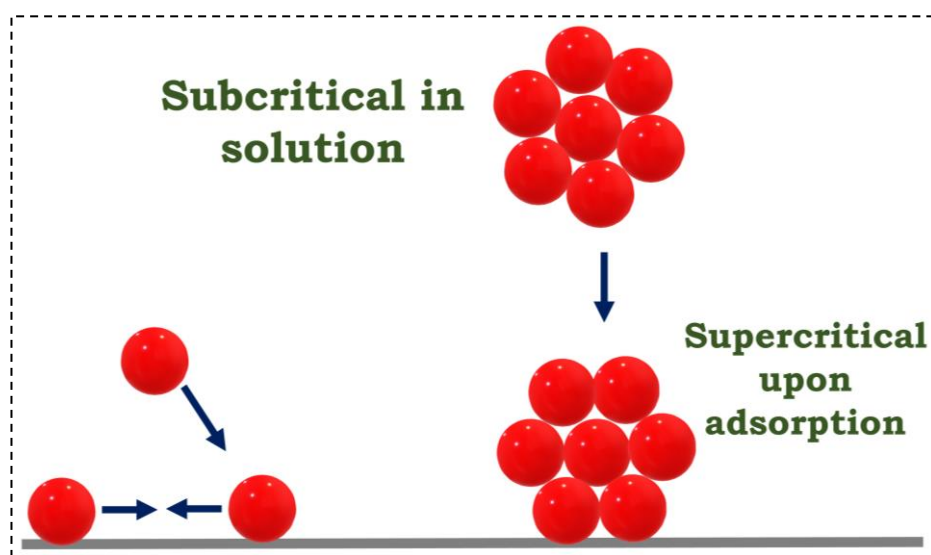


Figure 2.2 Processes on a solid surface that lead to heterogeneous nucleation [16].

b) Crystal Growth

Growth can proceed along different pathways, such as self-assembling processes and disintegration and reconstruction processes. In the self-assembling process, growth takes place through the self-assembly of particles following the formation of nuclei. Conversely, the second process involves growth through the rearrangement of particles, where aggregation and coalescence play a significant role and are commonly referred to as Ostwald ripening. Aggregation occurs when

individual particles adhere to each other, while coalescence refers to the merging of these particles. During the coalescence process, smaller or less stable nuclei near larger crystals dissolve, leading to their reduction in size or complete dissolution. This mechanism ultimately leads to the growth of larger crystals, as illustrated in Figure 2.3.

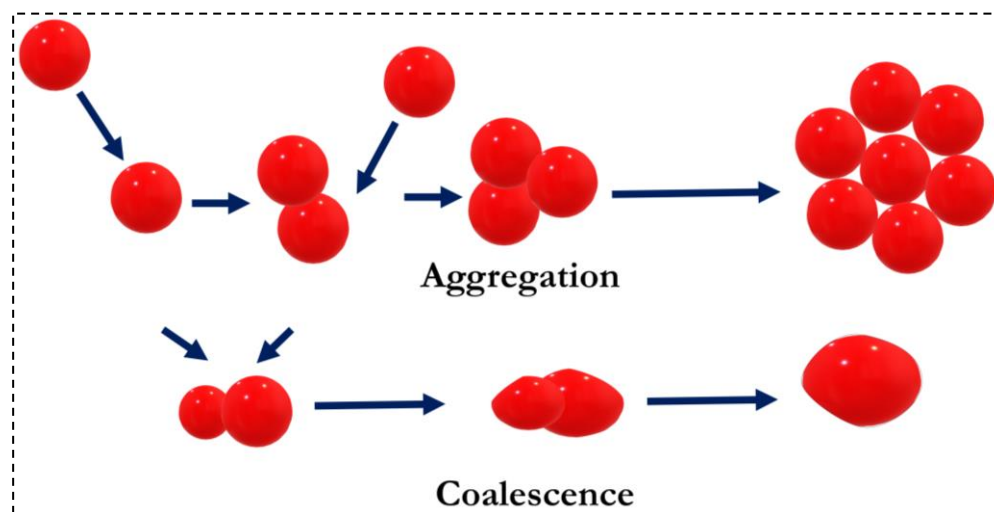


Figure 2.3 Particle growth via the processes of aggregation and coalescence [17].

c) Growth of material

CBS is highly effective for the preparation of nanomaterials that exhibit uniformity and uniform size and shape. Within this method, growth takes place through two distinct mechanisms: ion-by-ion and hydroxide cluster mechanisms.

i) Ion-by-Ion Growth Mechanism

Achieving a high level of saturation is essential for homogenous nucleation in the ion-by-ion growth mechanism. The presence of a heterogeneous environment, influenced by the surface and the availability of free ions, promotes nucleation. The solid surface plays a catalytic role in facilitating the nucleation process. After nucleation is initiated on the solid surface, the growth of the material is facilitated. Consequently, the material growth rate is accelerated at the nucleated site in comparison to other regions of the solid surface. The growth of the material endures until it encounters hindrances from different processes or disruptions caused by specific substances like impurities, inhibitors, or additives that alter the physical or chemical environment.

ii) Hydroxide Cluster Mechanism

This phenomenon is frequently observed in the growth of metal chalcogenide materials. The hydroxide cluster process is renowned for its simplicity, as it entails the replacement of hydroxide with chalcogenide in the solid phase, where the metal hydroxide is already in a solid state. When a solution contains a significant amount of hydroxide ions, these ions facilitate the formation of metal hydroxide ions. Acting as ligands to metal cations, hydroxide ions create insoluble colloidal clusters. These clusters are dispersed throughout the solution and also get deposited onto a solid surface, attracted by Van der Waals forces. The chalcogenide anions then react with the dispersed and deposited metal hydroxide clusters to form metal chalcogenide crystals. These crystals contribute to the formation of a material with a structure akin to crystallites. Essentially, hydroxide ions serve as intermediaries between metal ions and chalcogenide ions. Since each hydroxide cluster provides a nucleation site, this synthesis method typically results in smaller and more uniform crystals compared to the ion-by-ion growth mechanism [11].

2.2.4 Preparative Parameters of CBS Method

Achieving uniform material growth through the CBS method is contingent upon the rate of the underlying chemical reaction. The growth rate and particle size of the materials are determined by the degree of supersaturation in the solution and the availability of nucleation centers. The growth kinetics of the material are influenced by a range of factors, including pH, bath temperature, the nature of the solid surface, and the presence of complexing agents. The impact of preparative parameters on the growth mechanism is described as follows:

a) Temperature of Solution

The temperature of the bath plays a crucial role in influencing the rate of the reaction. With an increase in the solution temperature, the dissociation of the complex becomes more efficient, resulting in elevated kinetic energy (KE) for the molecules and improved interaction between ions. Moreover, the degree of supersaturation is affected by temperature, ultimately influencing the final particle size of the material, which can either increase or decrease as a result.

b) pH of solution

The level of supersaturation controls the rate of the reaction and synthesis process. By increasing the pH of the reaction bath, the stability of the complex formed by the metal ions can be enhanced, thereby decreasing the availability of free metal ions. This alteration influences the reaction rate and subsequently impacts the average size of particles.

c) Complexing Agent

Preparation in the CBS method commonly takes place in a supersaturated solution. Complexing agents are utilized to avoid abrupt precipitation of the material. These agents bind to the free metal ions in the solution, thereby decreasing their concentration. By increasing the amount of complexing agent, the concentration of free metal ions is further diminished, resulting in a reduction in the reaction rate. Consequently, this provides a means to regulate the particle size of the prepared material.

d) Nature of Solid Surface

The characteristics of the solid surface have a notable influence on the interfacial contacts of the material and the kinetics of the reaction. The presence of nucleation centers on the solid surface is vital for the initiation of nucleation and the subsequent growth of the material. Therefore, the cleaning process of the solid surface holds significant importance in the preparation of materials. Furthermore, the lattice parameters of the solid surface play a crucial role in the growth of the material. When the lattice parameters of the solid surface closely match those of the prepared material, it enhances the growth rate, leading to the attainment of the desired terminal size of particles.

2.2.5 Advantages of CBS Method

The CBS method provides several advantages for the preparation of nanomaterials:

- i. **Reproducibility:** CBS offers a reliable and consistent process for preparing nanomaterials. By controlling preparation parameters, it is possible to achieve desired material properties consistently.
- ii. **Scalability:** CBS is a scalable method that allows for the preparation of nanomaterials high yield. This makes it suitable for applications requiring

- a quantity of material, such as ESDs, photocatalysis, coatings thick film, filtration, and dye degradation.
- iii. **Simplicity and Convenience:** CBS utilizes equipment, such as a temperature controller, stirrer, and thermometer, making it a convenient method to perform the preparation of nanomaterial. It does not require complex instrumentation or elaborate setups.
 - iv. **Cost-effectiveness:** CBS is a cost-effective alternative method than other nanomaterial preparation methods like CVD methods. It utilizes readily available chemicals and simple equipment, contributing to its cost efficiency.
 - v. **Versatility:** CBS is compatible with a wide range of materials, including metals, oxides, sulfides, and hydroxides. This versatility allows for the preparation of diverse nanomaterials with different compositions and properties.
 - vi. **Control over Material Growth:** CBS enables precise control over various material properties, including size and shape, composition, uniformity, and morphology. By adjusting preparation conditions, it is possible to tailor the material characteristics to meet specific application requirements and uniformity of materials ensures consistent properties.

In summary, the CBS method offers simplicity, reproducibility, high yield, versatility, and cost-effectiveness, making it an attractive option for nanomaterial synthesis for industrial and research applications.

2.3 Successive Ionic Layer Adsorption and Reaction (SILAR) Method

2.3.1 Theoretical Background of SILAR Method

The SILAR method is a chemical-based approach used to synthesize thin films. Originally referred to as the multiple dipping chemical method, SILAR involves the sequential adsorption of ion layers onto a substrate, followed by the reaction of these adsorbed ions. Nicolau et al. [18] introduced the term SILAR to describe this particular process. In contrast to advanced physical deposition methods that necessitate a vacuum environment, the SILAR deposition method provides a cost-effective alternative. The advantage of SILAR lies in its ability to perform deposition under ambient conditions, eliminating the need for expensive

and intricate equipment. As a result, SILAR becomes a more economical and accessible approach for depositing thin films. In the conventional CBS and hydrothermal methods, a thin film is formed when the I_p surpasses the S_p . Moreover, this process also leads to the formation of undesired bulk precipitate in the solution, which cannot be eliminated and poses significant challenges, including material loss. To overcome these limitations, a modified approach known as SILAR has been introduced [19]. SILAR incorporates specific adjustments to address these issues effectively. By employing SILAR, the problems associated with the formation of unwanted bulk precipitate and material loss are successfully alleviated.

The SILAR method encompasses the adsorption and reaction of ions derived from precursor solutions, with the crucial step of rinsing using distilled water after each immersion. This rinsing process is essential to prevent homogeneous precipitation within the solution. By employing this strategy, the SILAR method effectively avoids the formation of unwanted precipitates and maintains the desired film formation on the substrate. Adsorption is the process by which a substance adheres to the surface of another substance through physical bonding, serving as the fundamental principle underlying this method. The phenomenon of adsorption involves the interaction of ions in the solution with the substrate surface, facilitated by various attractive forces. These forces can include cohesive forces, Van der Waals forces, or chemical attractive forces, and they play a significant role in the surface interaction between ions and the substrate. Various factors, such as solution temperature, substrate properties, and solution concentration chemical conditions can affect the adsorption process. In this process, the interaction between newly adsorbed ions (anions) and pre-adsorbed ions (cations) results in the formation of a thin film consisting of the desired material.

2.3.2 Mechanism of SILAR Method

The SILAR method is based on a step-by-step procedure of adsorption and reaction occurring on the surface of the substrate. This process involves the heterogeneous reaction between the solid phase of the substrate and the solvated ions present in the solution. To control this reaction, rinsing steps are carried out

after each adsorption and reaction step. These rinsing steps facilitate the interaction between the solid phase and the solvated ions, resulting in the formation of the desired thin film. The diagram presented in Figure 2.4 illustrates the sequential reaction steps employed in the SILAR deposition method.

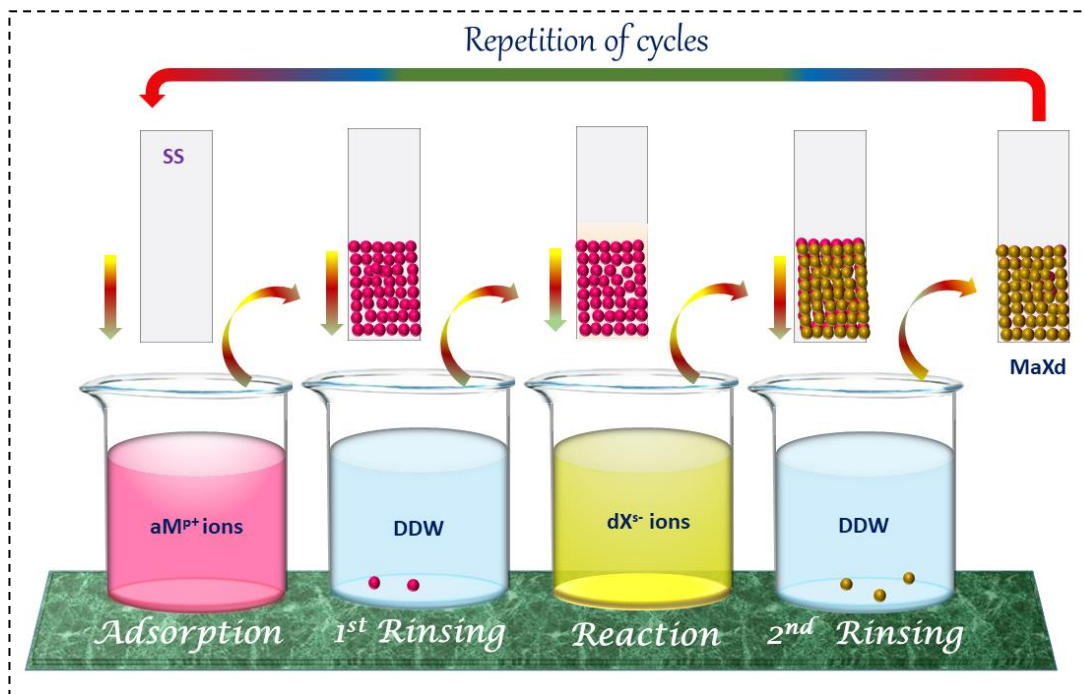
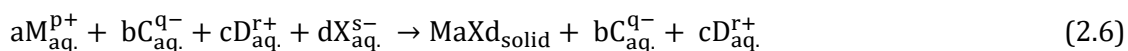


Figure 2.4 Schematic illustration of SILAR thin film deposition method.

This method is specifically developed for the preparation of thin films comprising water-soluble ionic or ion covalent compounds of the MaXd type. The deposition process involves a heterogeneous chemical reaction occurring at the interface between the solid substrate and the adsorbed cations (aM^{p+}) and anions (dX^{s-}).



In the aqueous cationic solution, the cations (i.e., metal ions) are represented by aM , where 'a' represents the number of cations and 'p+' denotes the charge on the cation. Similarly, in the same solution, the anions present along with the cations are denoted by bC , where 'b' represents the number of anions and 'q-' represents the charge on the anion. In the aqueous anionic precursor, the cations present along with the anions are represented by cD , where 'c' stands for the number of cations and 'r+' represents the charge on the cation. The anions in the

aqueous anionic precursor are represented by dX , where 'd' stands for the number of anions and 's-' represents the charge on the anion.

The SILAR deposition method consists of a four-beaker system, as depicted in Figure 2.4. This particular system is widely utilized for depositing various materials such as single or binary metal oxides, hydroxides, sulfides, selenides, phosphates, and many more. The deposition process can be conducted at ambient temperature or higher temperatures. The deposition and growth of the material can be influenced by different stages of the reaction, as outlined below:

a) Adsorption: The first beaker consists of a cationic precursor solution where adsorption takes place on the immersed substrates. At this stage, the presence of cations in the precursor solution leads to the formation of the Helmholtz electric double layer. This adsorbed layer comprises two distinct components: the inner layer, which carries a positive charge and comprises the cations (M^{p+}), and the outer layer, which carries a negative charge and consists of the counter ions (C^{q-}) associated with the cations specified in the general chemical reaction equation (2.6).

b) 1st Rinsing: It is commonly utilized to remove ions that have not undergone significant adsorption or are weakly bound to the diffusion layer. This action leads to the saturation of the Helmholtz electric double layer.

c) Reaction: This stage involves immersing the substrate into a third beaker containing a solution of anionic precursors, thereby completing the remaining half of the reaction. As a consequence of this immersion, a chemical reaction takes place between the surface species aM^{p+} and the anionic precursor X^{s-} , and leads to the neutralization of these species. The inherent instability of the ions involved contributes to the formation of a solid substance, $MaXd$, on the surface of the substrate.

d) 2nd Rinsing: During this step, any unreacted chemicals and excess chemical species, along with the byproducts generated from the reaction, can be effectively removed from the surface. Second rinsing represents the concluding stage of the complete reaction cycle.

The desired film thickness and growth can be achieved by optimizing the number of deposition cycles, which involves adjusting the precursor concentration, adsorption/reaction immersion duration, and rinsing duration. There are two factors to consider in the SILAR film formation process. Firstly, it is crucial to allocate at least one ion specifically to the substrate interface to aid in the formation of the film. Secondly, the growth rate per immersion must not exceed the lattice constant of the material. If the measured growth rate surpasses the lattice constant, it can result in the precipitation in the solution by the homogeneous growth.

2.3.3 Introduction to Nucleation and Film Growth in SILAR Method

a) Nucleation

Nucleation serves as the initial phase in the material deposition process in the SILAR method. The SILAR method encompasses nucleation through heterogeneous growth and transpires specifically on the surface of the substrate. In the SILAR method, the cationic and anionic precursor solutions are maintained separately, and the substrate is rinsed following each adsorption and reaction stage. Consequently, the occurrence of homogeneous nucleation is considerably minimized. Conversely, in the SILAR method, the predominant mechanism for material deposition primarily involves heterogeneous nucleation.

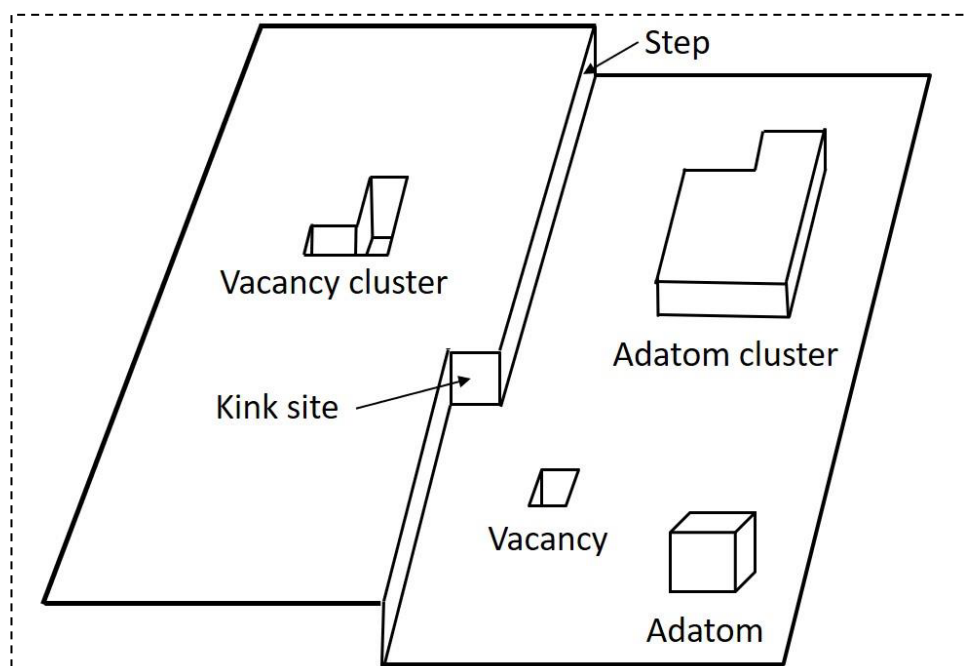


Figure 2.5 Schematic illustration of substrate surface featuring various forms of nucleation sites.

Figure 2.5 illustrates that the surface of the substrate offers a multitude of nucleation sites for deposition. Within this context, the smooth metal surface contains individual atoms referred to as adatoms, while the aggregation of multiple adatoms results in the formation of adatom clusters. Similarly, the absence of a single atom on the surface is denoted as a vacancy, whereas the combination of multiple vacancies is termed a vacancy cluster. Notably, crystal growth heavily relies on the presence of steps and kink sites [20]. Crucially, the addition and removal of atoms at the kink site facilitate the generation of new kink sites. During the initial cycles in the SILAR method, water-insoluble species are deposited onto the substrate, playing a crucial role as nucleation centers for the subsequent material growth. Consequently, in the SILAR method, adatoms predominantly serve as nucleation centers.

b) Film Growth

Thin film growth on the surface of metal substrates via nucleation sites can occur through three primary mechanisms such as Volmer-Weber, Stranski-Krastanov, and Frank-Van der Merwe. In the SILAR method, the development of the film typically begins after the 1st or 2nd deposition cycle, which is attributed to the presence of a monolayer of a water-insoluble compound formed during the initial SILAR cycle, which serves as a nucleation center for the subsequent film growth.

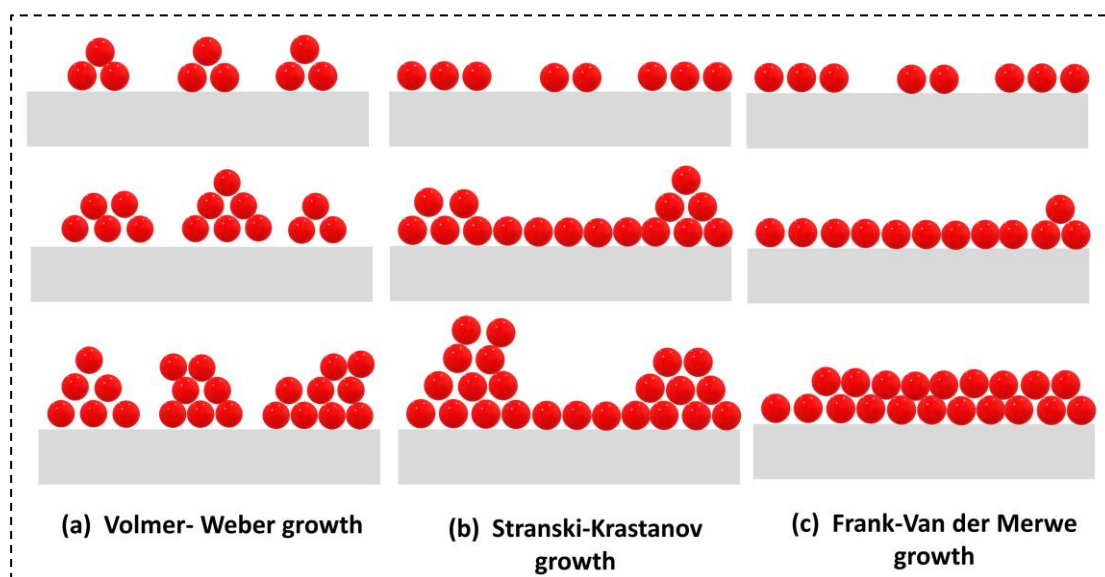


Figure 2.6 Schematic of thin film growth mechanisms.

i) Volmer-Weber Mechanism

In the Volmer-Weber growth mechanism, illustrated in Figure 2.6 (a), the interactions between adatoms are more pronounced than their interactions with the surface. Consequently, this leads to the formation of three-dimensional (3D) adatom clusters or islands. In the SILAR process, thin films form through the alternating adsorption of ions and their reaction on a substrate. When the Volmer-Weber mechanism occurs, the deposited material prefers to create clusters rather than a continuous film, as the ions exhibit stronger interactions among themselves than with the substrate and these clusters expand as more material adsorbs and reacts [21].

ii) Stranski-Krastanov Mechanism

The layer-plus-island growth is known as Stranski-Krastanov, as illustrated in Figure 2.6 (b). In this model, the initial stage involves 2D nucleation, which typically occurs within one or more atomic layers of the new phase, resulting in the formation of a few monolayers. Subsequently, a 3D nucleation process is triggered, leading to the formation of islands [21].

iii) Frank-van der Merwe Mechanism

The Frank-Van der Merwe growth mechanism, illustrated in Figure 2.6 (c), is one of the three primary modes by which thin films grow at a crystal surface or interface. It is commonly known as 'layer-by-layer growth.' In this mechanism, the atoms intended for deposition are more strongly attracted to the substrate than to each other, which distinguishes it from the layer-plus-island or Stranski-Krastanov growth model [22]. Thus, various preparative parameters influence the choice of a specific growth mechanism during material deposition.

2.3.4 Effect of Preparative Parameters

The growth kinetics of thin films in the SILAR method are dependent on various factors, such as the presence of a complexing agent, temperature, solution concentration, duration of adsorption and reaction, rinsing duration, and the composition of the reaction solution.

a) Adsorption and Reaction Time

The time taken for adsorption and reaction is of great significance in the formation of thin films. If the adsorption time is longer than the reaction time, the

film grows through a series of sequential reactions, resulting in a greater final thickness. Conversely, when the adsorption and reaction times are equal, a consistent reaction occurs, leading to uniform growth and the formation of a uniform film. The influence of adsorption and reaction time on film growth has been extensively studied and documented by Shinde et al. [23].

b) Rinsing time

It is crucial to incorporate rinsing steps between each immersion in order to prevent precipitation within the reaction bath. Immersing the substrate in a rinsing bath allows for the removal of loosely bound species from the surface. Sufficient rinsing time is vital to ensure the formation of a high-quality film. Also, rinsing time variation can alter the morphology and surface area of deposited films [24].

c) Concentration of Solution

The density of adsorbed ions on the surface is directly affected by the concentration of the precursor solution. Whereas ultra-low concentrations of solutions, thicker films are deposited, whereas lower concentrations yield thin and non-uniform films. This observation indicates that optimal concentrations of the precursor solution supply an adequate quantity of ionic species necessary for producing films of superior quality.

d) Complexing Agent

A complexing agent is a substance that possesses the capability to form a complex compound when combined with another substance in a solution. Chemical deposition methods often utilize various complexing agents such as ammonia (NH_3), ethylenediaminetetraacetic acid (EDTA), triethanolamine (TEA), etc. The ions of the complexing agent establish a binding with the metal ions, transforming them into complex ions. As a chemical reaction proceeds, metal ions are released and become accessible for interaction with other ions. In this regard, a complexing agent plays a pivotal role in maintaining the concentration of metal ions throughout the reaction. In the SILAR method, the gradual liberation of metal ions results in a reduced rate of film growth. By utilizing a complexing agent, it becomes feasible to control the kinetics of film growth.

e) Temperature

The degree to which a complex compound dissociates is affected by temperature. As the temperature rises, the dissociation becomes more prominent, resulting in a greater concentration of cations/anions and consequently leading to an elevated rate of deposition.

2.3.5 Advantages of SILAR Method

The SILAR method presents numerous advantages for thin film deposition [25]:

- i. **Cost-effectiveness:** SILAR is a cost-effective method due to its utilization of readily available and precursor solutions and Low cost-effective instruments.
- ii. **Versatility:** SILAR is suitable for a wide range of materials, including metal oxides, sulfides, chalcogenides, and composites deposition, making it a versatile method.
- iii. **Precise Film Thickness Control:** The number of deposition cycles can be adjusted in SILAR to achieve precise control over the film thickness according to specific requirements.
- iv. **Uniform Deposition:** SILAR enables the deposition of uniform and conformal films, ensuring consistent film properties across the substrate surface.
- v. **Tailorable Film Properties:** By modifying deposition parameters and precursor compositions, SILAR allows for the customization of thin film properties, including optical, electrical, and structural characteristics.
- vi. **Scalability:** SILAR can be scaled up for larger deposition areas, enabling the production of thin films on a commercial scale.

In summary, SILAR offers a cost-effective, versatile, and controllable method for thin film deposition with wide-ranging applications, particularly in the field of ESD.

2.4 Physicochemical Characterization Techniques

The effective functioning of a material is intricately tied to its diverse physicochemical characteristics, underscoring the importance of employing various techniques to characterize materials and conducting meticulous analysis.

These responsibilities carry substantial significance within the research domain. This procedure assists in the selection of suitable material for a particular application and allows for the determination of desired material properties while exploring avenues to improve them. In the present study, a range of material characterization techniques were utilized to examine the thin film electrodes in their as-deposited state. Within this section, a detailed elucidation is provided regarding the fundamental principles, instrumentation, and operational mechanisms of these techniques, offering a comprehensive depiction of their respective functions.

2.4.1 X-Ray Diffraction (XRD)

The XRD analysis is a prevalent analytical technique employed to ascertain the crystal structure of a sample being studied. This method offers valuable insights into the dimensions of the unit cell and the phase of the material, facilitating researchers in acquiring a thorough comprehension of the material's properties [26]. The analysis of XRD patterns enables the identification of material structures, determination of lattice parameters, assessment of strain, measurement of grain size, examination of epitaxy, analysis of defect structures, and evaluation of preferred orientation.

In the XRD technique, utilizing monochromatic radiation is a fundamental requirement and it is crucial for the determination of crystal structure, and interplanar distance, which is based on the diffraction angle specified by Bragg's law.

2.4.2 Fourier Transform-Infrared (FT-IR) Spectroscopy

FT-IR spectroscopy is an analytical technique employed to identify organic, polymeric, and inorganic materials. This technique utilizes infrared light to examine test samples and determine their chemical properties. The FT-IR instrument emits infrared radiation ranging from approximately $10,000\text{ cm}^{-1}$ to 100 cm^{-1} through a sample, where a portion of this radiation is absorbed, and another portion passes through. The absorbed radiations are transformed into rotational and/or vibrational energy within the sample's molecules. This process generates a signal at the detector, which is displayed as a spectrum, usually spanning from 4000 to 400 cm^{-1} . This spectrum serves as a molecular fingerprint

unique to each molecule or chemical structure, making FT-IR analysis an excellent technique for chemical identification [27].

2.4.3 Field Emission Scanning Electron Microscopy (FE-SEM) and Energy Dispersive X-ray (EDS) Spectroscopy

FE-SEM and EDS are essential techniques for material analysis. FE-SEM works by directing a focused electron beam at the sample's surface, which triggers the emission of secondary electrons. These electrons are then collected to produce highly detailed images that reveal the surface structure and fine details of the sample at the nanoscale. EDS is frequently used in conjunction with FE-SEM to determine the elemental composition of the material. When the electron beam interacts with the sample, it causes the atoms to emit characteristic X-rays specific to each element. EDS detects these X-rays and generates a spectrum, providing data on the sample's elemental composition. Together, FE-SEM and EDS deliver comprehensive insights into the sample's morphology and elemental distribution [28, 29].

2.4.4 X-ray Photoelectron Spectroscopy (XPS)

The analysis of surface chemistry plays a crucial role in understanding the effects of surface engineering. XPS is a widely accepted technique for characterizing surfaces and is recognized as a standard tool in this domain. XPS, which is also referred to as electron spectroscopy for chemical analysis, is a surface analysis technique used to investigate the chemical properties of a material's surface. By employing XPS, one can determine the elemental composition, empirical formula, chemical state, and electronic state of the elements present within the material. XPS is a technique that entails exposing a solid surface to X-ray irradiation while concurrently capturing the KE of emitted electrons originating (from the top 1-10 nm) of the material [30-33].

2.4.5 Thermogravimetric Analysis (TGA)

Thermal analysis involves examining changes in a sample's properties due to an imposed temperature change. Typically, the sample is in a solid state, and heating can cause melting, phase transitions, sublimation, and decomposition. The analysis of mass changes in a sample upon heating is called TGA. TGA tracks mass variations in a material as a function of temperature (or time) in a controlled

environment. It is primarily used to assess a material's thermal stability and composition. TGA is particularly valuable for studying dehydration, decomposition, and oxidation processes [34].

2.4.6 Brunauer-Emmett-Teller (BET) and Barrett-Joyner-Halenda (BJH)

The analysis of specific surface area and porosity in synthesized materials is conducted using Brunauer-Emmett-Teller (BET) analysis. Non-corrosive gases are commonly used to measure surface area and pore size. Nitrogen (N₂) is the most commonly employed gas for surface area measurement, chosen for its suitability and widespread applicability [35]. The amount of nitrogen (N₂) adsorbed onto the adsorbent material is measured under cryogenic conditions, usually at the temperature of liquid nitrogen (77 K), while varying the applied pressure [36]. The surface area calculated using the BET method based on adsorption isotherms of microporous solids may not provide an exact measure of the actual surface area. However, it serves as a practical value that can be employed for relative comparisons when evaluating the porosity of similar materials [37, 38].

The characterization of pore size distribution, known as Barrett-Joyner-Halenda (BJH) analysis, involves determining the distribution of pore volume based on pore size. It is widely recognized that the utilization of desorption isotherm values is more appropriate than adsorption isotherm values for evaluating the pore size distribution of an adsorbent.

2.4.7 Raman Spectroscopy

Raman spectroscopy is utilized to identify functional groups present in a material. This analytical technique involves subjecting a sample to monochromatic light, causing it to selectively absorb specific wavelengths and transmit the majority of the light. Raman spectroscopy offers numerous advantages, including its non-destructive nature, molecular identification capabilities, high specificity, rapid analysis, versatility, complementarity with other techniques, minimal interference, remote analysis capabilities, and safety. These qualities make Raman spectroscopy a valuable analytical tool in various scientific, industrial, and research applications [39].

2.4.8 High-Resolution Transmission Electron Microscopy (HR-TEM)

HR-TEM is a significant materials characterization technique that utilizes an electron beam passed through the sample. The primary distinction between FE-SEM and HR-TEM lies in the intensity of the primary electrons. In HR-TEM, the electrons have a considerably higher KE compared to FE-SEM. Additionally, in FE-SEM, electrons rebound off the sample, whereas in HR-TEM, they pass through the sample. This technique finds extensive applications across diverse scientific, educational, and industrial domains, offering insights into both elemental and compound structures. HR-TEM supplies information in both real space (through imaging mode) and reciprocal space (through diffraction mode), delivering detailed and high-quality images [40].

2.5 Electrochemical Characterization Techniques

A standard two or three-electrode electrochemical cell with an electrochemical workstation (ZIVE MP 1) was used to conduct the electrochemical measurements of the prepared electrodes. The working, reference, and counter electrodes were the thin film electrodes, the Hg/HgO, and the platinum (Pt) plate electrodes, respectively, and the electrolyte was an aqueous solution of 1 M KOH. Electrochemical investigations often utilize the three-electrode system, also called the half-cell system, to analyze the specific electrochemical properties of thin film electrodes. In contrast, the two-electrode system, known as the full-cell system, is preferred for assessing the performance of SC devices. The half-cell setup involves the inclusion of three electrodes within an electrolyte solution: the working electrode, the reference electrode, and the counter electrode. The diagram depicting the arrangement of the three-electrode cell system is shown in Figure 2.7 (a).

The electrochemical workstation is used to control the potential difference between the reference and working electrodes and monitor the current flow from the counter electrode to the working electrode. The measured current is directly proportional to the voltage difference between the working electrode and the reference electrode. To obtain a voltage signal, the current is converted using a current-to-voltage (I/E) converter. This converted voltage signal is then recorded over time by the data acquisition system. It is acknowledged that an ideal electrometer should have a high electrical resistance to minimize the input current.

This is crucial because the flow of current through a reference electrode can induce alterations in the actual potential, which can subsequently affect the precision of the collected data.

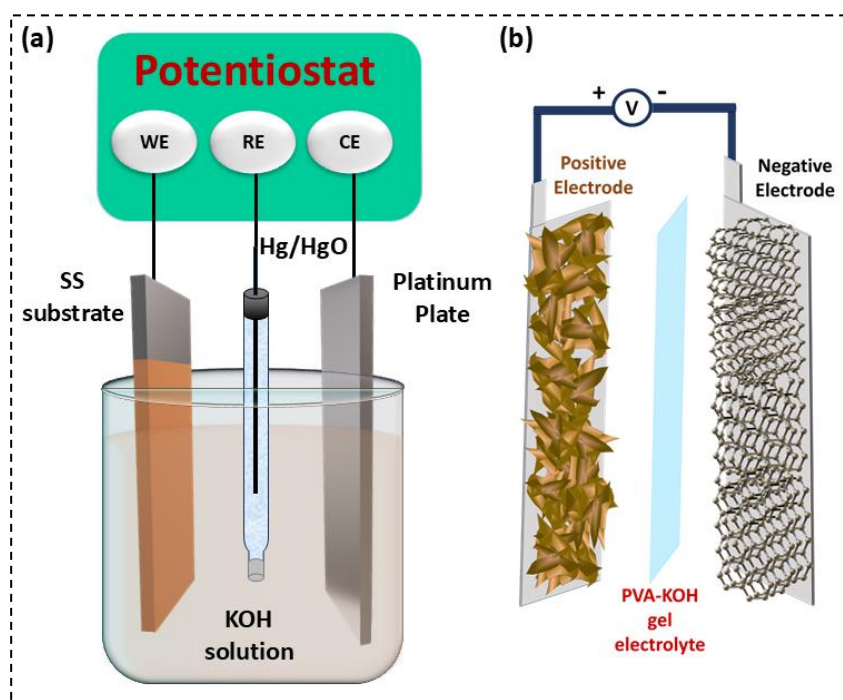


Figure 2.7 Schematic diagram of (a) half-cell electrochemical (three-electrode) system and (b) full-cell (two-electrode) systems.

In the full-cell configuration of a two-electrode system, two working electrodes are placed close to a solid electrolyte, which also functions as a separator. A schematic diagram presented in Figure 2.7 (b) showcases the arrangement of a two-electrode setup that closely resembles a packaged SC. This diagram provides a more comprehensive visualization of the electrode's electrochemical performance within the device. It is worth noting that in the electrochemical system, the potential range employed for the working electrodes in three-electrode systems is the contribution of potentials of anode and cathode that of the potential range used for the electrodes in two-electrode cells.

To maximize the SE of SCs, it is crucial to have a substantial capacitance and a wide operational potential window. However, these characteristics are contingent upon the selection of the working electrode material and electrolyte. Multiple techniques, including CV, GCD, and EIS, can be employed to examine the electrochemical capacitive performance of developed materials. When thin films

are utilized as active electrodes in SC devices, it becomes vital to comprehend and evaluate their electrochemical properties.

2.5.1 Cyclic Voltammetry (CV)

The CV technique is utilized to evaluate the electrode activity within an electrolyte solution. It is a valuable technique for obtaining prompt insights into redox processes and the kinetics of electron-transfer reactions. In CV experiments, the current is produced as a consequence of electron transitions occurring between the electrodes and the redox species. Within a three-electrode electrochemical cell, a potential is applied with respect to the reference electrode, and the current at the working electrode is quantified [41]. In the CV technique, the working electrode experiences a dynamic variation in potential within a predetermined range. When the potential reaches its limit, it is reversed to return to the initial value. A schematic diagram depicting this pattern of potential variation is shown in Figure 2.8 [41].

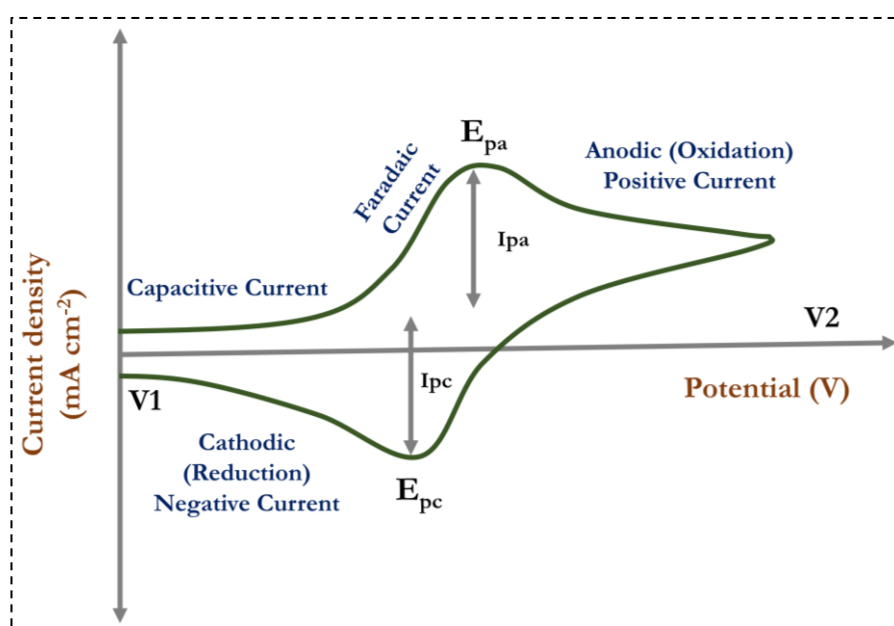


Figure 2.8 The CV curve of the single electrode with reversible redox reaction.

The CV curve shown in Figure 2.8 depicts a typical response of a single electrode to a reversible reaction. It showcases the anodic and cathodic peak currents, labelled as I_{pa} and I_{pc} , respectively, along with the corresponding anodic and cathodic peak voltages, denoted as E_{pa} and E_{pc} , as observed in the resulting voltammogram. These parameters offer valuable information about the

electrochemical characteristics of the electrode. When the analyte is consumed, and the diffuse double layer is established, the current response demonstrates a non-linear decline. During the reverse scan, the reduced analyte undergoes re-oxidation, leading to the generation of an anodic current with reverse polarity. [42]. In reversible electrochemical reactions, the reduction process is like the oxidation process but occurs in the opposite scan direction. This results in the appearance of an I_{pc} at the E_{pc} . In the case of a genuinely reversible process, the anodic and cathodic peak currents should have equal magnitudes but opposite directions. Hence, it is essential to carefully choose the initial (V1) and final (V2) potential values in CV measurements to ensure an accurate interpretation of the experimental findings.

The capacitance of SCs based on two or three-electrode configurations is determined using the following equation.

$$C_s = \frac{\int I(v)dv}{m \times v \times \Delta V} \quad (\text{for CV}) \quad (2.8)$$

The C_s of two or three-electrode-based SCs is determined using the given equation, which takes into account various parameters. These parameters include the scan rate (v) measured in mV s^{-1} , the current response (I) measured in A cm^{-2} , the operating potential window (ΔV) in V, and the mass (m) of the deposited material on the electrodes measured in gram.

2.5.2 Galvanostatic Charge-Discharge (GCD)

The GCD technique is widely used for assessing the electrochemical performance of SCs. In this method, a steady current is applied to the working electrode, and the potential is recorded over time. The observed behavior is typically presented in the form of a GCD curve, as shown in Figure 2.9 [41]. This curve serves as a valuable tool for evaluating the charge storage and release capabilities of the SC. It provides crucial insights into the dynamic response and energy storage characteristics of the device. It is worth noting that the GCD technique is an effective means of understanding and optimizing the performance of SCs. Applying a constant current to the working electrode results in a rapid increase in potential due to the presence of internal resistance. This increase in potential is a consequence of the depletion of reactant concentration at the

electrode surface. As the reaction proceeds, the concentration of reactants diminishes, causing a gradual elevation in potential. It is important to note that both the internal resistance and reactant depletion have a substantial impact on the observed characteristics during GCD experiments. In addition, the potential (V^*) experiences an instantaneous decline during the discharging phase due to the presence of internal resistance. To mitigate this effect and maintain a consistent voltage level, a constant current is applied during both the charging and discharging stages. This methodology guarantees voltage stability and enables precise assessment of the electrochemical performance without being affected by fluctuations caused by internal resistance.

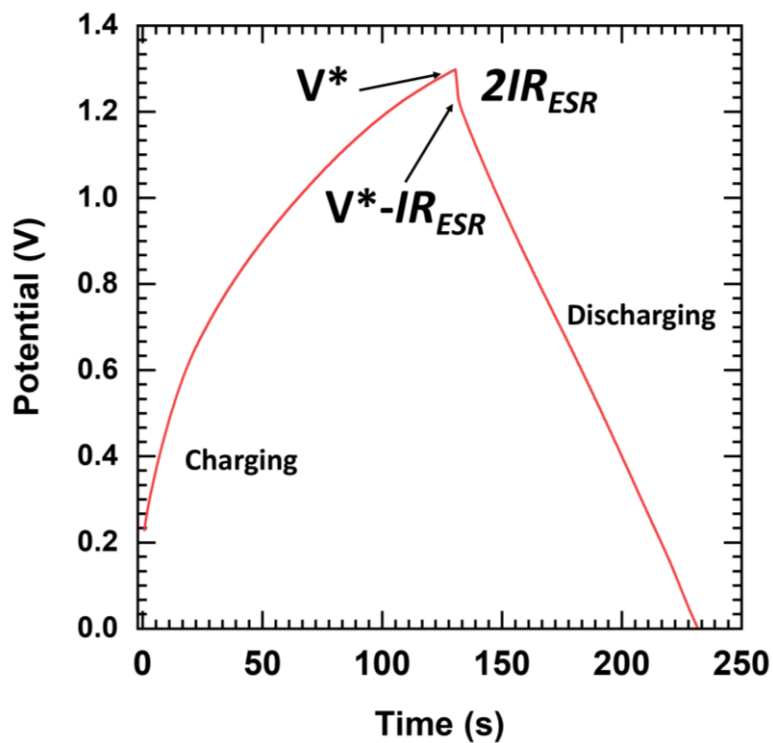


Figure 2.9 Plot of GCD curve.

The analysis of the GCD curve allows for the determination of the charge storage mechanism employed in a SC. If the GCD curve exhibits non-linear behavior, it indicates the presence of a pseudocapacitive charge storage mechanism. Conversely, a linear GCD curve suggests that the dominant mechanism of EDLC [41]. Therefore, by examining the GCD curve, it is possible to identify and confirm the specific charge storage mechanism utilized in the SC [43]. This analysis provides valuable insights into the SC's ED and PD capabilities. The Cs, ED, and PD

of SCs based on two or three-electrode configurations are determined using the equations 1.3, 1.4, and 1.4, respectively as given in Chapter 1.

2.5.3 Electrochemical Impedance Spectroscopy (EIS)

The EIS assesses the impedance characteristics of a material across a range of frequencies, offering insights into the resistance of the electrode-electrolyte interface and charge transfer processes [44]. A minor alternating current signal is administered to the SC cell throughout frequencies spanning from 10 mHz to 0.1 MHz. The resulting signals manifest as the current response to the applied alternating current signals. Analysis and interpretation of the EIS spectra are commonly carried out through Nyquist and Bode plots [45]. Figure 2.10 depicts Nyquist plots featuring equivalent circuits, incorporating the following circuit elements: R_s (solution resistance), R_{ct} (charge transfer resistance), CPE (constant phase element), and W (Warburg impedance element) [46]. The significance of the EIS technique lies in its ability to extract both frequency-dependent and independent electrical components from the Nyquist plot. Models employing equivalent circuits, composed of fundamental electric circuit elements like capacitors and resistors, are employed to replicate intricate electrochemical processes near the electrode-electrolyte interface [47]. Table 2.1 illustrates the elements within equivalent circuits and the equations describing their current-voltage relationships.

Table 2.1 Common electrical components.

Component	Current vs Voltage	Impedance
Resistor	$E = IR$	$Z = R$
Inductor	$E = L \, di/dt$	$Z = j\omega L$
Capacitor	$I = C \, dE/dt$	$Z = 1/j\omega C$

The resistor, being independent of frequency, lacks imaginary elements in its composition. The Nyquist plot presented in Figure 2.10 delineates the real and imaginary components of impedance. In this plot, the X-axis represents the real part, while the Y-axis represents the imaginary part. The inset diagram showcases a fitted equivalent circuit corresponding to the Nyquist plot. Within this figure, the semi-circular loop is indicative of the charge transfer resistance. Additionally, the

impedance of an electrochemical cell encompasses the crucial term of R_s . The resistance of the electrolytic solution is contingent upon factors such as ion concentration, ion type, temperature, and the geometry of the region through which electric current flows. The transfer of charges adheres to fixed kinetics, influenced by factors like reaction type, temperature, concentration, and potential of reaction products.

Furthermore, the phenomenon of ionic diffusion introduces an impedance known as W . It's worth noting that impedance is contingent upon the frequency of potential perturbation. W tends to diminish at higher frequencies because the diffusing reactant covers shorter distances. Additionally, the real-axis intercept observed at elevated frequencies corresponds to ohmic resistance. Conversely, at lower frequencies, the W increases as reactants need to diffuse over longer distances. Within the Nyquist plot, the W manifests as a diagonal line with a 45° inclination, attributed to the mass transport of ions. In EIS investigations, capacitors typically deviate from ideal behavior and exhibit characteristics akin to CPE [48]. To elaborate, an SC demonstrates capacitor-like behavior at low frequencies and behaves akin to a pure resistor at high frequencies. In the intermediate frequency range, the physical and morphological attributes of the electroactive material play a pivotal role in determining capacitance values, effectively functioning as a combination of resistors and capacitors [49]. Notably, the impedance response is heavily influenced by the operating voltage.

The acquired data is subjected to fitting with various interface parameters through algorithms that minimize the chi-square value. EIS holds significance as a crucial characterization technique applicable to diverse material systems, including plating, corrosion, fuel cells, batteries, and more. Moreover, EIS provides a means to ascertain capacitance as a function of frequency [47]. The electrochemical assessments detailed in Section 2.5 were scrutinized by employing the ZIVE MP1 electrochemical workstation. The gathered data served as the basis for determining the C_s of electrodes. EIS measurements were conducted under the following conditions: (i) Open circuit potential state within the frequency range of 100 kHz-100 MHz; (ii) Alternating current-perturbation with 10 mV amplitude a sinusoidal signal. For the analysis of inherent physical processes, the 'ZView

Impedance' equivalent circuit editor was employed to fit the equivalent circuit, aligning it with the experimental Nyquist plots.

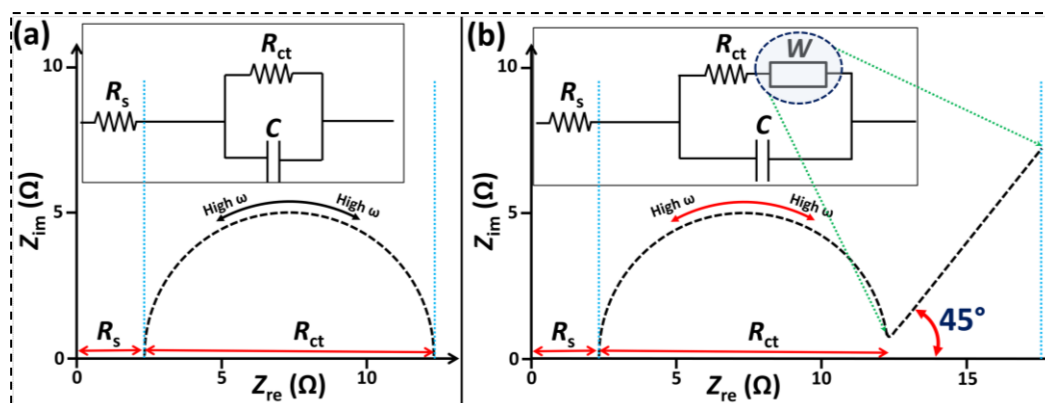


Figure 2.10 (a) Nyquist plot without Warburg and inset its Randles circuit and (b) Nyquist plot with Warburg and inset its Randles circuit.

2.6 References

- [1] R. Velmurugan and B. Subramanian, Physicochemical Approaches for Thin Film Energy Storage Devices through PVD Techniques, Management and Applications of Energy Storage Devices, (2022), 170.
- [2] B. Conway, Electrochemical Supercapacitors: Scientific Fundamentals and Technological Applications, Kluwer-Plenum, New York, (1999), 1-697.
- [3] B. Conway, V. Birss, J. Wojtowicz, J. Power Sources, 66, (1997), 1-14.
- [4] X. Cui, Y. Xu, X. Zhang, X. Cheng, S. Gao, H. Zhao, L. Huo, Sensor Actuat B-Chem., 247, (2017), 681-690.
- [5] G. Brammertz, B. Vermang, H. ElAnzeery, S. Sahayaraj, S. Ranjbar, M. Meuris, J. Poortmans, Thin Solid Films, 616, (2016), 649-654.
- [6] D. Minkov, G. Gavrilov, E. Marquez, S. Ruano, A. Stoyanova, Optik, 132, (2017), 320-328.
- [7] M. Feinaeugle, P. Gregorčič, D. Heath, B. Mills, R. Eason, Appl. Surf. Sci., 396, (2017), 1231-1238.
- [8] I. Gurrappa and L. Binder, Sci. Technol. Adv. Mater., 9, (2008), 1-11.
- [9] K. Chopra, I. Kaur, Thin film Device Application, Plenum Press, New York (1983), 101.
- [10] J. George, Preparation of Thin Films, Marcel Dekker, Inc., New York, (1992), 13-19.
- [11] G. Hodes, Chemical Solution Deposition of Semiconductor Films, Marcel Dekker Inc., New York, (2001), 388.
- [12] D. Dubal, R. Holze, P. Gomez-Romero, Sci. Rep., 4, (2014), 7349, 1-10.
- [13] R. Mane and C. Lokhande, Mater. Chem. Phys., 65, (2000), 1-31.
- [14] S. Pawar, B. Pawar, J. Kim, O. Joo, C. Lokhande, Curr. Appl. Phys., 11, (2011), 117-161.
- [15] B. Ezekoye, P. Offor, V. Ezekoye, F. Ezema, Int. J. Sci. Res., 2, (2013), 452-456.
- [16] R. Khatri and A. Patel, Int. J. Res. Appl. Sci. Eng. Technol, 6, (2018), 1705-1722.
- [17] J. Polte, CrystEngComm, 17, (2015), 6809-6830.
- [18] Y. Nicolau and J. Menard, J. Cryst. Growth, 92, (1988), 128-142.
- [19] H. Pathan and C. Lokhande, Bull. Mater. Sci., 27, (2004), 85-111.
- [20] L. Liu and A. Corma, Chem. Rev., 118, (2018), 4981-5079.
- [21] J. Prieto and I. Markov, Surf. Sci., 664, (2017), 172-184.
- [22] H. Wang, Z. Yao, G. Jung, Q. Song, M. Hempel, T. Palacios, G. Chen, M. Buehler, A. Aspuru-Guzik, J. Kong, Matter, 4, (2021), 3339-3353.
- [23] V. Shinde, T. Gujar, C. Lokhande, R. Mane, S. Han, Sens. Act. B, 123, (2007), 882-887.
- [24] S. Kumbhar, S. Bhosale, S. Pujari, V. Patil, N. Kumar, R. Salunkhe, C. Lokhande, U. Patil, Energy Technol., 11, (2023), 2300400, 1-16.
- [25] S. Ratnayake, J. Ren, E. Colusso, M. Guglielmi, A. Martucci, E. Gaspera, Small, 17, (2021), 2101666, 1-32.
- [26] A. Ali, Y. Chiang, R. Santos, Minerals, 12, (2022), 205, 1-25.

- [27] R. Nyquist and R. Kagel, *Infrared Spectra of Inorganic Compounds*, Academic Press INC, New York, (1971), 2-6.
- [28] G. McMahon, *Analytical instrumentation: a guide to laboratory, portable and miniaturized instruments*, John Wiley & Sons, (2008), 320.
- [29] J. Goldstein, D. Newbury, J. Michael, N. Ritchie, J. Scott, D. Joy, *Scanning Electron Microscopy and X-ray Microanalysis*, Springer, (2017), 573.
- [30] S. Kerber, T. Barr, G. Mann, W. Brantley, E. Papazoglou, J. Mitchell, J. Mater. Eng. Perform., 7, (1998), 334-342.
- [31] M. Koppelman and J. Dillard, *Dev. Sedimentol.*, 27, (1979), 153-166.
- [32] D. Hercules, L. Cox, S. Onisick, G. Nichols, J. Carver, *Anal. Chem.*, 45, (1973), 243-248.
- [33] M. Czuha and W. Riggs, *Anal. Chem.*, 47, (1975), 1836-1838.
- [34] B. Boyanov and A. Peltekov, *Bulg. Chem. Commun.*, 44, (2012), 17-23.
- [35] F. Ambroz, T. Macdonald, V. Martis, I. Parkin, *Small*, 2, (2018), 1800173, 1-17.
- [36] B. Zhang, P. Liu, Z. Huang, J. Liu, *ACS Omega*, 9, (2023), 10303-10313.
- [37] G. Ertl, H. Knozinger, F. Schuth, J. Weitkamp, *Handbook of Heterogeneous Catalysis*, Second Enlarged Edition, WileyVCH Verlag GmbH & Co. KGaA, Weinheim, Germany, (2008), 2-16.
- [38] A. Datar, Y. Chung, L. Lin, *J. Phys. Chem. Lett.*, 11, (2020), 5412-5417.
- [39] D. Wolverson, *Characterization of Semiconductor Heterostructures and Nanostructures*, (2008), 249-288.
- [40] D. Smith, *Handbook of Microscopy for Nanotechnology*, Springer, Boston, (2005), 427.
- [41] S. Dai, Y. Xi, C. Hu, X. Yue, L. Cheng, G. Wang, *J. Power Sources*, 274, (2015), 477-482.
- [42] G. Luongo, F. Giubileo, L. Genovese, L. Iemmo, N. Martucciello, A. Bartolomeo, *Nanomaterials*, 7, (2017), 158, 1-8.
- [43] T. Mathis, N. Kurra, X. Wang, D. Pinto, P. Simon, Y. Gogotsi, *Adv. Energy Mater.*, 9, (2019), 1902007-1902020.
- [44] H. Magar, R. Hassan, A. Mulchandani, *Sensors (Basel)*, 1, (2021), 6578, 1-8.
- [45] M. Orazem and B. Tribollet, *Preliminary Graphical Methods in Electrochemical Impedance Spectroscopy*, A John Wiley & Sons, Inc., New Jersey, (2008), 333.
- [46] C. Song, Z. Peng, X. Lin, H. Luo, M. Song, L. Jin, X. Xiao, H. Ji, *Front. Chem.*, 8, (2020), 1-9.
- [47] A. Lazanas and M. Prodromidis, *ACS Meas. Sci. Au*, 3, (2023), 162-193.
- [48] J. Huang, Y. Gao, J. Luo, S. Wang, C. Li, S. Chen, J. Zhang, *J. Electrochem. Soc.*, 167, (2020) 166503, 1-49.
- [49] V. Ganesh, S. Pitchumani, V. Lakshminarayanan, *J. Power Sources*, 158, (2006), 1523-1532.

CHAPTER-3

**Preparation of Cobalt
Vanadium Oxide/Reduced
Graphene Oxide Composite
Electrodes by CBS Method
and their Characterization
and Supercapacitive
Performance**

CHAPTER-3

Preparation of Cobalt Vanadium Oxide/Reduced Graphene Oxide Composite Electrodes by CBS Method and their Characterization and Supercapacitive Performance

Sr. No.	Title		Page No.
3.1	Introduction		67
3.2	Synthesis and Characterizations of Pristine Cobalt Vanadium Oxide and Cobalt Vanadium Oxide/Reduced Graphene Oxide Composite Electrodes by CBS Method		68
	3.2.A	Section-A: Chemical Bath Synthesis of Cobalt Vanadium Oxide Electrodes and Characterizations	
	3.2.A.1	Introduction	68
	3.2.A.2	Experimental Details	69
		3.2.A.2.1 Substrate	69
		3.2.A.2.2 Chemicals and Substrate Cleaning Procedure	69
		3.2.A.2.3 Preparation of Cobalt Vanadium Oxide	70
		3.2.A.2.4 Material Characterizations	71
	3.2.A.3	Results and Discussion	72
		3.2.A.3.1 Reaction Mechanism and Growth of Cobalt Vanadium Oxide Formation	72
		3.2.A.3.2 XRD Analysis	73
		3.2.A.3.3 FT-IR Analysis	74
		3.2.A.3.4 XPS Analysis	76
		3.2.A.3.5 FE-SEM and EDS Analysis	77
		3.2.A.3.6 BET and BJH Analysis	81
		3.2.A.3.7 Electrochemical Characterizations	83
		3.2.A.3.7.1 Electrochemical Experimental Setup	83
		3.2.A.3.7.2 CV Analysis	83
		3.2.A.3.7.3 GCD Analysis	87
		3.2.A.3.7.4 EIS and Stability Analysis	88
	3.2.A.4	Conclusions	90
		Section-B: Chemical Bath Synthesis of Cobalt Vanadium Oxide/Reduced Graphene Oxide Composite Materials and Characterizations	

	3.2.B.1	Introduction		91
	3.2.B.2	Experimental Details		91
		3.2.B.2.1	Chemicals	91
		3.2.B.2.2	Synthesis of Reduced Graphene Oxide	92
	3.2.B.3	Result And Discussion		93
		3.2.B.3.1	XRD Analysis	93
		3.2.B.3.2	Raman Analysis	94
	3.2.B.4	Electrochemical Characterizations of Reduced Graphene Oxide		95
		3.2.B.4.1	CV Analysis	95
		3.2.B.4.2	GCD Analysis	96
		3.2.B.4.3	EIS Analysis	96
	3.2.B.5	Synthesis of Cobalt Vanadium Oxide/Reduced Graphene Oxide		97
	3.2.B.6	Results And Discussion		99
		3.2.B.6.1	Reaction Mechanism and Growth of Cobalt Vanadium Oxide/Reduced Graphene Oxide Formation	99
		3.2.B.6.2	XRD Analysis	100
		3.2.B.6.3	FT-IR Analysis	101
		3.2.B.6.4	Raman Analysis	102
		3.2.B.6.5	XPS Analysis	103
		3.2.B.6.6	TG Analysis	105
		3.2.B.6.7	FE-SEM and EDS Analysis	106
		3.2.B.6.8	HR-TEM and EDS Analysis	109
		3.2.B.6.9	BET and BJH Analysis	110
		3.2.B.6.10	Electrochemical Analysis	112
			3.2.B.6.10.1 Electrochemical Setup	112
			3.2.B.6.10.2 CV Analysis	112
			3.2.B.6.10.3 GCD Analysis	114
			3.2.B.6.10.4 EIS and Stability Analysis	115
	3.2.B.7	Conclusions		116
3.3	References			117

3.1 Introduction

Over the past few decades, the need for a variety of applications in the consumer electronics, medicinal, clean energy, and environmental sectors has increased, making ESDs increasingly significant. Although ESDs have numerous advantages, their commercialization faces new challenges [1, 2]. Finding highly efficient ESD for storing and dispensing large amounts of SE is one of the significant challenges [3]. Therefore, HSCs have been developed to achieve higher ED, faster kinetics, longer cycle life, and enhanced safety with reduced costs [4]. The primary goal of HSCs is to develop electrode materials with higher EDs, similar to batteries while maintaining high-PDs and long cycling lifetimes [5, 6].

Consequently, a variety of materials with various morphologies and structures have been investigated as electrodes; nevertheless, transition metal hydroxides and oxides (TMHs/TMOs) are the most remarkable materials for HSCs owing to their high theoretical capacitance with notable ED [1, 6]. Although significant progress has been made in developing TMOs and TMHs for HSC electrodes, problems persist when relying solely on single TMO electrode material with limitations stemming from less capacitance, limited ED, and compromised rate capability owing to poor conductivity [6]. Therefore, modifying intrinsic features by rationally designing structural and morphological features through cation synergy in binary compounds becomes crucial to overcoming the restrictions associated with pristine TMO materials.

Vanadium oxides (V_yO_z) have been extensively researched over the last few decades as potential host materials for electrolyte cations, enabling multi-electron transfer reactions in energy storage applications [3]. Moreover, V_yO_z demonstrates a wide range of redox chemistry owing to their various oxidation states and coordination geometries, leading to distinct valence states and phase structures. The V_yO_z are renowned for their layered structures that predominantly consist of $[VO_6]$ octahedral geometry, which creates an intricate and robust arrangement; meanwhile, $[VO_4]$ tetrahedrons in the composition of V_yO_z add stability and unique properties. By sharing edges, corners, or faces, octahedral geometry can easily form 2D sheet structures, which is not only fascinating but also has significant practical applications in various fields [4]. One significant impediment to the effective kinetics of ion transport is the limited interlayer capacity of V_yO_z . Moreover, the

dissolution of V ions in the aqueous electrolyte solution causes a decrease in capacity values through cycling.

To address these issues, guest species like metal ions, water molecules, and organic molecules are proposed to be incorporated into V_yO_z to enlarge the interlayer space [5]. Therefore, several layered hydrated metal vanadates ($M_xV_yO_z \cdot nH_2O$) compounds have been scrutinized as cathode materials for metal ion batteries (MIBs), including $Cu_3V_2O_7(OH)_2 \cdot 2H_2O$ [7], $Ca_{0.24}V_2O_5 \cdot 0.83H_2O$ [8], $K_2V_6O_{16} \cdot 2.7H_2O$ [9], $Zn_3V_2O_7(OH)_2 \cdot 2H_2O$ [10], $Fe_5V_{15}O_{39}(OH)_9 \cdot 9H_2O$ [11], etc. Transition metal vanadium oxides ($TM_xV_yO_z$) have been extensively researched for various applications and are currently widely used in SC applications due to their diverse redox sites, superior planar electronic conductivity, and various structural prospects with different phases [12]. Within the mixed metal oxides family, $TM_xV_yO_z$ -based electrodes have attracted a lot of interest as high-capacity materials for SCs because of the structural variation with unique polymorphs and the multivalence state range of vanadium (V^{3+} to V^{5+}) [13].

3.2 Synthesis and Characterizations of Pristine Cobalt Vanadium Oxide and Cobalt Vanadium Oxide/Reduced Graphene Oxide Composite Electrodes by CBS Method

Section A, probes and reports a scalable CBS of porous nanosheets of CVO, the consequence of structural, morphological, and electrochemical properties of CVO electrodes by varying precursors (Co:V) molar concentration ratio. An increase in the vanadium precursor results in a change in structural and morphological evolution and consequently alters the electrochemical behavior of the CVO electrode. Moreover, an optimized high-performing CVO electrode material is used to prepare the composite with rGO for SC application is discussed in Section B.

3.2.A Section-A: Chemical Bath Synthesis of Cobalt Vanadium Oxide

Electrodes and Characterizations

3.2.A.1 Introduction

Generally, increasing the SSA to volume ratio is crucial for meeting energy-efficient demands and reducing material microstructure, which can regulate various energy storage mechanisms, from the battery to extrinsic pseudocapacitive types [14]. Despite these recent advances, it is imperative to develop a simple

synthetic approach for the preparation of CVO-based electrodes with an explicit structure and confined microstructure that can achieve superior electrochemical performance. Moreover, CBS is the most efficient method for synthesis among numerous chemical synthesis approaches for preparing materials since it is a simple, economically viable, and highly adaptable method to prepare material on a large area scale.

3.2.A.2 Experimental Details

3.2.A.2.1 substrate

The characteristics of the deposition substrate are crucial in the development of SC electrodes. The properties of the substrate material determine the mechanical strength of SC electrodes. Various substrates, including carbon-based paper, flexible metal substrates, graphene sponges, textiles, cables, titanium foil, carbon cloth, SS, NF, etc. serve as conductive support to facilitate the integration of active materials [15]. Up to this point, economical and environmentally friendly flexible substrates have been utilized in the production of flexible devices.

In the current study, the SS serves as the current collector for the direct synthesis of CVO. The material is grown directly on the conductive SS substrate without the incorporation of any polymer binder, following a binder-free approach. The in-situ growth of active materials on the conductive current collector is considered an efficient method for enhancing interfacial contact compared to the traditional method involving binder-enriched coatings. Furthermore, the SS substrate exhibits greater stability in both acidic and basic conditions compared to alternative metallic substrates. Additionally, the notable characteristics of being economical make the SS substrate particularly suitable for the fabrication of SCs [16-19].

3.2.A.2.2 Chemicals and Substrate Cleaning Procedure

Cobalt chloride hexahydrate ($\text{CoCl}_2 \cdot 6\text{H}_2\text{O}$), ammonium metavanadate (NH_4VO_3), Urea ($\text{CH}_4\text{N}_2\text{O}$), and potassium hydroxide (KOH) were taken from Sigma Aldrich and utilized without purification. The experiment utilizes 304-grade SS as a conducting substrate for the electrode preparation. Before using SS substrates, they were cleaned by a standard process; initially, zero-grade polish paper was used to polish the substrate surface and create nucleation centers. Further, the SS

substrate was washed with acetone and then ultrasonicated in double distilled water (DDW) for 15 min.

3.2.A.2.3 Preparation of Cobalt Vanadium Oxide

The thin films of CVO were synthesized using a convenient CBS approach. In CBS, the chemical bath was prepared by dissolving cobalt chloride hexahydrate and ammonium metavanadate precursors in 50 ml DDW with urea as a hydrolyzing agent. Further, well-cleaned SS substrates were placed vertically in the prepared bath, and the whole assembly was put in a water bath maintained at 95 °C constant temperature, as depicted in Figure 3.1. The reaction bath was kept for 9 h to get adherent deposition of CVO thin films over SS substrate with the desired thickness. Moreover, to probe the precursor's concentration variation, the different molar concentration compositions (ratios) of cobalt and vanadate precursors were taken out separately, such as 3:1 (0.075:0.025), 2:1 (0.066:0.034), 1:1 (0.05:0.05), 1:2 (0.034:0.066), and 1:3 (0.025:0.075), which are indicated by C-CV1, C-CV2, C-CV3, C-CV4, and C-CV5, respectively as shown in Table 3.1. After the deposition, the substrates were removed and rinsed with DDW to obtain the well-adherent brown-colored C-CV series thin films, as shown in Figure 3.1. Furthermore, the films of the C-CV series are used for morphological, structural, and electrochemical studies.

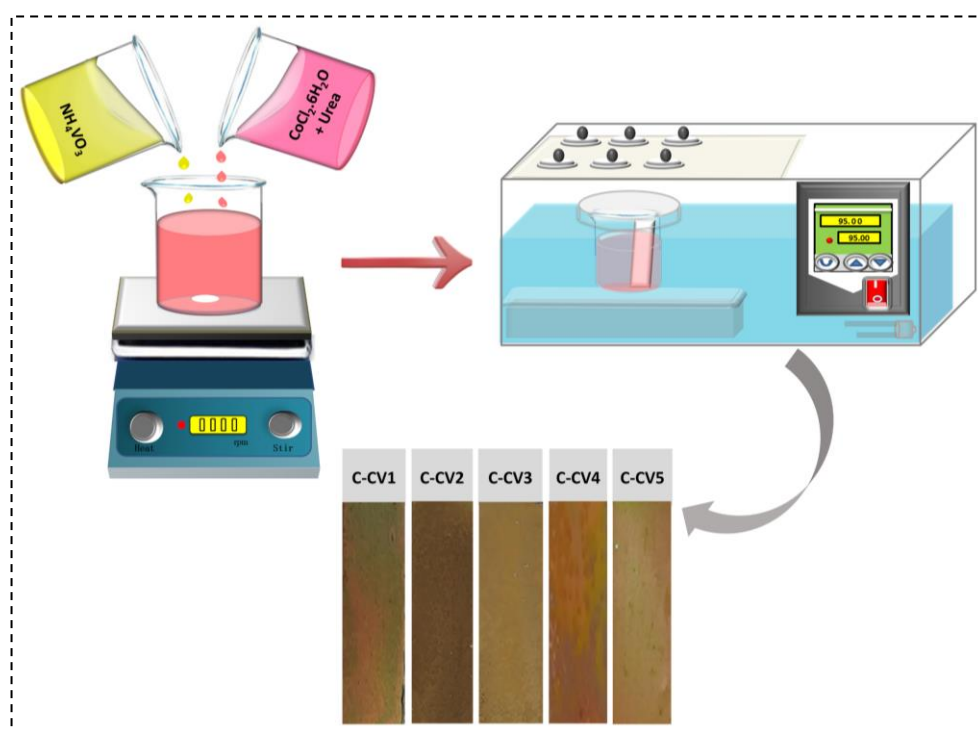


Figure 3.1 Schematic representation of precursors ratio variation of C-CV thin films by chemical bath synthesis method.

Table 3.1 Preparative parameters for the synthesis of C-CV series thin film electrodes.

Sr. No.	Sample Name	Precursors Molar Concentration Ratio (Co:V)	Temp.	Deposition Time
1	C-CV1	0.075:0.025	95 °C	9 h
2	C-CV2	0.066:0.034		
3	C-CV3	0.05:0.05		
4	C-CV4	0.034:0.066		
5	C-CV5	0.025:0.075		

3.2.A.2.4 Material Characterizations

To analyze the structural study of the C-CV series material, Rigaku Miniflex-600 was used with Cu K α ($\lambda=0.154$ nm) radiation to record the powder XRD patterns. FT-IR spectroscopy was used to identify the functional groups and chemical bonding of C-CV thin films using Bruker ALPHA II. By using an FE-SEM (JSM-7001F, JEOL instrument) outfitted with EDS, the surface morphological characteristics and specific elemental distribution of C-CV series thin films were studied. HR-TEM (JEOL, JEM-2100F) equipped with EDS was used to examine the C-CV and rGO composite morphology at higher magnifications. XPS was used to examine the chemical states of C-CV thin films (ESCALAB 250). TGA was performed using a thermal analyzer STA: Hitachi instrument with a heating rate of 20 °C per min. in an air atmosphere to measure the composition of CVO and rGO in the C-CVR composite. The gas sorption analyzer was used to investigate the C-CV materials' pore size distribution and SSA using N₂ adsorption/desorption isotherms (BELSORP mini II, Japan). GCD, CV, and EIS techniques were used to analyze the electrocatalytic activity of C-CV series electrodes. A standard three-electrode electrochemical cell with an electrochemical workstation called ZIVE MP1 was used to conduct the electrochemical measurements. The working, reference, and counter electrodes were the C-CV series electrodes, the Hg/HgO, and the Pt plate electrodes, respectively, and the electrolyte was an aqueous solution of 1 M KOH.

3.2.A.3 Results and Discussion

3.2.A.3.1 Reaction Mechanism and Growth of Cobalt Vanadium Oxide Formation

Hydrous thin films of C-CV were deposited on SS substrates utilizing a CBS method. This process encompasses three successive stages: nucleation, coalescence, and particle growth. Hydrous CVO thin films of the C-CV series (C-CV1, C-CV2, C-CV3, C-CV4, and C-CV5) are prepared to scrutinize the effect of concentration ratio variation and five different reaction baths consisting of different precursor concentrations (Co:V) along with 0.05 M urea (hydrolyzing agent) dissolved in aqueous bath and heated at 95 °C constant temperature for 9 h, as schematically shown in Figure 3.1. In the formation of C-CV series thin films, different reaction steps took place, as given below,

Initially, dissociation of cobalt chloride hexahydrate in the DDW takes place, as per reaction (3.1), and dissociates into Co^{2+} and Cl^- ions.



Similarly, ammonium metavanadate simultaneously dissociates in DDW as per the following equation (3.2),



Moreover, urea is crucial in controlling hydrolysis through delayed breakdown. The decomposition of urea at 368 K as per equation (3.3), which produces ammonia (NH_3) and carbon dioxide (CO_2).



Urea decomposition makes the solution alkaline, and alkaline conditions are most relevant to the formation of complexes with metal ions [20]. Finally, an overall reaction (3.4) causes for C-CV sample formation.



According to the above reaction mechanism, the growth of consistently brown-colored C-CV series thin films was effectively achieved by optimizing the deposition time at low temperatures. Notably, it was found that the C-CV series thin films were not optimally uniform before the 9 h reaction duration and after this

duration, a powdery film developed because of excessive material growth, which caused the film's outer layer to peel off.

The mass loading of C-CV materials placed on the substrate at various concentration ratios was calculated using the gravimetric weight difference method. The loading mass of the samples C-CV1, C-CV2, and C-CV3 increases as the cobalt concentration drops (0.57, 0.61, and 0.66 mg cm⁻²), and then loading mass declines for samples C-CV4 and C-CV5 (0.59 and 0.55 mg cm⁻²) due to the overgrowth of material, as shown in Figure 3.2, which demonstrates distinct growth rate of material over the SS substrate owing to increase in vanadate precursors concentration.

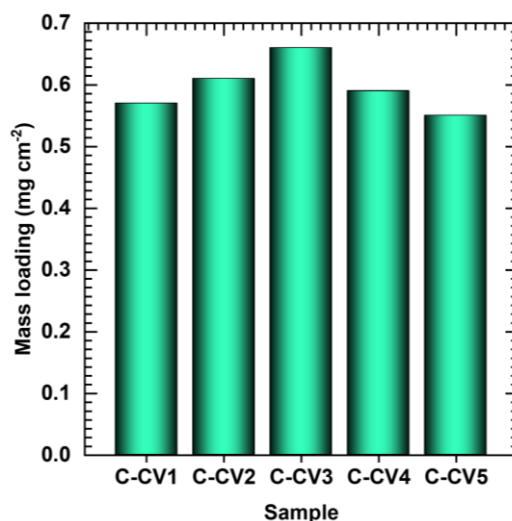


Figure 3.2 Bar diagram of loading mass of CVO on SS substrate.

3.2.A.3.2 XRD Analysis

The crystallographic characteristics were investigated by analyzing the XRD patterns, as depicted in Figure 3.3. Figure 3.3 displays the diffraction characteristics observed in the C-CV thin film series deposited onto the SS substrates, which solely displays SS peaks noted with an asterisk (*) symbol. The diffraction peaks with less intensity are observed in the C-CV1 to C-CV3 samples because SS peak intensity suppressed the material peak intensity. In this XRD pattern, the intense peaks of C-CV4 materials are observed. However, the crystalline peaks in the C-CV series are observed in Figure 3.3 for C-CV4 to C-CV5 in the 2θ range of 10° to 80°. Furthermore, the XRD pattern matches the phase of CoV₂O₆·4H₂O (JCPDS card no. 01-077-0485). The XRD patterns of all prepared

electrodes are consistent, verifying the creation of identical material. The sole distinction lies in the heightened intensity of the primary peaks observed from the C-CV3 to the C-CV5 electrode, indicating an escalation in vanadate concentration in the preparation solution (with a composition variation ranging from 1:1 to 1:3). The narrow and highly intense nature of all peaks suggests improved crystallinity and the favored growth of C-CV material on the SS substrate.

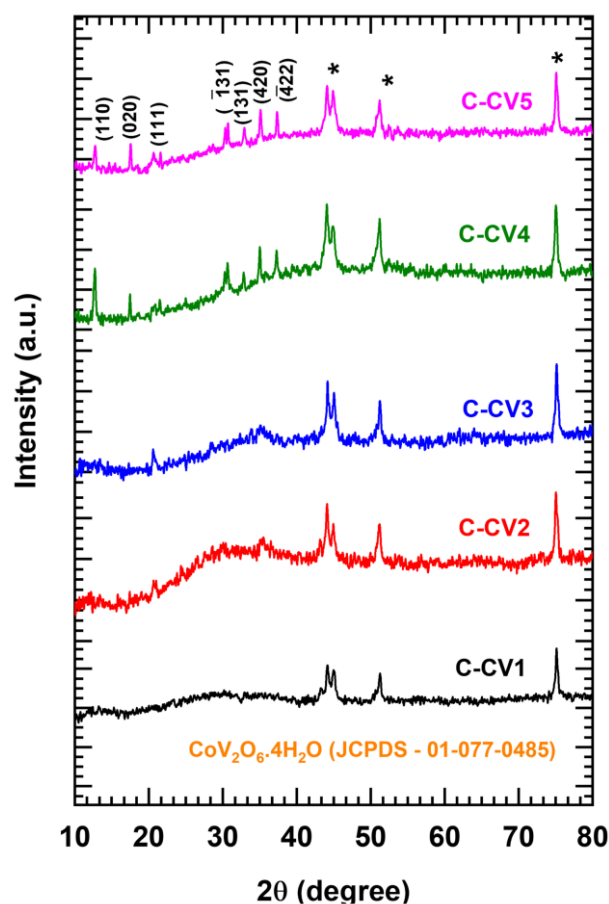


Figure 3.3 XRD patterns of precursors molar concentration ratio variation of C-CV series thin films on SS substrate.

The XRD analysis of the C-CV series electrodes indicates that increasing the concentration of vanadate precursor transforms the structure from poor to well-crystalline. The improved crystallinity in the C-CV series electrodes may demonstrate varying electrochemical behaviors, as each structure has advantages and disadvantages in charge storage. For instance, good crystallinity enhances electrochemical performance by providing a stable structure and improved charge transfer process [21, 22].

3.2.A.3.3 FT-IR Analysis

The molecular chemical bonds and functional groups present in the synthesized thin films of the C-CV series were investigated using FT-IR spectroscopy. Figure 3.4 shows FT-IR spectra of the C-CV series, with measurements performed between 400-4000 cm^{-1} range.

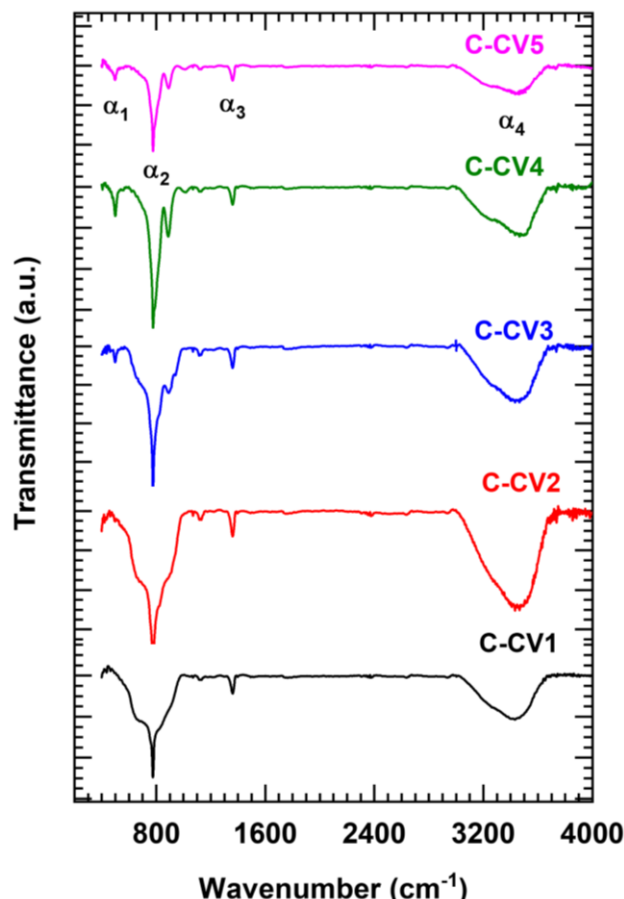


Figure 3.4 FT-IR spectra of C-CV thin films series (C-CV1, C-CV2, C-CV3, C-CV4, and C-CV5).

The metal-oxygen interaction, such as cobalt (Co) and oxygen (O), is responsible for the peak observed at 490 cm^{-1} , which is represented by the ' α_1 ' symbol [23]. The vanadyl group stretching vibration, which is associated with the out-of-plane and in-plane vibrational modes of V-O-V connected to the V-O, has been attributed to the well-built and typical peak (α_2) about 782 cm^{-1} [24]. The peak observed at α_3 (1366 cm^{-1}) is associated with carbonate (CO_3), which is entrapped in layers of $\text{CoV}_2\text{O}_6 \cdot 4\text{H}_2\text{O}$ structure released from urea decomposition [25]. Additionally, the broad spectrum observed at higher wavenumbers (around 3484 cm^{-1} , denoted as α_4) is attributed to the stretching vibrations of the O-H molecules originating from the trapped structural water. Based on the findings of

the XRD analysis, the FT-IR analysis exhibits similar bands present in all samples, confirming the existence of $\text{CoV}_2\text{O}_6 \cdot 4\text{H}_2\text{O}$ with adsorbed or trapped structural hydrous in the C-CV series samples. The results demonstrate that the CBS approach successfully prepared hydrous $\text{CoV}_2\text{O}_6 \cdot 4\text{H}_2\text{O}$ material and such a hydrous nature of materials may display better electrochemical performance [26].

3.2.A.3.4 XPS Analysis

Further investigation and determination of the oxidation state and chemical composition of the constituent elements was carried out using XPS analysis. The wide-range scan XPS spectra of the C-CV4 electrode are shown in Figure 3.5 (a). It displays distinct peaks linked to Co, V, O, and C. The short-range scan of the Co 2p XPS spectrum of the C-CV4 sample is shown in Figure 3.5 (b). The resulting spectrum shows two distinct peaks attributed to Co $2p_{1/2}$ and Co $2p_{3/2}$ at binding energies of 796.8 and 780.7 eV, respectively.

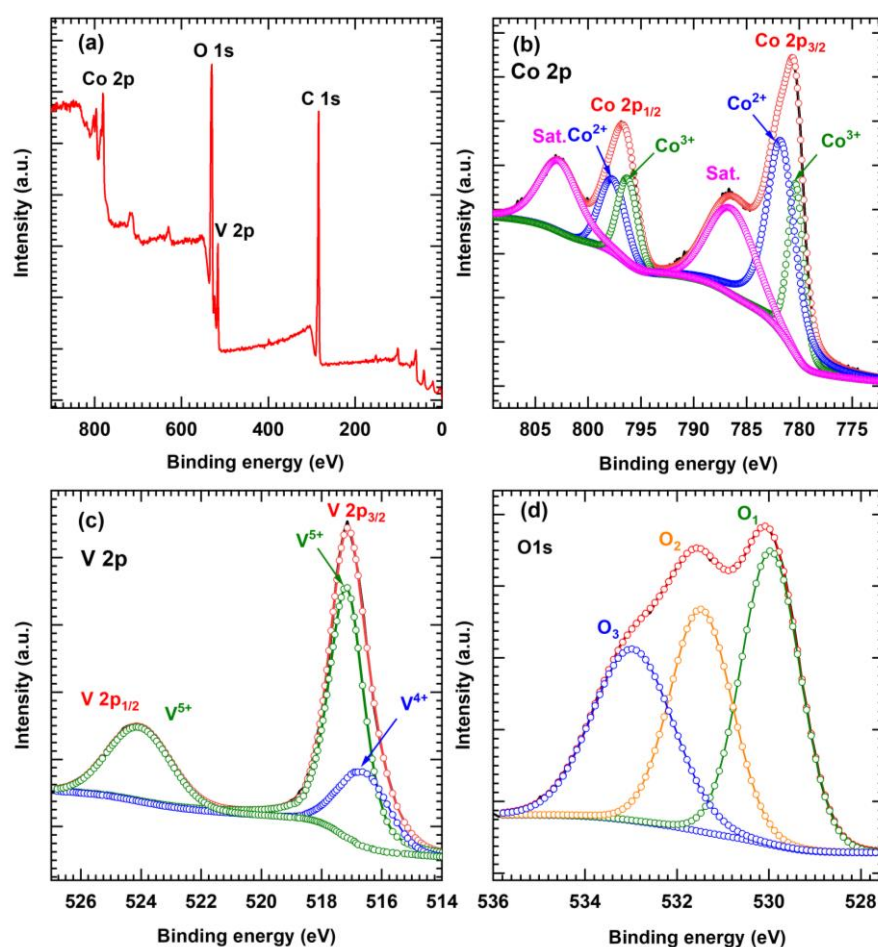


Figure 3.5 (a) XPS full survey spectra and the corresponding (b) Co 2p, (c) V 2p, and (d) O 1s of the sample C-CV4.

Further, these peaks deconvoluted into two peaks such as Co^{3+} (780.4 and 796.5 eV) and Co^{2+} (782.2 and 798.3 eV). The Co^{2+} peaks are more prominent than the Co^{3+} peaks, and the binding energies of 786.4 and 802.7 eV correspond to the satellite peaks [27]. Similar to this, the short-scan XPS spectrum of vanadium (V 2p) is divided into two distinct peaks that correspond to V 2p_{3/2} (517.2 eV) and V 2p_{1/2} (524.1 eV) and are indicative of the prominent V^{5+} (517.2 and 524.1 eV) and V^{4+} (516.6 eV) and states, respectively as shown in Figure 3.5 (c). Also, Figure 3.5 (d) displays the oxygen (O 1s) XPS spectrum, and the spectrum displays three noticeable oxygen contributions, with the peak O₁ at 529.9 eV commonly associated with a metal-oxygen bond. Additionally, the peaks O₂ and O₃ observed at binding energies of 531.4 and 532.9 eV are attributed to the presence of oxygen within the OH groups, indicating structural water in the prepared sample [28].

Therefore, the prevalence of cobalt (2+) and vanadium (5+) oxidation states in the thin films supports the preparation of C-CV material, specifically in the $\text{CoV}_2\text{O}_6 \cdot 4\text{H}_2\text{O}$ polymorph, and aligns with the findings obtained from XRD analysis.

3.2.A.3.5 FE-SEM and EDS Analysis

The surface morphological evolution of C-CV series electrodes with precursor variation was probed by FE-SEM at X1,000, X10,000, and X40,000 magnifications, as shown in Figure 3.6. Interestingly, it is observed that the morphology of C-CV series samples changes significantly with variation in the precursor concentrations of cobalt and vanadate. The FE-SEM image (Figure 3.6 (a1)) of the C-CV series sample at low magnification (X1,000) clearly illustrates the total coverage of interconnected flakes creating widely porous structures over the substrate. Fascinatingly, it is found that the interconnected flakes consist of juvenile scrambled flakes creating cavities on the surface and exhibiting sponge-like structure as shown in the FE-SEM image at higher magnification (X10,000) in Figure 3.6 (a2). Moreover, the FE-SEM image at a magnification of X40,000 in Figure 3.6 (a3) displays the grown immature flakes are very thin with porous walls, and the histogram in Figure 3.6 (a4) displays the calculated average thickness of nanoflakes wall of ~58 nm. Moreover, similar rigorous coverage of $\text{CoV}_2\text{O}_6 \cdot 4\text{H}_2\text{O}$ material over SS substrate for all C-CV series samples is depicted in FE-SEM images at low (X1,000) magnification (Figure 3.6 (b1-e1)). Intriguingly, the morphology of

samples C-CV1 to C-CV5 shows that 2D flakes are coagulated and foaming more compact structures of aligned 2D nanoflakes with the increase in vanadium precursor concentration, as shown in Figure 3.6 (a2-e2).

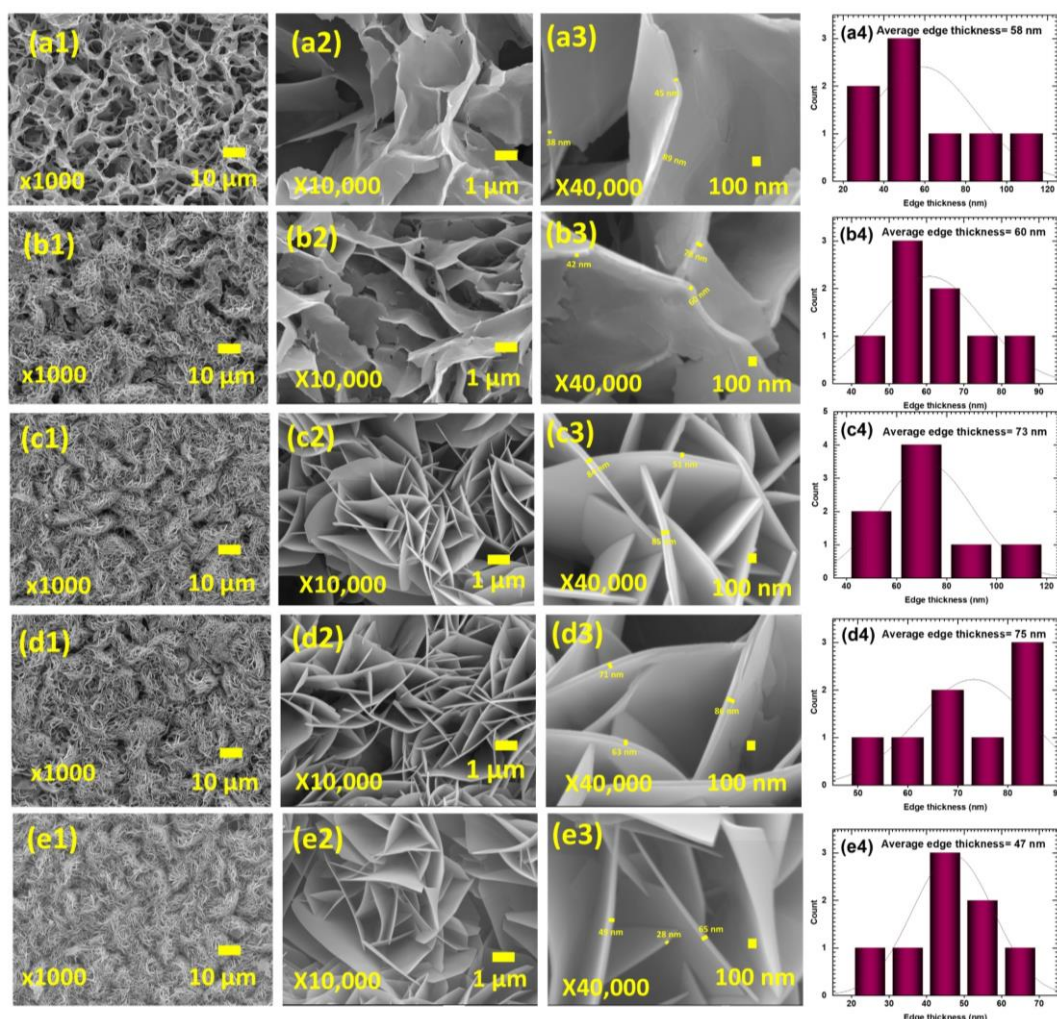


Figure 3.6 FE-SEM images and histograms of C-CV series thin films: (a1-a4) C-CV1, (b1-b4) C-CV2, (c1-c4) C-CV3, (d1-d4) C-CV4, and (e1-e4) C-CV5 at different magnifications of X1,000, X10,000, and X40,000.

Compact alignments of 2D nanoflakes reduce cavities created by the twisted 2D nanosheets, efficiently utilizing the area over the substrate and consequently possessing improved electrochemical active sites. Moreover, as the vanadate concentration increases in C-CV series samples, along with observed alteration in morphologies from scrambled to compactly aligned 2D nanoflakes, an increase in average flakes thickness from ~58 to ~75 nm up to C-CV4 sample is also observed, as histograms depicted in Figure 3.6 (a4-d4). Moreover, with excess vanadate content, the C-CV5 sample shows more compact structures of 2D nanosheet-like

with reduced average sheet thickness of ~ 65 nm, as depicted in Figure 3.6 (e3). The FE-SEM analysis shows that the thickness of the nanosheets increased with increased vanadate concentration at a specific concentration of precursors ratio (0.034:0.066, or 1:2), as schematically illustrated in Fig. 3.7, and it decreased with further increase vanadate precursor concentration with the ratio of 1:3 (Co:V). The XRD and FE-SEM findings indicate higher crystal intensity associated with well-grown nanosheets with increased thickness. Thus, structural and morphological evolution from poorly crystalline to well crystalline nanosheets suggests that the appropriate precursor composition of Co:V during chemical bath synthesis plays a crucial role in achieving crystalline C-CV thin films.

So, it is concluded that to achieve well crystalline and ordered 2D nanosheets, in the composition of Co and V precursors, vanadate precursor should be higher ($> 1:1$). More vanadate precursor concentration could lead to rapid heterogeneous growth of C-CV films over the SS substrate that could result into the oriented attachment of nanosheets and well crystalline thin films. Moreover, the interlinked structure of C-CV series sample nanosheets facilitates the generation of numerous spacious voids, fostering effective electrolyte penetration, which can abbreviate the route for ions transport throughout the GCD cycles [29, 30].

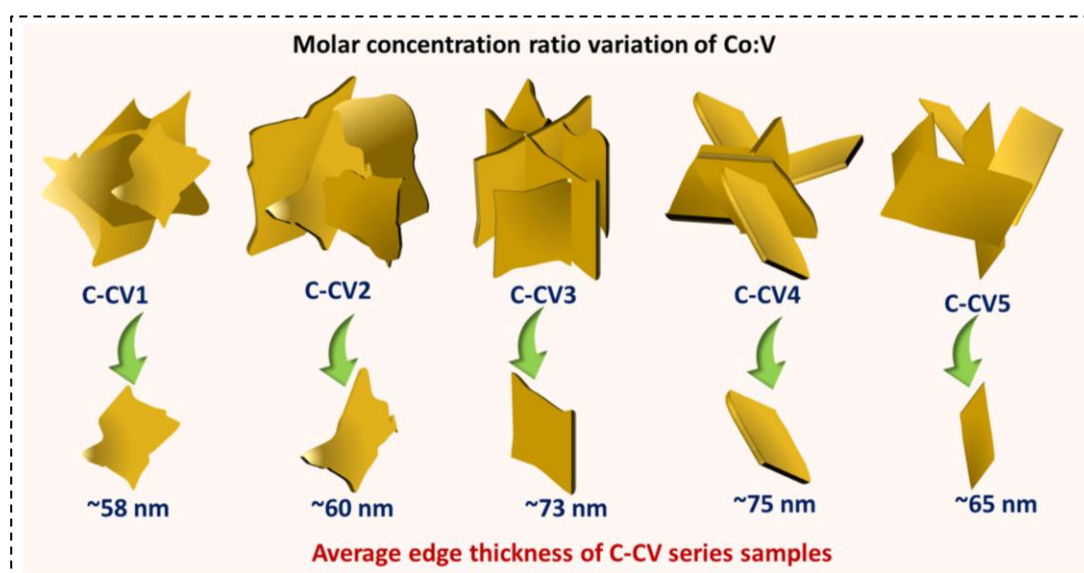


Figure 3.7 Schematic illustration of morphological changes of C-CV series samples.

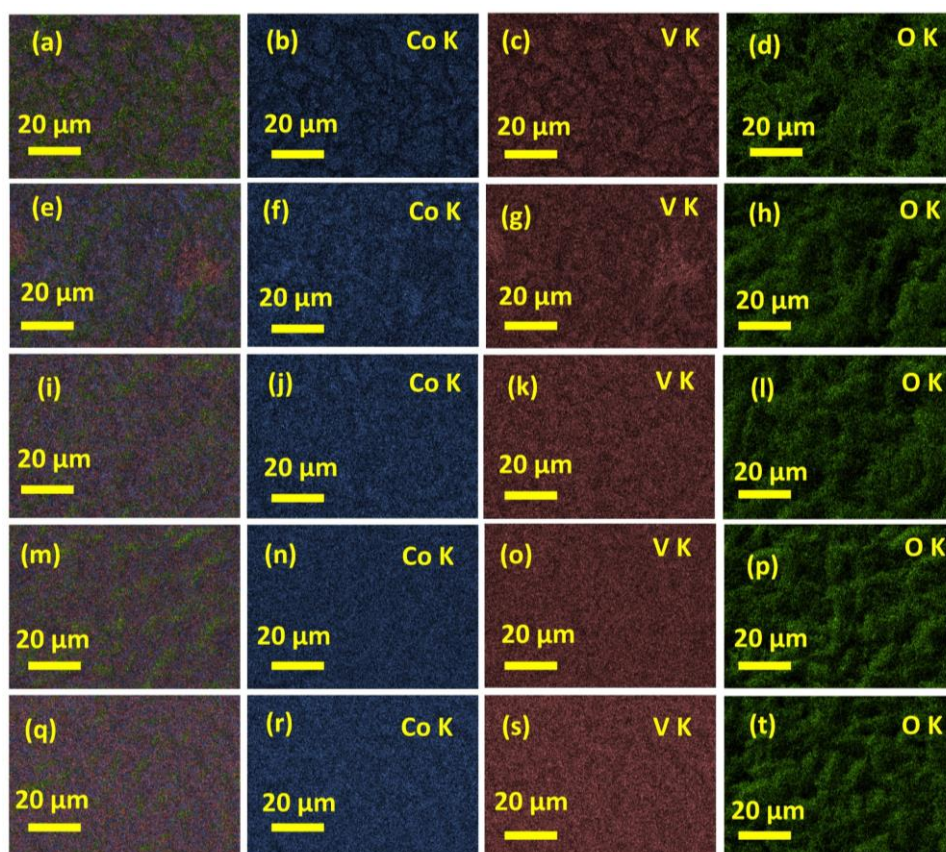


Figure 3.8 EDS mapping of (a-d) C-CV1, (e-h) C-CV2, (i-l) C-CV3, (m-p) C-CV4, and (q-t) C-CV5.

The EDS elemental mapping presented in Figure 3.8 of the chemical bath synthesized C-CV series thin films reveals the presence of cobalt, vanadium, and oxygen elements. Figure 3.8 depicts compositional images showing areas investigated (mixed colors) and elements of Co, V, and O in blue, brown, and green scales, respectively. It reveals a consistent allocation of Co, V, and O elements throughout the C-CV series samples. This analysis confirms the effective deposition of C-CV on the SS substrate irrespective of the variation of the molar concentration of precursors.

The EDS spectra with Co, V, and O peaks of C-CV series samples are displayed in Figure 3.9. The atomic percentage is mentioned in the inset of each spectrum, which confirms the formation of $\text{CoV}_2\text{O}_6 \cdot 4\text{H}_2\text{O}$ material with cobalt: vanadium atomic ratios of $\sim 1:1.70$, $1:1.92$, $1:1.96$, $1:2.03$, and $1:2.07$, respectively. The EDS results indicate that vanadium increases with an increase in vanadate precursor concentration during synthesis. The EDS result confirms molar ratio variation in cobalt and vanadate precursors concentration in C-CV series

electrodes with a slight change in atomic percentage, and it may be a reason for the alteration in morphology from scrambled to ordered 2D nanosheets.

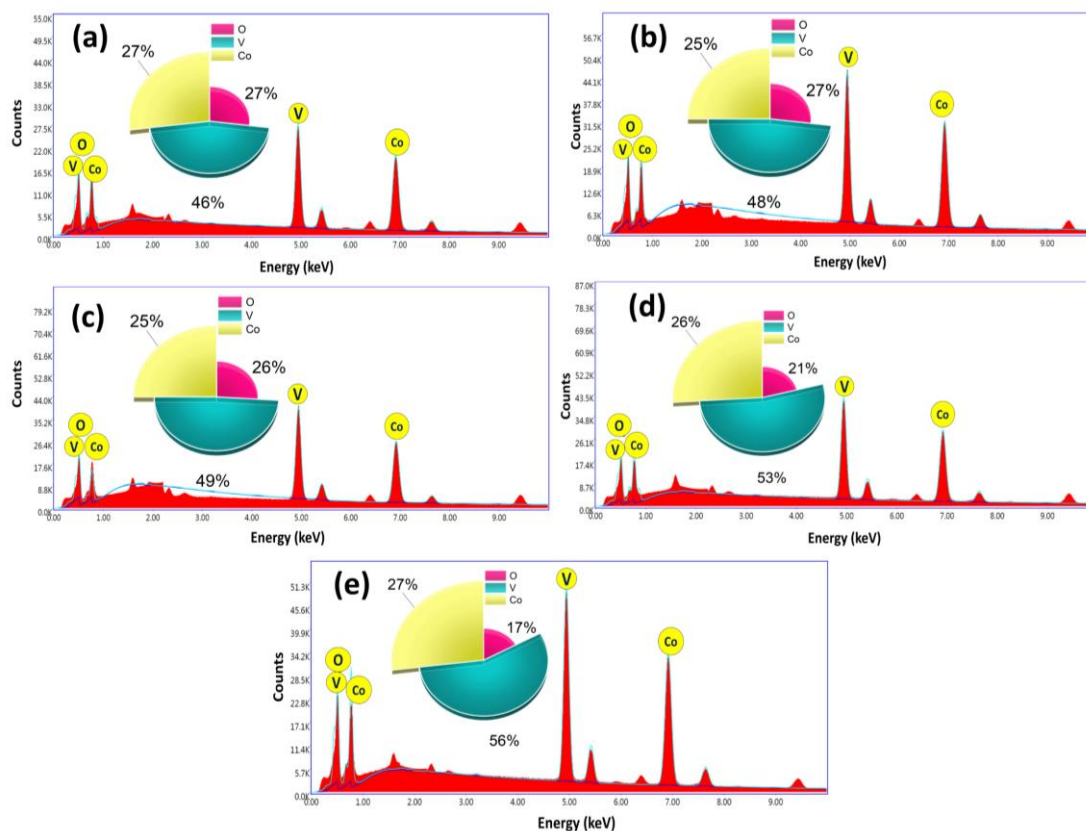


Figure 3.9 (a-e) EDS spectra of C-CV series samples.

3.2.A.3.6 BET and BJH Analysis

The SSA and porosity of the C-CV series samples were investigated using BET and BJH analysis. The N_2 adsorption-desorption curves of the C-CV series samples are shown in Figure 3.10. A type III isotherm with the H_3 type hysteresis loop can be seen in the detected isotherms of the C-CV series samples [31]. The type III isotherm is related to a crucial characteristic of mesoporous material, which uses a lesser amount of adsorption energy for structures with 2D nanosheets. Notably, in the C-CV series, C-CV4 presents a BET SSA of $87.5 \text{ m}^2 \text{ g}^{-1}$, which is higher than those of C-CV1 ($8 \text{ m}^2 \text{ g}^{-1}$), C-CV2 ($12.6 \text{ m}^2 \text{ g}^{-1}$), C-CV3 ($76.7 \text{ m}^2 \text{ g}^{-1}$), and C-CV5 ($46.9 \text{ m}^2 \text{ g}^{-1}$). For the C-CV1, C-CV2, C-CV3, C-CV4, and C-CV5 samples, the BJH analysis was also utilized to determine the pore size distribution, which is found to be 21.2, 13.2, 4.8, 3.7, and 6.9 nm, respectively, as demonstrated in the inset of Figure 3.10 (a-e). The observed BET analysis reveals that the C-CV4

electrode offers a large SSA of $87.5 \text{ m}^2 \text{ g}^{-1}$ and a favorable molar ratio of cobalt and vanadate (1:2) where the compact, well-ordered nanosheet-like morphology.

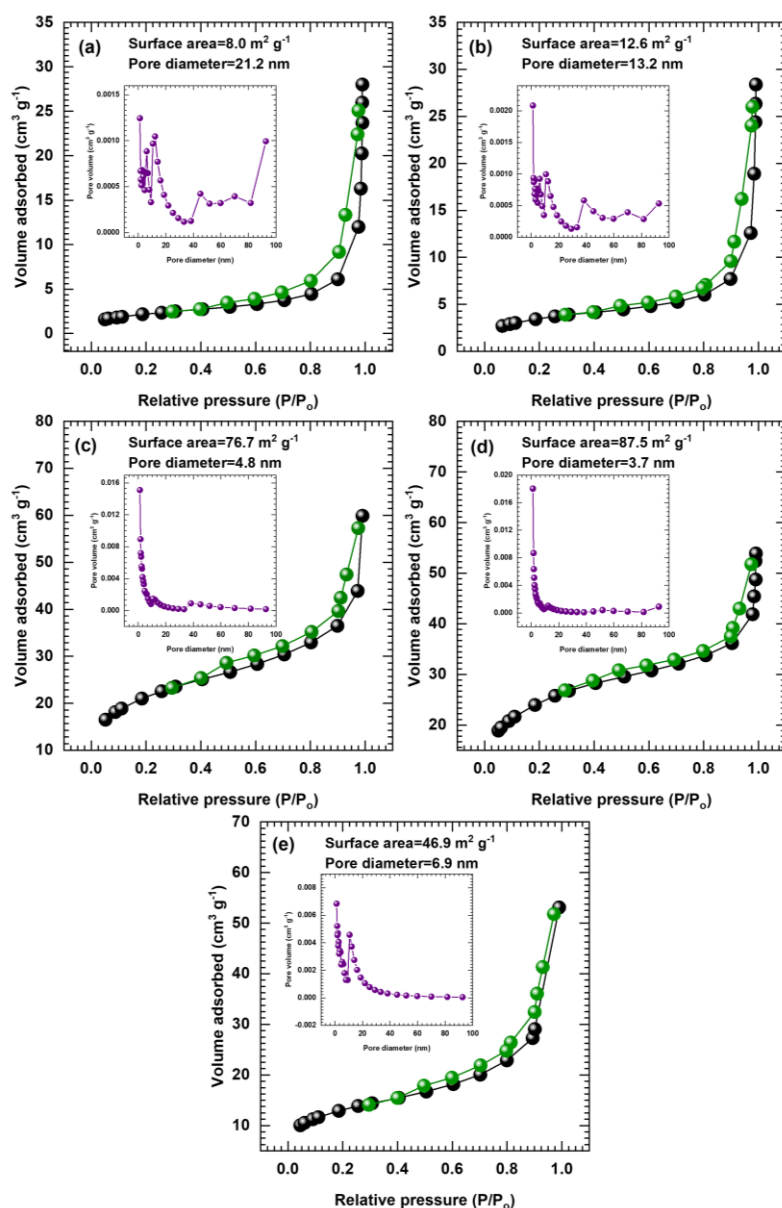


Figure 3.10 N_2 adsorption-desorption isotherms and inset pore size distribution of samples (a) C-CV1, (b) C-CV2, (c) C-CV3, (d) C-CV4, and (e) C-CV5.

It is observed that the scrambled nanoflakes create cavities and voids (C-CV1 sample), which inefficiently offer less SSA ($8 \text{ m}^2 \text{ g}^{-1}$); on the other hand, well-ordered 2D nanosheets observed for the C-CV4 sample increased vanadate concentration possess compact morphology with an efficient mesoporous structure that exhibits higher electroactive SSA. With its mesoporous nature, the greater SSA is useful for energy storage applications and can help provide more active sites with electrolyte ions at the electrochemical intercalation process. Thus,

the C-CV series material mesoporous structures and effective SSA can help to achieve outstanding electrochemical performance.

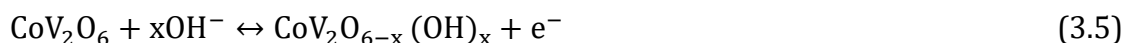
3.2.A.3.7 Electrochemical Characterizations

3.2.A.3.7.1 Electrochemical Experimental Setup

The assessment of the electrochemical performance of binder-free hydrous C-CV series thin film electrodes involves the examination of the effects of structural and morphological variations. A standard three-electrode electrochemical cell with an electrochemical workstation called ZIVE MP1 was used to conduct the electrochemical measurements. The working, reference, and counter electrodes were the C-CV series, Hg/HgO, and Pt plate electrodes, respectively, and the electrolyte was an aqueous solution of 1 M KOH. The electrochemical evaluation is conducted using electrochemical techniques such as CV, GCD, and EIS.

3.2.A.3.7.2 CV Analysis

In Figure 3.11 (a), the comparative CV curves of C-CV series electrodes at a fixed scan rate of 50 mV s⁻¹ in a range of 0 to 0.6 V potential window are displayed. The redox peaks observed for C-CV electrodes demonstrate OH⁻ ions from the electrolyte intercalating into the CoV₂O₆·4H₂O material during the charging process, whereas deintercalation takes place during the discharging phase as per the reversible redox reaction given below.



As shown in Figure 3.11 (a), the current response in the CV curves increases up to the C-CV4 sample, where the compact 2D nanosheet-like structure provides more electroactive sites owing to the high SSA. Additionally, the current response in the CV curve is reduced for the C-CV5 electrode, where the further thickness of 2D nanosheets is reduced, and subsequently, the SSA is reduced. The larger current response in the CV curve than the other electrodes indicates that the C-CV4 electrode prepared at Co:V bath composition of 1:2 (0.034:0.066) indicates a higher capacity of charge storage. The CV curves for the C-CV series electrodes at scan rates of 2 to 50 mV s⁻¹ are displayed in Figure 3.11 (b-f). All C-CV series electrodes show the quasi-rectangular shape of the CV curves, owing to multifarious redox peaks. The CV curves with strong redox peaks indicate that

charge storage occurs mainly through the intercalation and deintercalation of OH^- ions and redox reactions of $\text{Co}^{2+}/\text{Co}^{3+}$ and $\text{V}^{4+}/\text{V}^{5+}$, as described in equation 3.5.

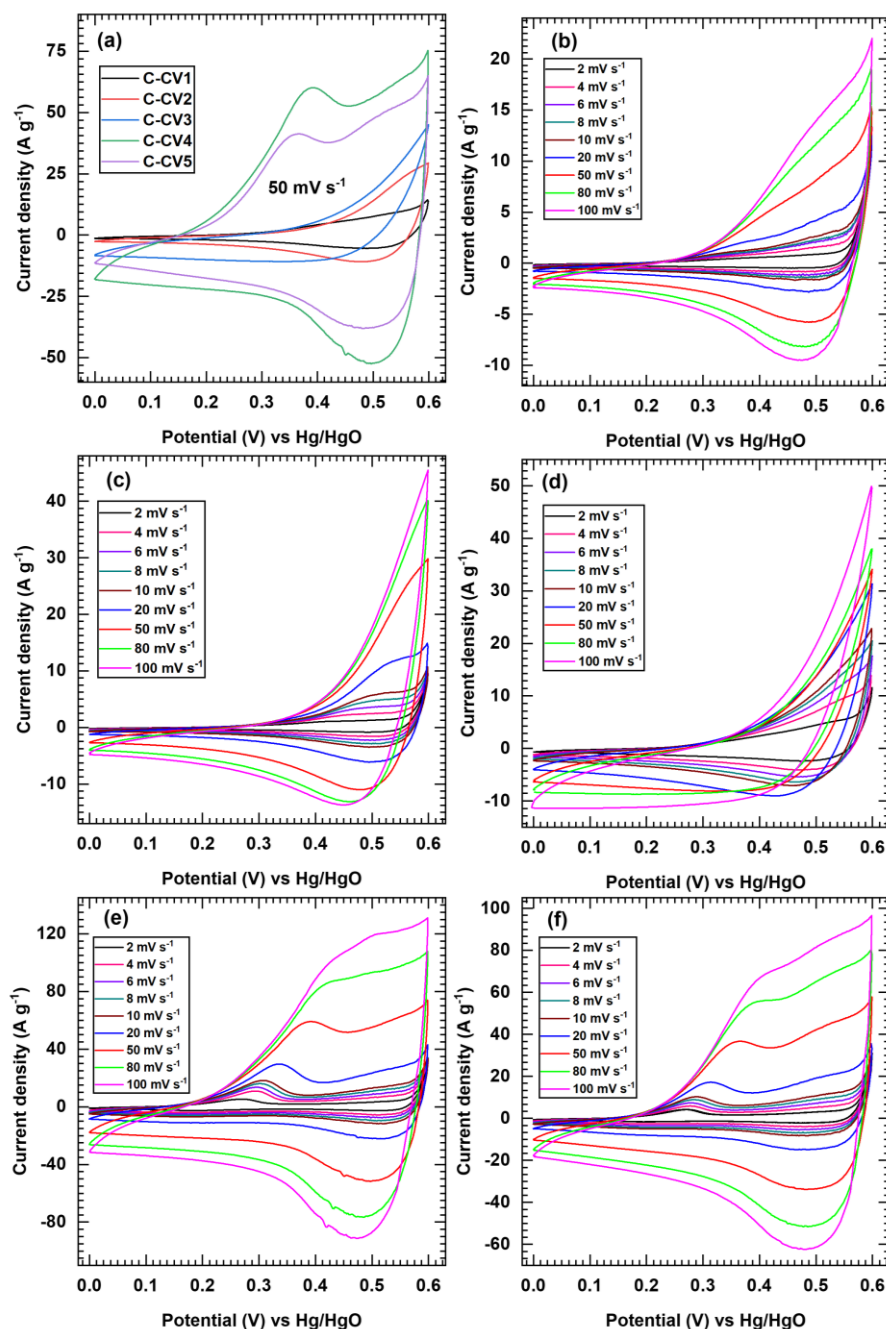


Figure 3.11 (a) At 50 mV s⁻¹ scan rate comparative CV curves and (b-f) CV curves of C-CV series electrodes at different scan rates (2-50 mV s⁻¹).

It has been observed that with a change in precursor composition content, there is a noteworthy change in the shape of the CV curves, with multifarious redox peaks producing a quasi-rectangular nature, attributed to the existence of extrinsic pseudocapacitive (surface controlled) to battery-like (diffusion controlled) charge

storage mechanism. Therefore, it is crucial to clearly distinguish between the charges stored by surface capacitive and bulk intercalation processes in C-CV electrodes. Hence, the 'Power's law' equation given below (equation 3.6) is used to calculate the contributions of surface capacitive controlled and diffusion controlled to determine the charge storage mechanism of the C-CV series electrodes [31]:

$$i = av^b \quad (3.6)$$

In equation (3.6), where both 'a' and 'b' are variables, the value of parameter 'b' is calculated from the slopes of $\log(i)$ vs $\log(v)$ plots. The parameter 'b' is most relevant on different values of 0.5 and 1, where the first value (0.5) denotes diffusion-limited faradaic intercalation and the second value (1) represents the capacitive behaviour of the material [32]. The slope of the linear fit on the graph generated by plotting $\log(\text{scan rate}, v)$ against $\log(\text{peak current}, i)$ gives an estimate of the value of 'b' (Figure 3.12 (a)). The prepared thin film electrodes from the C-CV series exhibit 'b' values that range from 0.52 to 0.92. Here, the change in 'b' values of C-CV1 to C-CV5 electrodes demonstrates the dominance of diffusive to capacitive charge storage mechanisms, as shown in Figure 3.12 (a).

The calculated 'b' value is 0.52 for the C-CV4 electrode, which can show higher peak current as well as area under CV curves than the other electrodes in the C-CV series. The C-CV4 sample shows that the transfer of charges is majorly regulated by a diffusion-controlled process, which suggests that the material can behave as a battery type. To acquire a better understanding of kinetics, the route reported by Chodankar et al. and Ekwere et al. [28, 33] has been used to analyze the respective contributions of the diffusion and surface-based processes to the entire electrochemical capacitive distribution. The total charge stored capacity (Q_{total}) of C-CV electrodes can be separated into two parts, such as the surface capacitive (Q_s) and diffusion controlled (Q_d), as given below in equation (3.7).

$$Q_{\text{total}} = Q_s + Q_d \quad (3.7)$$

Where Q_{total} refers to the total stored charge, Q_s denotes the charge stored at the surface of the material and is related to the EDLCs. On the other hand, Q_d represents the redox reactions that occur in the bulk of the material, and these reactions result from a sluggish diffusion process [34]. The charge storage kinetic analysis is conducted using CV curves measured at various scan rates to distinguish

between the various contributions. Particularly, Q_s can be calculated using the given below equation under the assumption of semi-infinite linear capacitive behaviour with scan rates.

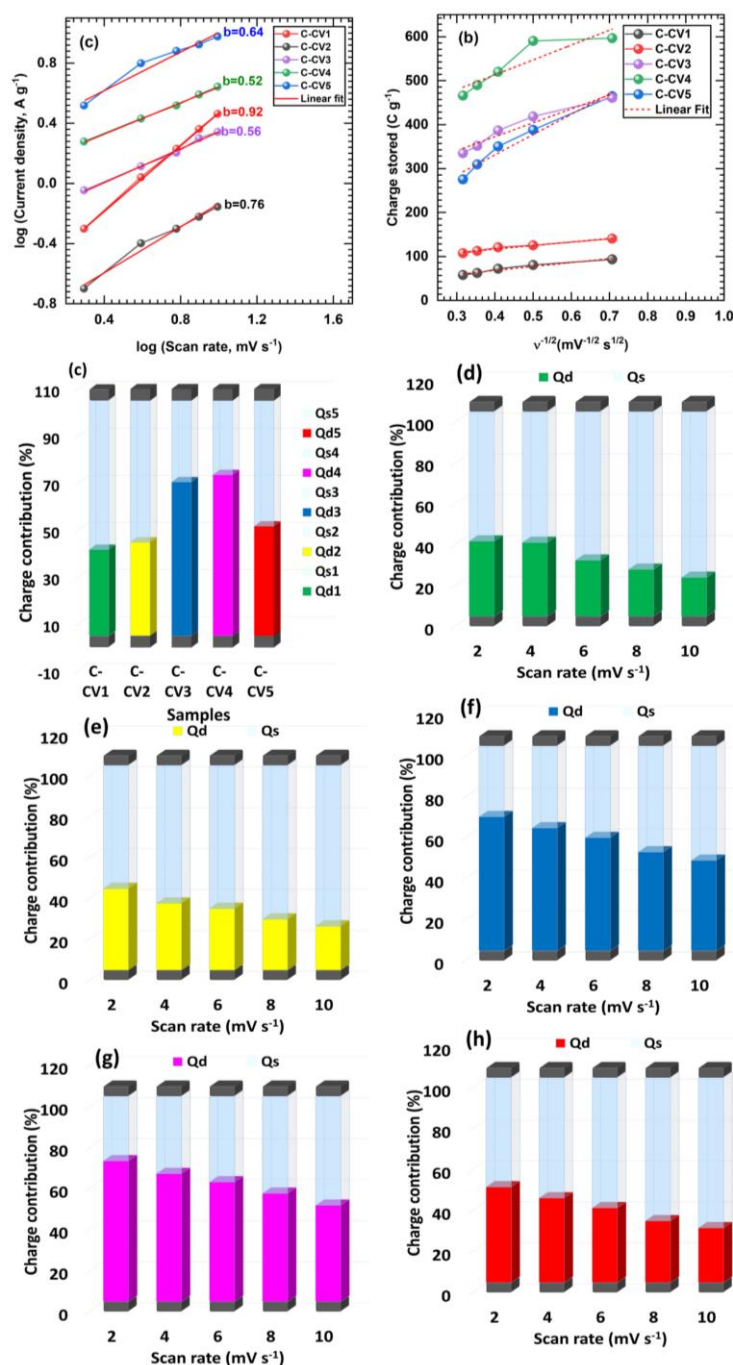


Figure 3.12 (a) The plot of log (peak current) vs the log (scan rate) for C-CV series electrodes, (b) the plot of the total charge against the reciprocal of the square root of scan rate for C-CV series electrodes, and (c) comparative plot of surface and diffusive charge contribution to C-CV series electrodes, and (d-h) charge contribution of C-CV series samples at different scan rates.

$$Q_{\text{total}} = Q_s + \text{Const. } v^{-1/2} \quad (3.8)$$

Figure 3.12 (b) shows the relationship between the total charge stored (Q_{total}) and the inverse square root of the scan rate ($v^{-1/2}$), which determines capacitive contribution (Q_s) through the intercept of the plot. Both Q_s and Q_d are quantified by the acquired comparative data of C-CV series electrodes at a fixed scan rate of 2 mV s^{-1} , as shown in Figure 3.12 (c). It displayed that the Q_d value increases from the C-CV1 up to the C-CV4 electrode, and then it slightly decreases for the C-CV5 electrode. Moreover, the charge contributions in the individual C-CV series sample electrodes with scan rates are displayed in Figure 3.12 (d-h), and the Q_s gradually rise upon increasing scan rates; the major contribution of 68.5% from diffusion-controlled (Q_d) is observed in total charge at 2 mV s^{-1} , whereas only 31.5% of capacitive behaviour demonstrated by C-CV4 electrode as shown in Figure 3.12 (g).

3.2.A.3.7.3 GCD Analysis

Furthermore, the profiles of GCD were analyzed and interpreted to evaluate the capacity of C-CV series thin film electrode materials for charge storage. GCD measurements investigate the electrochemical performance of prepared C-CV series electrodes, carried out within the optimal potential range of 0 to 0.5 V vs Hg/HgO. Comparative GCD curves of all C-CV series electrodes at a fixed current density of 1 A g^{-1} are shown in Figure 3.13 (a), demonstrating intercalative pseudocapacitive behavior, and C-CV4 exhibits longer discharge time than other electrodes.

Moreover, the GCD curves of the C-CV series electrodes at various current densities (1 to 5 A g^{-1}) are shown in Figure 3.13 (b-f). Consistent with the CV analysis, the C-CV4 electrode demonstrates maximum discharge time as compared to other concentration variation electrodes, demonstrating its greater electrochemical capacitive performance. At constant current density of 1 A g^{-1} , the comparative C_s (capacity) values for the C-CV1, C-CV2, C-CV3, C-CV4, and C-CV5 electrodes were found to be 76.8, 134.9, 362.9, 619.5, and 163.5 F g^{-1} (38.4, 67.4, 181.4, 309.7, and 81.7 C g^{-1}), respectively, as shown in Figure 3.13 (g). Furthermore, the C_s of the entire C-CV series electrodes at various current densities are shown in Figure 3.13 (h-i).

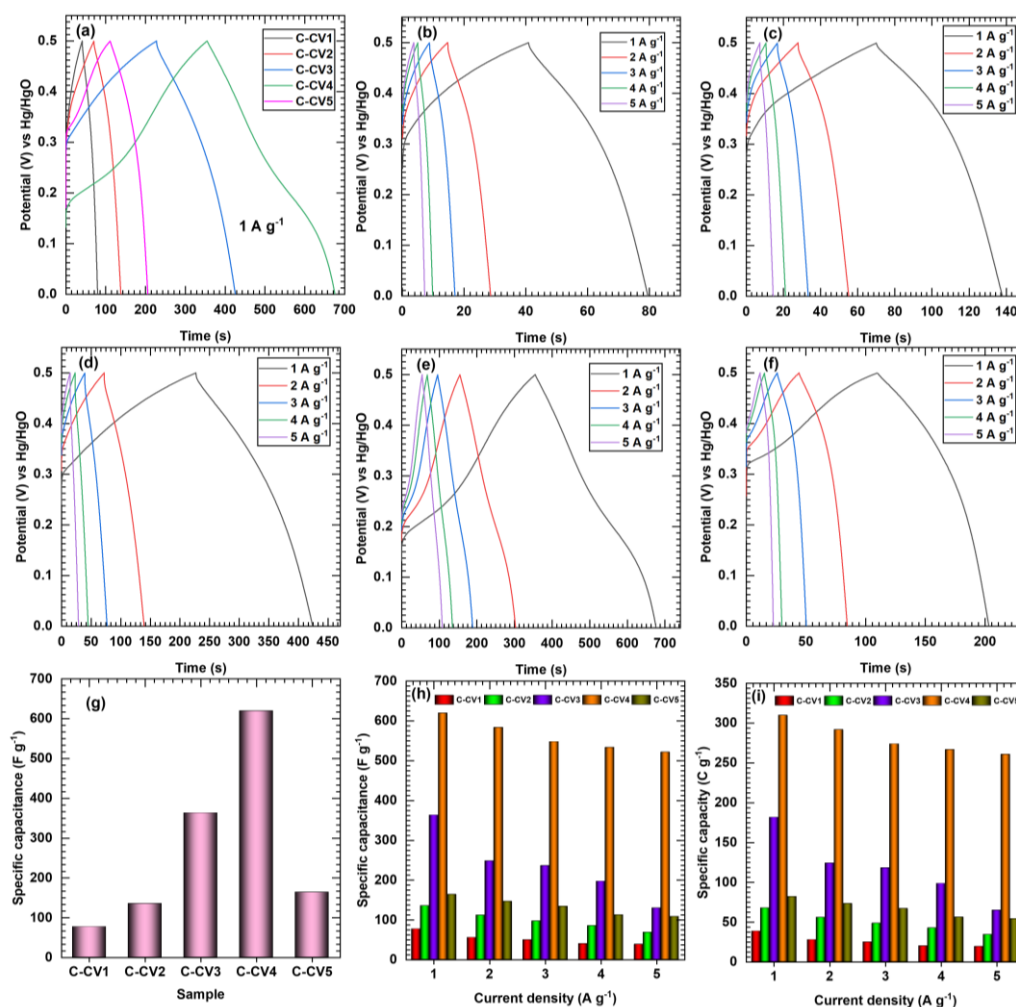


Figure 3.13 (a) Comparative GCD curves of C-CV series electrodes at 1 A g⁻¹ current density, (b-f) GCD curves at different current densities from 1 to 5 A g⁻¹ of C-CV series electrodes, (g) the bar diagram of Cs at 1 A g⁻¹ current density of C-CV series electrodes, (h) bar diagram of Cs vs current density and (i) bar diagram of specific capacity vs current density (1-5 A g⁻¹) of C-CV series.

3.2.A.3.7.4 EIS and Stability Analysis

Insights into the kinetics of electrochemical charge transfer of C-CV series electrodes were studied using EIS analysis. The Kramers-Kronig transformation analysis was accomplished in the frequency range of 10 mHz to 0.1 MHz to ensure the precision of the measurements. The ZView-Impedance software was used to match the equivalent electric circuit for impedance data fits, and an appropriate fitting was established as having a lower deviation of the total fit (Chi-square < 0.001). The C-CV series samples' typical Nyquist plots are shown in Figure 3.14 (a). The resulting impedance plots are fitted with an electrochemical Randle circuit,

which is shown as an inset in Figure 3.14 (a). A series connection is made between the R_{ct} and the R_s , which is indicated by the intercept on the X-axis [34]. The W component, which facilitates diffusion from the lower-frequency region, is coupled in series with the R_{ct} . The R_s values for the C-CV series electrodes range from 0.6 to 1.3 Ω . Also, in comparison to C-CV1 (266.1 Ω), C-CV2 (255.5 Ω), C-CV3 (209.7 Ω), and C-CV5 (214.3 Ω), the C-CV4 electrode has a much lower R_{ct} of 187.7 Ω , demonstrating its good electrochemical conductivity. The circuit-fitted values of C-CV series electrodes are depicted in Table 3.2.

Compared to other electrodes in the C-CV series, the high-performing C-CV4 electrode exhibits a lower R_{ct} value, and it suggests that the C-CV4 electrode's compact 2D nanosheet-like structure allow paths for facile charge transfer and helps contribute to its improved electrochemical performance. The long-term cycling capability of the C-CV4 electrode is evaluated through repeated GCD testing at a constant current density of 5 A g⁻¹, as displayed in Figure 3.14 (b), which depicts remarkable cycling stability, retaining 90.6% of its initial capacitance with 94.9% coulombic efficiency even after undergoing 5000 GCD cycles.

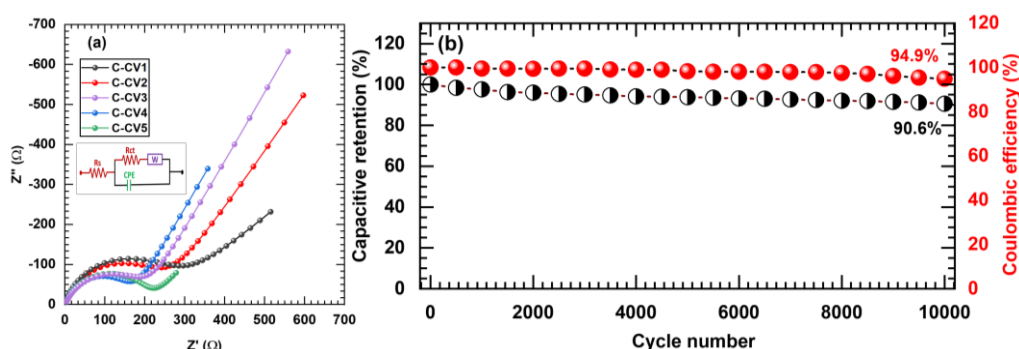


Figure 3.14 (a) Nyquist plots of C-CV series electrodes and (b) cyclic stability of C-CV4 electrode.

Table 3.2 EIS circuit fitted values of C-CV series electrodes.

Parameters/Sample	C-CV1	C-CV2	C-CV3	C-CV4	C-CV5
R_s (Ω)	0.60	0.95	1.35	0.99	0.93
R_{ct} (Ω)	266.1	255.5	209.7	187.7	214.3
$W(\Omega)$	0.0003	0.001	0.0012	0.0007	0.00006
CPE (mF)	0.42	0.33	0.35	0.41	0.62
CPE (n)	0.83	0.82	0.76	0.78	0.77

3.2.A.4 Conclusions

In conclusion, the hydrous $\text{CoV}_2\text{O}_6 \cdot 4\text{H}_2\text{O}$ electrode was successfully prepared on SS by the CBS approach. The XRD, FT-IR, and XPS analysis univocally confirm hydrous, monoclinic crystalline $\text{CoV}_2\text{O}_6 \cdot 4\text{H}_2\text{O}$ structure formation over SS substrate. Also, the variation in the precursors (Co:V) molar concentration ratio influences the rate of reaction kinetics, consequently leading to an alteration in the morphology from scrambled nanoflakes to compact ordered 2D nanosheets, which also leads to the creation of a distinct high SSA with mesoporous nature containing numerous electroactive sites. The hydrous CVO thin film electrode C-CV4 ($\text{CoV}_2\text{O}_6 \cdot 4\text{H}_2\text{O}$) prepared at 1:2 (Co:V) molar concentration performs the best electrochemical capacitive behavior and reaches its maximum C_s of 619.5 F g^{-1} (309.7 C g^{-1}) at a current density of 1 A g^{-1} . The increased high SSA ($87.5 \text{ m}^2 \text{ g}^{-1}$) and low impedance (R_s and R_{ct}) values demonstrated by the C-CV4 electrode and good cyclic stability are credited to enhanced electrochemical performance.

3.2.B Section-B: Chemical Bath Synthesis of Cobalt Vanadium Oxide/Reduced Graphene Oxide Composite Materials and Characterizations

3.2.B.1 Introduction

In the pursuit of efficient ESDs, considerable endeavors have been directed toward preparing appropriate anode and cathode materials with favourable geometries. Specifically, MTMOs have gained widespread utilization as cathode materials in SCs due to their diverse valence states, environmentally friendly characteristics, chemical stability, and cost-effectiveness [37]. Simultaneously, incorporating carbonaceous materials with MTMOs emerges as a potential strategy to enhance the stability of SCs. The incorporation of carbonaceous materials in MTMOs facilitates the utilization of multifunctional properties and synergistic effects inherent in each component of the composite material [38]. Among various carbonaceous materials, rGO stands out as a prominent choice due to its layered structures and 2D architecture [39]. The flexible nature of the rGO carbon matrix makes it an efficient protective layer for the nanostructures of TMOs, preventing pulverization during continuous intercalation/extraction of ions and accommodating volume changes. Additionally, the large SSA and ordered carbon 2D layer structure of rGO enable the accommodation of numerous charges and facilitate rapid charge transportation [40].

The study delves into the examination of the influence of varying concentrations of rGO in CVO material on the physicochemical properties of composite materials and their subsequent impact on supercapacitive performance. Concurrently, pristine CVO and CVO/rGO composite materials were synthesized with different rGO concentrations (0.1, 0.2, 0.3, and 0.4 mg ml⁻¹). The composite of CVO/rGO materials was synthesized in a powdered state and was coated onto SS substrates using a slurry coating method. Further, these prepared electrodes were used for physicochemical and electrochemical characterization techniques for SC application.

3.2.B.2 Experimental Details

3.2.B.2.1 Chemicals

Flakes of graphite, hydrogen peroxide (H₂O₂), potassium permanganate (KMnO₄), sodium nitrate (NaNO₃), hydrazine hydrate (H₆N₂O), polyvinyl alcohol

(PVA), potassium hydroxide (KOH), and N-methyl-2-pyrrolidone (NMP), Cobalt chloride hexahydrate ($\text{CoCl}_2 \cdot 6\text{H}_2\text{O}$), ammonium metavanadate (NH_4VO_3), Urea ($\text{CH}_4\text{N}_2\text{O}$) were taken from Sigma Aldrich and utilized without purification.

3.2.B.2.2 Synthesis of Reduced Graphene Oxide

Initially, GO was prepared using Modified Hummer's method. The procedure of Modified Hummer's method is as follows; 5 g of graphitic flakes and 2.5 g of NaNO_3 were combined with 120 ml of 95% H_2SO_4 . The mixture underwent stirring for 30 min. in an ice-water bath. While maintaining vigorous stirring, 15 g of potassium permanganate was slowly introduced to the suspension to ensure the reaction temperature stayed below 20 °C. Following the addition, the ice-water bath was removed, and the mixture continued stirring at room temperature overnight. Over time, the mixture transformed into a pasty consistency, with the color evolving to a light brownish shade.

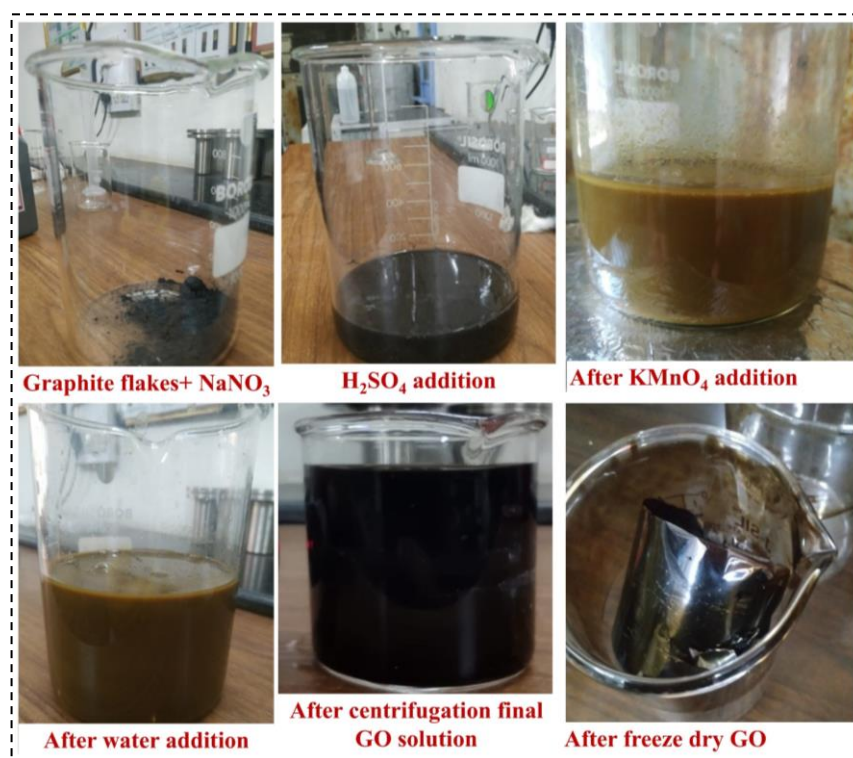


Figure 3.15 (a-f) Synthesis procedure of GO by Modified Hummer's method.

After the overnight stirring, 150 ml of H_2O was gradually added to the paste under vigorous agitation, resulting in a change in color to yellow. The diluted suspension underwent further stirring for 15 min. before the addition of 50 ml of 30% H_2O_2 to the mixture. For purification, the mixture underwent several washes with DDW until reaching a pH of ~ 7 . Following filtration and vacuum drying,

brownish GO was obtained, as depicted in Figure 3.15 (a-f). Furthermore, the prepared GO was crushed and used for the preparation of rGO. The reduction of functional groups of GO was done with the help of hydrazine hydrate [41].

The detailed procedure for producing rGO is as follows: Firstly, GO powder was dispersed as 1 mg GO into 1 ml DDW by ultrasonication. This dispersed solution was poured into the round bottom flask, assembled like the reflux method, and heated at 368 K. Then hydrazine hydrate was added, and the reaction was kept for 3 h at a constant temperature; after the reaction, this solution was centrifuged 2-3 times and washed using DDW. Finally, the obtained product was freeze-dried and further used for the synthesis of composite material.

3.2.B.3 Result and Discussion

3.2.B.3.1 XRD Analysis

The XRD patterns for both GO and rGO are depicted in Figure 3.16. In Figure 3.16, a highly intense peak at $2\theta = 10.4^\circ$, corresponding to the (001) plane, serves as confirmation for the existence of GO. The calculated d-spacing for the GO sample is approximately 0.80 nm, derived from the (001) plane position. This spacing is attributed to the insertion of oxygen-containing functional groups between the layers [42].

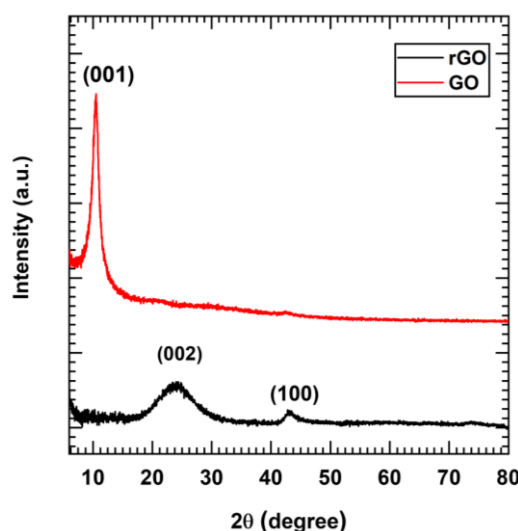


Figure 3.16 XRD patterns of GO and rGO.

Figure 3.16 displays the XRD pattern for rGO. The broad peaks observed at 24.4° and 42.9° are associated with the (002) and (100) planes of rGO. The calculated d-spacing for the (002) plane is approximately 0.36 nm for rGO. This

reduction in d-spacing indicates the stacking of GO nanosheets due to the elimination of oxygen-containing groups, affirming the formation of multilayered rGO nanosheets [43].

3.2.B.3.2 Raman Analysis

An essential experimental technique for examining the bonding characteristics of various carbon compounds is Raman spectroscopy. Raman investigations on rGO were carried out to investigate the properties of sp^2 domains and to gain a deeper knowledge of reduction reactions. Figure 3.17 displays two primary vibrations apparent within the 900 to 1800 cm^{-1} range for rGO. The D vibration band, arising from the breathing mode of j-point photons with A_{1g} symmetry, is identifiable at 1349.6 cm^{-1} in the Raman spectrum of rGO [44]. Conversely, the G vibration band, originating from the first-order scattering of E_{2g} phonons by sp^2 carbon, is observed at 1604.08 cm^{-1} . Additionally, the G vibration band is influenced by the stretching C-C bond, a characteristic feature present in all sp^2 carbon systems [45].

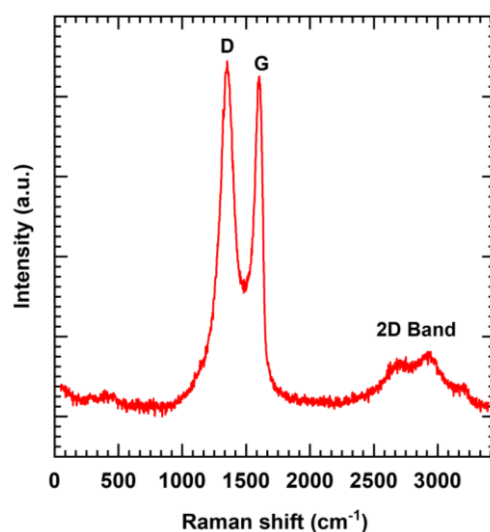


Figure 3.17 Raman spectrum of rGO.

Furthermore, the rGO also exhibits the 2D band, evident at 2703 cm^{-1} as depicted in Figure 3.17. The I_D/I_G ratio for rGO was found to be 1.08 and it is higher than compared to 0.93 for GO. The I_D/I_G ratio for rGO was observed to increase, attributed to the restoration of sp^2 carbon and a reduction in the average sizes of sp^2 domains during the reduction process. The heightened intensity of the D band also indicates the presence of more isolated graphene domains in rGO [46-48]. This

occurrence stems from the reduction process of GO to rGO, resulting in a reduction of residual oxygen-containing functional groups and inducing stacking in the rGO structure. The Raman analysis validates the successful reduction of GO to rGO.

3.2.B.4 Electrochemical Characterizations of Reduced Graphene Oxide

The rGO electrode was fabricated via the slurry coating method onto SS substrates. The slurry formulation comprised 80% rGO material, 15% carbon black, and 5% polyvinylidene fluoride (PVDF) dissolved in NMP. Following the slurry preparation, it was applied onto the SS substrate and dried at 50 °C. The prepared rGO electrodes were then utilized for investigating electrochemical performance. For electrochemical studies, a half-cell system was employed, comprising the rGO electrode as the working electrode, a Pt plate as the counter electrode, and a Hg/HgO electrode serving as the reference electrode.

3.2.B.4.1 CV Analysis

In Figure 3.18, the CV curves of the rGO electrode are depicted, showcasing reversible I-V curves at various scan rates ranging from 5 to 100 mV s^{-1} .

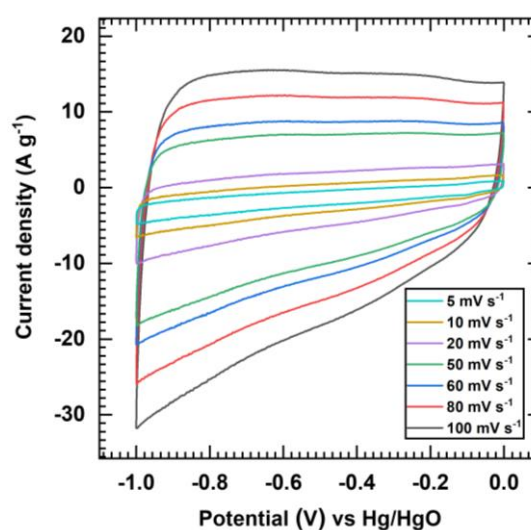


Figure 3.18 CV curves of rGO electrode at different scan rates.

These measurements were performed in 1 M KOH electrolyte and conducted within the optimized potential window, spanning from 0 to -1 V vs Hg/HgO. Notably, the CV curves exhibit a quasi-rectangular shape, which is a characteristic feature indicative of the EDLC-based capacitive behavior of the rGO electrode. This distinct shape suggests efficient charge storage mechanisms

associated with the surface adsorption/desorption of ions, further affirming the suitability of rGO for electrochemical energy storage applications.

3.2.B.4.2 GCD Analysis

The rGO electrode's GCD analysis is shown in Figure 3.19. Significantly, the rGO electrode's GCD curves show nearly linear charge-discharge behaviour, indicating that it is double-layer capacitive. This linear pattern indicates quick and effective mechanisms for storing and releasing charge, which is typical of SCs that rely on EDLC. In particular, with a current density of 2 A g^{-1} , a C_s of 290 F g^{-1} is attained for the rGO electrode. The excellent electrochemical performance of the rGO electrode is underscored by its notable high C_s value. Additionally, its ability to offer a wide range of potential windows is advantageous, particularly when considering fabricating HSDs with rGO anode material, as it facilitates the expansion of the working potential range.

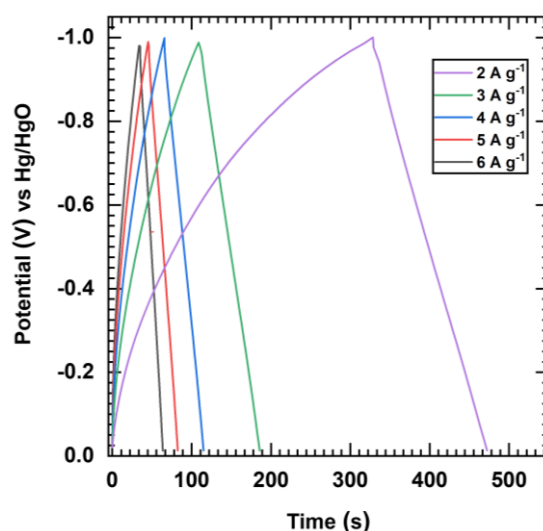


Figure 3.19 GCD curves of rGO electrode at 2-6 A g^{-1} current densities.

3.2.B.4.3 EIS Analysis

The Nyquist plot of the rGO electrode is shown in Figure 3.20. The fitted circuit and magnified view of the semicircle are shown in the inset of Figure 3.20. The circuit-fitted values of rGO electrodes are depicted in Table 3.3. The solution resistance, denoted by R_s in the fitted circuit, displays a value of 0.93Ω . The charge transfer resistance expressed as R_{ct} , is 4.75Ω . W stands for the Warburg impedance, which is 4.55Ω . Additionally, CPE is an acronym for the constant phase element i.e. general imperfect capacitor, which has a correction factor (n) of 0.86

and a capacitance value of 0.24 mF. These parameters shed light on the rGO electrode's impedance properties and electrochemical behaviour.

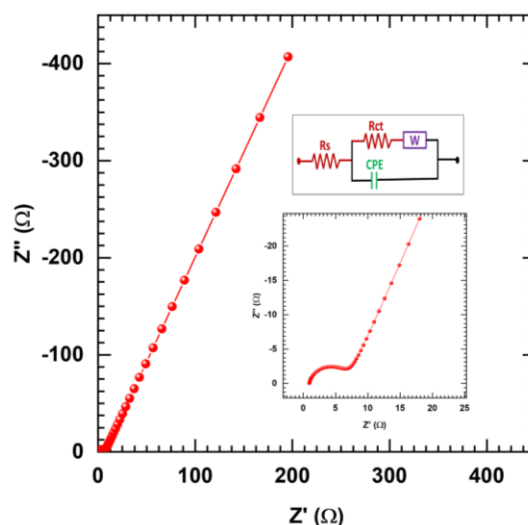


Figure 3.20 Nyquist plot of rGO, inset fitted circuit, and magnified view of a semicircle at a higher frequency.

Table 3.3 EIS circuit fitted values of rGO electrode.

Parameters/Sample	rGO
R_s (Ω)	0.93
R_{ct} (Ω)	4.75
$W(\Omega)$	4.55
CPE (mF)	0.24
CPE (n)	0.86

3.2.B.5 Synthesis of Cobalt Vanadium Oxide/Reduced Graphene Oxide

The pristine CVO and CVO/rGO composite materials were synthesized by the CBS method. The previously discussed Section A focuses on the optimization of pristine CVO material, to fine-tune its parameters for achieving maximum SC performance, which was synthesized using $\text{CoCl}_2 \cdot 6\text{H}_2\text{O}$ (0.034 M), NH_4VO_3 (0.066 M), and urea (0.05 M). These concentrations are used for the synthesis of pristine CVO and CVO/rGO composite materials. Also, in composite synthesis, the concentration of rGO was varied as 0.1, 0.2, 0.3, and 0.4 mg ml⁻¹. These prepared

solution baths were put at 95 °C temperature for 9 h. Upon the completion of the reaction time, the baths were left to cool naturally.

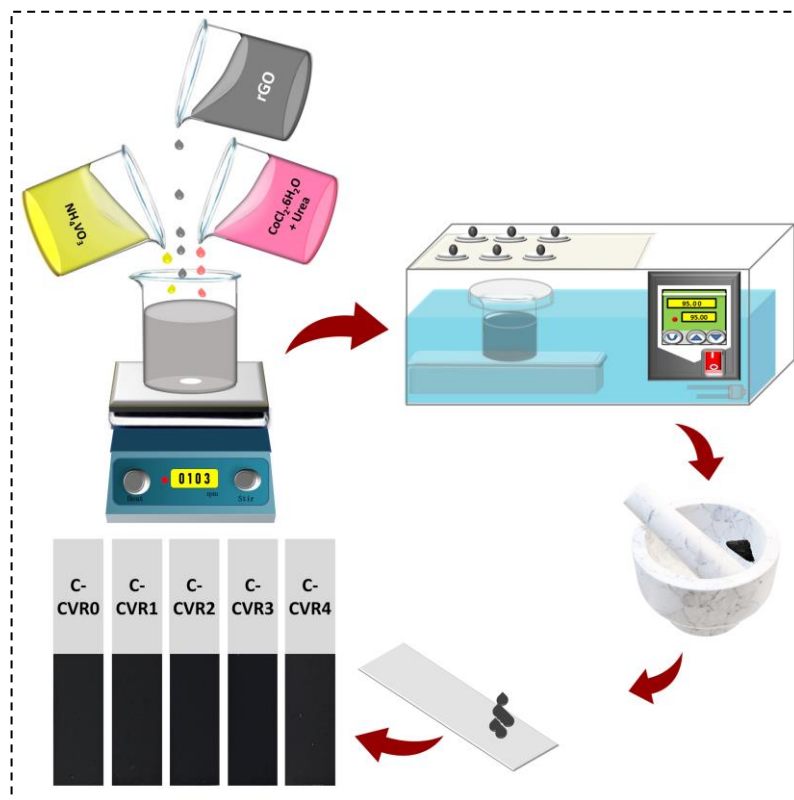


Figure 3.21 Schematic illustration of the preparation of C-CVR series electrodes by CBS method.

Table 3.4 Preparative parameters for the synthesis of C-CVR series electrodes.

Sr. No.	Sample Name	rGO Concentration (mg ml^{-1})
1	C-CVR0	0
2	C-CVR1	0.1
3	C-CVR2	0.2
4	C-CVR3	0.3
5	C-CVR4	0.4

The resulting precipitates were gathered, subjected to multiple washes with DDW using centrifugation, and subsequently dried at room temperature. Moreover, the obtained powders of pristine CVO which are denoted as C-CVR0, and

the composite materials CVO/rGO prepared at concentrations of 0.1, 0.2, 0.3, and 0.4 mg ml⁻¹ are also designated as C-CVR1, C-CVR2, C-CVR3, and C-CVR4, respectively, as mentioned in Table 3.4. The C-CVR series electrodes were prepared using the slurry coating method on SS substrates. The slurry was prepared by blending 80% C-CVR series material, 15% carbon black, and 5% PVDF in NMP. The prepared slurry was coated onto the SS substrate and dried at 50 °C. The prepared electrodes were used for electrochemical performance investigation. The synthesis procedure of electrodes is depicted in Figure 3.21. The loading mass of C-CVR series materials on SS substrate at 1x1 cm² area is maintained and displayed in Figure 3.22, which is ~0.65 mg cm⁻².

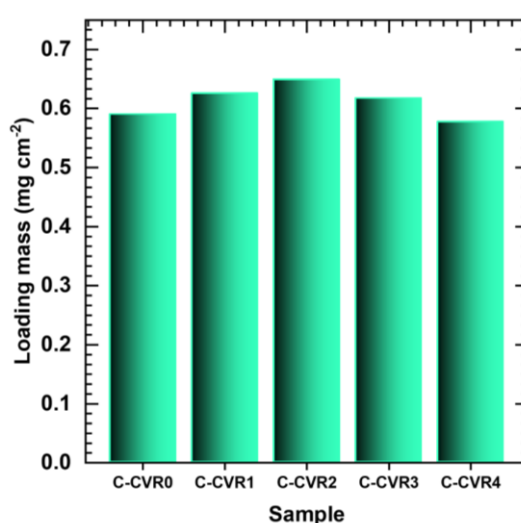


Figure 3.22 The plot of loading mass of C-CVR series on unit area of SS substrate.

3.2.B.6 Results and Discussion

3.2.B.6.1 Reaction mechanism

The CVO/rGO material was synthesized using a CBS method which is an effective 'bottom-up' strategy for nanostructure and microstructure synthesis. The CVO/rGO composite material of the C-CVR series was prepared to scrutinize the effect of rGO concentration variation in pristine C-CVR0. In the formation of C-CVR material CVO formation takes place following the similar reaction described in section 3.2.A.3.1, equation 3.4. Following the decomposition of urea as mentioned in equations 3.2, and 3.3, the solution turns alkaline, which is conducive to the formation of additional carboxyl, hydroxyl, and epoxy groups on the graphene surface. The increased presence of these functional groups facilitates the creation of more nucleation sites. Moreover, the formed ammine complexed metal ions,

according to equation 3.4, get attached over the functional groups and defect sites by electrostatic or Van-der Waal attractive forces. The large SSA of rGO allows to efficiently adsorb a substantial amount of amine-complexed ions. At the same time, vanadate ions reacted with the ammine complexed ions through the electrostatic attractive force (equation 3.4) and formed nuclei for further growth. Ultimately, the overall growth of CVO takes place over the rGO surface by stacking or oriented attachment of particles at nuclei. Based on the aforementioned reaction mechanism, the CVO was successfully grown over rGO nanosheets, and consistently brown-colored C-CVR powders were obtained.

3.2.B.6.2 XRD Analysis

The XRD patterns for powder rGO and C-CVR series samples, featuring varying concentrations of rGO, are illustrated in Figure 3.23.

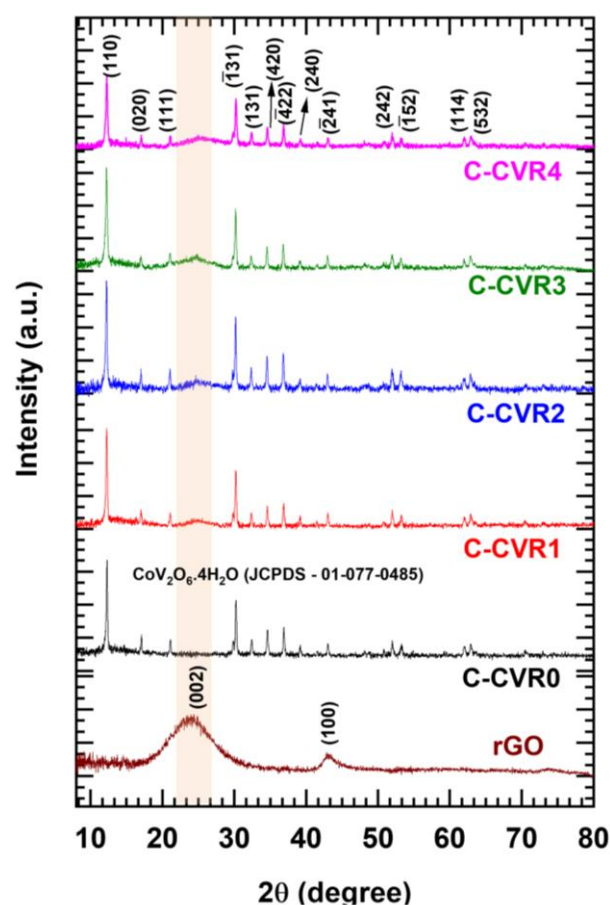


Figure 3.23 XRD patterns of rGO, pristine C-CVR0, and C-CVR1 to C-CVR4 composite material samples.

The C-CVR series samples exhibited crystalline peaks, similar peaks are identified in the pristine powder sample of C-CVR0 and composite powder samples

(C-CVR1, C-CVR2, C-CVR3). In these XRD patterns, distinctive peaks were observed for the C-CVR series samples at 12.2° , 17.1° , 21.1° , 30.2° , 32.4° , 34.6° , 36.9° , 39.1° , 40.0° , 52.0° , 53.3° , 62.0° , and 62.9° . These peaks are assigned to the crystal planes of (110), (020), (111), ($\bar{1}31$), (131), (420), ($\bar{4}22$), (240), ($\bar{2}41$), (242), ($\bar{1}52$), (114), and (532), respectively matched with the phase of $\text{CoV}_2\text{O}_6 \cdot 4\text{H}_2\text{O}$ (JCPDS card no. 01-077-0485). Also, an extra hump is observed at approximately $2\theta = 24.01^\circ$ in the composite materials (C-CVR1, C-CVR2, C-CVR3, and C-CVR4), which indicates the stacking of rGO sheets resulting from the elimination of oxygen-containing groups and interaction with CVO [43]. The intensity of the hump increases with the rising concentration of rGO which confirms the increasing amount of rGO in the C-CVR series. This observation confirms the successful preparation of pristine $\text{CoV}_2\text{O}_6 \cdot 4\text{H}_2\text{O}$ and the $\text{CoV}_2\text{O}_6 \cdot 4\text{H}_2\text{O}$ /rGO composite material with increasing rGO content.

3.2.B.6.3 FT-IR Analysis

FT-IR spectroscopy is an effective method for examining the formation of molecular bonds in the synthesized C-CVR series materials. The FT-IR spectrum of each sample in the CVO/rGO series and the pristine C-CVR0 are presented, covering the wavenumber range from 400 to 4000 cm^{-1} , as depicted in Figure 3.24. In the C-CVR series sample, an interaction between metal and oxygen, particularly Co and O, manifests as a peak at 490 cm^{-1} , denoted by the symbol ' ϵ_1 ' [24]. The well-defined and characteristic peaks at 782 cm^{-1} (ϵ_2) are attributed to the vanadyl group stretching vibration in the pristine C-CVR series samples [25]. The presence of carbonate (CO_3) entrapped in the layers of $\text{CoV}_2\text{O}_6 \cdot 4\text{H}_2\text{O}$ structure released from urea decomposition is indicated by the peak at ' ϵ_3 ' (1366 cm^{-1}) in the C-CVR series, moreover, additional shoulder peak at 1460 cm^{-1} is observed in composite C-CVR1 to C-CVR4 owing to carboxyl group from rGO [25, 49].

A prominent C-OH peak (φ_1) at 1027 cm^{-1} is observed in C-CVR1 to C-CVR4 samples, which correspond to the COOH (hydroxyl) stretching vibrations from rGO. Also, an absorption peak (φ_2) observed around 1612 cm^{-1} is attributed to the C=C bond of sp^2 hybridization of graphitic carbon [51]. The FT-IR analysis reveals the presence of CVO and rGO with adsorbed or trapped structural hydrous content in

the C-CVR series samples, which underscores the success of the CBS method in preparing $\text{CoV}_2\text{O}_6 \cdot 4\text{H}_2\text{O}/\text{rGO}$ composite material.

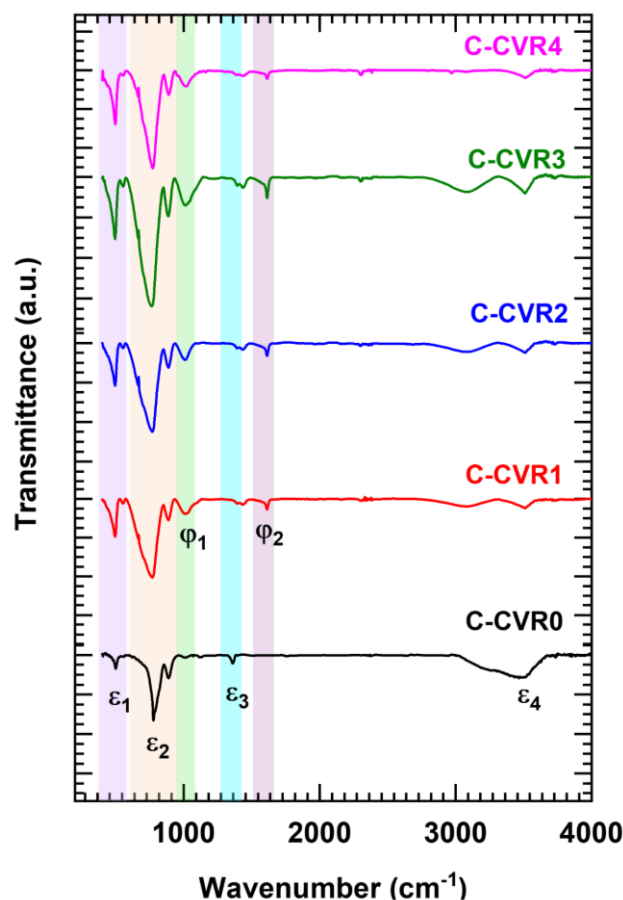


Figure 3.24 FT-IR spectra of pristine C-CVR0 and C-CVR1 to C-CVR4 samples.

3.2.B.6.4 Raman Analysis

The chemical bonding nature of the C-CVR series samples is conducted using the Raman spectroscopy technique. Raman spectra for rGO and C-CVR series materials are shown in Figure 3.25. In the C-CVR series samples, absorption bands manifest at 333, 467, and 840 cm^{-1} associated with asymmetric stretching of V-O-Co, Co-O, and symmetric vibration of V-O, respectively. With the increasing concentration of rGO, the intensity of C-CV peaks decreased. The emergence of a peak linked to the D band is a consequence of the breathing mode (aromatic rings) of k-point phonons with A_{1g} symmetry, discernible at 1340 cm^{-1} in rGO. The D band is associated with vibrations of carbons having sp^3 hybridization, indicating structural imperfections and defects induced during oxidation. The G band is detected around 1598 cm^{-1} in the rGO and C-CVR series, originating from the first-order scattering of E_{2g} phonons by sp^2 hybridized carbon, or the G band is related

to in-plane vibrations resulting from the stretching of C-C bonds in sp^2 hybridized carbon atoms found in graphitic materials [51]. Additionally, the I_D/I_G ratio, comparing the D-band (I_D) to the G-band (I_G), serves to evaluate the size of sp^2/sp^3 domains, yielding a calculated ratios of 1.01, 1.04, 1.06, 1.07, and 1.08 for rGO, C-CVR1, C-CVR2, C-CVR3, and C-CVR4, respectively [52, 53]. Such an increasing I_D/I_G ratio indicates the growth of CVO over the rGO nanosheets. In the higher frequency range of the Raman spectra, two additional bands of the 2D band are discernible. With an escalating concentration of rGO in C-CVR, the increase in the intensity of the CVO peak decreased. The increase in I_D/I_G ratio and the presence of the CVO band in all C-CVR samples corroborated the intimate growth of CVO on rGO and the formation of the CVO/rGO composite.

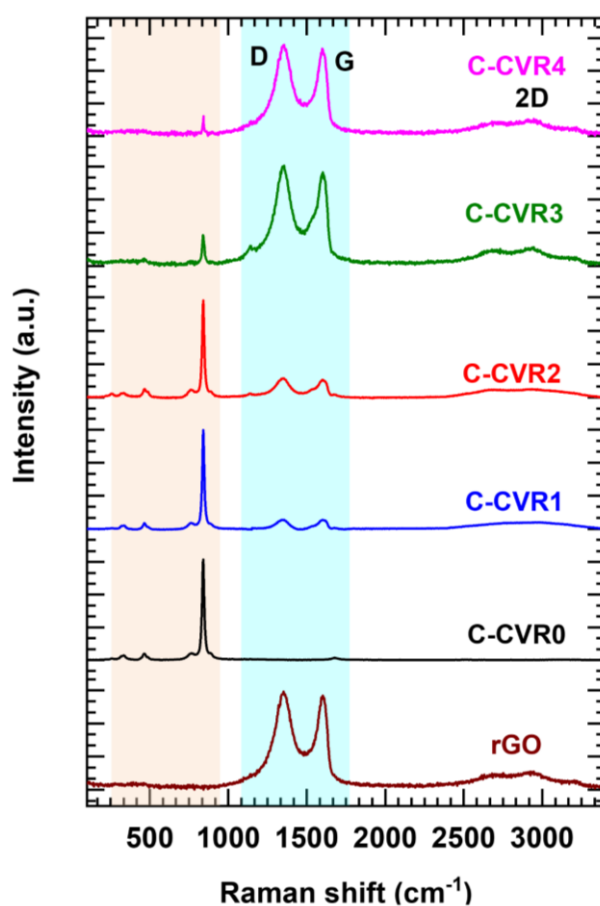


Figure 3.25 Raman spectra of rGO and C-CVR0 to C-CVR4 samples.

3.2.B.6.5 XPS Analysis

The surface composition and chemical states were analyzed using the XPS technique. The XPS survey spectrum of the pristine C-CVR0 and C-CVR3 samples, illustrated in Figure 3.26 (a), confirms the presence of Co, V, O, and C elements in

the sample. The short-range scan of the Co 2p XPS spectra of the C-CVR0 and C-CVR3 samples is shown in Figure 3.26 (b). The resulting spectra show two distinct peaks attributed to Co 2p_{1/2} and Co 2p_{3/2} at binding energies of 796.8 and 780.7 eV, respectively for pristine C-CVR0 and C-CVR3. These peaks were further deconvoluted into two distinct peaks for Co³⁺ and Co²⁺. The Co³⁺ peaks are attributed to 780.4 and 796.5 eV. The Co²⁺ peaks appeared at 782.2 and 798.3 eV for C-CVR0 and C-CVR3 samples. The Co²⁺ peaks were more prominent than the Co³⁺ peaks. Additionally, the binding energies corresponding to the satellite peaks were 786.4 and 802.7 eV [27]. Similar to this, the short-scan XPS spectrum of vanadium (V 2p) reveals two distinct peaks corresponding to V 2p_{3/2} and V 2p_{1/2} obtained at 517.2 eV and 524.1 eV, respectively for C-CVR0 and C-CVR3 samples. These values indicate the presence of prominent V⁵⁺ states (517.2 and 524.1 eV) and V⁴⁺ states (516.7 eV), as shown in Figure 3.26 (c) [54].

Also, Figure 3.26 (d) displays the oxygen (O 1s) XPS spectrum of C-CVR0 and C-CVR3 samples, and the spectrum displays three noticeable oxygen contributions, with the peak O₁ at 529.9 eV commonly associated with a metal-oxygen bond. Additionally, the peaks O₂ and O₃ observed at binding energies of 531.4 and 532.9 eV are attributed to the presence of oxygen within the OH groups, indicating structural water in the prepared electrode [28]. Additionally, the deconvoluted C 1s spectra of rGO and C-CVR3 samples, shown in Figure 3.26 (e), reveal four and three distinct peaks in the rGO and C-CVR3 samples, respectively. Figure 3.26 (e) highlights more prominent peaks in the rGO sample than the C-CVR3 sample, at 284.6 eV peak indicating the presence of C=C in-plane bonding associated with sp² hybridization. Furthermore, the XPS analysis indicates the presence of functional groups such as carboxylate carbon (O-C=O) and carboxyl (-COOH) at 288.3 and 289 eV, respectively in the rGO sample. Conversely, the bonding out of the plane involving sp³ hybridized C-C appears at 286.08 eV noticeably reduced, which suggests a further successful reduction of rGO. Among these functional groups, the carboxyl groups are reduced due to the bonding of CVO [55]. The XPS results indicate the presence of prominent Co²⁺ and V⁵⁺ oxidation states, along with the reduction in carbon functional groups, confirming the successful preparation of the CVO/rGO composite material.

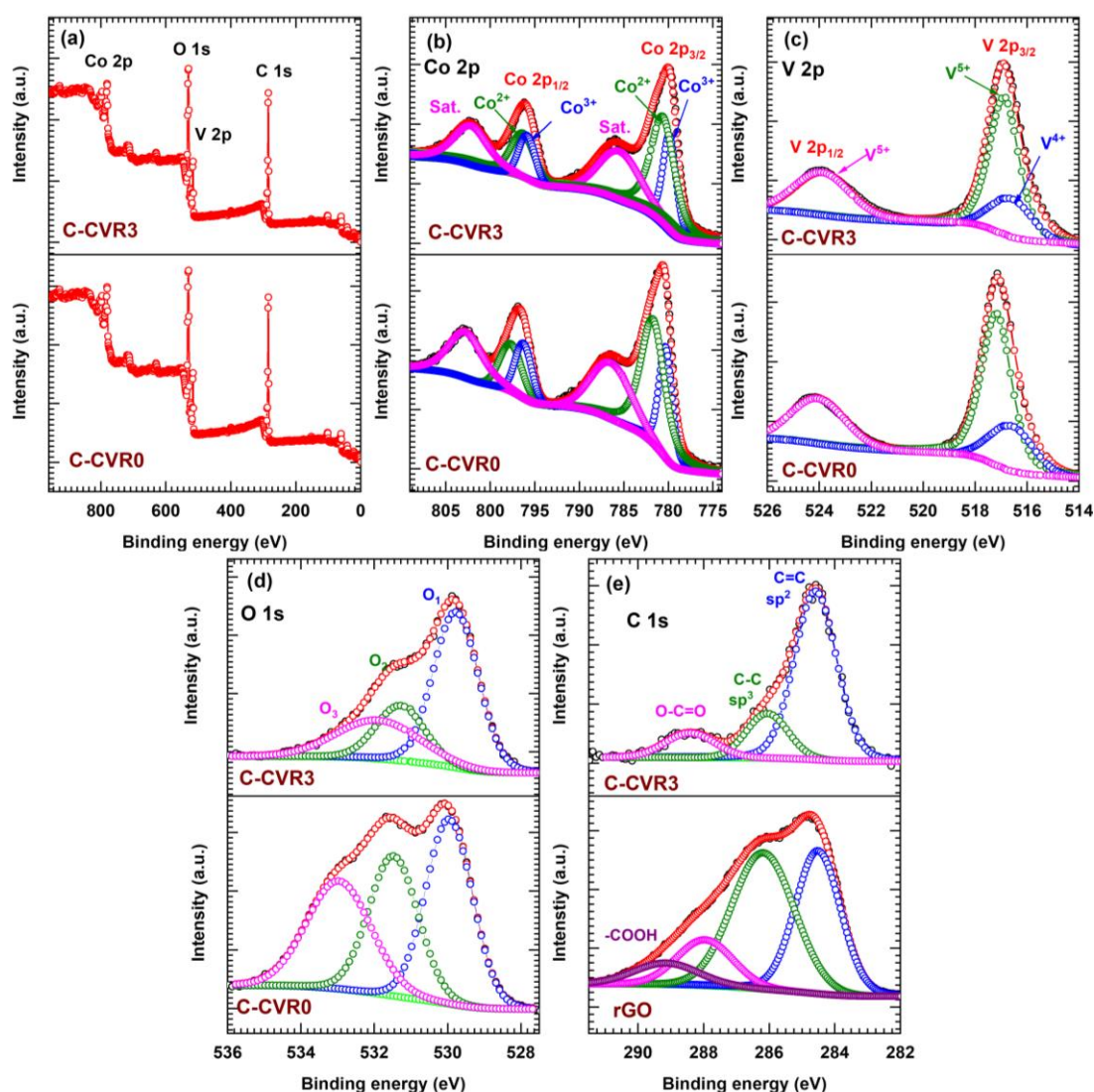


Figure 3.26 XPS spectra of pristine C-CVR0 and C-CVR3 samples and the corresponding (a) survey, (b) Co 2p, (c) V 2p, (d) O 1s, and (e) C 1s of the samples C-CVR3 and rGO.

3.2.B.6.6 TG Analysis

The rGO content in the composites was determined by analyzing the residual masses obtained from the TGA of the C-CVR series composite materials. Figure 3.27 presents the weight loss curves and derivative weight changes for the synthesized composite prepared through a CBS method. The weight loss observed below 200 °C is attributed to the evaporation of surface-adsorbed water and interlayer water [56]. A gradual weight loss is observed between 200 to 400 °C, attributed to the elimination of labile oxygen-containing functional groups and water vapor from the C-CVR series samples, resulting from the breakdown of these

oxygenated functional groups [57]. The TGA curve is consistent after 400 °C temperature for the pristine C-CVR0 sample. Moreover, significant weight loss is observed after in the temperature range from 400 to 700 °C in the C-CVR1 to C-CVR4 which is attributed to the decomposition of rGO via converging in CO₂. The TGA results show that as the concentration of rGO in the C-CVR series increases, the weight loss due to rGO decomposition. Furthermore, the content of CVO in the C-CVR is tentatively quantified from the weight loss due to rGO decomposition and the remaining residual of CVO. The CVO content are calculated to be 98.73%, 97.54%, 95.53, and 88.48% for C-CVR1, C-CVR2, C-CVR3, and C-CVR4, respectively. These results confirm the increasing rGO concentration during synthesis leads to the successful incorporation of rGO with varying content in CVO.

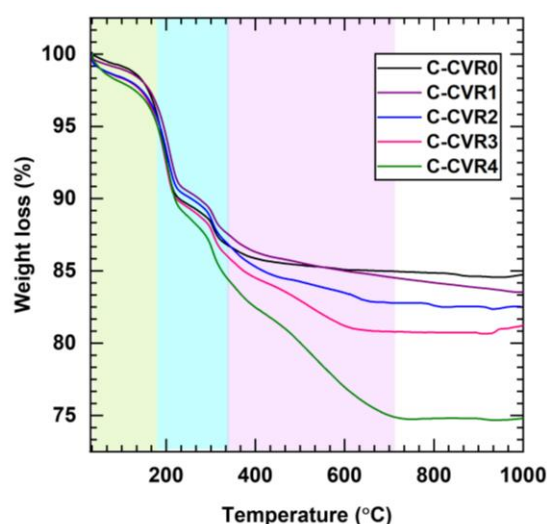


Figure 3.27 TGA plot of C-CVR series samples.

3.2.B.6.7 FE-SEM and EDS Analysis

The study delved into the surface morphological changes of C-CVR series electrodes with varying concentrations of rGO, examined through FE-SEM imaging at different magnifications (X1,000, X10,000, and X40,000), as depicted in Figure 3.28. Notably, the morphology of C-CVR series samples exhibited notable shifts with changes in rGO concentrations. The FE-SEM image (Figure 3.28 (a1)) of the pristine C-CVR0 sample at a lower magnification (X1,000) showcased a distinctive 2D plate-like structure. Intriguingly, upon closer inspection at higher magnification (X10,000) in Figure 3.28 (a2), it was evident that the cracked plates displayed a microplate-like arrangement. Furthermore, at a higher magnification of X40,000,

shown in Figure 3.28 (a3), the plates appeared to appear thinner, with the calculated average edge thickness around ~ 91 nm, as illustrated in the histogram (Figure 3.28 (a4)).

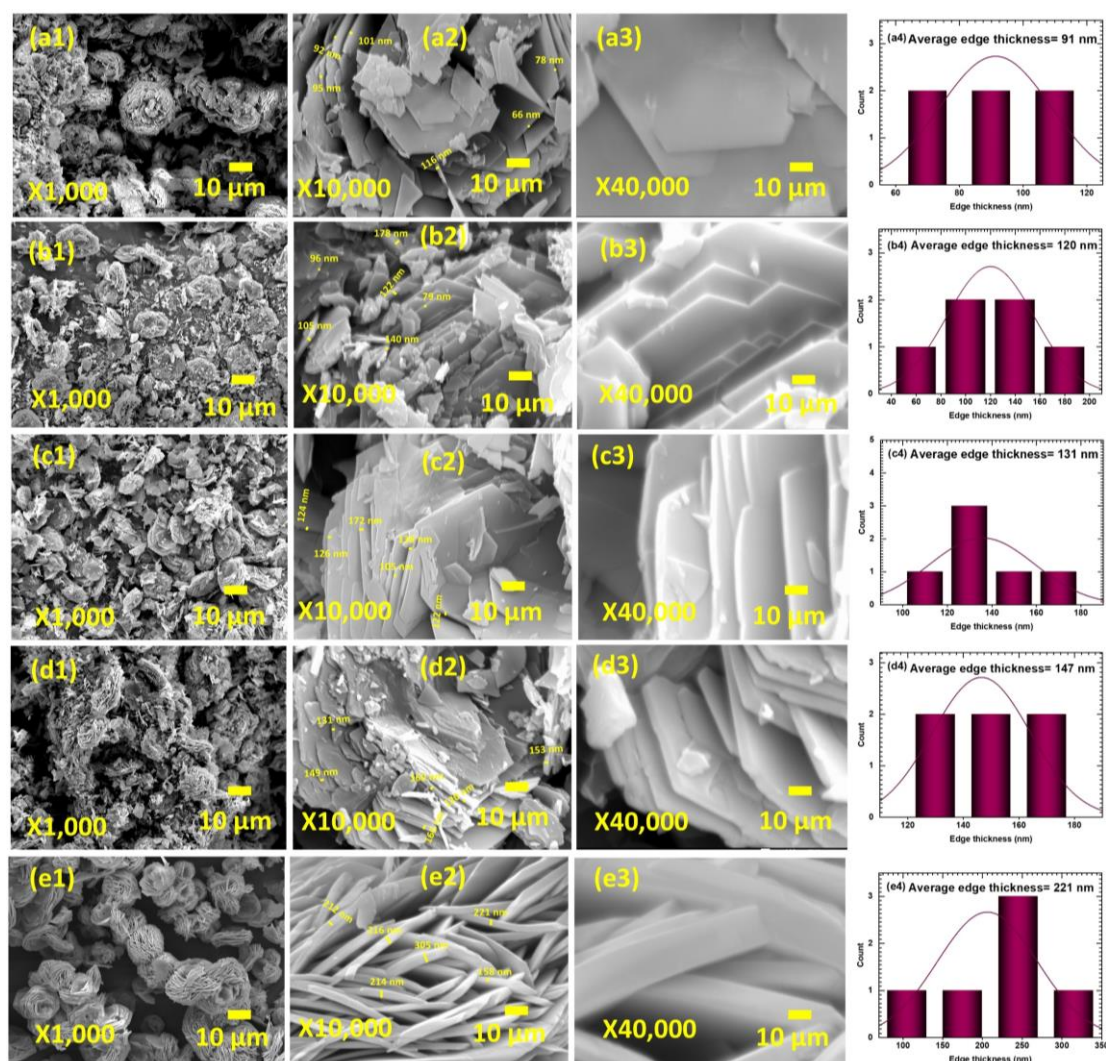


Figure 3.28 FE-SEM images and histograms of (a1-a4) C-CVR0, (b1-b4) C-CVR1, (c1-c4) C-CVR2, (d1-d4) C-CVR3, and (e1-e4) C-CVR4 samples.

Moreover, as rGO was incorporated into the C-CV material, the composite morphology evolved (Figure 3.27 (b1-e3)). With increasing concentrations of rGO, there was a discernible increase in the edge thickness of the microplate. Specifically, the average edge thickness of C-CVR1, C-CVR2, C-CVR3, and C-CVR4 samples measured 120, 131, 147, and 221 nm, respectively, as depicted in the histograms (Figure 3.27 (b4-e4)). Additionally, as the concentration of rGO increased, the microplate-like structures appeared to merge closely together. Notably, in the C-CVR4 sample, the microplate-like structures seemed

interconnected, as depicted in Figure 3.28 (e1). The study highlights the significant influence of rGO concentration on the surface morphology of C-CVR series samples, as observed through FE-SEM analysis. The evolution from distinctive microplate-like structures to interconnected microplate-like arrangements underscores the intricate relationship between material composition and morphological characteristics, offering valuable insights for optimizing electrode design in SCs.

The EDS elemental mapping illustrated in Figure 3.29 (a1-e5), concerning the CBS method of C-CVR series samples, demonstrates the presence of cobalt, vanadium, oxygen, and carbon elements. The sample C-CVR0 contains Co, V, and O. The figure portrays compositional images indicating the investigated areas (shown in mixed colors) and highlights the distribution of Co, V, O, and C elements represented in blue, brown, green, and violet colors, respectively.

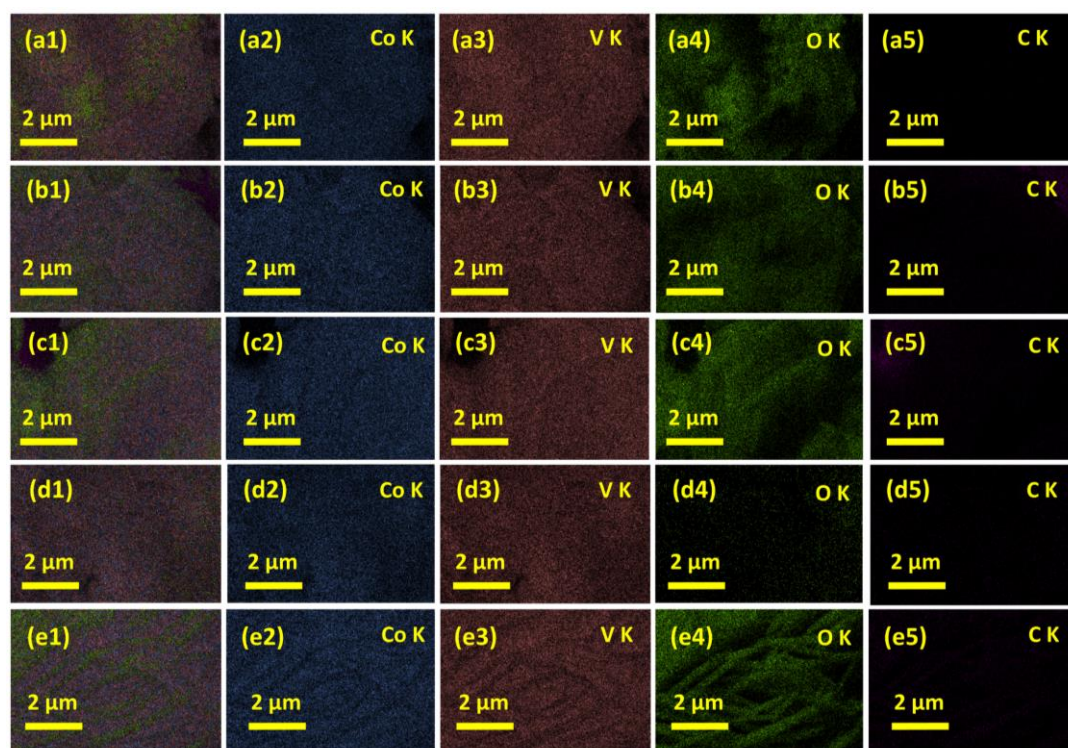


Figure 3.29 EDS mapping of (a1-a5) C-CVR0, (b1-b5) C-CVR1, (c1-c5) C-CVR2, (d1-d5) C-CVR3, and (e1-e5) C-CVR4.

Notably, the consistent presence of Co, V, O, and C elements across all samples in the C-CVR series confirms the successful preparation of CVO/rGO composite material. The EDS spectra with Co, V, O, and C peaks of C-CVR series samples are displayed in Figure 3.30. The atomic percentages are mentioned in the

inset of each spectrum, which confirms the formation of $\text{CoV}_2\text{O}_6 \cdot 4\text{H}_2\text{O}$ material with an increasing atomic percentage of C. The EDS results indicate that C increases with an increase in rGO concentration during synthesis. The EDS result confirms rGO concentration variation in C-CVR series samples with a change in atomic percentage of C, which may be a reason for the change in morphology from dispersive microplates to interconnected microplates with an increasing edge thickness of plates.

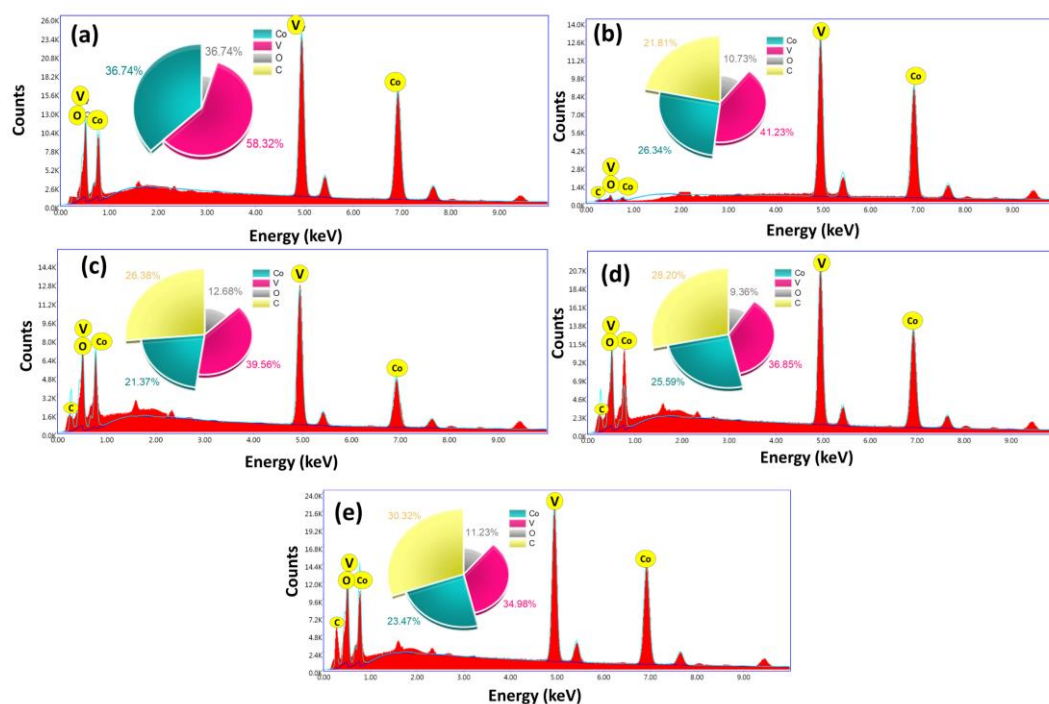


Figure 3.30 EDS spectra of C-CVR series samples.

3.2.B.6.8 HR-TEM and EDS Analysis

The composite structure of CVO/rGO was further confirmed by HR-TEM analysis, as displayed in Figure 3.31 (a), where a typical HR-TEM image of C-CVR3 microplates is presented. The HR-TEM image shows that the microplates are thoroughly coated on the surface of the rGO sheets. The rGO nanosheets are interconnected and form a porous structure, which provides a large amount of ion diffusion channels and enlarges the effective contact area between the electrode and electrolyte [58, 59].

Figure 3.31 (b-d) displays higher magnification HR-TEM images of C-CVR3. The interplanar distance was calculated through line profile analysis, and the lattice fringes depicted in Figure 3.31 (e) were then analyzed and fitted using

DigitalMicrograph software. The lattice spacing of 0.30 nm corroborates the existence of crystalline planes corresponding to ($\bar{1}31$) in $\text{CoV}_2\text{O}_6 \cdot 4\text{H}_2\text{O}$. Figure 3.31 (f-j) illustrates the HR-TEM coupled with EDS mapping of the C-CVR3 material. The validation of the development of the CVO/rGO composite structure is evidenced by the uniform distribution of cobalt, vanadium, oxygen, and carbon. The uniform distribution of CVO and rGO validates the CVO/rGO composite in the C-CVR series material.

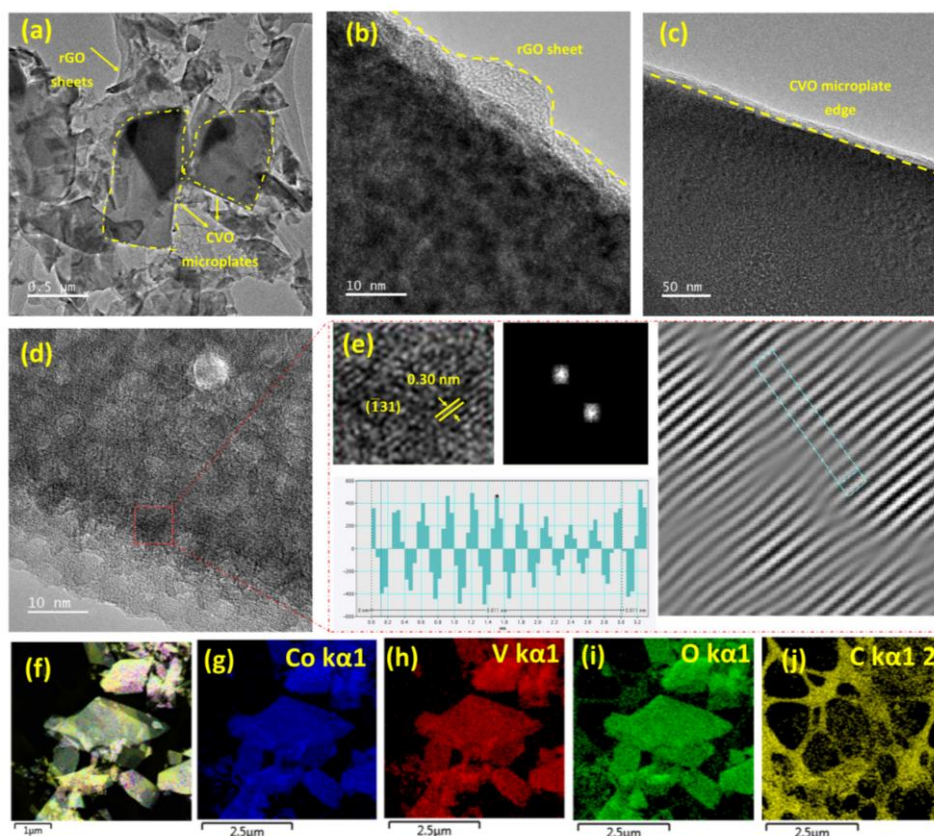


Figure 3.31 (a-d) HR-TEM images of C-CVR3 sample, (e) HR-TEM lattice fringes with line profile showing ($\bar{1}31$) hkl plane of CVO/rGO composite material, and (f-j) Co, V, O, and C elemental mapping of C-CVR3.

3.2.B.6.9 BET and BJH Analysis

The BET technique was employed to assess the SSAs of the C-CVR series samples, aiming for a more comprehensive examination of the porous structure. The BET analysis revealed a type-III isotherms profile with an H3-type hysteresis loop, as depicted in Figure 3.32 (a-e), showcasing the measured adsorption-desorption isotherms for all samples. The SSA values for the C-CVR0, C-CVR1, C-CVR2, C-CVR3, and C-CVR4 samples are 9.2, 10.3, 10.7, 27.8 and 20.4 $\text{m}^2 \text{g}^{-1}$,

respectively. Notably, a substantial change in SSA is observed with an increase in the content of rGO in the material [60]. The SSA ascends to sample C-CVR3 but decreases for sample C-CVR4 due to the aggregation of rGO sheets at higher concentrations.

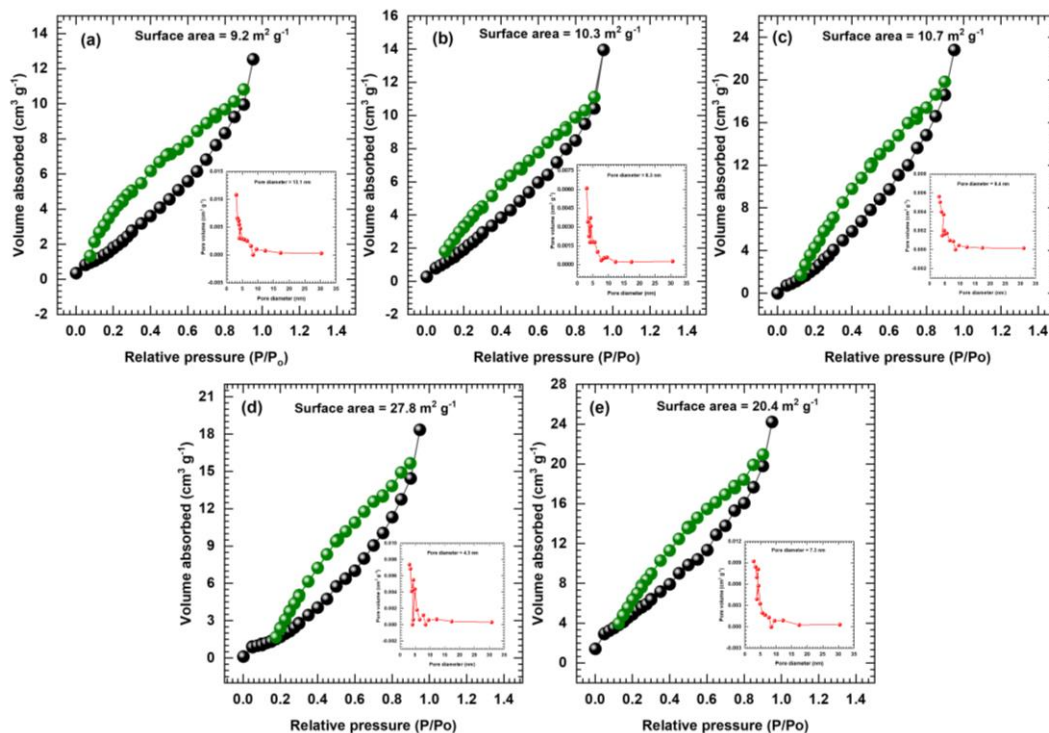


Figure 3.32 Adsorption-desorption isotherms of SSA and inset pore size distribution of samples (a) C-CVR0, (b) C-CVR1, (c) C-CVR2, (d) C-CVR3, and (e) C-CVR4.

Furthermore, the BJH technique was employed to generate pore-size distribution curves for the C-CVR series samples, revealing a trend of narrowing that signifies particle homogenization, as illustrated inset of Figure 3.32 (a-e). The average pore diameters obtained for the C-CVR0, C-CVR1, C-CVR2, C-CVR3, and C-CVR4 samples are 13.1, 8.3, 7.4, 4.3, and 7.3 nm, respectively, confirming the mesoporous nature of the C-CVR series samples. These results imply that variations in rGO concentration influenced distinct growth kinetics, impacting both the resulting SSA and porous structure. The observations suggest that an increased SSA provides a more electrochemically active surface, creating an efficient pathway for ion transportation within the material. Consequently, the electrochemical capacitive performance of such a material is enhanced, as capacitance is directly proportional to the SSA of electrode materials [61].

3.2.B.6.10 Electrochemical Analysis

3.2.B.6.10.1 Electrochemical Setup

In the C-CVR series electrodes, variations in rGO concentration alter the physicochemical properties. The impact of these variations on supercapacitive performance was assessed through electrochemical characterization using a three-electrode system. The system comprises C-CVR series electrodes as the working electrodes, a Pt serving as the counter electrode, and Hg/HgO employed as the reference electrode in 1 M KOH electrolyte.

3.2.B.6.10.2 CV Analysis

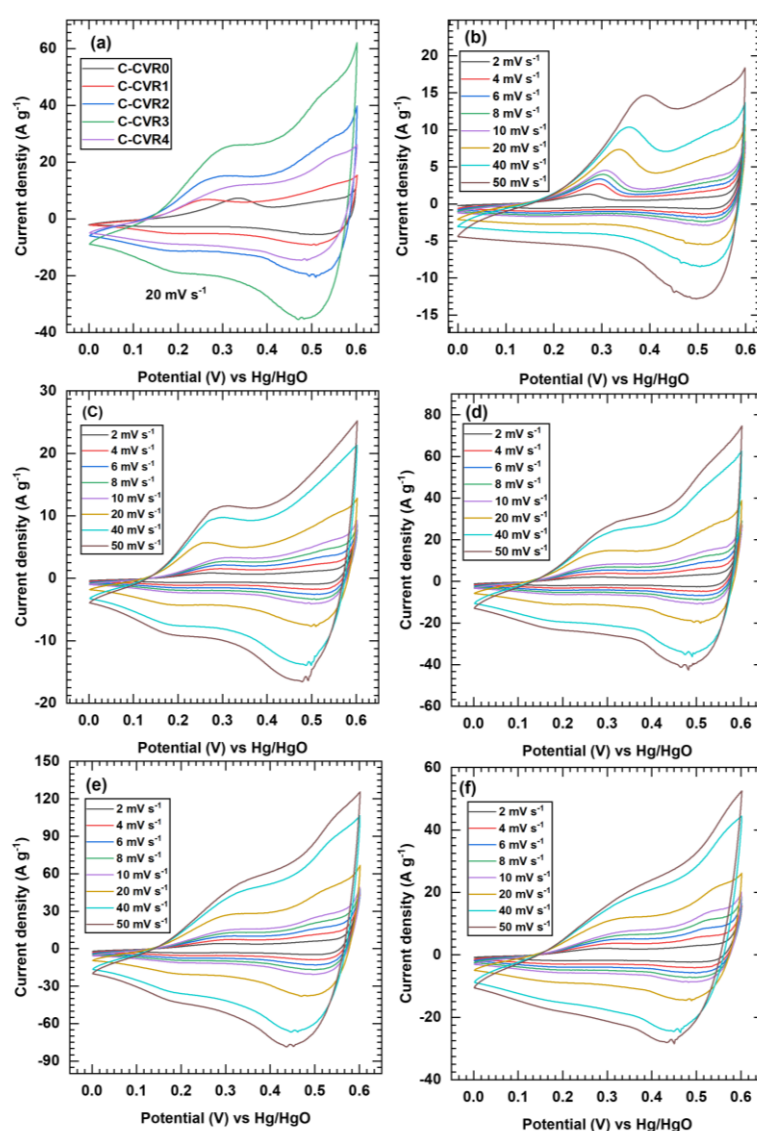


Figure 3.33 (a) At 20 mV s⁻¹ scan rate comparative CV curves of pristine C-CVR0 and C-CVR1 to C-CVR4 composite electrodes, (b-f) CV curves of pristine C-CVR0 and C-CVR1 to C-CVR4 composite electrodes at different scan rates (2-50 mV s⁻¹).

The corresponding CV curves for the C-CVR0, C-CVR1, C-CVR2, C-CVR3, and C-CVR4 electrodes, as illustrated in Figure 3.33 (a), conducted at a constant scan rate of 20 mV s^{-1} within the potential range of 0 to 0.6 V/Hg/HgO.

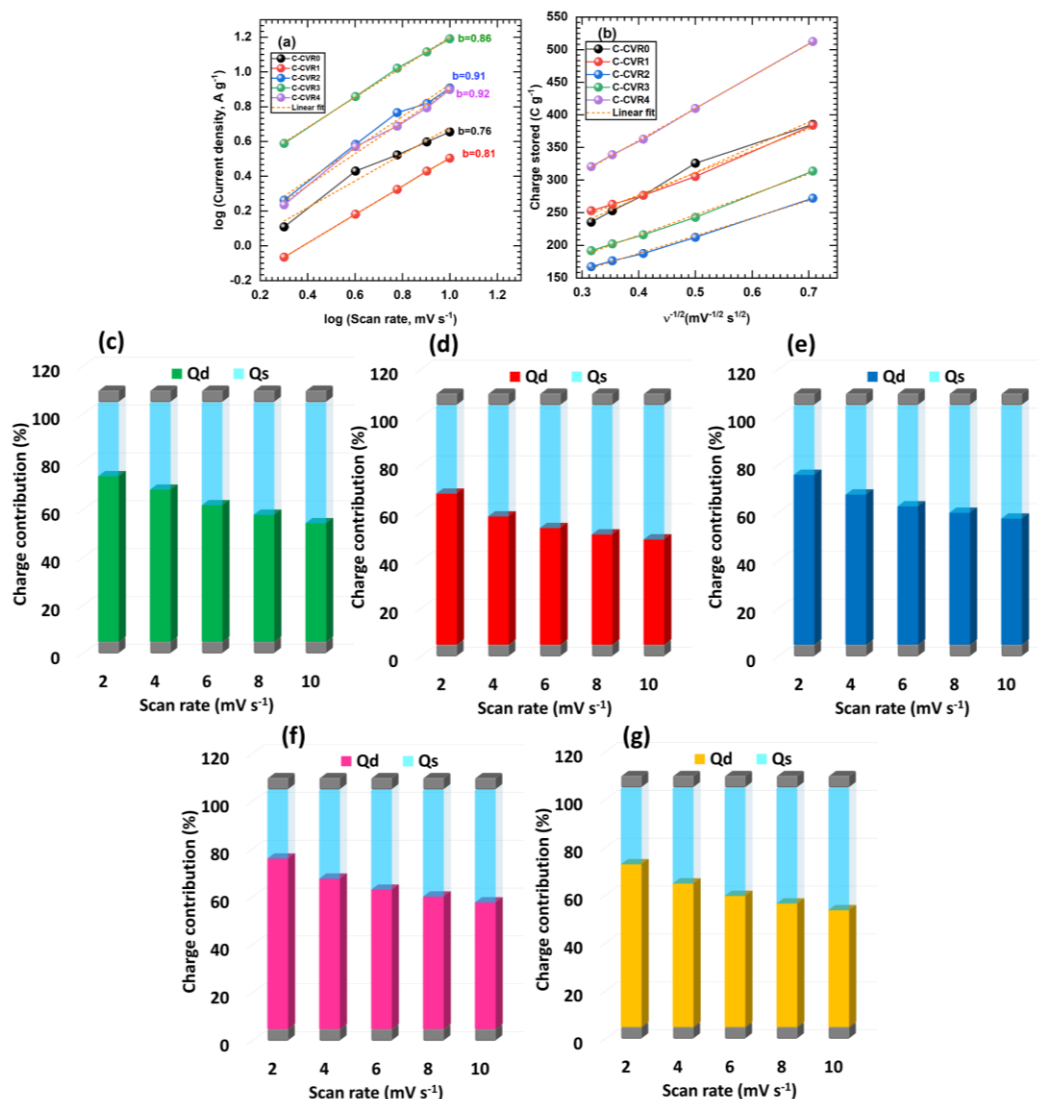


Figure 3.34 (a) Plot of $\log(\text{scan rate, mV s}^{-1})$ vs $\log(\text{current density, A}^{-1})$ for C-CVR series electrodes, (b) the plot of the total charge against the reciprocal of the square root of potential scan rate for C-CVR series electrodes, and (c-g) plots of surface and diffusive charge contribution of C-CVR series at different scan rate.

Moreover, the cumulative area under the CV curve for the C-CVR3 electrode exceeds that of the C-CVR0, C-CVR1, C-CVR2, and C-CVR4 electrodes. This disparity suggests that the C-CVR3 electrode exhibits the highest charge storage capacity. This maximum capacity is attributable to the mesoporous structure and increased SSA of the C-CVR3 electrode, enabling efficient penetration of electrolyte ions into the interior of the electrode and offering an optimum surface for charge storage

[62]. The CV curves for all electrodes at varying scan rates from 2 to 50 mV s^{-1} are presented in Figure 3.33 (b-f). Additionally, it is crucial to delve into the electrochemical kinetics of the C-CVR series electrodes to reveal their charge storage mechanism explicitly. The 'b' values for C-CVR0, C-CVR1, C-CVR2, C-CVR3, and C-CVR4 are 0.76, 0.81, 0.91, 0.86, and 0.92, respectively, as illustrated in Figure 3.34 (a).

These electrodes exhibit 'b' values within the range of 0.5 to 1, indicating that the overall charge storage capacity of the electrode is influenced by both surface-controlled and diffusive-controlled processes, characteristic capacitive, diffusive, and battery-type behavior [32]. In Figure 3.34 (b), the correlation between Q_{total} and $v^{-1/2}$ is displayed. This relationship allows the determination of the capacitive contribution (Q_s) through the intercept of the plot. The findings suggest that the Q_d value of the C-CVR3 electrode surpasses that of other electrodes, namely C-CVR0, C-CVR1, C-CVR2, and C-CVR4. Furthermore, the charge contributions in the corresponding electrodes of the C-CVR series at various scan rates are depicted in Figure 3.34 (c-g).

3.2.B.6.10.3 GCD Analysis

Moreover, the profiles of GCD were examined and interpreted to assess the charge storage capacity of the C-CVR series electrodes. Figure 3.35 (a) illustrates the comparative GCD plots for the C-CVR series electrode at constant current density 1 A g^{-1} in 0 to 0.5 V/Hg/HgO potential window and different current densities GCD profiles of C-CVR series electrodes as shown in Figure 3.35 (b-f).

The C-CVR3 shows maximum charging and discharge time than other electrodes such as C-CVR0, C-CVR1, C-CVR2, and C-CVR4. At a fixed current density of 1 A g^{-1} , the respective C_s (capacity) values for the C-CVR0, C-CVR1, C-CVR2, C-CVR3, and C-CVR4 electrodes were determined to be 551.7 F g^{-1} (275.8 C g^{-1}), 709.7 F g^{-1} (354.8 C g^{-1}), 896.6 F g^{-1} (448.3 C g^{-1}), 1345.2 F g^{-1} (672.6 C g^{-1}), and 668.9 F g^{-1} (334.4 C g^{-1}), as depicted in Figure 4.35 (g) and Figure 3.35 (h). In summary, the C-CVR3 electrode's elevated SSA enables convenient access for electrolyte ions, resulting in superior capacitive performance compared to the pristine C-CVR0 and other electrodes in the CVO/rGO composite electrodes.

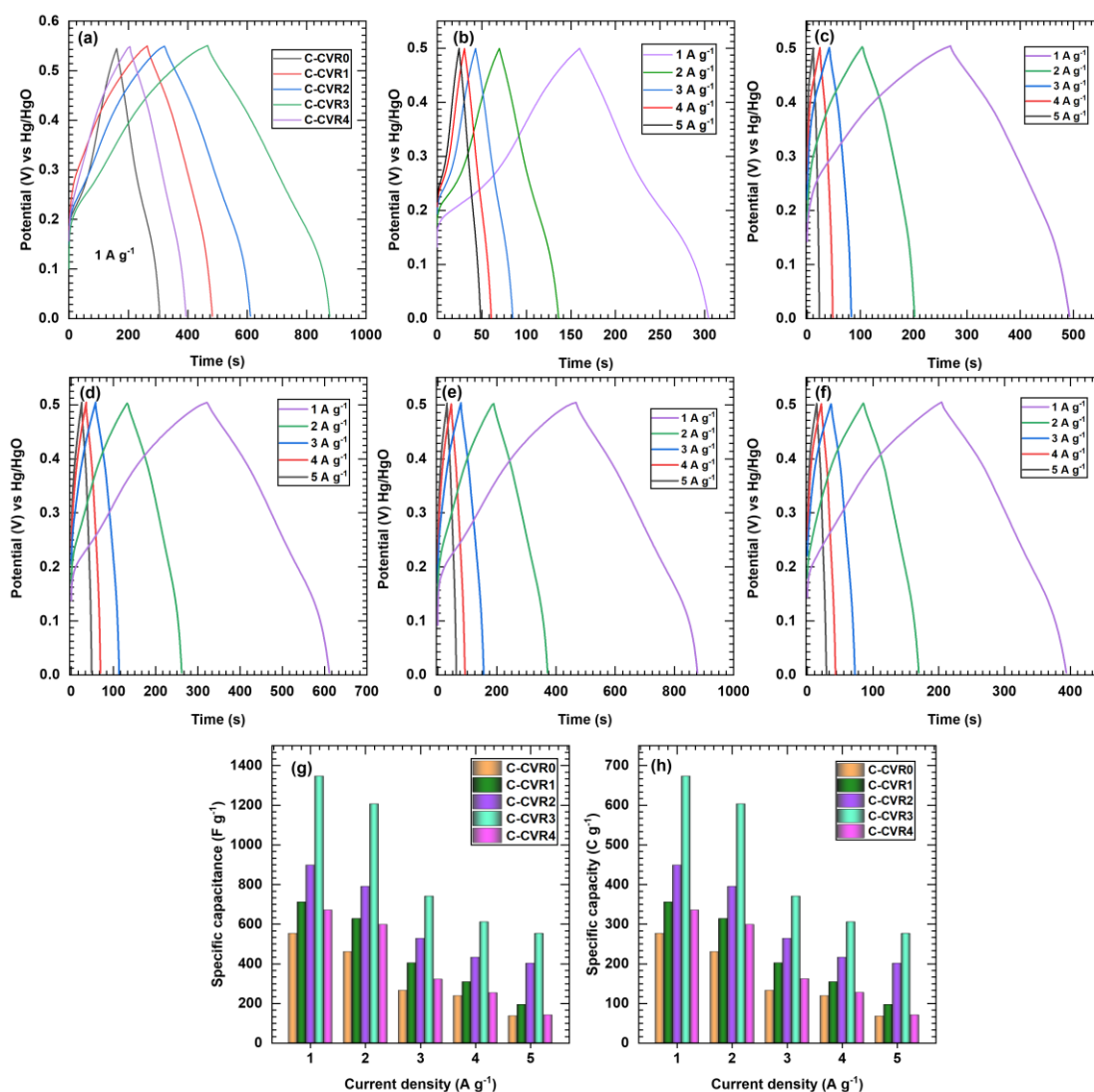


Figure 3.35 (a) The comparative GCD curves of C-CVR series electrodes at fixed current density (1 A g⁻¹), (b-f) the GCD curves of C-CVR0, C-CVR1, C-CVR2, C-CVR3, and C-CVR4 electrodes at different current densities from 1-5 A g⁻¹, (g) plot of C_s vs current density, and (h) plot of specific capacity vs current density.

3.2.B.6.10.4 EIS and Stability Analysis

An exploration of the electrochemical charge transfer kinetics of C-CVR series electrodes was conducted through EIS analysis. The testing of these electrodes was carried out within a frequency range spanning from 10 mHz to 0.1 MHz in a 1 M KOH solution. The characteristic Nyquist plots for all the samples are presented in Figure 3.36 (a). In comparison to R_{ct} values of C-CVR0 (200 Ω), C-CVR1 (146.3 Ω), C-CVR2 (110.5 Ω), and C-CVR4 (131.1 Ω), the value for C-CVR3 electrode is notably lower 63.4 Ω , indicating superior electrochemical conductivity. The circuit-fitted values of C-CVR series electrodes are depicted in Table 3.5. Unlike

the rest of the electrodes in the C-CVR series, the C-CVR3 electrode stands out for its exceptional performance, characterized by a lower R_{ct} value. The results indicate that the microplate-like structure of the C-CVR3 electrode facilitates efficient routes for charge transfer, thereby enhancing its electrochemical capabilities.

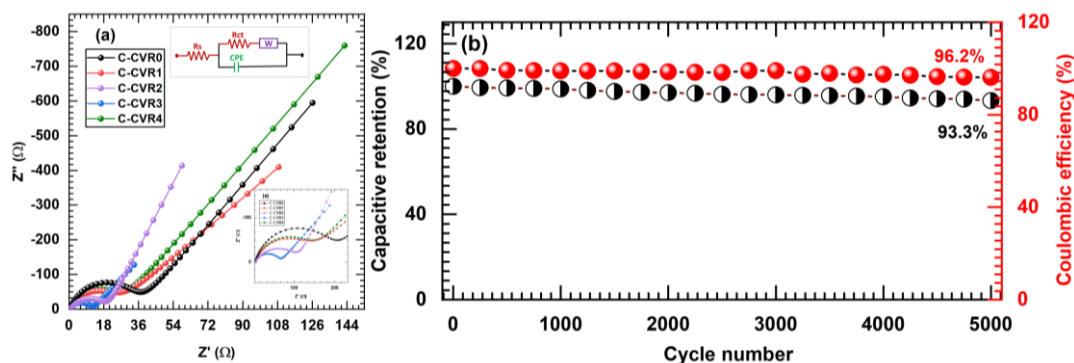


Figure 3.36 (a) Nyquist plot of C-CVR series electrodes, and (b) cyclic stability of C-CVR3 electrode.

Table 3.5 EIS circuit fitted values of C-CVR series electrodes.

Parameters/Sample	C-CVR0	C-CVR1	C-CVR2	C-CVR3	C-CVR4
R_s (Ω)	0.83	1.01	0.94	0.71	1.02
R_{ct} (Ω)	200	146.3	110.5	63.4	131.1
W (Ω)	0.0046	0.00025	0.00041	0.00071	0.0090
CPE (mF)	0.13	0.22	0.31	0.56	0.24
CPE (n)	0.81	0.77	0.65	0.67	0.79

The long-term cycling performance of the C-CVR3 electrode was evaluated through repeated GCD tests at a constant current density of 5 A g^{-1} , as depicted in Figure 3.35 (b). The findings demonstrate remarkable cycling durability, with the electrode maintaining 93.3% of its initial capacitance with 96.2% coulombic efficiency for the C-CVR3 electrode even after completing 5000 GCD cycles.

3.2.B.7 Conclusions

In conclusion, CVO/rGO composite material electrodes were synthesized using the CBS method with varying rGO content. The XRD analysis confirmed the crystalline nature of the CVO/rGO composite materials. Additionally, the formation of CVO/rGO composite material via FT-IR, Raman, EDS, and XPS, observing their

corresponding bonds and the Co, V, O, and C content in the prepared sample. From FE-SEM and HR-TEM analysis, the formation of the microplates-like structure of CVO over the rGO nanosheets is confirmed. The variation of rGO content in the CVO/rGO composite with increasing rGO concentration during synthesis is confirmed by TG analysis. The C-CVR3 electrode with optimum composition (95.53%/4.47 %) of CVO/rGO exhibited superior performance than other electrodes, attributed to the enhanced SSA ($27.8 \text{ m}^2 \text{ g}^{-1}$) and increased conductivity (Low R_s and R_{ct}). The C-CVR3 achieved maximum Cs of 1345.2 F g^{-1} at 1 A g^{-1} , which is 2.5 folds compared to the pristine C-CVR0 electrode. These findings suggest that the CVO/rGO composite electrode outperforms pristine materials with the addition of 4.4% rGO in CVO material. The outstanding performance of the C-CVR3 electrode material suggests that it can be used as a cathode in HSD fabrication.

3.3 References

- [1] M. Guan, Q. Wang, X. Zhang, J. Bao, X. Gong, Y. Liu, *Front. Chem.*, 8, (2020), 390, 1-14.
- [2] N. Mahmood, I. Castroa, K. Pramod, K. Khoshmanesh, S. Bhargava, K. Kalantar-Zadeh, *Energy Stor. Mater.*, 16, (2019), 455-480.
- [3] T. Zhou, Q. Han, L. Xie, X. Yang, L. Zhu, X. Cao, *Chem. Rec.*, 4, (2022), e202100275.
- [4] T. Jenkins, J. Alarco, I. Mackinnon, *ACS Omega*, 6, (2021), 1917-1929.
- [5] H. Irfan, K. Racik, S. Anand, *Mod. Electron. Mater.*, 4, (2018), 31-40.
- [6] S. Chakraborty, B. Petel, E. Schreiber, E. Matson, *Nanoscale Adv.*, 3, (2021), 1293-1318.
- [7] S. Zhang and L. Ci, *Micro Nano Lett.*, 7, (2012), 1101-1104.
- [8] L. Ma, N. Li, C. Long, B. Dong, D. Fang, Z. Liu, Y. Zhao, X. Li, J. Fan, *Adv. Funct. Mater.*, 29, (2019), 1906142, 1-10.
- [9] B. Sambandam, V. Soundharrajan, S. Kim, M. Alfaruqi, J. Jo, S. Kim, V. Mathew, Y. Sun, J. Kim, *J. Mater. Chem. A*, 6, 2018, 15530-15539.
- [10] S. Ni, G. Zhou, S. Lin, X. Wang, Q. Pan, F. Yang, D. He, *Mater. Lett.*, 63, (2009), 2459-2461.
- [11] Q. Wei, Q. Wang, Q. Li, Q. An, Y. Zhao, Z. Peng, Y. Jiang, S. Tan, M. Yan, L. Mai, *Nano Energy*, 47, (2018), 294-300.
- [12] J. Jiang, Y. Li, J. Liu, X. Huang, C. Yuan, X. Lou, *Adv. Mater.*, 24, (2012), 5166-5180.
- [13] V. Nguyen, F. Saria, J. Ting, *RSC Adv.*, 12, (2022), 29170-29176.
- [14] V. Patil, N. Kumar, R. Salunkhe, J. Gunjekar, C. Lokhande, M. Mali, V. Parale, H. Park, D. Mhamane, U. Patil, *J. Chem. Eng.*, 485, (2024), 150055, 1-17.
- [15] L. Yu, J. Zhang, Y. Dang, J. He, Z. Tobin, P. Kerns, Y. Dou, Y. Jiang, Y. He, S. Suib, *ACS Catal.*, 9, (2019), 6919-6928.
- [16] H. Sharkawy, D. Sayed, A. Dhmees, R. Aboushahba, N. Allam, *ACS Appl. Energy Mater.*, 3, (2020), 9305-9314.
- [17] D. Dubal, J. Kim, Y. Kim, R. Holze, C. Lokhande, W. Kim, *Energy Technol.*, 2, (2014), 325-341.
- [18] S. Palchoudhury, K. Ramasamy, R. Gupta, A. Gupta, *Front. Mater.*, 5, (2019), 1-9.
- [19] P. Katkar, S. Marje, V. Parale, C. Lokhande, J. Gunjekar, H. Park, U. Patil, *Langmuir*, 37, (2021), 5260-5274.
- [20] S. Marje, P. Katkar, S. Kale, A. Lokhande, C. Lokhande, U. Patil, *J. Alloys Compd.*, 779, (2019), 49-58.
- [21] S. Pujari, S. Kadam, Y. Ma, S. Jadhav, S. Kumbhar, S. Bhosale, J. Gunjekar, C. Lokhande, U. Patil, *J. Energy Storage*, 52, (2022), 105037, 1-15.
- [22] R. Rajalakshmi, K. Remya, C. Viswanathan, N. Ponpandian, *Nanoscale Adv.*, 3, (2021), 2887-2901.
- [23] G. Barbosa, C. Graeff, H. Oliveira, *Eclet. Quím.*, 30, (2005), 7-15.

- [24] M. Isacfranklin, C. Deepika, G. Ravi, R. Yuvakkumar, D. Velauthapillai, B. Saravanakumar, *Ceram. Int.*, 46, (2020), 28206-28210.
- [25] J. Gunjekar, B. Hou, A. Inamdar, S. Pawar, A. Ahmed, H. Chavan, J. Kim, S. Cho, S. Lee, Y. Jo, S. Hwang, T. Kim, S. Cha, H. Kim, H. Im, *Small*, 14, (2018), 1703481, 1-10.
- [26] J. Mitchell, M. Chagnot, V. Augustyn, *Annu. Rev. Mater. Res.*, 53, (2023), 1-23.
- [27] B. Huang, W. Wang, T. Pu, J. Li, C. Zhao, L. Xie, L. Chen, *J. Chem. Eng.*, 375, (2019), 121969, 1-43.
- [28] N. Chodankar, D. Dubal, S. Ji, D. Kim, *Small*, 15, (2019), 1901145, 1-11.
- [29] S. Jadhav, A. Jadhav, A. Kadam, *Electrochim. Acta*, 426, (2022), 140845, 1-9.
- [30] H. Li, Y. Zhu, S. Dong, L. Shen, Z. Chen, X. Zhang, G. Yu, *Chem. Mater.*, 28, (2016), 5753-5760.
- [31] H. Qiu, X. Sun, S. An, D. Lan, J. Cui, Y. Zhang, W. He, *Dalton Trans.*, 49, (2020), 6391-6397.
- [32] V. Kushwaha, K. Mandal, A. Gupta, P. Singh, *Dalton Trans.*, 53, (2024), 5435-5452.
- [33] P. Ekwere, M. Ndipingwi, C. Ikpo, S. Yussuf, K. Nwambaekwe, O. Uhuo, E. Iwuoha, *J. Energy Storage*, 63, (2023), 106853.
- [34] Z. Le, F. Liu, P. Nie, X. Li, X. Liu, Z. Bian, G. Chen, H. Wu, Y. Lu, *ACS Nano*, 11, (2017), 2952-2960.
- [35] J. Sheppard, B. Hambly, B. Pendley, E. Lindner, *Analyst*, 142, (2017), 930-937.
- [36] B. Hambly, J. Sheppard, B. Pendley, E. Lindner, *Electroanalysis*, 29, (2017), 681-689.
- [37] S. Yuan, X. Duan, J. Liu, Y. Ye, F. Lv, T. Liu, Q. Wang, X. Zhang, *Energy Storage Mater.*, 42, (2021), 317-369.
- [38] Y. Pathaare, A. Reddy, P. Sangrulkar, B. Kandasubramanian, A. Satapathy, *Hybrid Advances*, 3, (2023), 100041, 1-19.
- [39] A. Smith, A. LaChance, S. Zeng, B. Liu, L. Sun, *Nano Mater. Sci.*, 1, (2019), 31-47.
- [40] H. An, Y. Li, Y. Feng, Y. Cao, C. Cao, P. Long, S. Li, W. Feng, *Chem. Commun.*, 54, (2018), 2727-2730.
- [41] D. Marcano, D. Kosynkin, J. Berlin, A. Sinitskii, Z. Sun, A. Slesarev, L. Alemany, W. Lu, J. Tour, *ACS Nano*, 4, (2010), 4806-4814.
- [42] A. Sumair, I. Hussain, N. Hashim, M. Shafiqullah, M. Muhammad, *Curr. Nanosci.*, 15, (2019), 420-429.
- [43] M. Edokali, R. Bocking, M. Mehrabi, A. Massey, D. Harbottle, R. Menzel, A. Hassanpour, *Chem. Eng. Res. Des.*, 199, (2023), 659-675.
- [44] S. Thakur and N. Karak, *Carbon* 50, (2012), 5331-5339.
- [45] M. Dresselhaus, A. Jorio, M. Hofmann, G. Dresselhaus, R. Saito, *Nano Lett.*, 10, 751-758 (2010).
- [46] F. Low, C. Lai, S. Hamid, *Ceram. Int.*, 41, (2015), 5798-5806.
- [47] P. Cui, J. Lee, E. Hwang and H. Lee, *Chem. Commun.*, 47, (2011), 12370-12372.
- [48] F. Tuinstra and J. L. Koenig, *The J. Chem. Phys.*, 53, (1970), 1126-1130.
- [49] S. Veerasingam and R. Venkatachalapathy, *Infrared Phys. Technol.*, 66, (2014), 136-140.
- [50] P. Devi, M. Srivastava, N. Kim, J. Lee, D. Mishra, *Compos. B Eng.*, 227, (2021), 109384, 1-14.
- [51] F. Yin, S. Wu, Y. Wang, L. Wu, P. Yuan, X. Wang, *J. Solid State Chem.*, 237, (2016), 57-63.
- [52] A. Bakour, M. Baitoul, O. Bajjou, F. Massuyeau, E. Faulques, *Mater. Res. Express*, 4, (2017), 025031, 1-15.
- [53] S. Hafiz, R. Ritikos, T. Whitcher, N. Razib, D. Bien, N. Chanlek, *Sensor Actuator B Chem.*, 193, (2014), 692-700.
- [54] S. Bhosale, S. Kumbhar, S. Pujari, V. Patil, N. Kumar, R. Salunkhe, C. Lokhande, J. Gunjekar, U. Patil, *J. Energy Storage*, 72, (2023), 108417, 1-16.
- [55] M. Biesinger, *Appl. Surf. Sci.*, 597, (2022), 153681.
- [56] Y. Liu, H. Hsi, K. Li, C. Hou, *ACS Sustain. Chem. Eng.*, 4, (2016), 4762-4770.
- [57] M. Zong, Y. Huang, N. Zhang, H. Wu, *J. Alloys Compd.*, 644, (2015), 491-501.
- [58] Z. Zhao, X. Teng, Q. Xiong, H. Chi, Y. Yuan, H. Qin, Z. Ji, *Sustain. Mater. Technol.*, 29, (2021), e00313.
- [59] K. Li, B. Zhao, J. Bai, H. Ma, Z. Fang, X. Zhu, Y. Sun, *Small*, 16, (2020), 2001974, 1-9.
- [60] A. Abakumov, I. Bychko, O. Voitsihovska, R. Rudenko, P. Strizhak, *Mater. Lett.*, 354, (2024), 135417 1-4.
- [61] A. Alazmi, C. Wan, P. Costa, F. Brushett, *J. Energy Storage*, 50, (2022), 104192, 1-11.
- [62] H. Zhang, J. Tian, X. Cui, J. Li, Z. Zhu, *Carbon*, 201, (2023), 920-929.

CHAPTER-4

**Preparation of Cobalt
Vanadium Oxide/Reduced
Graphene Oxide Composite
Electrodes by SILAR Method
and their Characterization
and Supercapacitive
Performance**

CHAPTER-4

Preparation of Cobalt Vanadium Oxide/Reduced Graphene Oxide Composite Electrodes by SILAR Method and their Characterization and Supercapacitive Performance

Sr. No.	Title		Page No.
4.1	Introduction		119
4.2	Synthesis and Characterizations of Pristine Cobalt Vanadium Oxide and Cobalt Vanadium Oxide/Reduced Graphene Oxide Composite Electrodes by SILAR Method		119
	4.2.A	Section-A: SILAR Synthesis of Cobalt Vanadium Oxide Electrodes and Characterizations	
	4.2.A.1	Introduction	120
	4.2.A.2	Experimental Details	120
		4.2.A.2.1 Chemicals and Substrate Cleaning Procedure	120
		4.2.A.2.2 Preparation of Cobalt Vanadium Oxide Thin Films	121
		4.2.A.2.3 Material Characterizations	122
	4.2.A.3	Results and Discussion	122
		4.2.A.3.1 Reaction Mechanism and Growth of Cobalt Vanadium Oxide Formation	122
		4.2.A.3.2 XRD Analysis	124
		4.2.A.3.3 FT-IR Analysis	125
		4.2.A.3.4 XPS Analysis	125
		4.2.A.3.5 FE-SEM and EDS Analysis	127
		4.2.A.3.6 BET and BJH Analysis	129
		4.2.A.3.7 Electrochemical Characterizations	130
		4.2.A.3.7.1 Electrochemical Experimental Setup	130
		4.2.A.3.7.2 CV Analysis	130
		4.2.A.3.7.3 GCD Analysis	133
		4.2.A.3.7.4 EIS and Stability Analysis	135
	4.2.A.4	Conclusions	136
	4.2.B	Section-B: SILAR Synthesis of Cobalt Vanadium Oxide/Reduced Graphene Oxide Composite Electrodes and Characterizations	

	4.2.B.1	Introduction		137
	4.2.B.2	Experimental Details		138
		4.2.B.2.1	Synthesis of Cobalt Vanadium Oxide/Reduced Graphene Oxide	138
	4.2.B.3	Results And Discussion		140
		4.2.B.3.1	Reaction Mechanism and Growth of Cobalt Vanadium Oxide/Reduced Graphene Oxide Formation	140
		4.2.B.3.2	XRD Analysis	140
		4.2.B.3.3	FT-IR Analysis	141
		4.2.B.3.4	Raman Analysis	142
		4.2.B.3.5	XPS Analysis	143
		4.2.B.3.6	TG Analysis	145
		4.2.B.3.7	FE-SEM and EDS Analysis	146
		4.2.B.3.8	HR-TEM and EDS Analysis	148
		4.2.B.3.9	BET and BJH Analysis	149
		4.2.B.3.10	Electrochemical Analysis	151
			4.2.B.3.10.1 CV Analysis	151
			4.2.B.3.10.2 GCD Analysis	153
			4.2.B.3.10.3 EIS and Stability Analysis	154
	4.2.B.4	Conclusions		155
4.3	References			156

4.1 Introduction

Among available electrochemical ESDs, aqueous electrochemical ESDs (AEESDs) systems are considered a promising alternative to batteries owing to their non-toxic nature, low cost, and superior safety [1-3]. However, AEESDs suffer from ED than the batteries due to the poor performance of electrode materials [4, 5]. Therefore, a highly anticipated tactic to enhance the ED of AEESDs is to refine the storage capacity of electrodes by controlling the physical (e.g., crystallinity, hydrous nature, conductivity) and morphological (e.g., SSA, porosity, particle size) characteristics of storing materials.

TMOs are the favourite because of their special properties; multivalent states can provide ideal pseudocapacitance, proceeding electrons and ions intercalation into a metallic compound lattice, along with good intrinsic stability [6-8]. Several single TMOs like IrO_2 , Co_3O_4 , V_2O_5 , MnO_2 , RuO_2 , NiO , etc. [3], and MTMOs such as NiFe_2O_4 , NiCo_2O_4 , $\text{Co}_3\text{V}_2\text{O}_8$, MnCo_2O_4 , $\text{Ni}_3\text{V}_2\text{O}_8$, etc. have been investigated as cathode material in SCs. Moreover, MTMOs and their composites with carbonaceous materials such as rGO, CNTs, etc. possess high charge-storing performance due to good electric conductivity, various valance states, electrochemical activity, etc., owing to the synergistic effects of different metals or carbonaceous materials compared to single TMOs [9]. Among several TMOs, CVO and its composite with rGO is gaining attention as cathode material in HSCs.

Also, rationalizing the microstructure of material can lead to a change in the pseudocapacitive charge-storing mechanism from intercalation to extrinsic pseudocapacitive type. Hence, it is crucial to finely tune the features of electrode materials, such as electrical conductivity, surface area, and porous structure, by preparing binder-free electrodes using a novel synthesis approach to accomplish an advanced capacity of electrodes. Therefore, CVO and CVO/rGO composite thin films are directly deposited on an SS substrate without the use of a binder, employing a SILAR method. Additionally, the examination of the physicochemical properties of synthesized binder-free CVO and CVO/rGO composite thin films was carried out.

4.2 Synthesis and Characterizations of Pristine Cobalt Vanadium Oxide and Cobalt Vanadium Oxide/Reduced Graphene Oxide Composite Electrodes by SILAR Method

This chapter is segmented into two parts, denoted as Section A and B. Section A focuses on the SILAR synthesis of pristine binder-free CVO thin film electrodes and its subsequent morphological, structural, and electrochemical characterizations. Section B focuses on the SILAR synthesis of binder-free CVO/rGO composite thin films and their subsequent morphological and structural characterizations of SC performance.

4.2.A Section-A: SILAR Synthesis and Characterization of Cobalt Vanadium Oxide Thin Films

4.2.A.1 Introduction

The electrochemical performance of MTMO compounds may vary based on several factors such as the specific synthesis process, the synergistic effect among metal atoms, augmentation of active sites, facilitation of channels for electrolyte ion migration, elevated SSA, and enhanced porosity. Moreover, decreasing the size or crystallinity (nanomaterials) of battery-type materials can illustrate pseudocapacitive activities and are referred to as extrinsic pseudocapacitive materials. However, extrinsic materials endure low PD and poor stability, excluding exceptional ED. Therefore, developing cost-effective energy storage materials with high SSA, maximum Cs, and promising cycle life is necessary to prepare advanced energy values. Therefore, the binder-free SILAR synthesis approach is demonstrated for the first time to prepare nanostructured CVO thin film electrodes by controlling growth dynamics. Herein, we have studied the effect of variation in dip time (in adsorption, reaction, and rinsing baths) for CVO thin films and their structural morphological properties are tuned to achieve high electrochemical performance.

4.2.A.2 Experimental Details

4.2.A.2.1 Chemicals and Substrate Cleaning Procedure

$\text{CoCl}_2 \cdot 6\text{H}_2\text{O}$ (cobalt chloride), NH_4VO_3 (ammonium metavanadate), $\text{C}_6\text{H}_{15}\text{NO}_3$ (triethanolamine (TEA)), potassium hydroxide (KOH) were bought from Sigma Aldrich (AR grade), and used as precursor without any purification. The SS 304 grade was purchased from the market and used as conducting substrates for the deposition of CVO. Before using SS substrates, for the deposition of CVO, they were cleaned by a standard process, which is discussed in Chapter 3, section 3.2.A.2.2.

4.2.A.2.2 Preparation of Cobalt Vanadium Oxide Thin Films

The thin films of CVO are prepared using a simple chemical SILAR method. In one beaker, 0.05 M $\text{CoCl}_2 \cdot 6\text{H}_2\text{O}$ precursor dissolved in DDW and an occurred pink-colored solution was used as a cationic precursor. Also, 0.05 M NH_4VO_3 precursor dissolved in DDW at 60 °C temperature at constant stirring, and after cooling, 0.05M $\text{C}_6\text{H}_{15}\text{NO}_3$ was added dropwise into the NH_4VO_3 solution to maintain pH around 8.5 and used as an anionic precursor. For rinsing purposes, DDW is used. The prepared solution beakers were placed in the sequence of $\text{CoCl}_2 \cdot 6\text{H}_2\text{O}$, DDW, NH_4VO_3 , and again DDW, respectively, as shown in a schematic of the SILAR method in Figure 4.1.

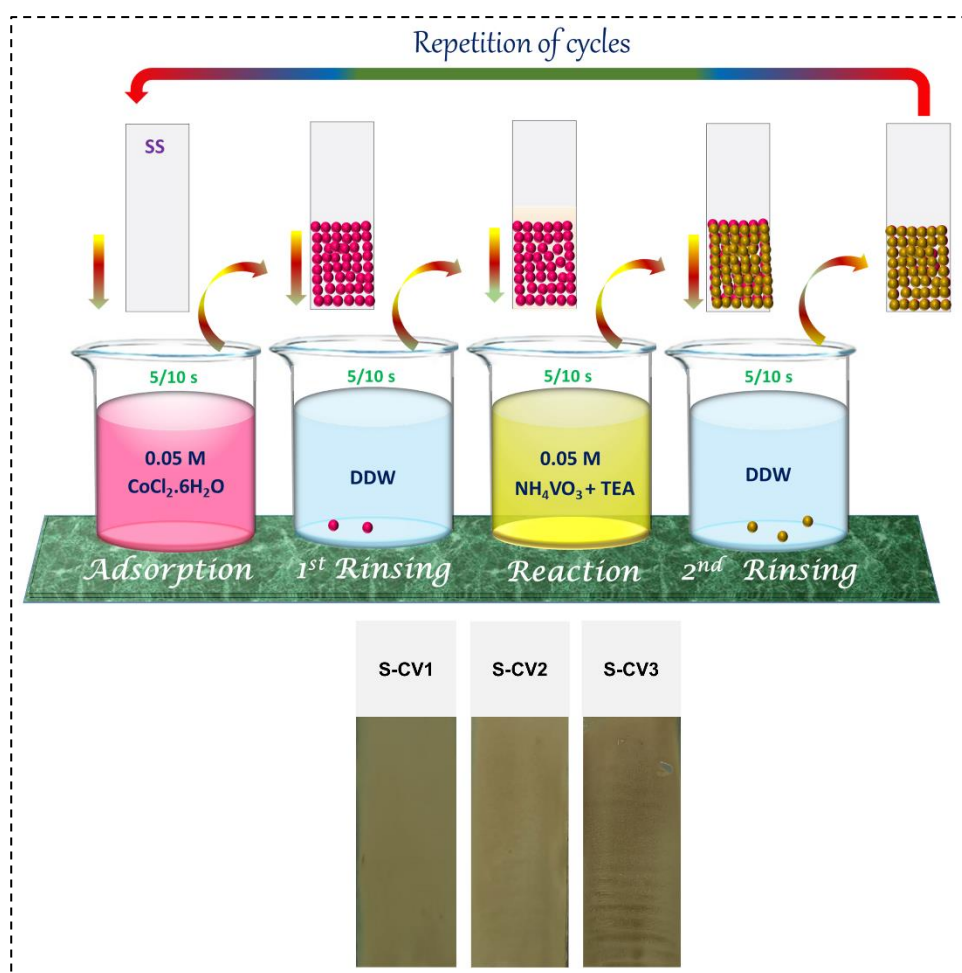


Figure 4.1 Schematic representation of dip time variation of S-CV series thin films by SILAR method.

The pre-cleaned SS substrates were immersed vertically in each placed beaker for the desired time called dipping time. In the synthesis process, the dipping time of adsorption/reaction to rinsing is varied in proportion of 1:2, 1:1,

and 2:1, as given in Table 4.1, for S-CV deposition on the SS substrate and denoted by S-CV1, S-CV2, and S-CV3, respectively. As a result, the uniform deposition of brownish S-CV series thin films occurred at room temperature after continuous 150 SILAR cycles. To study the impact of dipping time variation, all other preparative parameters were kept constant, such as the concentration of precursors, deposition cycles (150), deposition temperature, etc. These S-CV series thin films were exercised for further structural, morphological, and electrochemical characterizations.

Table 4.1 Preparative parameters for the synthesis of S-CV series thin film electrodes.

Sr. No.	Sample Name	Adsorption Time (s)	1 st Rinsing Time (s)	Reaction Time (s)	2 nd rinsing Time (s)	Temp.	pH
1	S-CV1	5	10	5	10	R.T.	~8.5
2	S-CV2	5	5	5	5		
3	S-CV3	10	5	10	5		

4.2.A.2.3 Material Characterizations

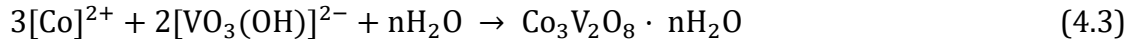
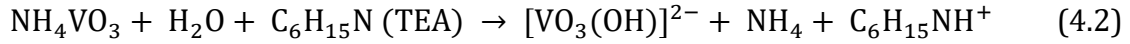
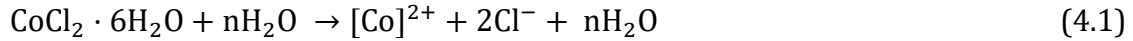
All the characterization techniques outlined in Chapter 3, section 3.2.A.2.4 were employed to analyze the CVO and CVO/rGO composite thin film electrodes.

4.2.A.3 Results and Discussion

4.2.A.3.1 Reaction Mechanism and Growth of Cobalt Vanadium Oxide Formation

The current study uses the SILAR method to prepare binder-free S-CV series thin film electrodes at room temperature. The SILAR method works on the adsorption of cations followed by a reaction with anions on the substrate surface while rinsing in DDW baths. In the cationic bath, Co^{2+} cations are obtained from the dissociation of cobalt chloride in the DDW at room temperature, as described in reaction (4.1). These cations get adsorbed at nucleation centres of the well-cleaned SS substrate. Further adsorbed cations react with anions where metavanadate $[\text{VO}_3(\text{OH})]^{2-}$ anions are obtained from dissociating ammonium metavanadate at 60 °C in DDW at around 8.5 pH maintained using TEA, as per the

reactions given in 4.2. Thus, the deposition of the S-CV series occurs in thin film form as per reaction 4.3.



After 150 cycles, as-prepared films were dried at ambient temperature; the brown-colored S-CV series thin films were obtained, as shown in Figure 4.1. The thicknesses of S-CV series thin films are determined by the gravimetric weight difference process using deposited mass per unit area (mg cm^{-2}) over SS substrate after 150 cycles, as depicted in Figure 4.2.

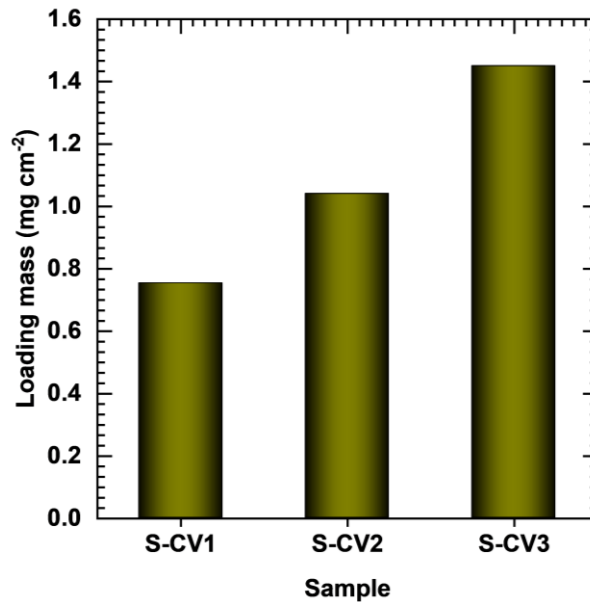


Figure 4.2 Plot of loading mass of S-CV on SS substrate.

The graph reveals that the dipping time variation alters the mass loading over the SS substrate. As a result, a maximum thickness is observed for the S-CV3 sample; however, sample S-CV1 shows less thickness, and it concludes that less rinsing time demonstrates faster growth of the material and effectively increases thickness. Hence, the growth rate of S-CV series thin film deposition is strongly influenced by dipping time variation, and such a change in the growth dynamics of the S-CV series thin films can lead to a change in the physicochemical properties. Consequently, it may influence the pseudocapacitive properties of S-CV series electrodes. So, apart from the apparent advantages of quality yield and

cost-effectiveness, control over growth dynamics and, subsequently, the thickness of the S-CV series thin film are the prime advantages of the SILAR method. So, one can efficiently manipulate electrode material properties according to the prerequisites of the electrochemical application.

4.2.A.3.2 XRD Analysis

The SILAR-synthesized S-CV series thin films were characterized by different techniques in which the XRD is used for the structural study. Figure 4.3 shows XRD patterns of crystalline S-CV thin film electrodes prepared with varying dipping times. Three peaks of the S-CV series are intensely associated with 2θ degrees of 21.02° , 30.05° , and 35.4° , denoted by the ‘*’ symbol, and are observed in all S-CV series samples. The obtained diffraction peaks indicate the formation of an orthorhombic phase of $\text{Co}_3\text{V}_2\text{O}_8$ (JCPDS card no.- 01-074-1486), which are attributed to the (200), (002) and (320) of (hkl) planes, respectively. Also, peaks associated with angles 44.9° , 51.5° , and 75.2° showed the SS peaks, which are indicated by the ‘*’ symbol.

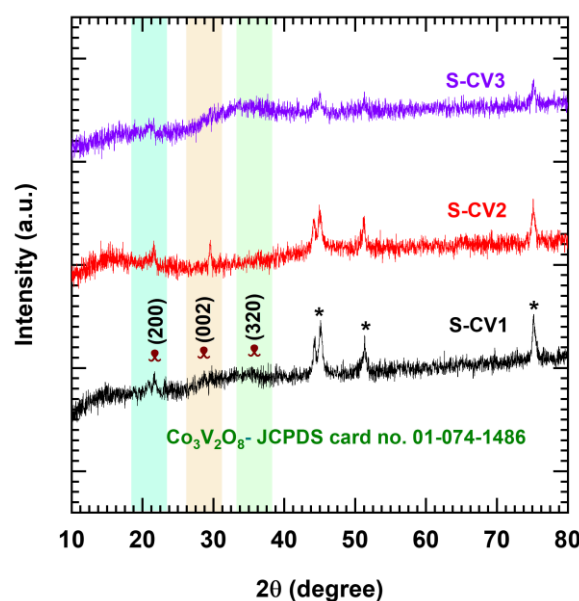


Figure 4.3 (a) XRD patterns of S-CV series thin films with dip time variation (S-CV1, S-CV2, and S-CV3).

The effect of growth dynamics is significantly evident from the XRD peak intensity of the materials; the S-CV2 sample shows a slightly higher intensity than the S-CV1 sample. The peak intensity of the S-CV1 sample is more elevated than sample S-CV3, and such different diffraction peak intensities are attributed to the change in growth kinetics of material with variation in dipping time. The XRD

results suggest that a slow S-CV series thin film growth rate can lead to the formation of material with improved crystallinity. Moreover, the obtained nanocrystalline nature of S-CV series thin film electrodes can exhibit exceptional electrochemical capacitive performance [10].

4.2.A.3.3 FT-IR Analysis

The FT-IR peaks scrutiny of prepared S-CV series materials was accomplished in 400 to 4000 cm^{-1} region and exhibited in Figure 4.4. The peaks are located at a range of 410-435 cm^{-1} (γ_1), which correlates to the cobalt-oxygen stretching mode. The well-built and typical peaks (γ_2) about 451, 776, and 1073 cm^{-1} have been attributed to the vanadyl group stretching vibration belonging to the out-of-plane and in-plane vibrational modes of V-O-V related to the V-O, respectively [11].

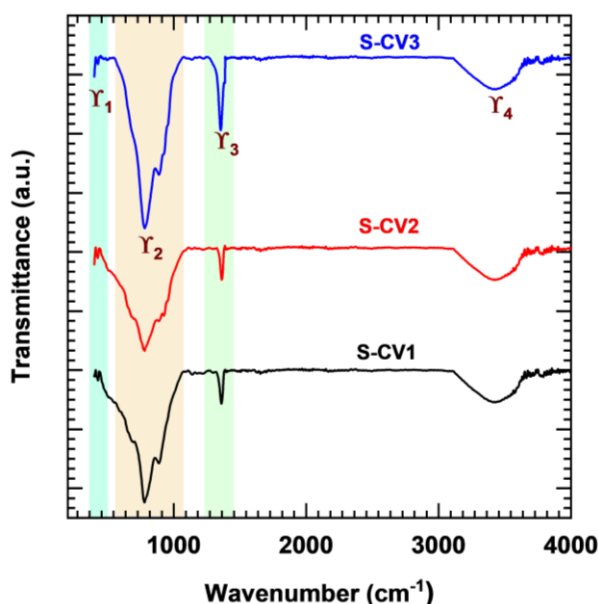


Figure 4.4 FT-IR spectra of S-CV series materials (S-CV1, S-CV2, and S-CV3).

The (γ_3) peak at 1310 cm^{-1} is associated with the C-O stretching from impurities of TEA in the prepared material [12]. The stretching vibrations of the O-H molecules from the structural water are responsible for the broad range at higher wavenumbers between 3109 and 3660 cm^{-1} (γ_4) [13]. According to the FT-IR result, the prepared S-CV series materials are hydrous, which can be beneficial for SC application.

4.2.A.3.4 XPS Analysis

The XPS study of the S-CV sample was conducted to scrutinize the chemical composition with states of elements of prepared S-CV thin films. The total survey spectrum of sample S-CV2 is shown in Figure 4.5 (a), which depicts Co 2p, V 2p, O 1s, and C 1s peaks. The spectrum of Co 2p shown in Figure 4.5 (b) split into two core binding energies, i.e., Co 2p_{1/2} and Co 2p_{3/2} at 796.8 and 780.7 eV, respectively. Also, those energies deconvoluted into two valance states such as Co³⁺ and Co²⁺; Co 2p_{1/2} split at 796.4 and 797.9 eV, and Co 2p_{3/2} split at 780.4 and 782 eV, respectively. In the cobalt spectrum, two satellite peaks are identified at binding energies of 802.9 and 786.4 eV [14]. Furthermore, the V 2p spectrum is demonstrated in Figure 4.5 (c), where the vanadium spectrum is deconvoluted into two primary energies of V 2p_{1/2} and V 2p_{3/2} at 524 and 516.5 eV, respectively.

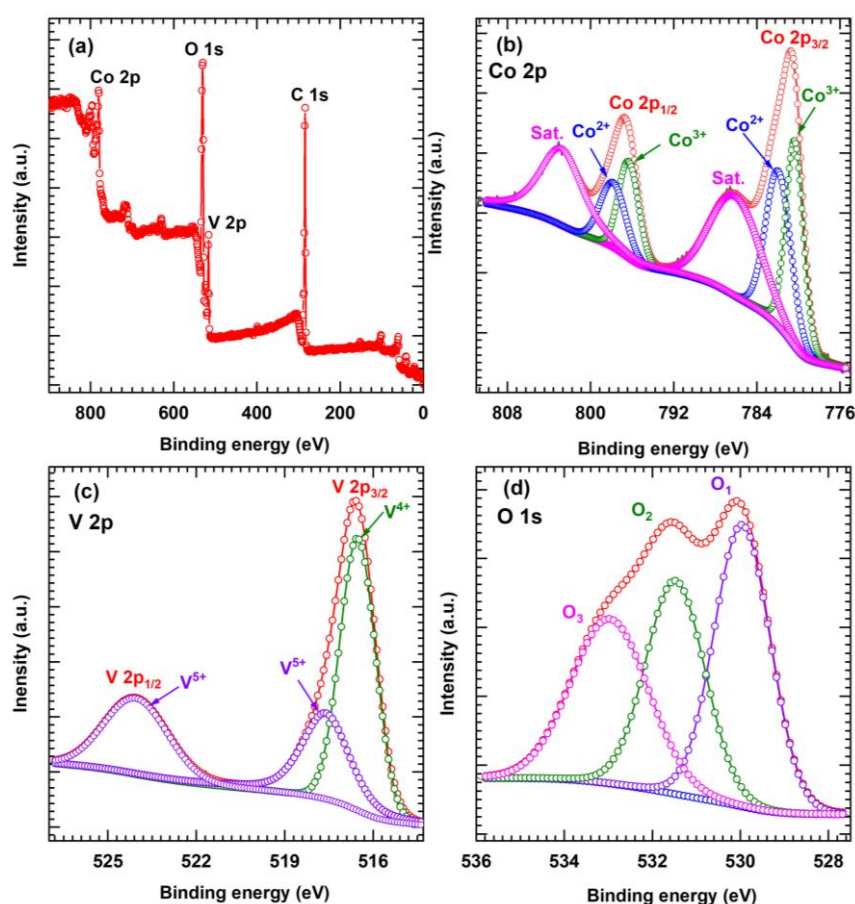


Figure 4.5 (a) XPS full survey spectra and the corresponding (b) Co 2p, (c) V 2p, and (d) O 1s of the sample S-CV2.

The V 2p_{3/2} split into two valance states are attributed to the V⁴⁺ and V⁵⁺ at energies of 516.5 and 517.6 eV, respectively, and other peaks at 523.08 eV and 524.48 eV correspond to the V⁴⁺ and V⁵⁺ valance states, respectively. Also, the

deconvoluted O 1s spectrum is displayed in Figure 4.5 (d), and there are three deconvolute peaks: O₁, O₂, and O₃ at 529.9, 531.4, and 532.9 eV binding energies, respectively. The characteristic O₁ is the oxygen related to lattice oxygen, and the second peak of O₂ is attributed to the oxygen vacancies [7, 15, 16]. At 529.9 eV, the O₃ peak corresponds to the oxygen of water absorbed by the surface or hydroxyl species. In conclusion, the dominant states of Co²⁺ and V⁵⁺ support the formation of hydrous S-CV in the polymorph of Co₃V₂O₈ in thin films, which agrees with the XRD result.

4.2.A.3.5 FE-SEM and EDS Analysis

The growth dynamics variation on the morphology of S-CV series thin films is probed by FE-SEM analysis. The morphologies of prepared samples at different dipping times are shown in Figure 4.6 (a1, b1, c1) at different magnifications. It is observed that fine spherical particles are deposited over the SS substrates. Also, the morphology contains porous structures with voids and cavities that can help easy access to the electrolyte.

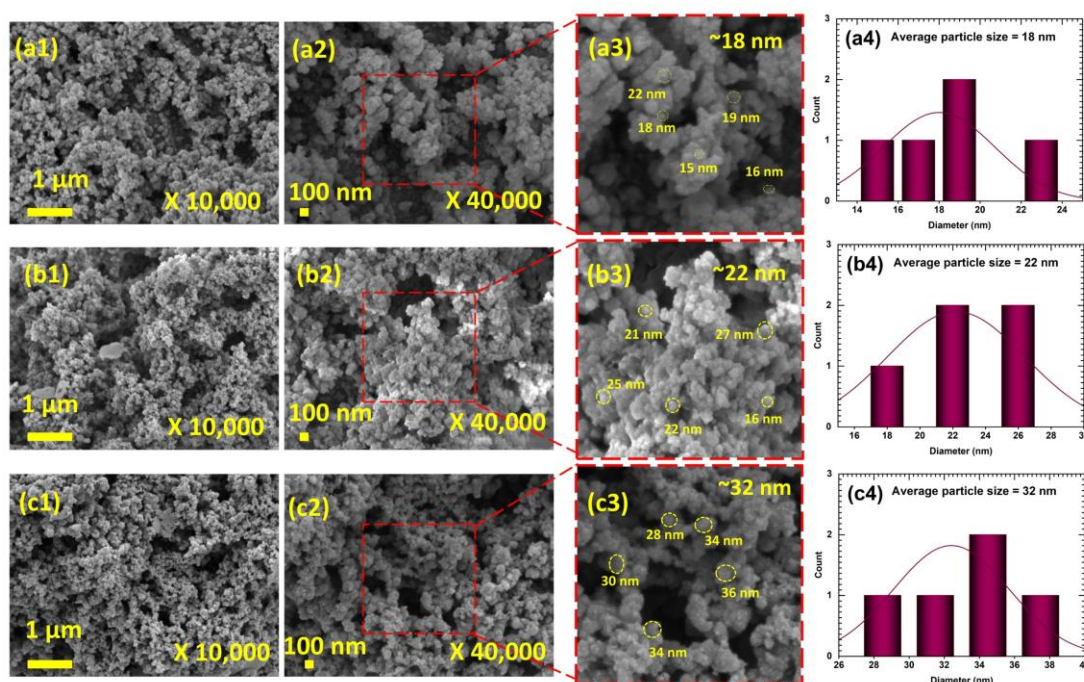


Figure 4.6 FE-SEM and histogram images of S-CV series samples: (a1-a4) S-CV1, (b1-b4) S-CV2, and (c1-c4) S-CV3 at different magnifications.

At higher magnification, it can be seen that these spherical particles consist of nanoparticles and are interconnected with each other, as shown in Figure 4.6 (a2, b2, c2). However, even with aggregation of nanoparticles present

in morphology, which are acquiescent with high aspect ratio particles, they can physically proceed to enhance the clearness of their electrolytes from surfaces [25, 26].

Furthermore, the particle size is determined from the magnified image shown in Figure 4.6 (a3, b3, c3) and Figure 4.6 (a4, b4, c4) show the histograms of S-CV1, S-CV2, and S-CV3, the average particle size is found to be ~ 18 , 22, and 32 nm, respectively. It is observed that the average particle size increases as rinsing time decreases, owing to faster growth kinetics resulting in the agglomeration of the particles at a less rinsing time. On the other hand, double rinsing time compared to adsorption and reaction time leads to the formation of a compact thin film with a smaller particle size in the S-CV1 sample. Furthermore, the elemental composition of S-CV was probed using EDS mapping, as shown in Figure 4.7.

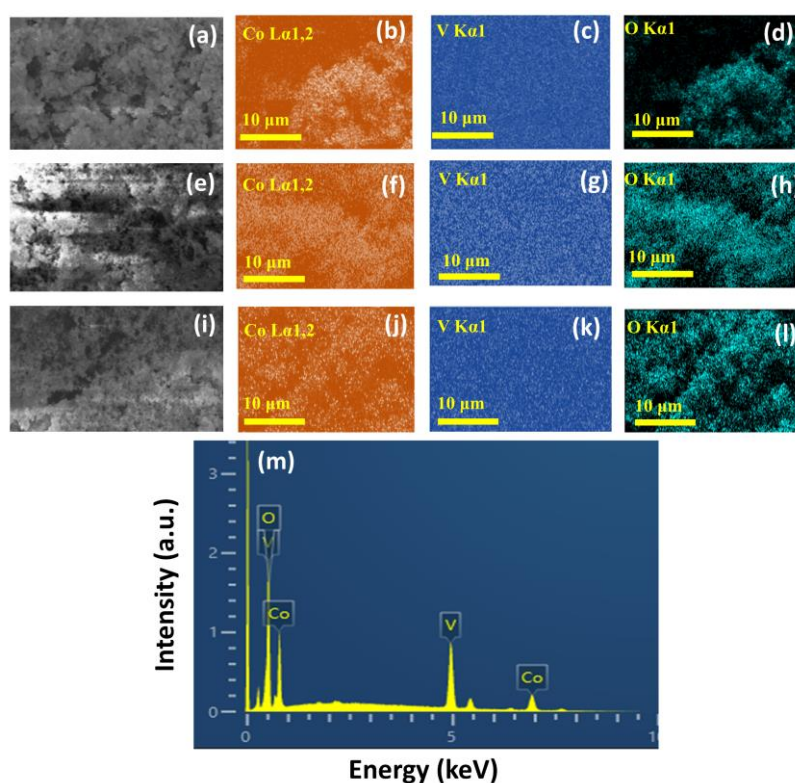


Figure 4.7 EDS mapping of CVO thin film samples (a-d) S-CV1, (e-h) S-CV2, (i-l) S-CV3, and (m) EDS spectrum of S-CV2 thin film.

The EDS mapping depicts that Co, V, and O elements are present in all the S-CV series samples, as illustrated in orange, blue, and green in Figure 4.7 (a-l). Also, EDS analysis confirms atomic percentages of 36%, 29%, and 35% of Co, V,

and O elements, respectively, in the S-CV2 sample. As a result, the FE-SEM and EDS analysis confirms the preparation of nanostructured, porous S-CV material in thin film form.

4.2.A.3.6 BET and BJH Analysis

The SSA of the S-CV1, S-CV2, and S-CV3 samples was analyzed by adsorption and desorption of N₂ isotherms, as shown in Figure 4.8 (a-c). The obtained isotherms showed type-III isotherm with H3 type hysteresis loop in the P/P₀ (relative pressure) range of 0.04-0.9 by the International Union of Pure and Applied Chemistry (IUPAC) classification. Using BET, the calculated SSA is found to be 54.9, 74.3, and 18.6 m² g⁻¹ for S-CV1, S-CV2, and S-CV3 samples, respectively. The maximum SSA obtained for the S-CV2 sample confirms that dipping time influences the SSA of the prepared S-CV material. Also, the pore diameter is measured by the BJH technique and shown in the inset of Figure 4.8 (a-c).

The obtained mean pore size diameters of S-CV1, S-CV2, and S-CV3 samples are 9.5, 9.1, and 17.8 nm, respectively, and confirm the mesoporous nature of the S-CV series samples. The maximum SSA is obtained for S-CV2 owing to the optimum average particle size and pore size distribution. However, the S-CV1 and S-CV3 exhibited low SSA due to the compact morphology with fine nanoparticles and larger average particle size with a wide porous structure. The results concluded that the different growth kinetics due to changes in dipping time influence the resultant SSA and porous structure. Thus, obtaining a larger SSA envisioned that the S-CV nanoparticles could exhibit good supercapacitive performance [17]. The higher SSA can offer a highly electrochemically active surface by creating an easy path for ion transportation in the material; consequently, it proved the higher electrochemical capacitive performance [18].

All the structural analysis confirms the growth dynamics variation from S-CV1 to S-CV3, ultimately influencing the morphology, pore size distribution, and SSA of nanostructured S-CV (Co₃V₂O₈·nH₂O) thin film electrodes, which are viable to accomplish high pseudocapacitive performance.

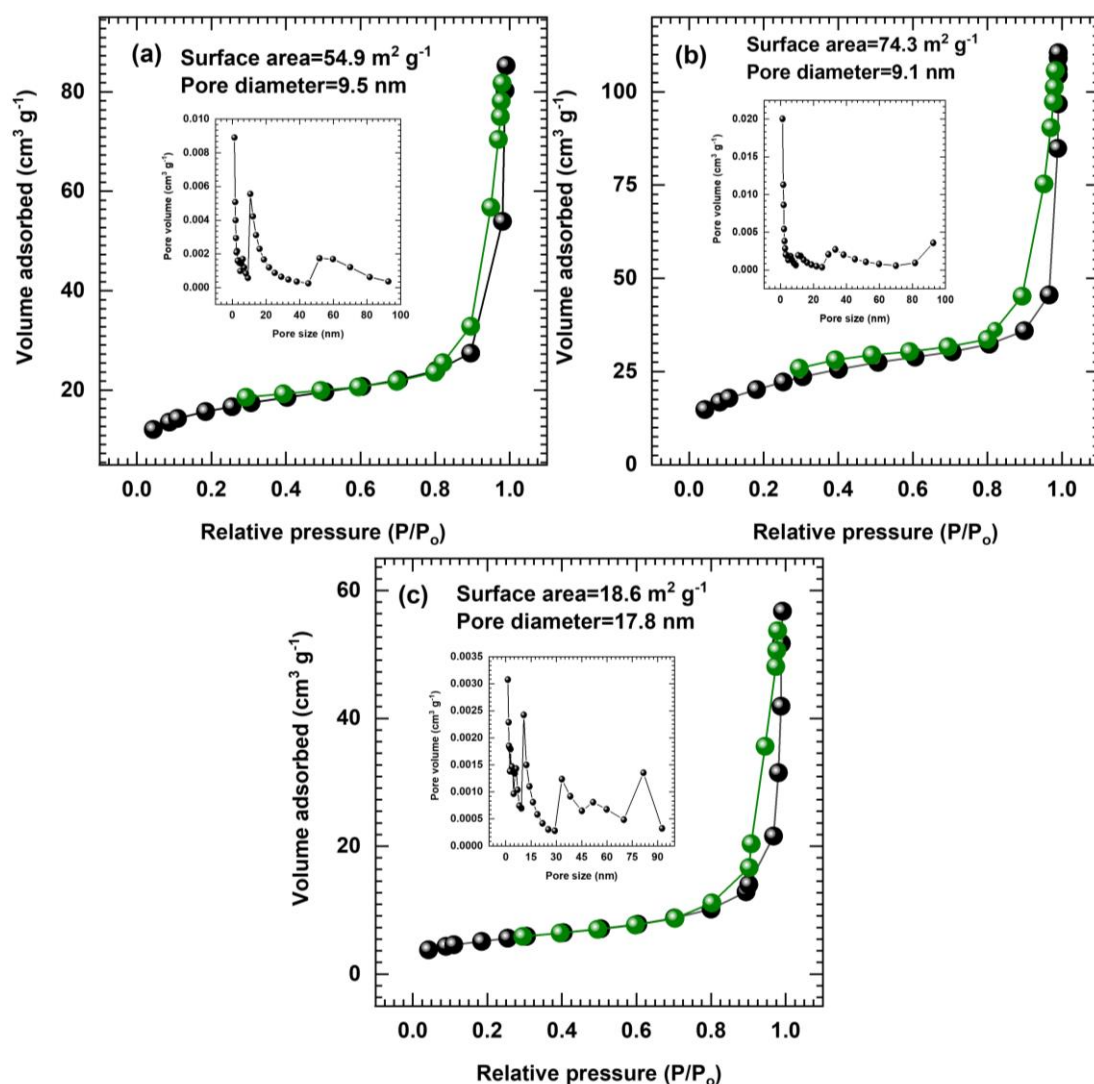


Figure 4.8 Adsorption-desorption isotherms and inset pore size distribution of samples (a) S-CV1, (b) S-CV2, and (c) S-CV3.

4.2.A.3.7 Electrochemical Characterizations

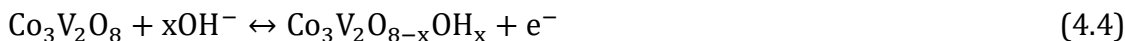
4.2.A.3.7.1 Electrochemical Experimental Setup

The setup of the three-electrode system is described in Chapter 3, section 3.2.A.3.7, where S-CV series electrodes as working electrodes.

4.2.A.3.7.2 CV Analysis

The correlative CV curves of samples S-CV1, S-CV2, and S-CV3 at a fixed 20 mV s^{-1} scan rate in the potential range of $0\text{--}0.6 \text{ V/Hg/HgO}$ are displayed in Figure 4.9 (a). All S-CV series thin film electrodes depict individual redox pairs related to the Faradaic reversible redox responses among $\text{Co}_3\text{V}_2\text{O}_8$ to $\text{Co}_3\text{V}_2\text{O}_{8-x}\text{OH}_x$. Thus, redox pairs correspond to the intercalation of OH^- ions into the S-CV, while, the

charging phenomenon occurs, and electrolyte ions are deintercalated whenever discharging occurs, as given in the following reaction (4.4).



Also, the absolute area under the CV curve of the S-CV2 electrode is larger than the S-CV1 and S-CV3 electrodes, representing that the S-CV2 has a maximum capacity for charge storage. Due to the mesoporous structure and high SSA of the S-CV2 electrode, electrolyte ions permeate effortlessly in the interior of an electrode and enable maximum area for charge storage. Thus, it shows an increment in the current under the curve of the S-CV2 electrode compared to other electrodes. The CV curves of the S-CV1, S-CV2, and S-CV3 electrodes at different scan rates of 2 to 50 mV s^{-1} are displayed in Figure 4.9 (b-d). When the voltage scan rate increases, the area under the CV curve increases, although the redox pairs shift slightly in the CV loop owing to the polarization effect [19, 20].

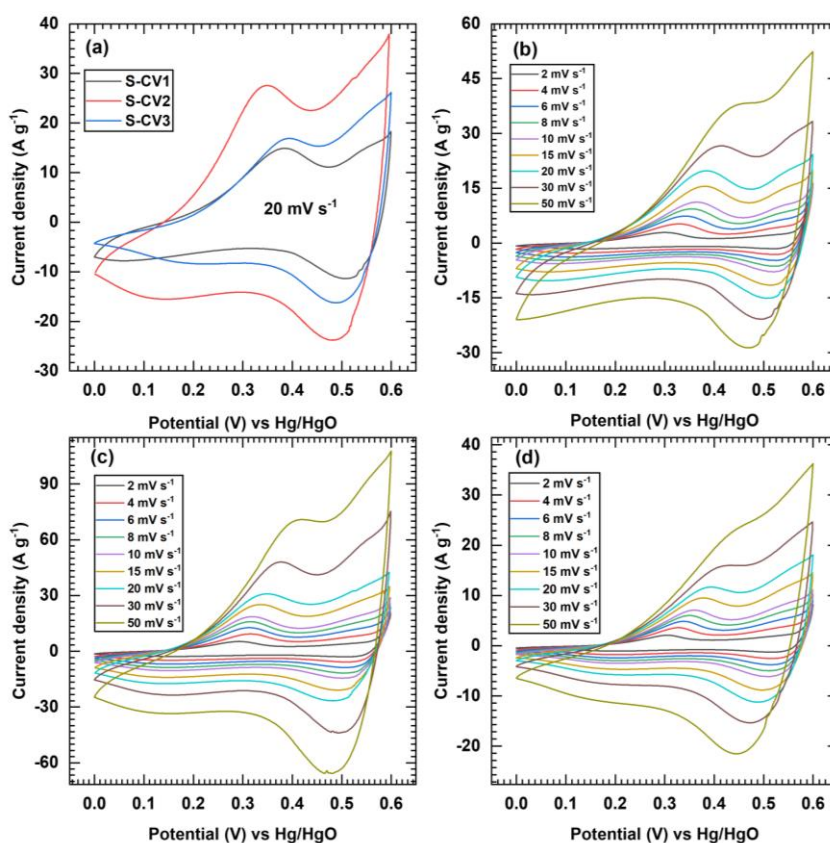


Figure 4.9 (a) At 20 mV s^{-1} scan rate, comparative CV curves of S-CV series electrodes, CV curves of (b) S-CV1, (c) S-CV2, and (d) S-CV3 at different scan rates.

Furthermore, in a direction to divulge the mechanism of charge storage of S-CV series electrodes, their electrochemical kinetics are prodigious to study [21].

The scan rate (v) versus peak current (i) in the CV area under the loop satisfied the 'Power's law' as given in Chapter 3, equation (3.6) [22]. When the value of 'b' is near 0.5, the diffusion-controlled electrochemical charge storage process is dominant, and the surface capacitive process is conquered when the value 'b' is near 1 [23]. The 'b' values of the S-CV1, S-CV2, and S-CV3 are 0.86, 0.81, and 0.78, respectively, as depicted in Figure 4.10 (a-c), and it deduced that the S-CV series material exhibits more surface capacitive charge storage process, i.e., extrinsic pseudocapacitive behavior owing to nanoparticle like morphology.

Additionally, using the Trasatti method, the surface capacitive contribution in the charge storage was determined [24], and additional insight into the kinetics of charge storage of electrodes is examined, illustrating the battery type (diffusion-controlled) and pseudocapacitive owing to surface extrinsic charge storage. The pseudocapacitive charge on the surface (Q_s) and battery type (Q_d) is measured by the total current response from CV. The total charge, i.e., Q_{total} is the combination of battery and diffusive type, as mentioned in Chapter 3 equation (3.7) [25, 26]. Moreover, the charge contributions were calculated using CV curves since the Q_d varies with $v^{-1/2}$, and Q_s is independent of scan rate (v) as mentioned in Chapter 3 equation (3.8).

The plot of Q_{total} vs $v^{-1/2}$ is shown in Figure 4.10 (d), and the Y-axis intercept represents the capacitive contribution of the S-CV series electrodes. The slow scan rates are designated for estimating Q_s on the Y-axis and calculating the charge contribution in S-CV series electrodes. The charge contribution from Q_s is lower in the S-CV3 electrode and higher in other S-CV series electrodes, as shown in Figure 4.10 (e). The charge contribution from the Q_s , i.e., surface pseudocapacitive, is attributed to the nanostructured morphology and high SSA of S-CV series electrodes, and this result further ensures that the miniaturization of material size is crucial to attain the pseudocapacitance. Also, a contribution from Q_s increases with the scan rate and accomplishes battery type process (diffusive), leading to slow scan rates. Therefore, the S-CV series material displays a diffusive (battery-type) behavior at the lower scan rate and higher scan rates, showing a capacitive nature, as shown in Figure 4.10 (f-h) [27].

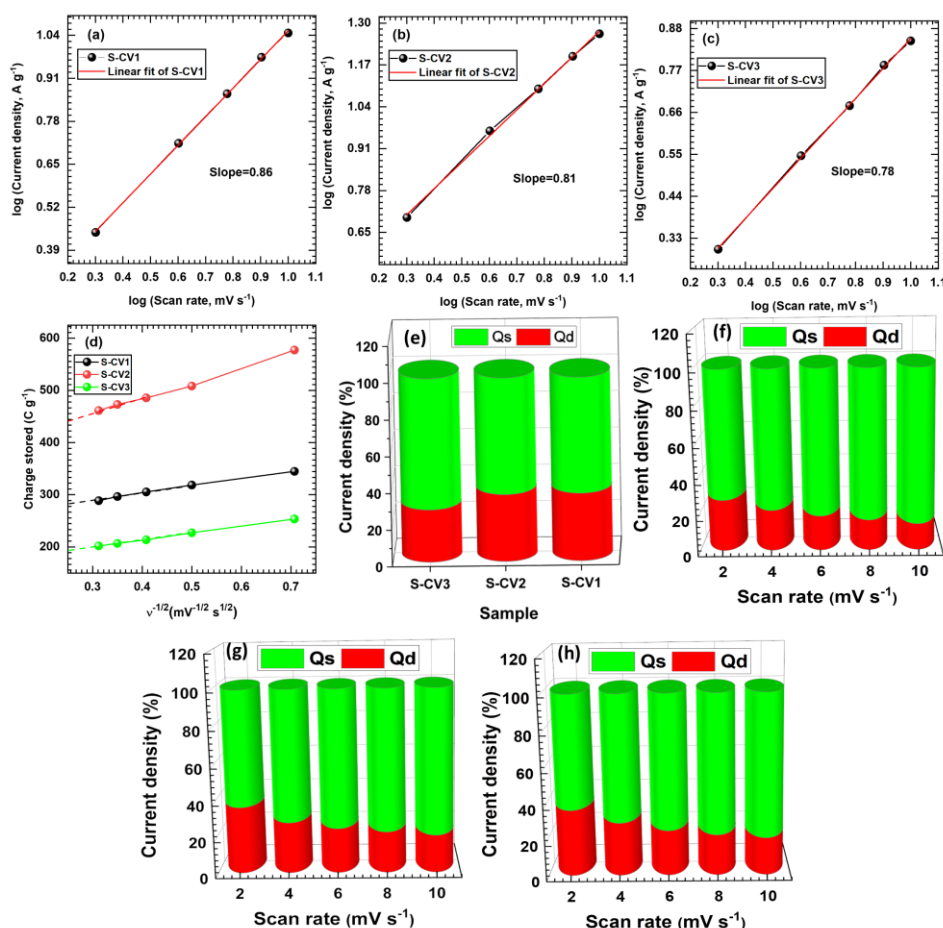


Figure 4.10 Plot of \log (current density, A g^{-1}) versus \log (scan rate, mV s^{-1}) for electrode (a) S-CV1, (b) S-CV2, and (c) S-CV3, (d) the plot of total charge against the reciprocal of the square root of scan rate for S-CV series electrodes, (e) comparative plot of surface and diffusive charge contribution at fixed scan rate (S-CV1, S-CV2, and S-CV3), and (f-h) plots of surface and diffusive charge contribution of S-CV series at different scan rate.

4.2.A.3.7.3 GCD Analysis

The GCD analysis is further used for the electrochemical performance evaluation of S-CV series thin film electrodes. The comparative GCD curves of S-CV1, S-CV2, and S-CV3 electrodes at 2 A g^{-1} constant current density are displayed in Figure 4.11 (a). All-tested S-CV series electrodes characteristically show bell-shaped, symmetric charging-discharging curves, typically representing intercalation-type pseudocapacitive charge storage mechanisms. In the pseudocapacitive type, charge storage contains two concepts: surface oxidation-reduction and intercalative type [28]. The GCD/CV curve analysis depicts that S-CV series electrodes possess a combination of intercalation type and extrinsic

pseudocapacitive behaviour owing to their nanostructured morphologies and augmented SSA. Figure 4.11 (b-d) displays GCD curves of S-CV series electrodes at different current densities. It can be seen that, as the current density decreases, GCD time increases, representing typical electrochemical reactions step rate by the diffusion of ions. Consequently, at the higher current densities, the ions of electrolyte access the outer surfaces of active material and hardly reach the interior of the material, hence, internal space is not fully used for abundant redox reactions [29]. The Cs of dipping time-varied S-CV electrodes are calculated by the standard formula mentioned in Chapter 1 (equation 1.3).

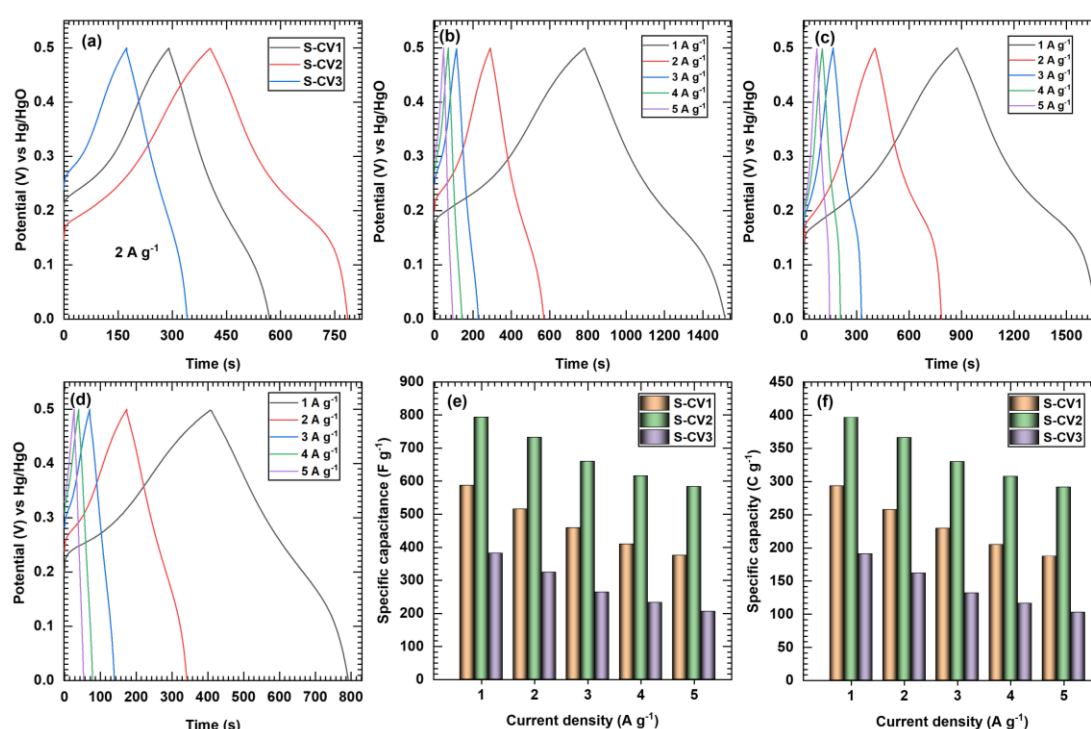


Figure 4.11 (a) The comparative GCD curves of S-CV series electrodes at fixed current density, (b-d) the GCD curves of S-CV series electrodes at different current densities from 1-5 A g⁻¹, (e) plot of Cs vs current density, and (f) plot of specific capacity vs current density.

The calculated Cs and specific capacity of S-CV series electrodes at distinct current densities are shown in Figure 4.11 (e, f). The maximum Cs of 793.5 F g⁻¹ (specific capacity 396.7 C g⁻¹) at 1 A g⁻¹ is obtained for the S-CV2 electrode and maintains Cs of 582.6 F g⁻¹ (291.3 C g⁻¹) at 5 A g⁻¹ current density, representing excellent capacitance retention even at a high current density. The S-CV1 and S-CV3 electrode exhibits maximum Cs of 586.4 F g⁻¹ (293.2 C g⁻¹) and 381.1 F g⁻¹

(190.5 C g⁻¹) at 1 A g⁻¹, respectively, which is relatively less than S-CV2 electrode. The maximum Cs obtained for the S-CV2 electrode is attributed to the maximum SSA of the S-CV2 electrode compared to the other S-CV1 and S-CV3 electrodes. The improved electrochemical performance of the S-CV2 thin film electrode is mainly ascribed to the mesoporous structure and maximum SSA; moreover, the synergy between cobalt and vanadium implies enhanced electrical conductivity and multifarious valences.

4.2.A.3.7.4 EIS and Stability Analysis

The S-CV series electrodes are further characterized using the EIS technique to understand better physicochemical mechanisms involved in electrochemical charge storage. The Nyquist plots of S-CV series electrodes are shown in Figure 4.12 (a), and the assessed minimum R_s , R_{ct} , and W values of 0.53 Ω , 1.23 Ω , and 5.265 Ω , respectively are observed for the S-CV2 electrode. The circuit-fitted values of S-CV series electrodes are depicted in Table 4.2. The vertical line has almost a phase angle of -90° in the low-frequency range, indicating the capacitive behaviour of the S-CV series electrodes, and little inclination suggests a small W caused by ion diffusion in the active material. Also, the R_s and R_{ct} values are associated with electrolyte and faradaic leakage current resistance. All the S-CV series electrodes indicate minute R_s and R_{ct} values, which is attributed to the binder-free synthesis of S-CV materials on conductive SS substrate by the SILAR method. Among all three S-CV series electrodes, the S-CV2 electrode exhibits less R_s and R_{ct} values owing to the elevated SSA with the mesoporous morphology, resulting in an enhanced electrochemical capacitive performance.

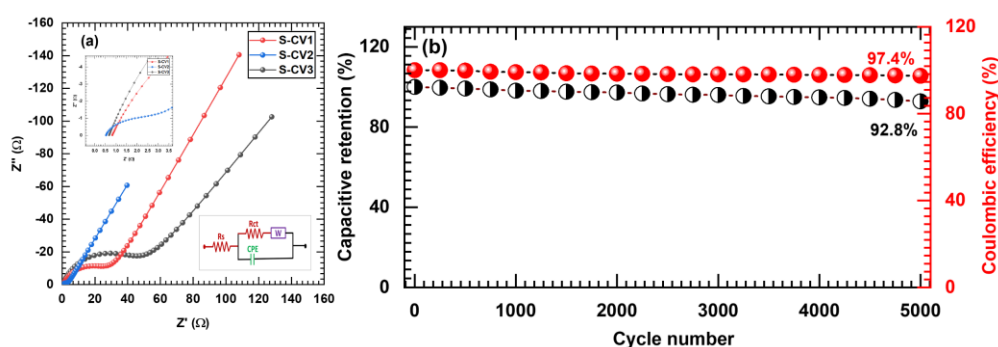


Figure 4.12 (a) Nyquist plots of S-CV series electrodes, and (b) cyclic stability of S-CV2 electrode.

Table 4.2 EIS circuit fitted values of S-CV series electrodes.

Parameters/Sample	S-CV1	S-CV2	S-CV3
R_s (Ω)	0.82	0.53	0.67
R_{ct} (Ω)	29.89	1.23	47.6
$W(\Omega)$	0.73	5.26	0.027
CPE (mF)	2.03	2.00	1.35
CPE (n)	0.77	0.83	0.80

Furthermore, the cycling stability performances of the S-CV2 electrode over 5000 charge-discharge cycles at 5 A g^{-1} were tested as presented in Figure 4.12 (b). After 5000 cycles, the S-CV2 electrode demonstrates 92.8% capacitive retention with 97.4% coulombic efficiency. So, the cyclic stability is higher, which is attributed to the facile interface with electrolyte owing to the high SSA and mesoporous nature. Moreover, the slightly decreased cyclic stability of the electrode may be linked to the little degradation of material and/or the formation of undesired intermediate or side products during intercalation and deintercalation [30].

4.2.A.4 Conclusions

In conclusion, the growth dynamics-based SILAR method productively synthesizes S-CV ($\text{Co}_3\text{V}_2\text{O}_8 \cdot n\text{H}_2\text{O}$) thin film electrodes having nanoparticles-like morphology with high SSA and mesoporous structure. The altered growth dynamics of S-CV series thin film electrodes result in a change in morphology, SSA, and porous structure, which ultimately influences the electrochemical performance of the electrodes. The as-prepared S-CV thin film electrodes at optimal (1:1) dip time variation exhibited elevated SSA with a mesoporous nature and enhanced intercalation-type pseudocapacitive performance with the highest Cs of 793 F g^{-1} at 1 A g^{-1} , owing to the maximum SSA of $74.3 \text{ m}^2 \text{ g}^{-1}$. In conclusion, SILAR is a feasible approach to produce binder-free, mesoporous, CVO thin film electrodes with tuned surface area and optimized SILAR conditions that can be used for strategic introduction of the rGO to make a binder-free CVO/rGO composite electrodes.

4.2.B Section-B: SILAR Synthesis of Cobalt Vanadium Oxide/Reduced Graphene Oxide Composite Electrodes and Characterizations for Supercapacitor Application

4.2.B.1 Introduction

SCs are categorized into EDLCs and pseudocapacitors based on their charge storage mechanism. Carbon derivatives are employed in the fabrication of EDLCs, while metal oxides and conducting polymers are utilized for pseudocapacitors [31]. Notably, pseudocapacitors exhibit higher Cs compared to EDLCs due to the rapid Faradaic reactions occurring at the electrode surface. Another advantageous aspect of pseudocapacitors is their cost-effectiveness [32]. Predominantly, commercial SCs heavily depend on carbonaceous materials, which exhibit low ED, limiting their applications [33].

Over the past decades, extensive research has been conducted to advance electrode materials and apply them in the fabrication of high-performance SCs. Various types of nanostructured electrode materials, including metal oxides, metal sulfides, polymers, CNTs, and GO, have been thoroughly investigated for SC design [34]. However, to further enhance performance in terms of ED, PD, and extended cyclic life, there is a current emphasis on developing hybrid nanostructured electrode materials. However, SCs produced with metal oxide-based nanostructures of this kind often face challenges such as low specific capacity and inadequate stability, attributed to issues like poor ionic conductivity and volume changes during charging/discharging [35]. To address these concerns, metal oxide nanoparticles are combined with diverse polymeric and carbon-based materials, including CNTs, CNFs, and GO. This approach proves beneficial in attaining superior electrochemical properties, such as improved Cs, ED/PD, and cyclic stability, owing to synergistic effects among their sub-components.

The SILAR method is a cost-effective and simple approach employed for the synthesis of various nanostructures. This method involves controlling parameters such as thickness, dipping time, pH, SILAR cycles, and precursor concentrations. In the current study, CVO/rGO materials were synthesized using the SILAR method. The research explores the impact of varying concentrations of

rGO on the physicochemical properties and their influence on supercapacitive performance. Simultaneously, pristine CVO and CVO/rGO composites were synthesized at different concentrations (0.1, 0.2, and 0.3 mg ml⁻¹) of rGO. An electrochemical study of CVO/rGO composite electrodes was conducted to compare with pristine CVO electrode and determine the most effective cathode electrode for SC device fabrication.

4.2.B.2 Experimental Details

4.2.B.2.1 Synthesis of Cobalt Vanadium Oxide/Reduced Graphene Oxide

For the synthesis of CVO/rGO composite thin films, initially, the rGO was synthesized by the chemical method, as discussed in Chapter 3, Section B, subsection 3.2.B.2.2. The SILAR method, known for its simplicity and cost-effectiveness, was employed for the deposition of CVO/rGO composite thin films at room temperature as illustrated schematically in Figure 4.13 (a).

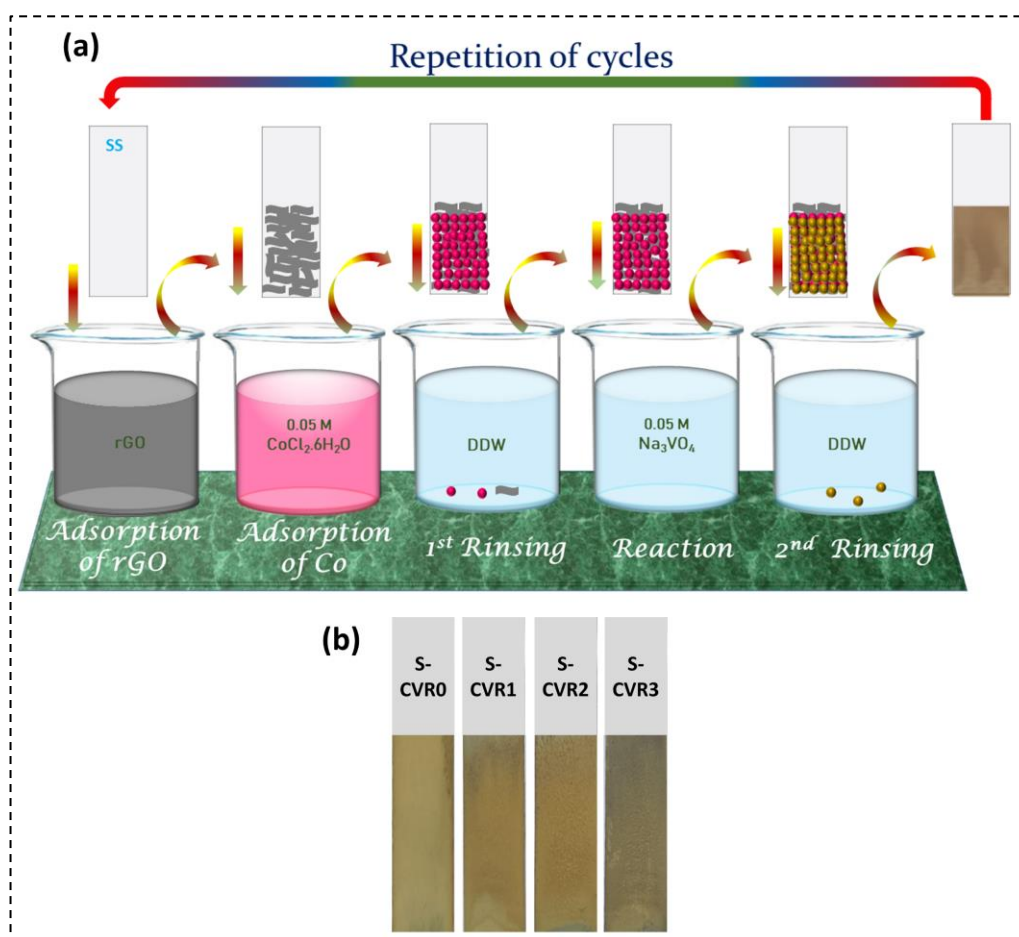
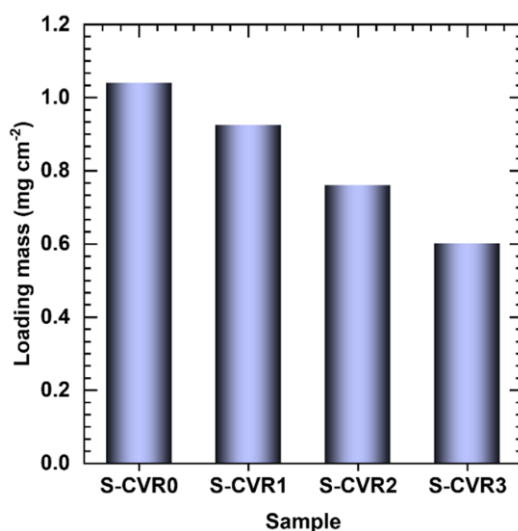


Figure 4.13 (a) Schematic representation of SILAR synthesis of CVO/rGO composite and (b) photographs of S-CVR series thin films.

Table 4.3 Preparative parameters for the synthesis of S-CVR series electrodes.

Sr. No.	Sample Name	rGO Concentration (mg ml ⁻¹)
1	S-CVR0	0
2	S-CVR1	0.1
3	S-CVR2	0.2
4	S-CVR3	0.3

As depicted in Figure 4.13 (a), the SILAR method was modified with a five-beaker system by introducing an additional beaker containing rGO suspension. Previous optimization efforts were determined and the adsorption time (5 s), first rinsing time (5 s), reaction time (5 s), and second rinsing time (5 s) for 150 cycles were kept constant, which produced well-adherent, uniform, and best performing supercapacitive thin films electrodes. Tryer to the growth of each successive layer of CVO, the substrate was dipped in an rGO suspension beaker (consisting of 0, 0.1, 0.2, and 0.3 mg ml⁻¹ concentrations) for 5 s.

**Figure 4.14** Bar diagram of loading mass on 1x1 cm² SS substrate.

The resulting CVO and CVO/rGO thin films were denoted as S-CVR0 and S-CVR1, S-CVR2, and S-CVR3, respectively, and photographs of S-CVR series thin films are illustrated in Figure 4.13 (b). The detailed SILAR synthesis parameters of S-CVR series thin films are depicted in Table 4.3. The mass loading over per

unit area was determined using the mass difference method, as depicted in Figure 4.14. It was observed that the mass loading over the substrate decreases with increasing concentration of rGO. Such decreasing in mass loading can be attributed to the distinct growth rate and lower density of rGO.

4.2.B.3 Results and Discussion

4.2.B.3.1 Reaction Mechanism and Growth of Cobalt Vanadium Oxide/Reduced Graphene Oxide Formation

The CVO/rGO material was synthesized using a SILAR method, a highly effective 'layer-by-layer' approach for the preparation of nanostructures. Various CVO/rGO composite materials, labeled as the S-CVR series (S-CVR1, S-CVR2, and S-CVR4) are synthesized to investigate the impact of varying rGO concentrations on pristine S-CVR0. In the initial step, Co^{2+} ions adsorb onto the surface of rGO through electrostatic interactions with its functional groups. After the first rinsing process, vanadate $(\text{VO}_4)^{2-}$ ions react in the anionic bath solution leading to the formation of CVO on the rGO, as described in the reaction (equation 4.3). Once this layer is established, the next SILAR cycle involves the deposition of another rGO layer on the pre-deposited CVO layer. This procedure of alternating CVO and rGO layer deposition is repeated for up to 150 SILAR cycles, as shown schematically in Figure 4.13 (a). The prepared S-CVR series electrodes were used for physicochemical analysis.

4.2.B.3.2 XRD Analysis

The XRD patterns of rGO, S-CVR series composite thin films with varying concentrations of rGO were examined and are presented in Figure 4.15. From Figure 4.15, it is observed that XRD patterns for the S-CVR series samples display three distinct peaks at similar positions in all samples confirming the formation of the $\text{Co}_3\text{V}_2\text{O}_8$ phase (JCPDS card no. 01-074-1486). In addition to CVO peaks, the broad peak observed in samples S-CVR1 to S-CVR3 at around $2\theta=25.2^\circ$ indicates the stacking of rGO sheets resulting from the removal of oxygen-containing groups [36]. Moreover, it signifies the formation of multilayered rGO nanosheets with a (002) plane. Furthermore, it is observed that the intensity of the (002) plane peak rises proportionally with an increase in the concentration of rGO. This

finding confirms the successful formation of the $\text{Co}_3\text{V}_2\text{O}_8/\text{rGO}$ composite on SS substrate.

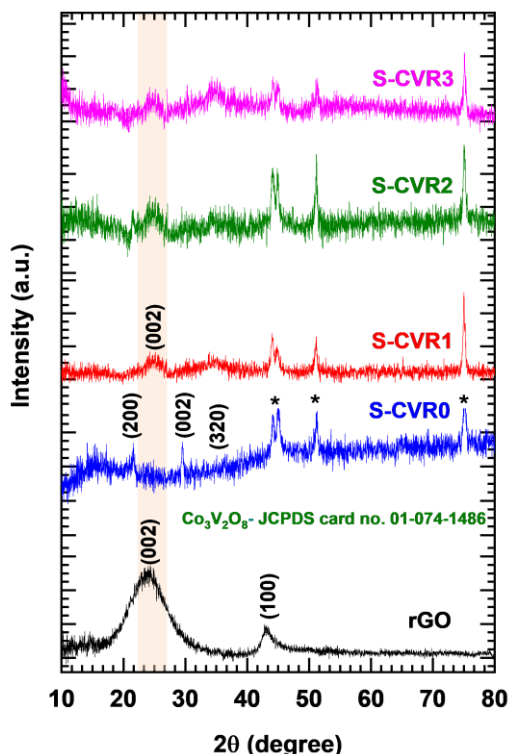


Figure 4.15 XRD patterns of rGO, S-CVR series samples.

4.2.B.3.3 FT-IR Analysis

FT-IR spectroscopy is a proficient technique for scrutinizing the establishment of molecular bonds within the synthesized S-CVR series composite material. The FT-IR spectra for all the materials in the S-CVR series displayed, spanning the 400 cm^{-1} to 4000 cm^{-1} wavenumber, as illustrated in Figure 4.16. In the S-CVR series samples, peaks at 422 cm^{-1} (γ_1) signify cobalt-oxygen stretching and a strong peak at 451 cm^{-1} is attributed to the out-of-plane vanadyl group stretching. Also, peaks observed at 776 , and 1073 cm^{-1} (γ_2) correspond to the in-plane V-O-V modes related to V-O [11]. Moreover, upon the addition of rGO into the CVO, the additional peak observed in the S-CVR1 to S-CVR3 samples is attributed to C-C bonds of the sp^2 features at 1642 cm^{-1} , which confirms the presence of rGO in the prepared material. Additionally, a peak with a shoulder at 1310 cm^{-1} is observed in S-CVR series samples, which is due to not only C-O stretching from impurities of TEA but also the carboxyl group present in rGO [12]. At 3400 cm^{-1} , the broad peak was observed in all S-CVR series samples, which is correspond to the presence of structural water in the sample [13]. As indicated by

the FT-IR results, the S-CVR series samples exhibit a hydrous nature, which can be beneficial for SCs.

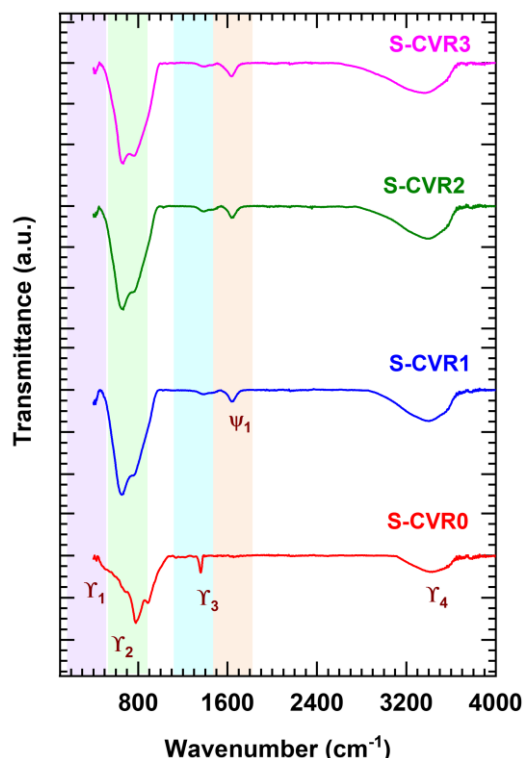


Figure 4.16 FT-IR spectra of S-CVR series samples.

4.2.B.3.4 Raman Analysis

The Raman spectra for rGO and the S-CVR series materials are presented in Figure 4.17. In the S-CVR series samples, absorption bands manifest at 334, 519, and 804 cm^{-1} associated with asymmetric stretching of V-O-Co, stretching of Co-O, and symmetric vibration of V-O, respectively. As the rGO concentration increases, the intensity of the CVO peaks reduces.

Moreover, calculated I_D/I_G ratios for rGO, S-CVR1, S-CVR2, and S-CVR3 are 1.01, 1.0, 1.04, and 1.08, respectively [38, 39], which indicates the reduction of functional groups and growth of CVO over the rGO nanosheets. In the higher frequency region of the Raman spectra, two additional bands, the 2D band, and the D+G band are observed [40]. As the rGO content in CVO increases, the intensity of the D and G bands becomes more pronounced, while the peaks of S-CV diminish. The rise in the I_D/I_G ratio, along with the presence of the CVO band in all S-CVR samples, confirmed the growth of CVO on rGO nanosheets and the indicating successive formation of the CVO/rGO composite in the S-CVR series.

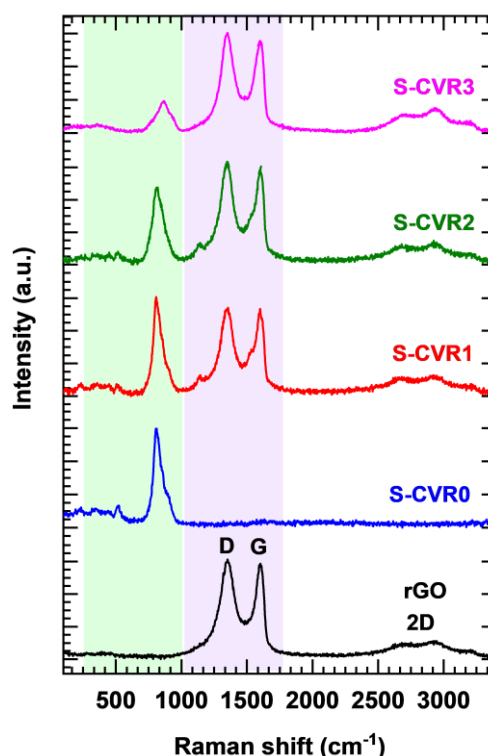


Figure 4.17 Raman spectra of rGO, S-CVR series samples.

4.2.B.3.5 XPS Analysis

The surface composition and chemical states of the samples were analyzed using XPS. The XPS survey spectrum for the pristine S-CVR0 and S-CVR2 samples, presented in Figure 4.18 (a), confirms the presence of Co, V, O, and C. A more detailed examination of the Co 2p spectra for both samples, shown in Figure 4.18 (b), reveals two distinct peaks for Co 2p_{1/2} and Co 2p_{3/2} at binding energies of 796.8 eV and 780.7 eV, respectively, in the S-CVR0 sample, with similar values observed across the S-CVR2 sample. Upon deconvolution, these peaks split into two distinct peaks, representing Co³⁺ at 780.4 eV and 796.4 eV, and Co²⁺ at 782 eV and 797.9 eV for both S-CVR0 and S-CVR2 samples. Notably, Co³⁺ peaks were more pronounced than Co²⁺ peaks. Satellite peaks were also observed at binding energies of 786.4 eV and 802.9 eV [14]. Similarly, the V 2p XPS spectra, displayed in Figure 4.18 (c), show two prominent peaks corresponding to V 2p_{3/2} at 516.5 eV and V 2p_{1/2} at 524 eV for both S-CVR0 and S-CVR2, indicating the presence of V⁵⁺ states. Additionally, a minor V⁵⁺ state was detected at 516.5 eV. The O 1s spectra, presented in Figure 4.18 (d), reveal three significant oxygen contributions, the peak at 529.9 eV (O₁) is associated with metal-oxygen bonds,

while the peaks at 531.4 eV (O_2) and 532.9 eV (O_3) correspond to oxygen in hydroxyl groups, indicative of structural water in the electrodes [7, 15, 16].

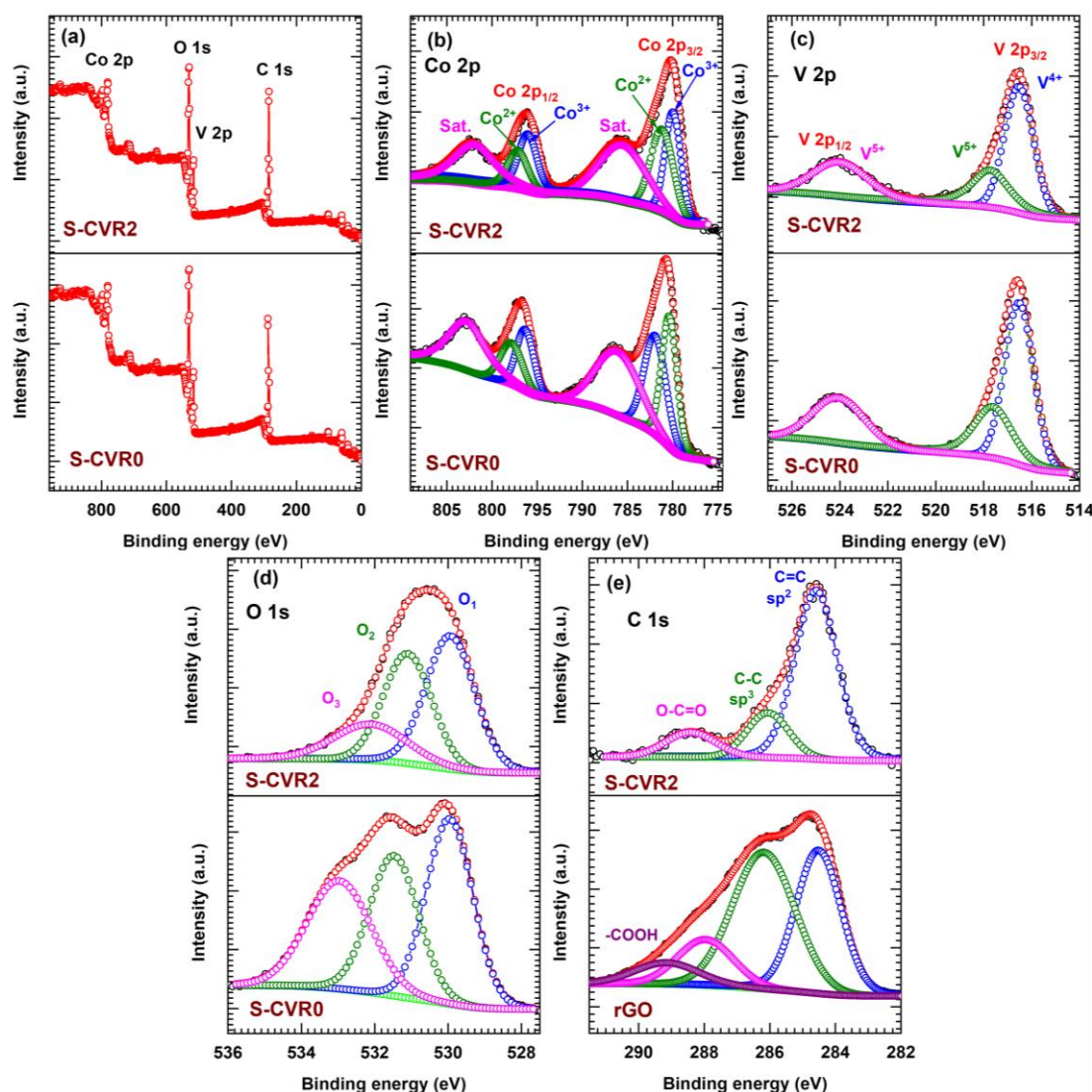


Figure 4.18 XPS spectra of pristine S-CVR0 and S-CVR2 samples and the corresponding (a) survey, (b) Co 2p, (c) V 2p, (d) O 1s, and (e) C 1s of the samples S-CVR2 and rGO.

In Figure 4.18 (e), the C 1s spectra for the rGO and S-CVR2 samples reveal four peaks in the rGO sample and three in S-CVR2. A prominent peak at 284.6 eV in the rGO sample indicates C=C bonding associated with sp^2 hybridization, while the peak at 286.08 eV, corresponding to sp^3 hybridized C-C bonds, shows reduced intensity, suggesting successful further reduction of rGO.

Additionally, functional groups like carboxylate (O-C=O) and carboxyl (-COOH) are observed at 288.3 eV and 289.0 eV, respectively, with the carboxyl

group being reduced in the S-CVR2 composite. The intensity of carbon peak related to carboxyl and carboxylate groups is reduced in sample S-CVR2 composite compared to the rGO sample [41, 42]. The XPS results confirm the prominent Co^{3+} and V^{4+} oxidation states, as well as the presence of functional groups, affirming the successful synthesis of the CVO/rGO composite material.

4.2.B.3.6 TG Analysis

The rGO content in the composites was determined by examining the residual masses obtained from TGA analysis of the S-CVR series composite materials. Figure 4.19 illustrates the weight loss curves and derivative weight changes for the composite synthesized via the SILAR method. The weight loss below 150 °C is attributed to the evaporation of adsorbed surface water owing to environmental moisture and interlayer water [43]. A gradual decline in weight almost 400 °C is attributed to the removal of labile oxygen-containing functional groups and structural water vapor from the S-CVR series, caused by the decomposition of these oxygenated groups [44].

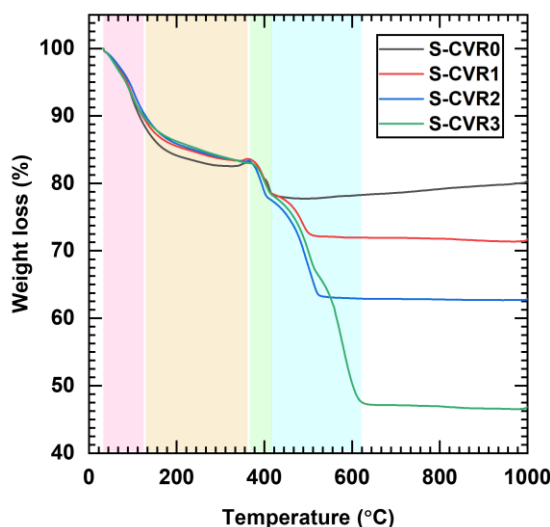


Figure 4.19 TGA plot of S-CVR series samples.

In the pristine S-CVR0 sample, the TGA curve is consistent after 400 °C, confirming stabilization of the $\text{Co}_3\text{V}_2\text{O}_8$ phase. However, substantial weight loss occurs in S-CVR1 to S-CVR3 after 400 to 600 °C, which is linked to the breakdown of rGO. The compositions of CVO and rGO are calculated from TGA data as follows; 90.2% CVO and 9.8% rGO in S-CVR1, 78.8% CVO and 21.2% rGO in S-CVR2, and 58.7% CVO and 41.3% rGO in S-CVR3. These findings confirm the successful

synthesis of CVO/rGO composites with different rGO content by increasing rGO concentrations.

4.2.B.3.7 FE-SEM and EDS Analysis

To investigate the surface morphology of S-CVR series thin films, the FE-SEM images at different magnifications are shown in Figure 4.20 (a1-d3). In Figure 4.20 (a1-a3), FE-SEM images reveal that the pristine S-CVR0 sample is composed of an agglomeration of nanoparticles, as discussed in section (4.2.A.3.5). Moreover, Figure 4.20 (b1-b3), (c1-c3), and (d1-d3) are displayed the FE-SEM images of S-CVR1, S-CVR2, and S-CVR3, respectively. When the CVO material is composite with rGO, the morphology transforms from agglomerated nanoparticles to a marigold-like structure, as shown in Figure 4.19 (b1-d3). As the concentration of rGO increases, the size of the marigold-like structure decreases, attributed to the incorporation of rGO nanosheets.

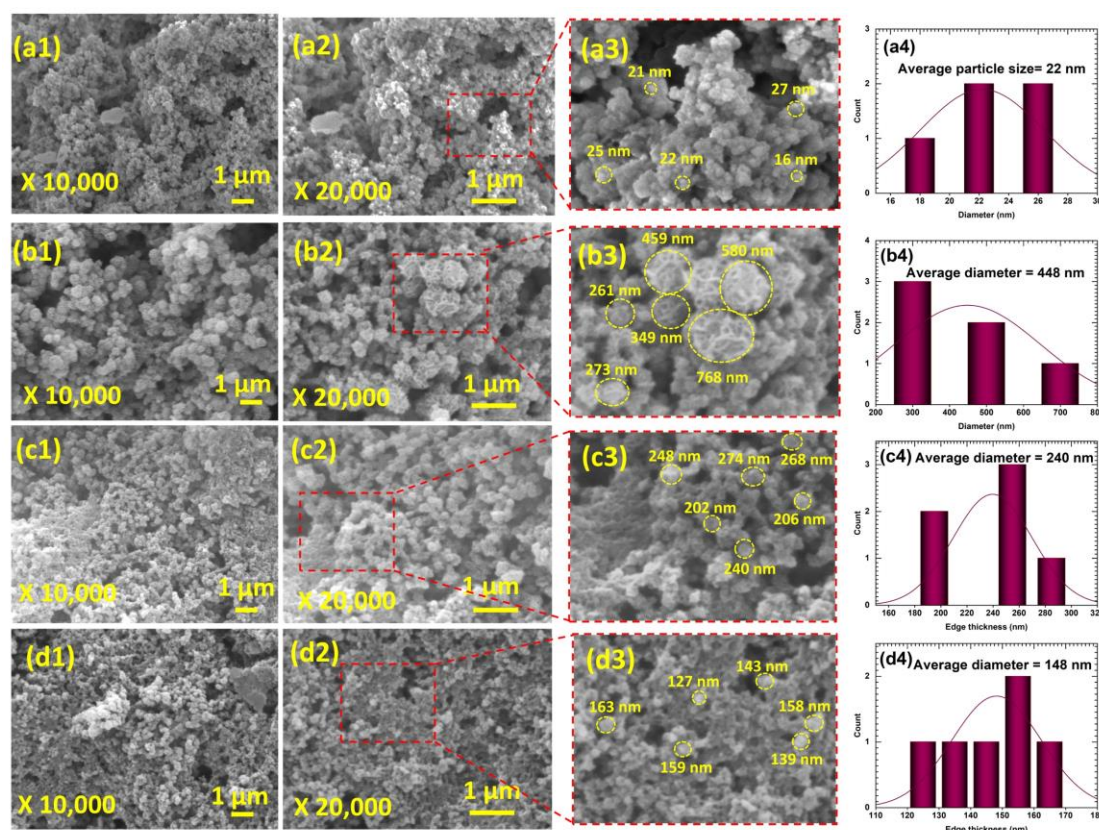


Figure 4.20 FE-SEM images and histograms of (a1-a4) S-CVR0, (b1-b4) S-CVR1, (c1-c4) S-CVR2, and (d1-d4) S-CVR3 thin films.

Figure 4.20 (a4-d4) depicts histograms illustrating the average size of particles and marigold-like particles in S-CVR series thin films. The observed average particle and marigold-like particle sizes for S-CVR0, S-CVR1, S-CVR2, and S-CVR3 are 22, 448, 240, and 148 nm, respectively. The transition from interconnected nanoparticle to marigold-like particle formation after the introduction of rGO highlights the complex interplay between material composition (CVO/rGO) and morphological features. Such change in morphology is accredited to the contribution of functional groups from rGO acting as nucleation sites in the growth mechanism, where distinct growth mechanisms formed marigold-like structures consisting of nanoflakes. These findings provide significant insights into enhancing electrode design for high-performing SCs.

The EDS micrographs of CVO/rGO display a uniform distribution of Co, V, O, and C elements throughout the entire micrograph area, as shown in the composite overlay image of all elements (Figure 4.21 (a1-c1)). Similar distribution patterns are observed in the elemental mapping of pristine S-CVR0 nanoparticles (section 4.2.A.3.5).

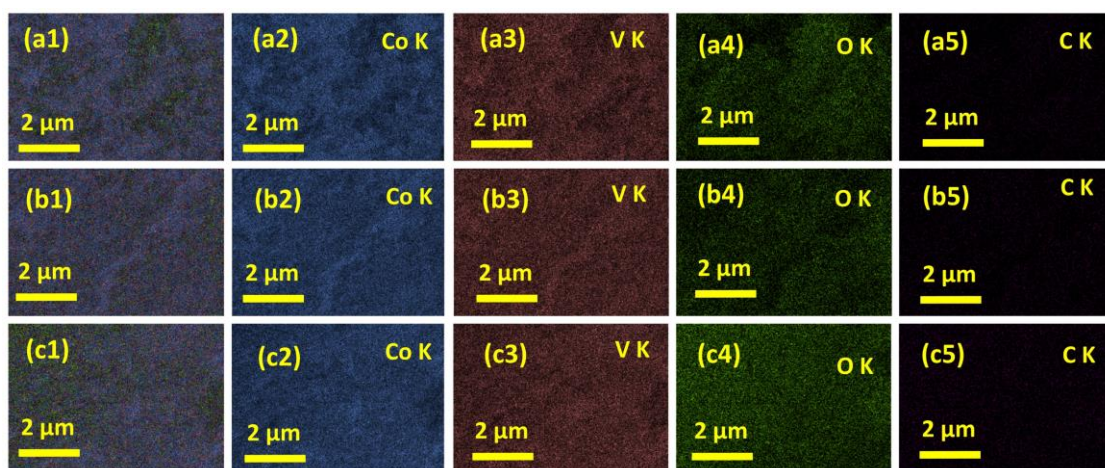


Figure 4.21 EDS mapping of CVO/rGO series samples.

The EDS spectra reveal that in CVO/rGO composites, the atomic percentage of various elements, including Co, V, O, and C, is illustrated in the inset of Figure 4.22. Consequently, the EDS spectra findings suggest that with an increasing concentration of rGO, the atomic percentage of C increases. Also, the EDS analysis confirmed the formation of the CVO/rGO composite material.

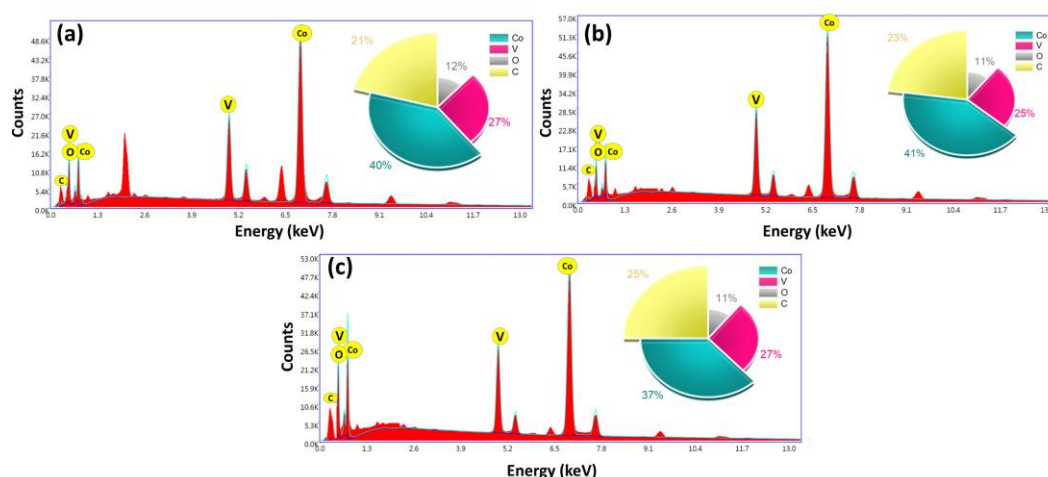


Figure 4.22 EDS spectra of CVO/rGO composite series samples.

4.2.B.3.8 HR-TEM and EDS Analysis

After conducting FE-SEM analysis of the S-CVR series samples, a high-resolution morphological study of the S-CVR2 sample was carried out using HR-TEM analysis. Figure 4.23 (a) illustrates the HR-TEM images of the S-CVR2 sample at various magnifications; an HR-TEM image showcasing the marigold-like particles with interconnected nanoflake-like structures. The HR-TEM image shows that the particles consisting of nanosheets of S-CVR2 are thoroughly grown on the surface of the rGO nanosheets, as displayed in Figure 4.23 (b). The composite of CVO/rGO forms a highly porous structure comprising 2D CVO nanoflakes over 2D nanosheets of rGO, enhancing the availability of ion diffusion pathways and expanding the effective contact area between the electrode and electrolyte [45, 46].

The determination of interplanar distance was carried out using line profiles with the lattice fringes depicted in Figure 4.23 (e). The measured lattice distance of 0.30 nm validates the presence of the (002) crystalline plane within CVO. The lattice patterns observed in S-CVR2, as depicted in Figure 4.23 (f), indicate a nanocrystalline structure of $\text{Co}_3\text{V}_2\text{O}_8 \cdot n\text{H}_2\text{O}$ characterized by circular rings corresponding to planes (200), (002), and (320) in the SAED pattern. Additionally, Figure 4.23 (g-k) showcases the EDS mapping in HR-TEM of the S-CVR2 material. The CVO/rGO composite structure's development is validated by the uniform distribution of Co, V, O, and C. The HR-TEM images, SAED pattern, and EDS mapping affirm the formation of $\text{Co}_3\text{V}_2\text{O}_8 \cdot n\text{H}_2\text{O}/\text{rGO}$ composite in the S-

CVR2 sample and the morphology of 2D nanoflakes grown over 2D nanosheets, can provide improved electrochemical performance.

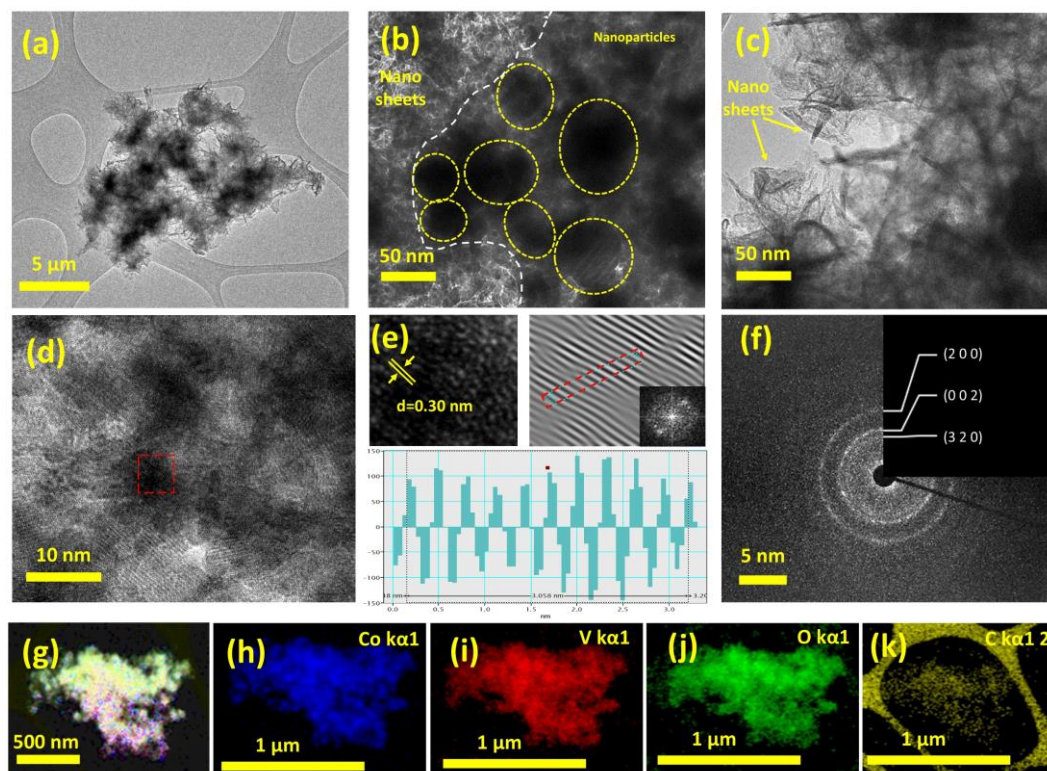


Figure 4.23 (a-d) HR-TEM images of S-CVR2 sample, (e) HR-TEM lattice fringes with line profile showing (002) hkl plane of CVO/rGO composite material, (f) SAED pattern, and (g-k) Co, V, O, and C elemental mapping of S-CVR2.

4.2.B.3.9 BET and BJH Analysis

The BET technique was utilized to evaluate the SSAs of the S-CVR series samples to do a more thorough investigation of the porous structure. The BET analysis revealed the type-III isotherm profile which can be seen in Figure 4.24 (a-d), which shows the measured adsorption-desorption isotherms for S-CVR series samples. The obtained isotherms showed type-III isotherm with H3 type hysteresis loop and the SSA values for the S-CVR0, S-CVR1, S-CVR2, and S-CVR3 samples are 74, 118, 208, and 70.2 m² g⁻¹, respectively. It is observed that there is a significant change in the SSA as the concentration of rGO in the material increases. The SSA increases up to sample S-CVR2 but decreases for sample S-CVR3 due to the aggregation of rGO nanosheets at higher concentrations.

Additionally, the pore-size distribution curves of the S-CVR series samples were obtained using the BJH technique and exhibited a narrowing trend,

signifying the homogenization of the particles (inset of Figure 4.24). The obtained average pore diameters of S-CVR0, S-CVR1, S-CVR2, and S-CVR3 samples are 9, 8, 7.3, and 8.7 nm, respectively, and confirm the mesoporous nature of the S-CVR series samples. The findings suggest that the variations in rGO concentration led to distinct growth kinetics, impacting the resulting SSA and porous structure than the pristine S-CVR0 sample.

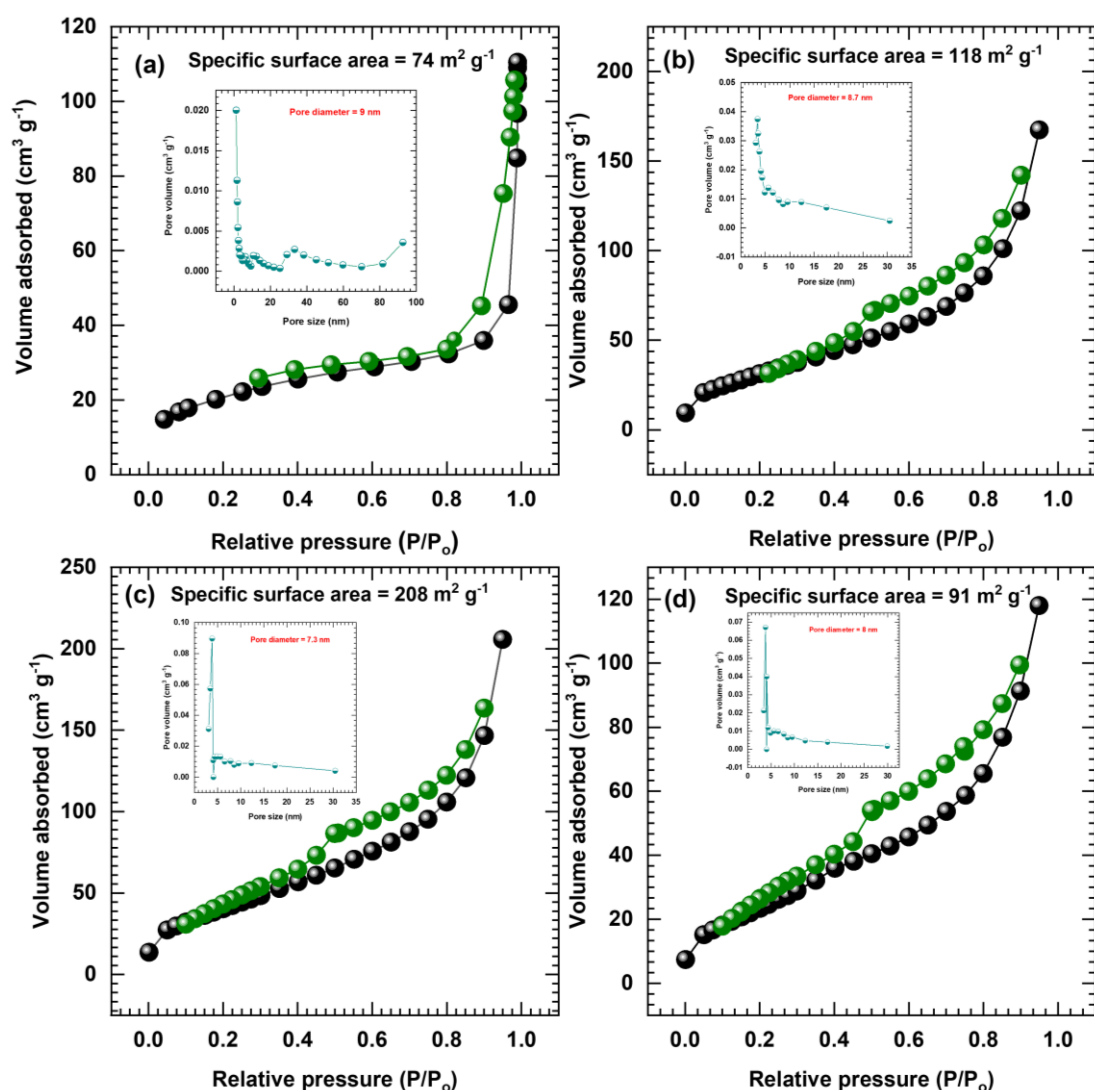


Figure 4.24 Adsorption-desorption isotherms and inset BJH plots of (a) S-CVR0, (b) S-CVR1, (c) S-CVR2, and (d) S-CVR3 samples.

An improved SSA and mesoporous structure provides a more electrochemically active surface and facilitate an efficient path for ion transportation within the material, respectively. The electrochemical capacitive

performance of the material is enhanced, as capacitance is directly dependent on the SSA of the electrode materials [47].

4.2.B.3.10 Electrochemical Analysis

In S-CVR series thin film electrodes, the physicochemical properties are altered by rGO concentration variation, and its impact on supercapacitive performance was analyzed through electrochemical characterization by forming a three-electrode system. The same three-electrode system is referred to as discussed in section (3.2.A.3.7.1). Among them, the S-CVR series of electrodes serves as the working electrode.

4.2.B.3.10.1 CV Analysis

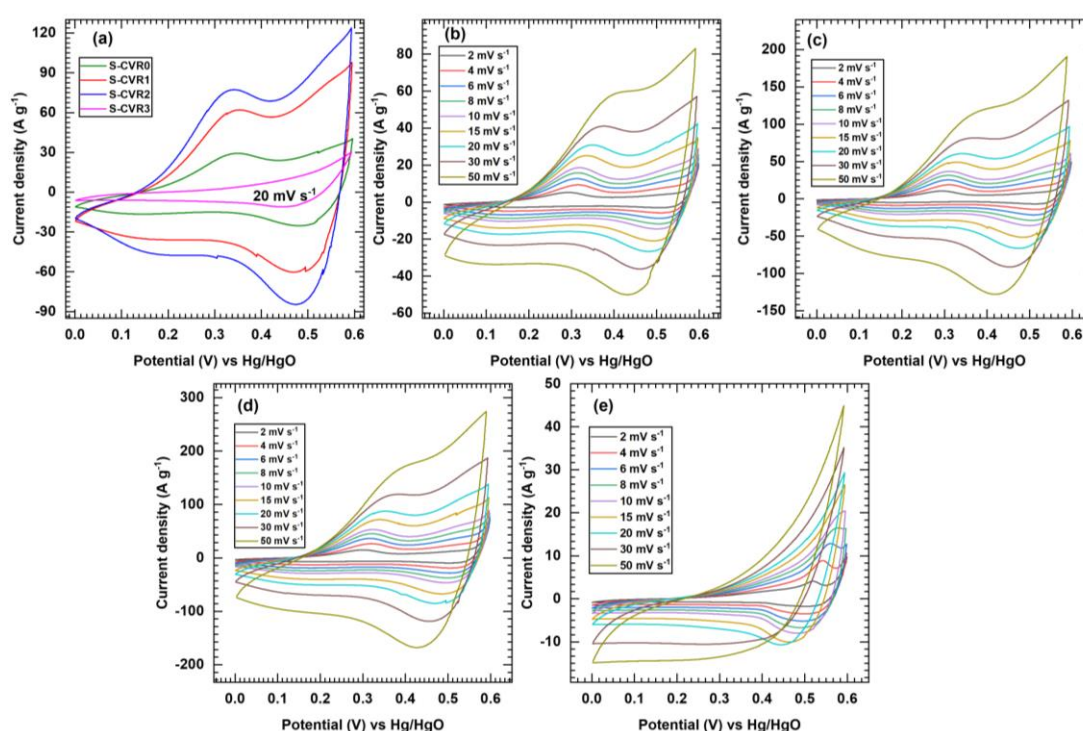


Figure 4.25 (a) At 20 mV s^{-1} scan rate comparative CV curves of S-CVR series electrodes, (b-e) CV curves of S-CVR0, S-CVR1, S-CVR2, and S-CVR3 electrodes at different scan rates ($2\text{--}50 \text{ mV s}^{-1}$).

Figure 4.25 (a) presents the correlated CV curves for the S-CVR0, S-CVR1, S-CVR2, and S-CVR3 electrodes, conducted at a constant scan rate of 20 mV s^{-1} within the potential range of $0\text{--}0.6 \text{ V/Hg/HgO}$. During charging, OH^- ions intercalate into the S-CV, while during discharging, electrolyte ions deintercalate, as per equation 4.4 (Subsection 4.2.A.3.7.2). The CV curves of the S-CVR series

electrodes at different scan rates of 2 to 50 mV s^{-1} are displayed in Figure 4.25 (b-e). Furthermore, the total area under the CV curve of the S-CVR2 electrode surpasses that of the S-CVR0, S-CVR1, and S-CVR3 electrodes, indicating that the S-CVR2 electrode possesses the highest charge storage capacity. This enhanced capacity can be attributed to the mesoporous structure and elevated SSA of the S-CVR2 electrode, facilitating the easy penetration of electrolyte ions into the electrode's interior and providing a maximized area for charge storage.

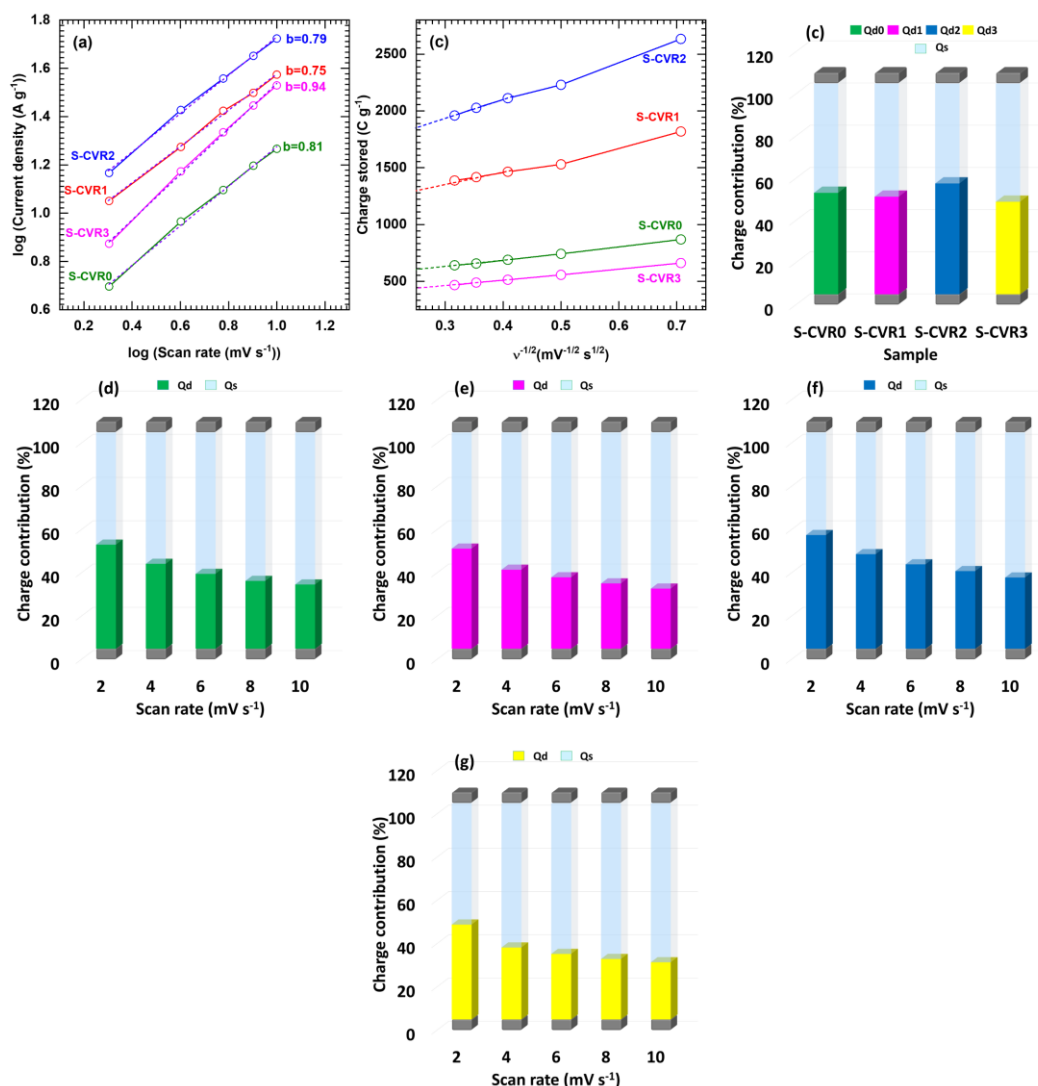


Figure 4.26 (a) Plot of log (current density, A g^{-1}) versus log (scan rate, mV s^{-1}) for S-CVR series electrodes, (b) the plot of total charge against the reciprocal of the square root of potential scan rate for S-CVR series electrodes, (c) comparative plot of surface and diffusive charge contribution at fixed scan rate (S-CVR series), and (d-g) plots of surface and diffusive charge contribution of S-CVR series at different scan rate.

Moreover, to explicitly unveil the charge storage mechanism of the S-CVR series electrodes, investigating their electrochemical kinetics is crucial. The relationship between ' v ' and peak current ' i ' in the CV area under the loop adheres to the 'Power's law' (equation no. 3.6). The ' b ' values of the S-CVR0, S-CVR1, S-CVR2, and S-CVR3 are 0.81, 0.75, 0.79, and 0.94, respectively, as depicted in Figure 4.26 (a). The ' b ' values of the S-CVR series electrodes suggest the electrode's overall charge storage capacity. The correlation between the Q_{total} and the $v^{-1/2}$ is depicted in Figure 4.26 (b), it enables the determination of the capacitive contribution (Q_s) through the intercept of the plot.

The determination of both Q_s and Q_d is based on the collected comparative data from the S-CVR series electrodes at a constant scan rate of 2 mV s^{-1} , as illustrated in Figure 4.26 (c). Additionally, the charge contributions in the respective electrodes of the S-CVR series at different scan rates are illustrated in Figure 4.26 (d-g). The results indicate that the Q_d value of the S-CVR2 electrode is higher than the other electrodes, however, higher Q_s were obtained for the S-CVR3 electrode owing to the high content of rGO.

4.2.B.3.10.2 GCD Analysis

The profiles of GCD were examined and interpreted to assess the charge storage capacity of the thin film electrode materials in the S-CVR series. Figure 4.27 (a) displays comparative GCD plots for all S-CVR series electrodes at a consistent current density of 1 A g^{-1} , revealing intercalative pseudocapacitive behavior. Notably, S-CVR2 exhibits a maximum discharge time compared to the other electrodes. Additionally, Figure 4.27 (b-e) illustrates the GCD plots for the S-CVR series electrode at different current densities ranging from 1 to 5 A g^{-1} . At a fixed current density of 1 A g^{-1} , the respective C_s (capacity) values for the S-CVR0, S-CVR1, S-CVR2, and S-CVR3 electrodes were determined to be 793 F g^{-1} (396.7 C g^{-1}), 1693.3 F g^{-1} (846.6 C g^{-1}), 2346.3 F g^{-1} (1173.1 C g^{-1}), and 583 F g^{-1} (291.5 C g^{-1}), as depicted in Figure 4.27 (f, g). In summary, the S-CVR2 electrode's elevated SSA enables convenient access for electrolyte ions, resulting in superior capacitive performance (~ 2.5 times) compared to the pristine S-CVR0 and other electrodes in the S-CVR series.

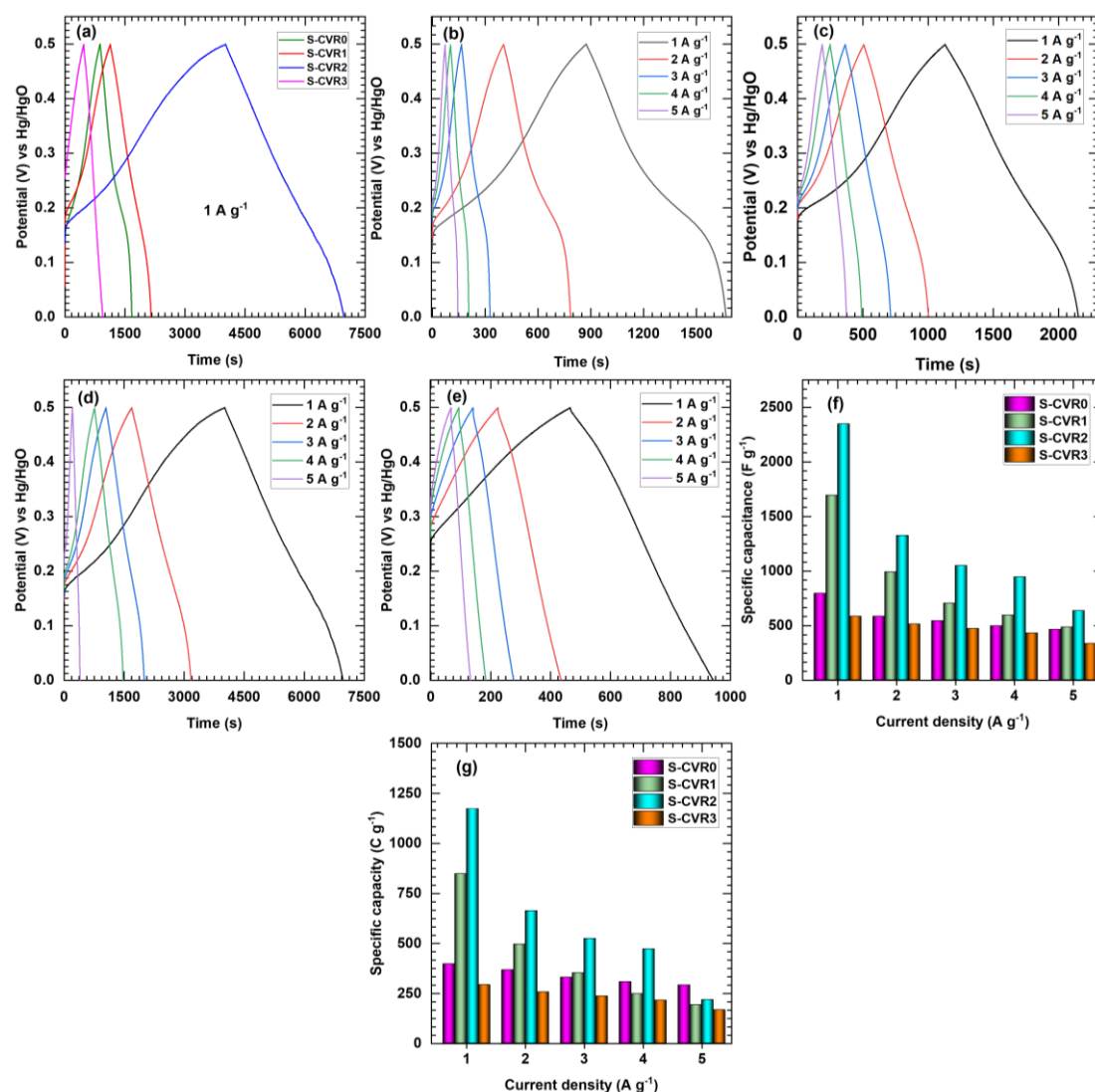


Figure 4.27 (a) The comparative GCD curves of S-CVR series electrodes at fixed current density (1 A g^{-1}), (b-e) the GCD curves of S-CVR0, S-CVR1, S-CVR2, and S-CVR3 electrodes at different current densities from 1 to 5 A g^{-1} , (f) bar diagram of Cs vs current density, and (g) bar diagram of specific capacity vs current density.

4.2.B.3.10.3 EIS and Stability Analysis

An exploration of the electrochemical charge transfer kinetics of S-CVR series electrodes was conducted through EIS analysis frequency range spanning from 10 MHz to 0.1 MHz . The characteristic Nyquist plots for S-CVR samples are presented in Figure 4.28 (a). Additionally, in contrast to S-CVR0 (1.23Ω), S-CVR1 (0.12Ω), S-CVR2 (0.10Ω), and S-CVR3 (0.22Ω), the S-CVR2 electrode exhibits a significantly lower R_{ct} of 0.10Ω , indicating its favorable electrochemical conductivity. Other circuit-fitted values are depicted in Table 4.4. In contrast to

the other electrodes within the S-CVR series, the S-CVR2 electrode displays superior performance, owing to reduced R_s , R_{ct} , and W values.

This observation implies that the close interaction of the marigold-like particles of CVO with the 2D rGO nanosheets in sample S-CVR2 electrode facilitates convenient pathways for charge transfer, contributing to its enhanced electrochemical performance.

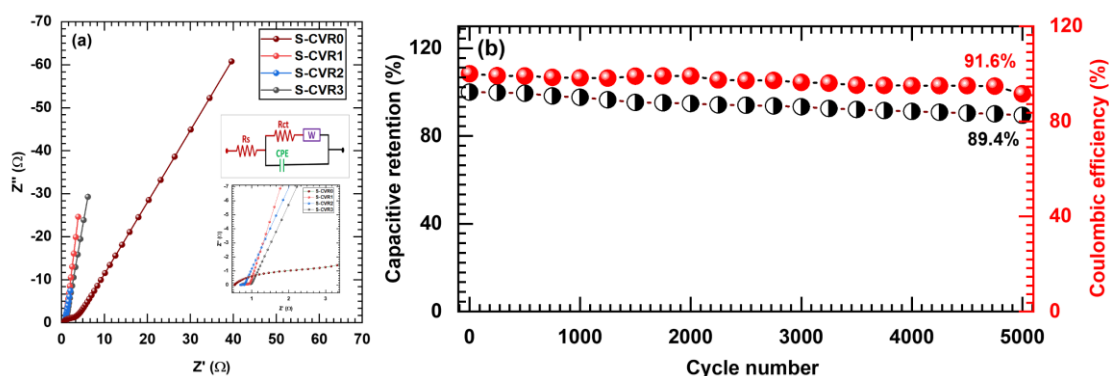


Figure 4.28 (a) Nyquist plot of S-CVR series electrodes, and (b) cyclic stability of S-CVR2 electrode.

Table 4.4 EIS circuit fitted values of S-CVR series electrodes.

Parameters/Samples	S-CVR0	S-CVR1	S-CVR2	S-CVR3
R_s (Ω)	0.53	0.72	0.68	0.70
R_{ct} (Ω)	1.23	0.12	0.10	0.22
$W(\Omega)$	5.26	0.30	0.035	0.20
CPE (mF)	2.00	3.00	8.00	5.00
CPE (n)	0.83	0.90	0.84	0.93

The enduring cycling performance of the S-CVR2 electrode was assessed by subjecting it to repeated 5000 GCD cycles test at a consistent current density of 5 A g^{-1} , as illustrated in Figure 4.28 (b). The results reveal impressive cycling stability, with the electrode retaining 89.4% of its initial capacitance with 91.6% coulombic efficiency even after undergoing 5000 GCD cycles.

4.2.B.4 Conclusions

In conclusion, CVO/rGO composite electrodes were successfully synthesized using the SILAR method, adding different concentrations of rGO. XRD

analysis confirmed the nanocrystalline structure of the $\text{Co}_3\text{V}_2\text{O}_8 \cdot n\text{H}_2\text{O}/\text{rGO}$ composites. Additionally, the formation of the CVO/rGO composites was verified through FT-IR, Raman, EDS, and XPS, which revealed the presence of Co, V, O, and C and their respective bonds in the S-CVR series samples. Moreover, TG analysis confirms the incorporation of 9.8, 21.2, and 41.3% rGO in the S-CVR1, S-CVR2, and S-CVR3 samples, respectively, and which attains the maximum SSA of $208 \text{ m}^2 \text{ g}^{-1}$ for sample S-CVR2. The S-CVR series electrodes were tested for their supercapacitive properties, with the S-CVR2 electrode showing superior performance compared to the other electrodes, particularly the pristine S-CVR0, due to enhanced conductivity from the increased rGO content in the CVO. The optimized S-CVR2 exhibited a substantial C_s (specific capacity) of 2346.3 F g^{-1} (1173.1 C g^{-1}) at 1 A g^{-1} , notable cyclic stability, retaining 89.4% of its initial value after 5000 cycles, along with low R_s and R_{ct} values. These results indicate that the CVO/rGO composite electrodes outperform their pristine counterparts, with the optimal 21.2% rGO content improving conductivity and facilitating electron transfer pathways without hindering the active material.

4.3 References

- [1] X. Wang, Y. Zhang, J. Zheng, X. Liu, C. Meng, *J. Colloid Interface Sci.*, 554, (2019), 191-201.
- [2] Y. Zhang, X. Jing, Y. Cheng, T. Hu, C. Meng, *Inorg. Chem. Front.*, 5, (2018), 2798-2810.
- [3] P. Shinde and S. Jun, *ChemSusChem*, 13, (2020), 11-38.
- [4] J. Yan, Q. Wang, T. Wei, Z. Fan, *Adv. Energy Mater.*, 4, (2014), 1300816, 1-43.
- [5] S. Huang, X. Zhu, S. Sarkar, Y. Zhao, *APL Mater.*, 7, (2019), 100901, 1-9.
- [6] W. Low, P. Khiew, S. Lim, C. Siong, E. Ezeigwe, *J. Alloys Compd.*, 775, (2019), 1324-1356.
- [7] S. Marje, P. Deshmukh, J. Gunjekar, C. Lokhande, U. Patil, *Energy fuels*, 35, (2021), 14110-14121.
- [8] H. Wang, H. Zhang, D. Zhang, J. Chen, S. Zhang, S. Zhang, J. Yu, Q. Wu, Q. Li, *ACS Appl. Mater. Interfaces*, 14, (2022), 8106-8114.
- [9] K. Le, Me. Gao, D. Xu, Z. Wang, G. Wang, G. Lu, W. Liu, F. Wang, J. Liu, *Inorg. Chem. Front.*, 7, (2020), 3646-3656.
- [10] W. Lv, C. Yang, G. Meng, R. Zhao, A. Han, R. Wang, J. Liu, *Sci. Rep.*, 9, (2019), 10831, 1-8.
- [11] G. Barbosa, C. Graeff, H. Oliveira, *Ecl. Quím.*, 30, (2005), 7-15.
- [12] D. Malavekar, V. Lokhande, V. Mane, S. Kale, R. Bulakhe, U. Patil, I. In, C. Lokhande, *J. Solid State Electrochem.*, 24, (2020), 2963-2974.
- [13] C. Zeinalipour-Yazdi and E. Loizidou, *Chem. Phys.*, 550, (2021), 111295.
- [14] P. Katkar, S. Marje, S. Pujari, S. Khalate, A. Lokhande, U. Patil, *Langmuir*, 37, (2021), 5260-5274.
- [15] D. Chao, X. Xia, J. Liu, Z. Fan, C. Ng, J. Lin, H. Zhang, Z. Shen, H. Fan, *Adv Mater.*, 26, (2014), 5794-5800.
- [16] H. Chen, D. Yang, X. Zhuang, D. Chen, W. Liu, Q. Zhang, H. Hng, X. Rui, Q. Yan, S. Huang, *Nano Res.*, 13, (2020), 1867-1874.
- [17] M. Aghazadeh, I. Karimzadeh, M. Ganjali, *J. Mater. Sci. Mater. Electron.*, 47, (2018), 3026-3036.
- [18] X. Dong, Y. Yang, B. Wang, Y. Cao, N. Wang, P. Li, Y. Wang, Y. Xia, *Adv. Sci.*, 7, (2020), 2000196, 1-8.
- [19] J. William, I. Babu, G. Muralidharan, *J. Chem. Eng.*, 422, (2021), 130058, 1-15.
- [20] C. Li, D. Ma, Q. Zhu, *Nanomater.*, 12, (2022), 848.

-
- [21] S. Luo, J. Li, J. Lu, F. Tao, J. Wan, B. Zhang, X. Zhou, C. Hu, *Mater. Today Phys.*, 17, (2021), 100337, 1-11.
- [22] L. Chen, Z. Yang, J. Wu, H. Chen, J. Meng, *Electrochim. Acta*, 330, (2020), 135347.
- [23] S. Pujari, S. Kadam, Y. Ma, Jadhav, S. Kumbhar, S. Bhosale, J. Gunjekar, C. Lokhande, U. Patil, *J. Energy Storage*, 22, (2022), 52105037, 1-15.
- [24] C. Huang, J. Zhang, N. Young, H. Snaith, P. Grant, *Sci. Rep.*, 6, (2016), 25684.
- [25] J. Kim, V. Augustyn, B. Dunn, *Adv. Energy Mater.*, 2, (2012), 141-148.
- [26] G. Muller, J. Cook, H. Kim, S. Tolbert, B. Dunn, *Nano Lett.*, 15, (2015), 1911-1917.
- [27] S. Marje, V. Patil, V. Parale, H. Park, P. Shinde, J. Gunjekar, C. Lokhande, U. Patil, *Chem. Eng. J.*, 429, (2022), 132184.
- [28] V. Augustyn, J. Come, M. Lowe, J. Kim, P. Taberna, S. Tolbert, H. Abruña, P. Simon, B. Dunn, *Nat. Mater.*, 12, (2013), 518-522.
- [29] G. Raju, E. Pavitra, G. Nagaraju, S. Sekhar, S. Ghoreishian, C. Kwak, J. Yu, Y. Huh, Y. Han, *J. Mater. Chem. A*, 6, (2018), 13178-13190.
- [30] Y. Gono, Y. Kimura, K. Yashiro, S. Watanabe, S. Hashimoto, T. Kawada, *J. Electrochem. Soc.*, 161, (2014), 11.
- [31] A. Tundwal, H. Kumar, B. Binoj, R. Sharma, G. Kumar, R. Kumari, A. Dhayal, A. Yadav, D. Singh, P. Kumar, *RSC Adv.*, 14, (2024), 9406-9439.
- [32] S. Balasubramaniam, A. Mohanty, S. Balasingam, S. Kim, A. Ramadoss, *Nano-Micro Lett.*, 12, (2020), 85.
- [33] R. Yadlapalli, R. Alla, R. Kandipati, A. Kotapati, *J. Energy Storage*, 49, (2022), 104194.
- [34] Z. Zhai, L. Zhang, T. Du, B. Ren, Y. Xu, S. Wang, J. Miao, Z. Liu, *Mater. Des.*, 221, (2022), 111017.
- [35] T. Wang, H. Chen, F. Yu, X. Zhao, H. Wang, *Energy Storage Mater.*, 16, (2019), 545-573.
- [36] M. Edokali, R. Bocking, M. Mehrabi, A. Massey, D. Harbottle, R. Menzel, A. Hassanpour, *Chem. Eng. Res. Des.*, 199, (2023), 659-675.
- [37] F. Yin, S. Wu, Y. Wang, L. Wu, P. Yuan, X. Wang, *J. Solid State Chem.*, 237, (2016), 57-63.
- [38] A. Bakour, M. Baitoul, O. Bajjou, F. Massuyeau, E. Faulques, *Mater. Res. Express*, 4, (2017), 025031.
- [39] S. Muhamma, R. Ritikos, T. Whitcher, N. Razib, D. Bien, N. Chanlek, *Sensor Actuator B Chem.*, 193, (2014), 692-700.
- [40] B. Ma, R. Rodriguez, A. Ruban, S. Pavlov, E. Sheremet, *Phys. Chem. Chem. Phys.*, 21, (2019), 10125-10134.
- [41] M. Biesinger, *Appl. Surf. Sci.*, 597, (2022), 153681.
- [42] X. Chen, X. Wang, D. Fang, *Fuller. Nanotub. Carbon.*, 28, (2020), 1048-1058.
- [43] Y. Liu, H. Hsi, K. Li, C. Hou, *ACS Sustain. Chem. Eng.*, 4, (2016), 4762-4770.
- [44] M. Zong, Y. Huang, N. Zhang, H. Wu, *J. Alloys Compd.*, 644, (2015), 491-501.
- [45] Z. Zhao, X. Teng, Q. Xiong, H. Chi, Y. Yuan, H. Qin, Z. Ji, *Sustain. Mater. Technol.*, 29, (2021), e00313.
- [46] K. Li, B. Zhao, J. Bai, H. Ma, Z. Fang, X. Zhu, Y. Sun, *Small*, 16, (2020), 2001974.
- [47] S. Rajagopal, R. Vallikkattil, M. Ibrahim, D. Velez, *Condens. Matter*, 7, (2022), 6.

CHAPTER-5

Fabrication of Hybrid Supercapacitor Devices and Performance Evaluation

CHAPTER-5

Fabrication of Hybrid Supercapacitor Devices and Performance Evaluation

Sr. No.	Title		Page No.
5.1	Introduction		159
5.2	Fabrication of Hybrid Supercapacitor Devices and Performance Evaluation		159
	5.2.A	Section-A: Fabrication of Aqueous and Solid-State Hybrid Supercapacitor Devices: Utilizing C-CVR3 electrode prepared by CBS Method	
	5.2.A.1	Experimental Details	160
		5.2.A.1.1 Electrode Preparation	160
		5.2.A.1.2 Fabrication of Aqueous Hybrid Supercapacitor Device	160
	5.2.A.2	Results and Discussion	161
		5.2.A.2.1 Electrochemical Performance Evaluation of C-CVR3//KOH//rGO (C-AHSD)	161
		5.2.A.2.1.1 CV Analysis	161
		5.2.A.2.1.2 GCD Analysis	163
		5.2.A.2.1.3 EIS and Stability Analysis	164
		5.2.A.2.2 Fabrication and Electrochemical Performance Evaluation of C-CVR3//PVA-KOH//rGO (C-SHSD)	165
		5.2.A.2.2.1 CV Analysis	166
		5.2.A.2.2.2 GCD Analysis	166
		5.2.A.2.2.3 EIS and Stability Analysis	168
		5.2.A.2.2.4 Practical Demonstration of C-SHSD	168
	5.2.B	Section-B: Fabrication of Aqueous and Solid-State Hybrid Supercapacitor Devices: Utilizing S-CVR2 electrode prepared by SILAR Method	
	5.2.B.1	Experimental Details	170
		5.2.B.1.1 Electrode Preparation	170
	5.2.B.2	Results and Discussion	170
		5.2.B.2.1 Fabrication of S-CVR2//KOH//rGO (S-AHSD)	170
		5.2.B.2.2 Electrochemical Performance Evaluation of S-AHSD	170

			5.2.B.2.2.1	CV Analysis	170
			5.2.B.2.2.2	GCD Analysis	171
			5.2.B.2.2.3	EIS and Stability Analysis	172
		5.2.B.2.3	Fabrication and Electrochemical Performance Evaluation of S- CVR2///PVA-KOH//rGO (S-SHSD)		173
			5.2.B.2.3.1	CV Analysis	173
			5.2.B.2.3.2	GCD Analysis	174
			5.2.B.2.3.3	EIS and Stability Analysis	174
			5.2.B.2.3.4	Practical Demonstration of S-SHSD	175
5.3	Conclusions				176
5.4	References				176

5.1 Introduction

SCs, alternatively referred to as electrochemical capacitors, play a crucial role in connecting the functionalities of batteries and traditional capacitors. Their extensive adoption in various domains is attributed to their notable attributes, including high PD, prolonged lifespan, adaptability to a broad spectrum of temperatures, and eco-friendly operations [1-3]. Despite these advantages, the primary obstacle facing SCs in broadening their applications is the need to enhance ED. Enhancing ED is achievable through the implementation of an HSC, wherein two distinct electrode materials and aqueous electrolytes are employed [4]. This configuration proves effective in broadening the voltage window of the cell, consequently leading to a more substantial increase in ED as per the equation $E = 0.5 \cdot CV^2$ [5, 6]. Consequently, the investigation of state-of-the-art HSC, exhibiting favorable electrochemical properties to meet market requirements, has recently emerged as a prominent research focus.

In recent times, there has been a growing fascination with HSCs, comprised of two distinct electrode types featuring dissimilar active materials [7]. This configuration has garnered considerable attention due to its potential to provide dual benefits of elevated specific capacity and an expansive operational voltage range, which results in a notable improvement in ED [4]. The effectiveness of an HSC is intricately linked to the characteristics of the electrode materials. Thus, it is imperative to innovate and fabricate sophisticated electrode materials to augment the electrochemical performance of HSCs.

Nonetheless, the SCs may fall short in delivering satisfactory ED/PD or efficiencies and encounter a substantial reduction in Cs under high current conditions. As a result, there is a notable emphasis on enhancing the Cs of SCs, particularly their performance at elevated current densities. Being pursued through the metal oxide composite with carbon-based materials like rGO designed to amplify SSAs and address these limitations [8].

5.2 Fabrication of Hybrid Supercapacitor Devices and Performance Evaluation

In this chapter fabrication of HSDs in both aqueous and solid states are discussed utilizing a CVO/rGO composite electrode. It is recognized for its superior performance, CVO/rGO as the cathode and rGO are the anode materials

used to achieve enhanced capacitive capabilities of HSCs. The chapter is organized into two segments A and B. Segment 'A' focuses on the chemical bath synthesized and best-performed C-CVR3 electrodes utilized for the fabrication of aqueous and solid-state HSD (CVO/rGO//rGO) and its electrochemical performance evaluation. Segment 'B' focuses on the SILAR synthesized and best-performed S-CVR2 electrodes utilized for the fabrication of aqueous and solid-state HSD (CVO/rGO//rGO) and their electrochemical performance evaluation.

5.2.A Section-A: Fabrication of Aqueous and Solid-State Hybrid Supercapacitor Devices: Utilizing C-CVR3 Electrode Prepared by CBS Method

5.2.A.1 Experimental Details

5.2.A.1.1 Electrode Preparation

The preparation of the cathode CVO/rGO composite (prepared by CBS method) and anode rGO electrodes, involved preparing a slurry consisting of the active material (CVO/rGO composite or rGO), carbon black, and PVDF in a mass ratio of 80:15:5, respectively, with a trace amount of NMP. Subsequently, these resulting slurries were evenly applied to a thoroughly polished SS substrate by using the optimum amount of loaded mass, calculated according to the mass balancing equation as follows [13],

$$\frac{m_+}{m_-} = \frac{C_- \times \Delta V_-}{C_+ \times \Delta V_+} \quad 5.1$$

Where m_+ , C_+ , and ΔV_+ are the loading mass of cathode material, cathode material C_s , and potential window of cathode material, respectively. Also, m_- , C_- , and ΔV_- are the loading mass of anode material, anode material C_s , and potential window of anode material, respectively.

5.2.A.1.2 Fabrication of Aqueous Hybrid Supercapacitor Device

Enhancing the potential window (V) is crucial for increasing ED (E), given their proportional relationship ($E \propto V^2$). However, achieving a high potential window has posed challenges, resulting in limited research in this area [9]. The primary strategies employed to expand V in SCs have predominantly involved the utilization of different electrolytes. For instance, employing an organic electrolyte, known for its resistance to decomposition, enables reaching higher voltages ($\geq 2.5V$) [10]. Nevertheless, drawbacks such as poor ionic conductivity, toxicity,

and costliness accompany organic electrolytes. Using ionic liquids as electrolytes can also extend the voltage window, but their low ionic conductivity results in diminished C_s for electrodes [11]. Consequently, opting for a mild and environmentally benign aqueous electrolyte with a satisfactory working voltage window is deemed preferable when striving to develop a high-voltage device [12].

The composite of the CVO/rGO (C-CVR3) electrode is tested (detailed in Chapter 3, section 3.2.B.6.10) as a cathode material through the preparation of an aqueous HSD (C-AHSD). Also, rGO is used as the anode electrode material along with 1 M KOH. This constructed C-AHSD cell is identified explicitly as the C-CVR3/rGO//KOH//rGO as schematically represented in Figure 5.1.

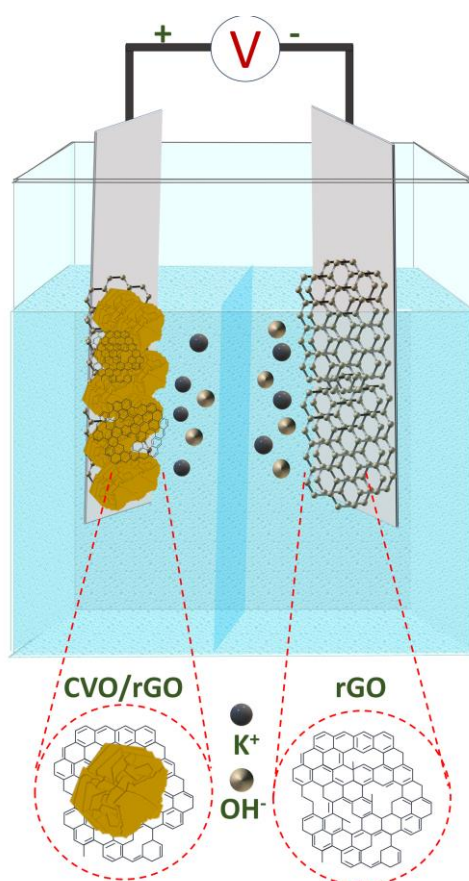


Figure 5.1 Schematic representation of C-AHSD.

5.2.A.2 Results and Discussion

5.2.A.2.1 Electrochemical Performance Evaluation of C-CVR3//KOH//rGO (C-AHSD)

5.2.A.2.1.1 CV Analysis

Although gaining a basic grasp of electrochemical behavior is necessary, assessing the practicality of the prepared C-CVR3 electrode is also essential. In an HSC system, the excellent $\text{CoV}_2\text{O}_6 \cdot 4\text{H}_2\text{O}/\text{rGO}$ composite (C-CVR3) with high electrochemical performance is assessed as a cathode. The construction of a C-AHSD (C-CVR3//rGO) that uses rGO as the anode and C-CVR3 as a cathode in a 1 M KOH electrolyte, as demonstrated in Figure 5.2.

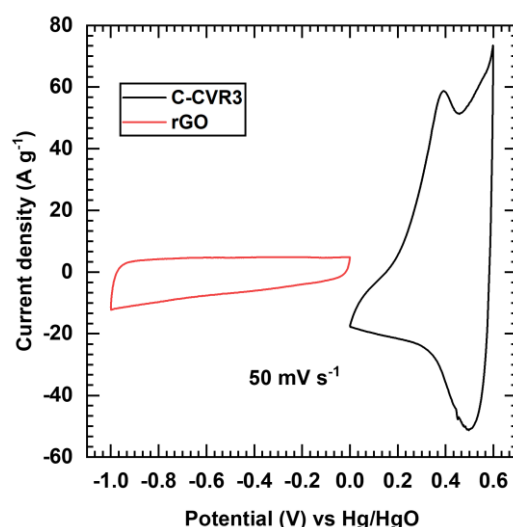


Figure 5.2 Comparative CV curves plot of rGO and C-CVR3 electrode at 50 mV s^{-1} scan rate.

The C-CVR3 and rGO electrodes show the benefit of having independent working potentials, which can help to improve the voltage of the C-AHSD. The distinct operating potential window of electrodes is shown in Figure 5.2. As shown in Figure 5.2, the C-CVR3 electrode performs very well in the positive potential range of 0 to 0.6 V, while the rGO electrode performs effectively in the potential range of 0 to -1 V. By measuring CV curves at different voltage ranges, such as 0 to 1.2, 1.3, 1.4, 1.5, 1.6, and 1.7 V, at a fixed scan rate of 50 mV s^{-1} , as illustrated in Figure 5.3 (a), it is possible to figure out the exact operational voltage range for C-AHSD. Since the water-splitting process can take place above 1.6 V, the optimized voltage range of 0 to 1.6 V is suitable for the C-AHSD. The C-AHSD CV curves are shown in Figure 5.3 (b) at various scan rates from 5-100 mV s^{-1} . At each scan rate, C-AHSD exhibits a semi-rectangular CV shape with small redox peaks, pointing to the charge storage mechanism of the pseudocapacitive type [14]. The CV curves continue to have a near-consistent shape even at higher scan rates.

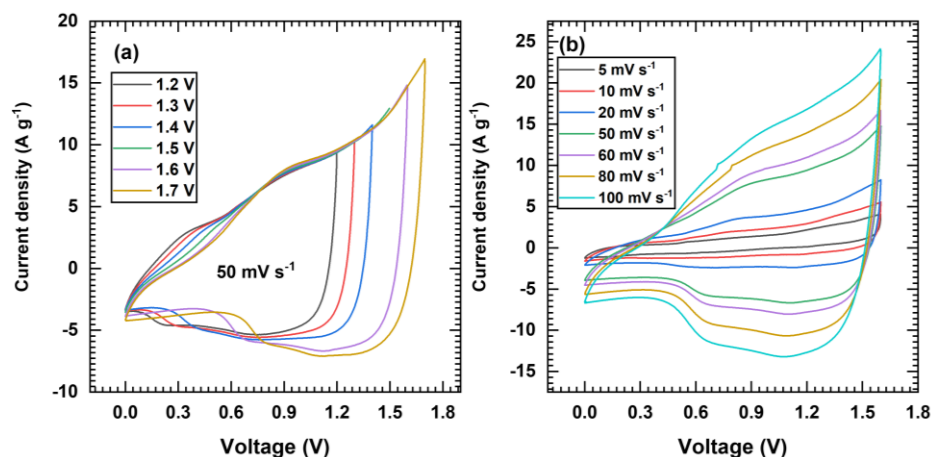


Figure 5.3 (a) Voltage variation in CV curves of C-AHSD at fixed scan rate (50 mV s^{-1}), and (b) CV curves of C-AHSD at different scan rates in optimal voltage 0 to 1.6 V.

5.2.A.2.1.2 GCD Analysis

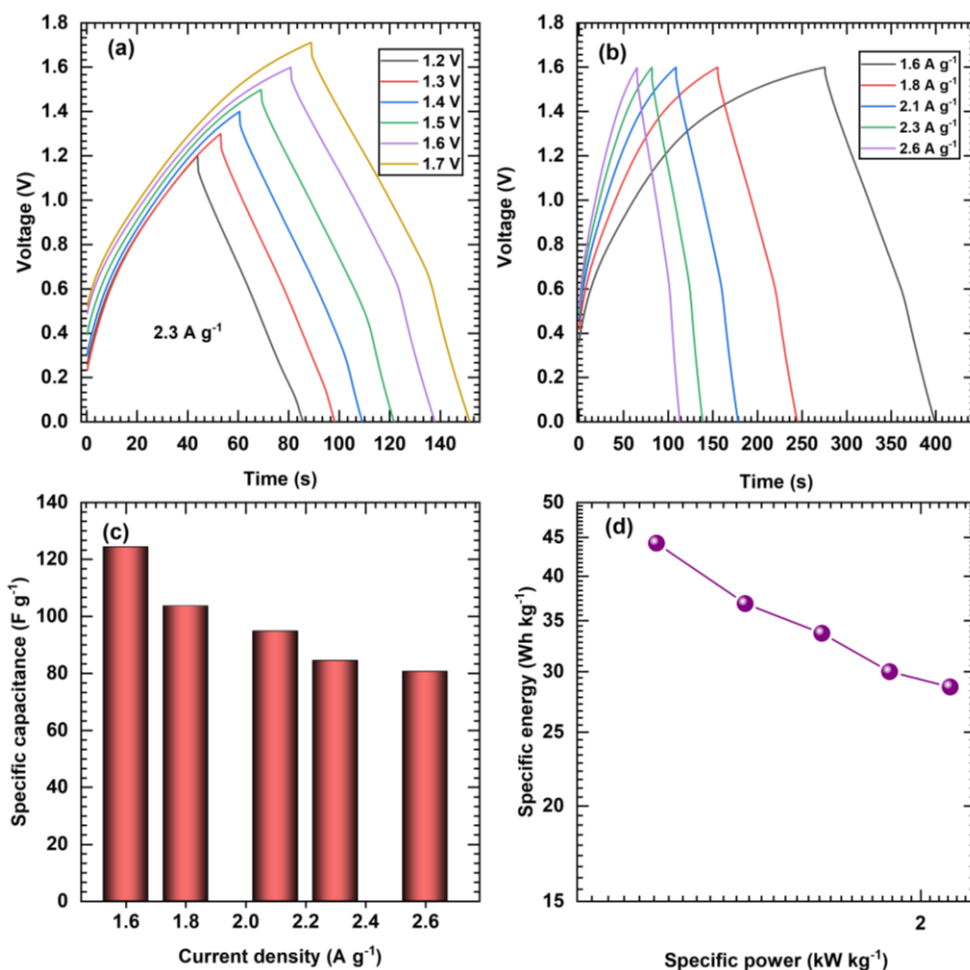


Figure 5.4 (a) Voltage window variation GCD curves of C-AHSD at fixed current density (2.3 A g^{-1}), (b) GCD curves of C-AHSD at different current densities (1.6 to 2.6 A g^{-1}), (c) bar diagram of C_s vs current density, and (d) Ragone plot of C-AHSD.

The measurement of GCD curves at different voltage ranges, such as 0 to 1.2, 1.3, 1.4, 1.5, 1.6, and 1.7 V, at a fixed current density of 2.3 A g^{-1} , as illustrated in Figure 5.4 (a), suggests appropriate voltage range is 0 to 1.6 V for C-AHSD. Figure 5.4 (b) shows the results of GCD tests performed at various current densities (1.6 to 2.6 A g^{-1}) to examine the improved charge storage capacities and rapid discharge performance of the C-AHSD. The C-AHSD displays quasi-linear discharge profiles with prolonged charge-discharge durations at all investigated current densities. This behavior suggests that the device has a significant amount of storage for energy capacity because it exhibits pseudocapacitive characteristics [15]. For the C-AHSD, the C_s values were found to be 124.3, 103.6, 94.7, 84.3, and 80.5 F g^{-1} at current densities of 1.6, 1.8, 2.1, 2.3, and 2.6 A g^{-1} , respectively as displayed in Figure 5.4 (c). The Ragone plot (Figure 5.4 (d)) shows the C-AHSD's SE and SP, which were calculated from the GCD parameters and obtained a maximum SE of 44.2 Wh kg^{-1} with 1.2 kW kg^{-1} of SP.

5.2.A.2.1.3 EIS and Stability Analysis

The EIS helps to identify the cause of the remarkable electrochemical results of the C-AHSD. Figure 5.5 (a) shows the C-AHSD's Nyquist plot and the accompanying equivalent circuit as an inset. Due to its minimal R_s (2.22Ω), R_{ct} (69.2Ω), and W (0.012Ω) values and high CPE value (1.0 mF), with a correction factor of n (0.67). The C-AHSD demonstrates favorable electrochemical conductive properties and outstanding storage capability.

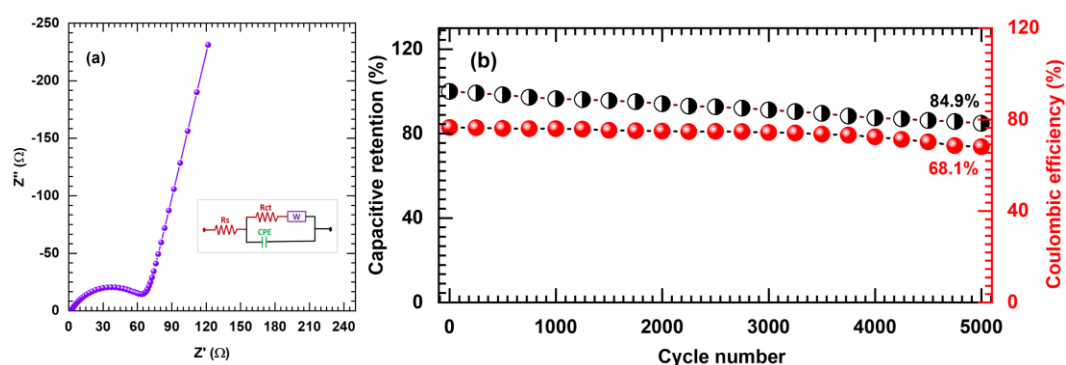


Figure 5.5 (a) Nyquist plot of C-AHSD and (b) Plot of capacitance retention and Coulombic efficiency vs cycle number.

The C-AHSD displays remarkable cycling stability, according to the cycle stability test (shown in Figure 5.6 (b)), maintaining 84.9% of its pristine capacitance with 68.1% coulombic efficiency after 5000 cycles at 2.6 A g^{-1} . The

results of this study demonstrate the beneficial effects of the high SSA of C-CVR3 on improving conductivity, improving charge transport characteristics, and promoting the quick diffusion of electrolyte ions during electrochemical reactions. In addition to the favorable physicochemical features of the C-CVR3 electrode, a rational combination with the rGO electrode is responsible for the superior electrochemical performance of C-AHSD.

5.2.A.2.2 Fabrication and Electrochemical Performance Evaluation of C-CVR3//PVA-KOH//rGO (C-SHSD)

The solid-state HSD (C-SHSD) has become a fascinating subject due to its potential uses in portable and flexible properties [17]. Its significant strengths include practical transport and user-friendliness because of its leakproof and lightweight characteristics. The emerging best-performed C-CVR3 ($4 \times 4 \text{ cm}^2$) was used as a cathode, and rGO ($4 \times 4 \text{ cm}^2$) as an anode for constructing the C-SHSD (Figure 5.6) (discussed in 5.2.A.1.1). A PVA-KOH gel electrolyte was used as the electrolyte and separator medium. The PVA was combined with potassium hydroxide (KOH) to form an electrolyte gel to make a S-SHSD. The PVA (1.5 g) was dissociated in 15 ml of DDW at 343 K while vigorously stirred. Further, the PVA solution was combined with 5 ml of a 1 M KOH solution while continuously agitated to create a viscous and clear solution. This gel was used for C-SHSD fabrication as a separator and electrolyte [16]. The fabrication of C-SHSD was carried out as illustrated in photographs in Figure 5.6.

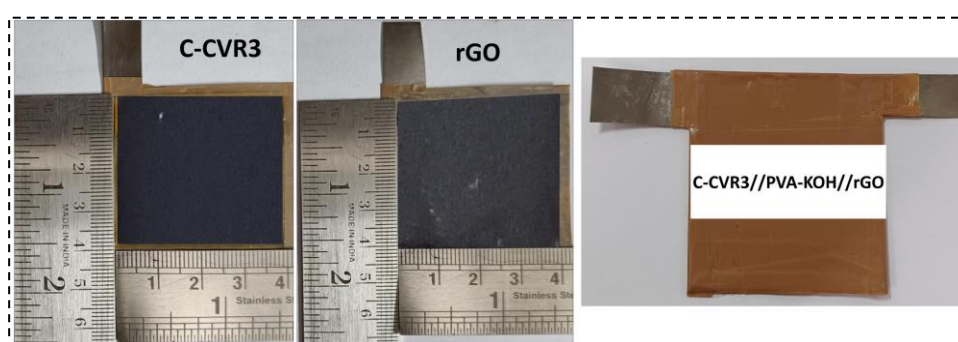


Figure 5.6 Photographs of $4 \times 4 \text{ cm}^2$ electrodes of rGO, C-CVR3, and fabricated leakproof device.

These two electrodes were coated with a gel electrolyte to create a thin electrolyte layer and then allowed to air-dry at room temperature to remove any moisture from the gel. To prevent short-circuiting along the edges, insulating tape

was applied around the sides of the electrodes. The electrodes were then paired together to assemble a solid-state device using the gel electrolyte. The completed device was wrapped in plastic tape for additional sealing. To enhance the contact between the gel electrolyte and the active materials on the electrodes, the assembled device was subjected to 0.5 tons of pressure for 5 h. After this process, the solid-state asymmetric device was successfully fabricated.

5.2.A.2.2.1 CV Analysis

To assess the operational voltage of C-SHSD, CV test experiments are conducted across various voltage ranges, employing fixed scan rates of 50 mV s^{-1} , as shown in Figure 5.7 (a). The C-SHSD demonstrates a consistent CV curve, showing no sudden surge in current across an extensive voltage range from 0 to 1.7 V. According to the CV analysis, C-SHSD can function securely within the recommended voltage window of 0 to 1.6 V, avoiding any electrolyte polarization issues [14]. Figure 5.7 (b) depicts the CV plot of the C-SHSD at varying scan rates between 5 to 100 mV s^{-1} . The configuration of the CV curves indicates a larger area under the curve, showcasing the pseudocapacitive behavior of the C-SHSD. Regardless of the scan rate, all CV curves maintain their shape, indicating the outstanding capacitive performance of the C-SHSD.

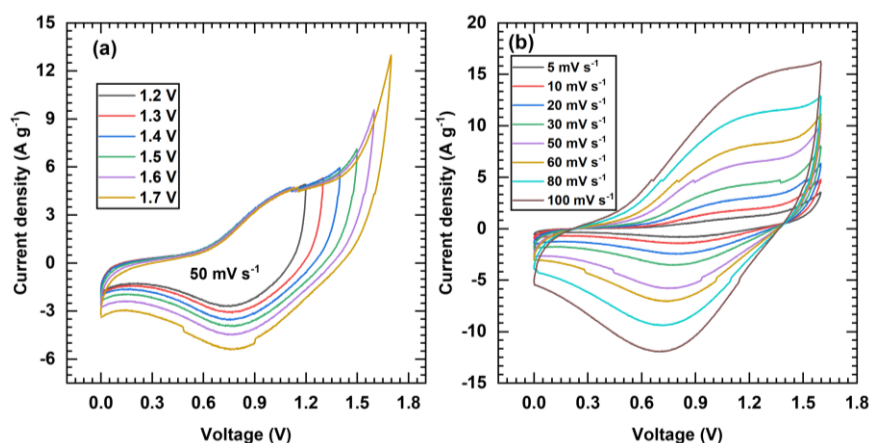


Figure 5.7 (a) CV curves of voltage variation (C-SHSD) at fixed scan rate (50 mV s^{-1}) and (b) CV curves at different scan rates 5 to 100 mV s^{-1} at optimal voltage range (0 to 1.6 V).

5.2.A.2.2.2 GCD Analysis

The electrochemical capacitive behavior of the C-SHSD is further explored through GCD analysis. Figure 5.8 (a) displays the GCD curves of the C-SHSD at

various voltage windows at 1.2 to 1.7 V under a constant current density of 2.6 A g⁻¹.

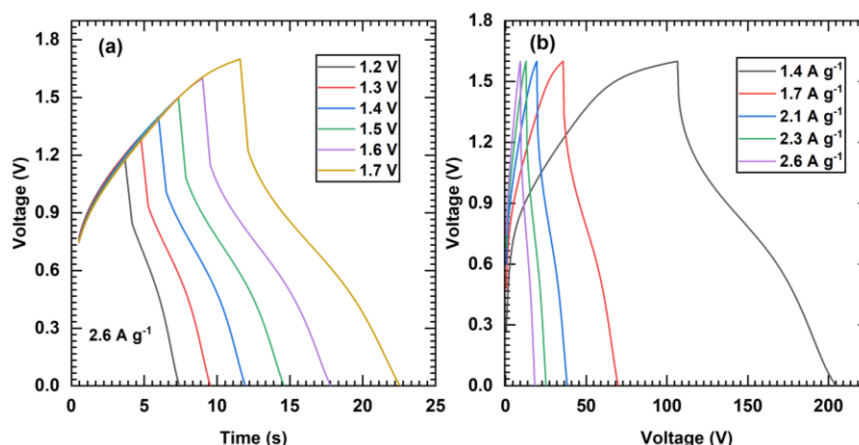


Figure 5.8 The GCD curves of C-SHSD (a) variation of voltage window (0 to 1.2-1.6 V) and (b) at different current densities from 1.4 A g⁻¹ to 2.6 A g⁻¹.

The performance of the C-SHSD is notably superior up to a voltage of 1.6 V. Additionally, Figure 5.8 (b) illustrates the GCD curves of the C-SHSD at different current densities. The better electrochemical capacitive behaviour with the non-linear bell-shaped GCD curves is ascribed to advantageous reversible redox processes and intercalation/deintercalation charge storage mechanisms [18-20]. Figure 5.9 (a) shows the Cs of the C-SHSD, which was determined using GCD curves. With a current density of 1.4 A g⁻¹, the C-SHSD achieves its maximum Cs of 92.1 F g⁻¹. The C-SHSD achieved a maximum SE of 32.7 Wh kg⁻¹ with SP of 1.1 kW kg⁻¹, as displayed in Ragone plot Figure 5.9 (b). These results demonstrate the C-SHSD's superior energy storage capabilities.

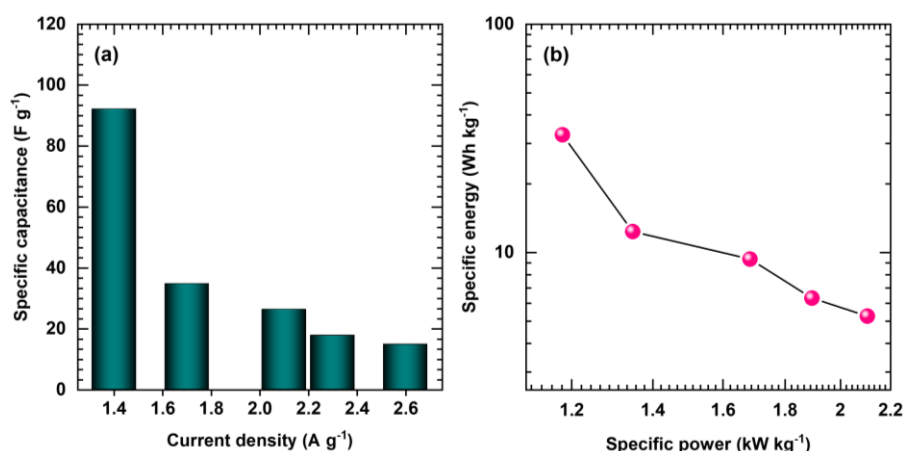


Figure 5.9 (a) Bar diagram of Cs vs current density and (b) Ragone plot of C-SHSD.

5.2.A.2.2.3 EIS and Stability Analysis

The EIS analysis was conducted on the C-SHSD, applying a bias voltage in the frequency range of 10 mHz to 0.1 MHz to probe its robust electrochemical conductivity. As depicted in Figure 5.10 (a), the Nyquist plot was subjected to fitting with an equivalent circuit (inset) using Zview software. In this context, the R_s value was determined to be approximately $0.79\ \Omega$. Additionally, the obtained low R_{ct} , W , CPE , and n values for the C-SHSD measured approximately $213.1\ \Omega$, $0.045\ \Omega$, $0.50\ \text{mF}$, and 0.83 , respectively. Therefore, the low R_s and R_{ct} show the capacitive performance of the C-SHSD. Figure 5.10 (b) shows that a cyclic-stability test on the C-SHSD involved 5000 GCD cycles at $2.6\ \text{A g}^{-1}$, and impressively, the C-SHSD has outstanding cycle stability despite repeated cycling and maintained 78.3% of its capacitance retention with 81.7% coulombic efficiency.

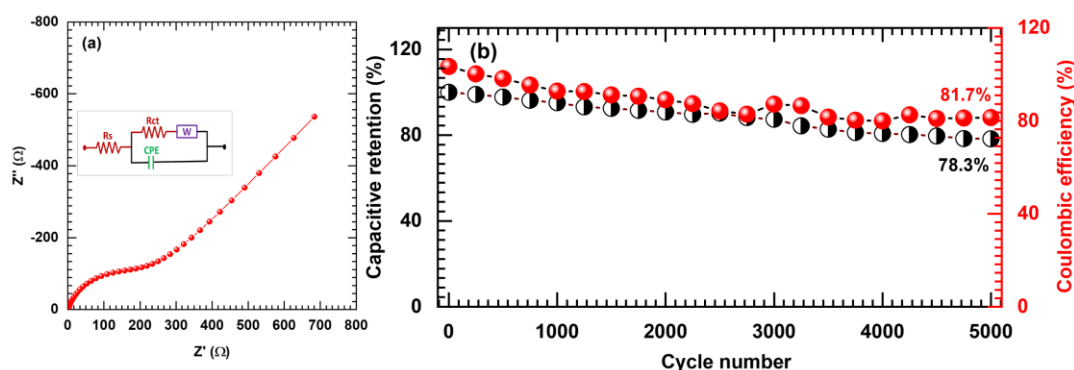


Figure 5.10 (a) The Nyquist plot of C-SHSD (inset: fitted equivalent circuit) and (b) the capacitive retention and Coulombic efficiency vs cycle number plot of C-SHSD.

5.2.A.2.2.4 Practical Demonstration of C-SHSD

To evaluate practical use, two C-CVR3//PVA-KOH//rGO devices were linked in series and used to glow light-emitting diodes (LEDs), as shown in Figure 5.11 (a-c). These C-SHSD devices were charged for 30 s and then discharged by the LED lamp. As part of the discharge process, the LED lamp first glows brightly (5 s), demonstrating the outstanding power output capacity of C-SHSD. The LED lamp's continued, steady lighting illustrates C-SHSD's high ED. Given the excellent results obtained for C-SHSD, this investigation has the potential to provide new paths for the preparation of innovative nanostructured CVO/rGO composite electrode materials by the CBS method, particularly for incredibly effective HSCs.

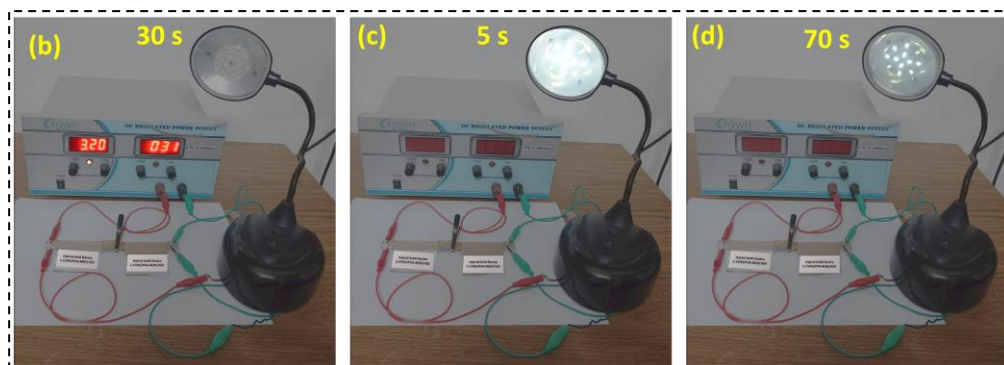


Figure 5.11 (a-c) C-CVR3//PVA-KOH//rGO C-SHSD practical demonstration photographs.

5.2.B Section-B: Fabrication of Aqueous and Solid-State Hybrid Supercapacitor Devices: Utilizing S-CVR2 electrode prepared by SILAR Method

5.2.B.1 Experimental Details

5.2.B.1.1 Electrodes Preparation

The best-performing S-CVR2 thin film electrodes, as described in section 4.2.B.2.1, were tested as a cathode in HSC device fabrication. Moreover, the rGO electrode prepared using the slurry coating method described in section 5.2.A.1.1 was used as an anode in the HSD.

5.2.B.2 Results and Discussion

5.3.B.2.1 Fabrication of S-CVR2//KOH//rGO (S-AHSD)

The S-AHSD made of S-CVR2//KOH//rGO is fabricated using a similar procedure and electrode preparation described in subsection 5.2.A.1.2 in this chapter.

5.2.B.2.2 Electrochemical Performance Evaluation of S-AHSD

5.2.B.2.2.1 CV Analysis

Based on an evaluation by the three-electrode system, the rGO and S-CVR2 electrodes have different potential windows, as displayed in Figure 5.12. The different working potential windows are beneficial for the enhancement of the voltage of C-AHSD.

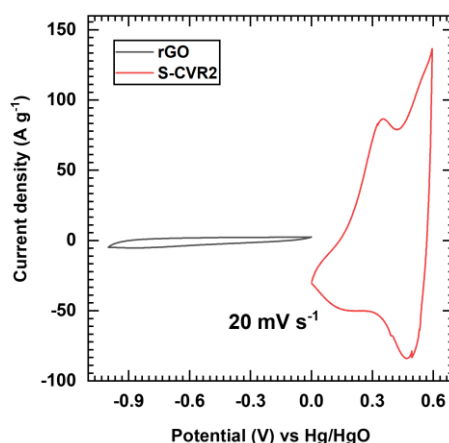


Figure 5.12 Comparative CV curves of rGO and S-CVR2 at 20 mV s⁻¹ scan rate.

For the S-CVR2//KOH//rGO C-AHSD, the potential window range of 0 to 1.7 V was carried out at 50 mV s⁻¹ scan rate, as shown in Figure 5.13 (a), to conclude the voltage of the device. The result optimizes the 0 to 1.6 V voltage suitable for the S-CVR2//KOH//rGO S-AHSD since the water-splitting process can

occur after 1.6 V. Therefore, the CV curves were carried out at various scan rates from 5 to 100 mV s^{-1} in the voltage of 0 to 1.6 V and displayed in Figure 5.13 (b). The quasi-rectangular nature of CV loops suggests the pseudocapacitive behavior of the S-AHSD.

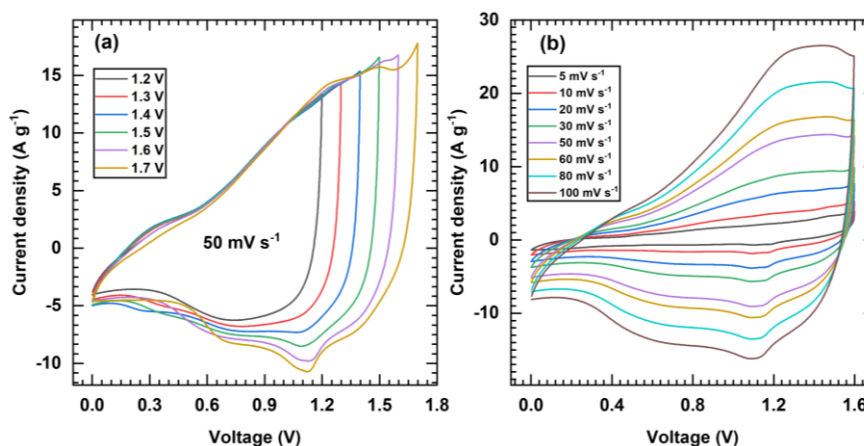


Figure 5.13 (a) Voltage variation in CV curves of S-AHSD at fixed scan rate 50 mV s^{-1} , and (b) CV curves of S-AHSD at different scan rates in the voltage range of 0 to 1.6 V.

5.2.B.2.2.2 GCD Analysis

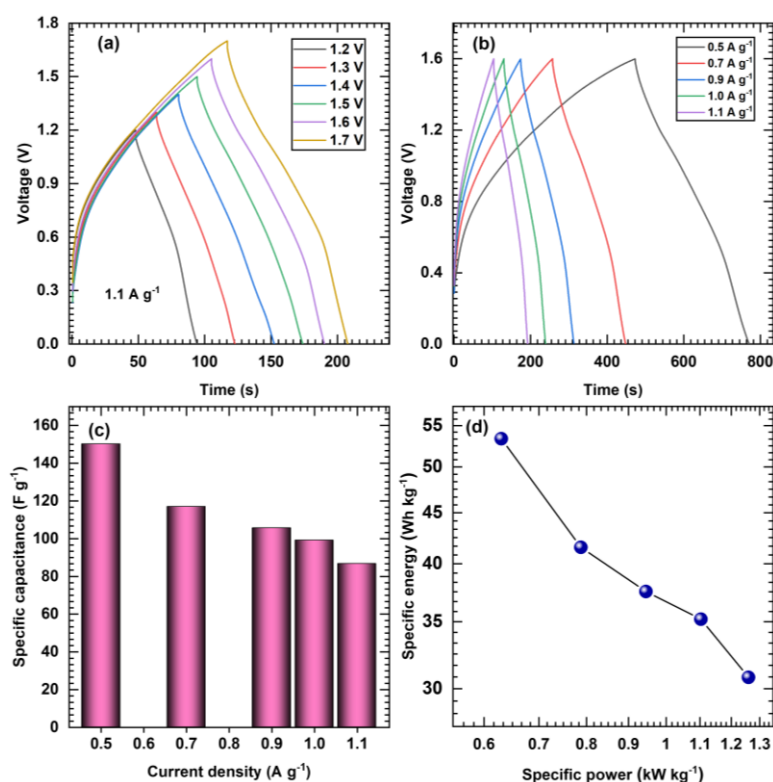


Figure 5.14 (a) Voltage variation GCD curves of S-AHSD at fixed current density, (b) GCD curves of S-AHSD at different current densities (0.5 to 1.1 A g^{-1}), (c) plot of C_s vs current density, and (d) Ragone plot of S-CVR2//KOH//rGO S-AHSD.

The GCD curves of S-AHSD were tested in various voltages of 0 to 1.7 V, as shown in Figure 5.14 (a), at 1.1 A g⁻¹ current density. The GCD plots in the optimized voltage of 0 to 1.6 V, at current densities of 0.5 to 1.1 A g⁻¹, are displayed in Figure 5.14 (b). The GCD curves are not precisely triangular, suggesting the excellent pseudocapacitive performance of the S-AHSD. The Cs values of the S-AHSD are 150 F g⁻¹ at 0.5 A g⁻¹ and maintain Cs of 86.6 F g⁻¹ at 1.1 A g⁻¹, as displayed in Figure 5.14 (c). The S-AHSD achieved a maximum SE of 53.3 Wh kg⁻¹ at 0.6 kW kg⁻¹ SP and a minimum SE of 30.7 Wh kg⁻¹ at 1.2 kW kg⁻¹ SP, as shown in Figure 5.14 (d) of the Ragone plot.

5.2.B.2.2.3 EIS and Stability Analysis

The EIS analysis was also done to understand ion migration's kinetics in the S-AHSD, and the Nyquist plot is shown in Figure 5.15 (a) with an analogous fitted circuit inset of the figure. The S-AHSD shows less R_s and R_{ct} of 1.61 Ω and 50.25 Ω . Also, the W , CPE, and n values are 0.39 Ω , 0.93 mF, and 0.72, respectively. The small values of R_s and R_{ct} indicate efficient ion transportation and outstanding electrochemical conduction of the constituent electrode. Additionally, the vertically inclined lines in the low-frequency region indicate a lesser W impedance for the diffusion of electrolyte ions between the respective electrodes in S-AHSD. The cycling stability of S-AHSD was checked by continuing given 5000 cycles of GCD at the constant current density of 1.1 A g⁻¹ and maintained 85.2% capacitive retention with 73.8% coulombic efficiency, as shown in Figure 5.15 (b). The electrochemical performance of S-AHSD demonstrates a positive impact of CVO/rGO composite electrodes prepared by the SILAR method owing to binder-free synthesis as compared to the CBS method.

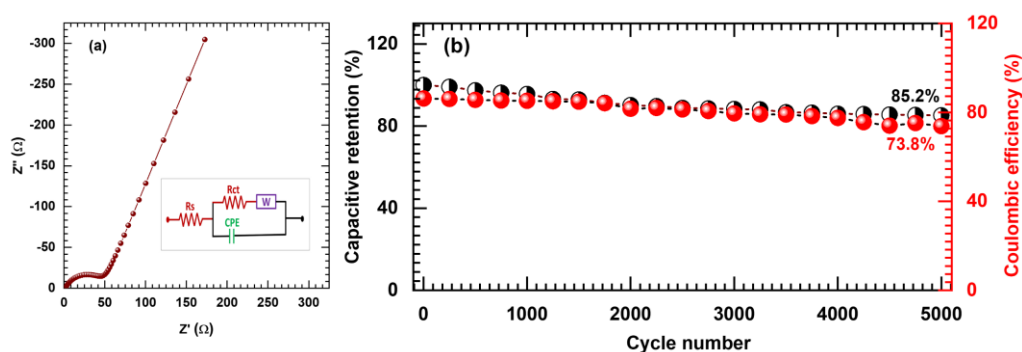


Figure 5.15 (a) The Nyquist plot of S-AHSD (inset: fitted equivalent circuit) and (b) plot of the capacitive retention and Coulombic efficiency vs cycle number.

5.2.B.2.3 Fabrication and Electrochemical Performance Evaluation of S-CVR2//PVA-KOH//rGO (S-SHSD)

The rGO and S-CVR3 electrodes were prepared on a large area of the SS substrate (4x4 cm²), as shown in Figure 5.16. The fabrication procedure of S-SHSD is similar to that discussed in section (5.2.A.1.1).

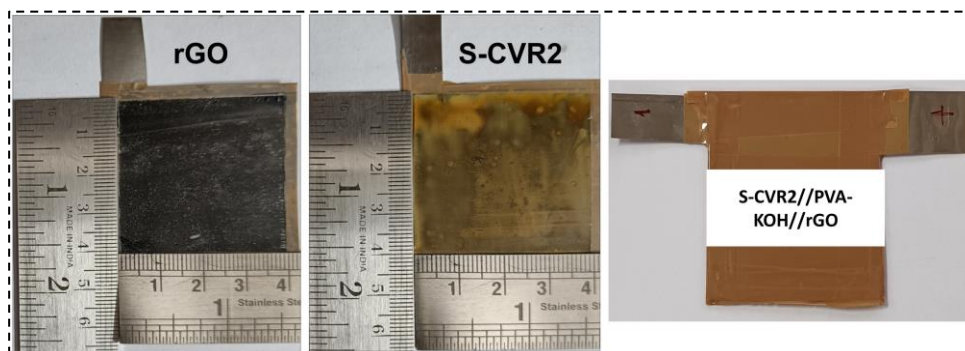


Figure 5.16 Photographs of 4x4 cm² electrodes of rGO, S-CVR2, and fabricated S-CVR2//PVA-KOH//rGO S-SHSD.

5.2.B.2.3.1 CV Analysis

The optimization of the voltage for the S-SHSD is depicted in Figure 5.17 (a), wherein the voltage is systematically optimized through variation of voltage range from 0 to 1.2 V and subsequently up to 1.7 V. By concluding this voltage variation analysis, the voltage range of 0 to 1.6 V for CV and it is perfect for the device study.

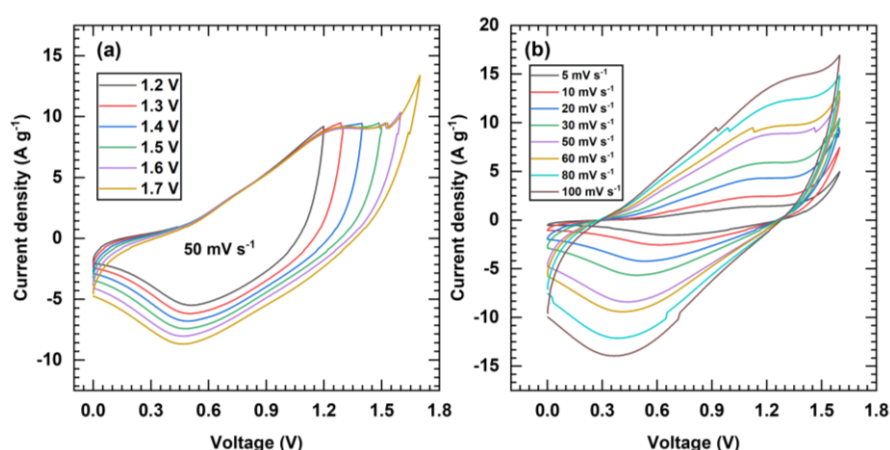


Figure 5.17 (a) Voltage variation CV curves of S-SHSD at fixed scan rate (50 mV s⁻¹), and (b) CV curves of S-SHSD at different scan rates in the optimal voltage of 0 to 1.6 V.

In Figure 5.17 (b), the CV curves of the S-SHSD are depicted at varying scan rates ranging from 5 to 100 mV s⁻¹. Even at the elevated scan rate of 100 mV s⁻¹,

the S-SHSD exhibits characteristic pseudo-rectangular CV shapes, indicating the pseudocapacitive nature and swift redox reaction kinetics of the S-CVR2 and rGO electrodes.

5.2.B.2.3.2 GCD Analysis

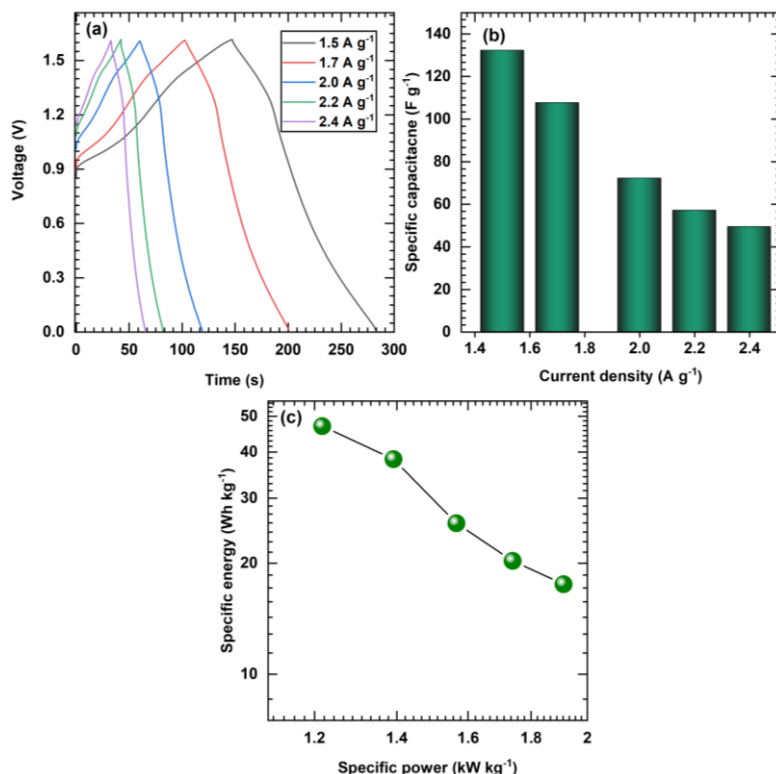


Figure 5.18 (a) The GCD curves of S-SHSD, (b) bar diagram of Cs vs current density, and (c) Ragone plot of S-SHSD.

The electrochemical capacitive characteristics of the S-SHSD are further examined through GCD analysis. In Figure 5.18 (a), the GCD curves of the S-SHSD are depicted at different current densities ranging from 1.5 A g⁻¹ to 2.4 A g⁻¹. Notably, the S-SHSD exhibits superior performance at lower current density, and the GCD curves show a pseudocapacitive nature. The Cs of the S-SHSD were determined based on the GCD curves at various current densities (1.5 to 2.4 A g⁻¹), as depicted in Figure 5.18 (b). At a current density of 1.5 A g⁻¹, the S-SHSD demonstrated a maximum Cs of 132.2 F g⁻¹. The S-SHSD displays a maximum SE of 47 Wh kg⁻¹ at SP of 1.2 kW kg⁻¹ as illustrated Ragone plot in Figure 5.18 (c).

5.2.B.2.3.3 EIS and Stability Analysis

EIS analysis of S-SHSD was carried out as illustrated in Figure 5.20 (a) and the equivalent circuit is shown inset of Figure 5.19 (a). In this context, the R_s value was determined to be approximately 0.73 Ω . Additionally, the measured R_{ct} , W ,

CPE, and n values for the S-SHSD were notably low, approximately 43.28Ω , 0.20Ω , 0.27 mF , and 0.87 , respectively. These low R_s and R_{ct} values indicate the superior capacitive performance of the S-SHSD. In Figure 5.19 (b), the cyclic stability of the S-SHSD was evaluated through a test involving 5000 GCD cycles at 2.6 A g^{-1} . The S-SHSD demonstrated outstanding cycle stability, maintaining 80.6% of its capacitance retention with 82.4% coulombic efficiency repeated cycling.

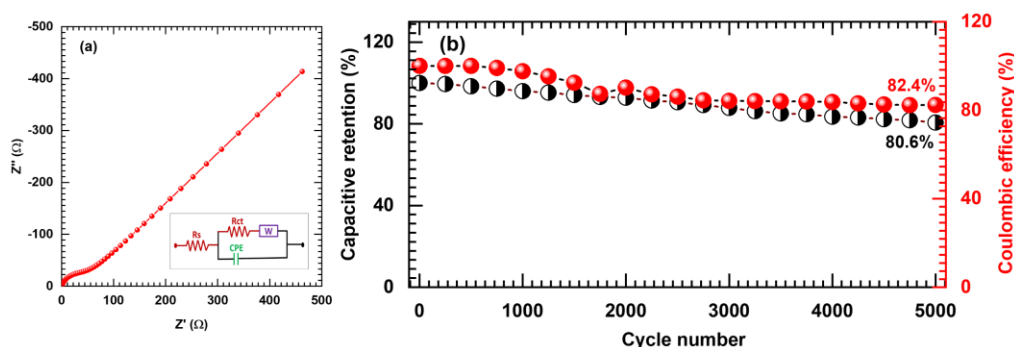


Figure 5.19 (a) Nyquist plot of S-SHSD and (b) plot of capacitive retention and Coulombic efficiency vs cycle number.

5.2.B.2.3.4 Practical Demonstration of S-SHSD

A pair of S-SHSD devices were connected in series and utilized to illuminate LEDs for assessing the practical applicability of S-SHSD, as depicted in Figure 5.20 (a-c). These S-SHSDs underwent a charging duration of 30 s, followed by discharge through the LED lamp. During the discharge phase, the LED initially emitted a bright light for 10 s, showcasing the remarkable power output capability of S-SHSD. The sustained, consistent illumination (120 s) of the LED lamp further underscores the high ED of S-SHSD.

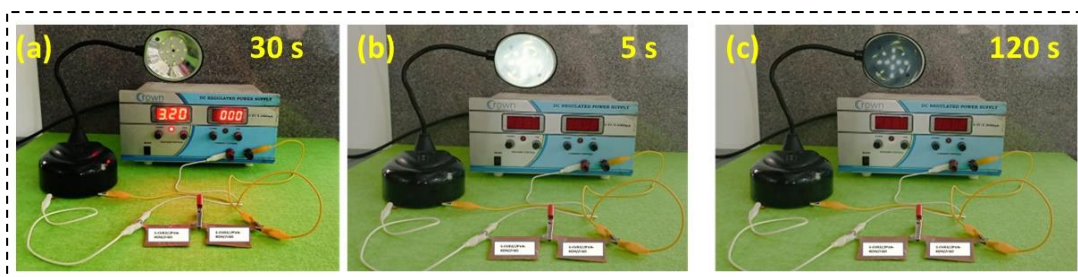


Figure 5.20 Photographs of glowing LED using S-SHSDs.

Furthermore, the obtained SE and SP of S-AHSD and S-SHSD are compared with previous reports [21-42], as given in Chapter 1, Table 1.2. Some reports [22, 25, 35] display maximum performance slightly higher than the present work due to

the use of NF as a conductive substrate since NF can add its self-capacitance in the alkaline device. This present work uses only SS as a conductive substrate, which avoids the redox reaction in the alkaline electrolyte; hence, the obtained SE and SP originated from the C-CVR3 or S-CVR2 and rGO materials. With the promising outcomes achieved for S-AHSD and S-SHSD in this study, this investigation holds the potential to pave the way for novel approaches in the synthesis of nanostructured (marigold-like particles of CVO over 2D rGO nanosheets) electrode materials, particularly for highly efficient HSCs.

5.3 Conclusions

In conclusion, the successful fabrication of HSDs utilizing CVO/rGO (CBS and SILAR methods) as cathode electrodes and rGO as an anode electrode has been demonstrated. The CBS deposited C-AHSD showcased a maximum Cs of 124.3 F g^{-1} , coupled with an SE of 44.2 Wh kg^{-1} at an SP of 1.2 kW kg^{-1} . Moreover, the C-SHSD exhibited a noteworthy Cs of 92.1 F g^{-1} at 2.6 A g^{-1} , with a SE of 32.7 Wh kg^{-1} at 1.1 kW kg^{-1} SP. Additionally, the CBS-prepared C-SHSD displayed a 78.3% capacitive retention over 5000 cycles. On the other hand, the SILAR synthesized S-AHSD demonstrated a maximum Cs of 150 F g^{-1} at 0.5 A g^{-1} , achieving a SE of 53.3 Wh kg^{-1} at 0.6 kW kg^{-1} SP. Furthermore, the S-SHSD outperformed its C-SHSD counterpart, attaining the highest Cs of 132.2 F g^{-1} at 1.5 A g^{-1} current density, with a SE of 47 Wh kg^{-1} at a SP of 1.2 kW kg^{-1} . Additionally, the S-SHSD exhibited an impressive 80.6% capacitive retention over 5000 cycles. In conclusion, the S-AHSD and S-SHSD demonstrate excellent supercapacitive properties compared to the C-AHSD and C-SHSD. These findings suggest that SILAR synthesized CVO/rGO composite with optimal composition is suitable as cathode material in HSDs. Moreover, findings suggest a significant potential for the application of S-SHSD in various portable electronic devices.

5.4 References

- [1] J. Castro-Gutiérrez, A. Celzard, V. Fierro, *Front. Mater.*, 7, (2020), 217.
- [2] M. Sanayee and M. Arvand, *Sci. Rep.*, 13, (2023), 20838.
- [3] R. Kötz, M. Carlen, *Electrochim. Acta*, 45, (2000), 2483-2498.
- [4] M. Pathak, D. Bhatt, R. Bhatt, B. Bohra, G. Tatrari, S. Rana, M. Arya, N. Sahoo, *Chem. Rec.*, 24, (2023), e202300236.
- [5] W. Zheng, Z. Li, G. Han, Q. Zhao, G. Lu, X. Hu, J. Sun, R. Wang, C. Xu, *J. Energy Storage*, 47, (2022), 103675.
- [6] S. He and W. Chen, *Nanoscale*, 7, (2015), 6957-6990.
- [7] A. Afif, S. Rahman, A. Azad, J. Zaini, M. Islan, A. Azad, *J. Energy Storage*, 25, (2019), 100852.
- [8] L. Mai, F. Yang, Y. Zhao, X. Xu, L. Xu, Y. Luo, *Nat. Commun.*, 2, (2011), 381.

-
- [9] C. Zhong, Y. Deng, W. Hu, J. Qiao, L. Zhang, J. Zhang, *Chem. Soc. Rev.*, 44, (2015), 7484-7539.
- [10] D. Wang, S. Liu, L. Jiao, G. Fang, G. Geng, J. Ma, *Carbon*, 119, (2017), 30-39.
- [11] J. Feng, Y. Wang, Y. Xu, Y. Sun, Y. Tang, X. Yan, *Energy Environ. Sci.*, 14, (2021), 2859-2882.
- [12] S. Azari, M. Rahmanifar, M. El-Kady, A. Noori, M. Mousavi, R. Kaner, *J. Iran. Chem. Soc.*, 14, (2017), 2579-2590.
- [13] N. Chodankar, H. Pham, A. Nanjundan, J. Fernando, K. Jayaramulu, D. Golberg, Y. Han, D. Dubal, *Small*, 16, (2020), 2002806.
- [14] S. Sadavar, N. Padalkar, R. Shinde, A. Patil, U. Patil, V. Magdum, Y. Chitare, S. Kulkarni, S. Kale, R. Bulakhe, D. Bhange, S. Kochuveedu, J. Gunjakar, *Energy Stor. Mater.*, 48, (2022), 101-113.
- [15] S. Sharma and P. Chand, *Results Chem.*, 5, (2023), 100885.
- [16] S. Kumbhar, S. Bhosale, S. Pujari, V. Patil, N. Kumar, R. Salunkhe, C. Lokhande, U. Patil, *Energy Technol.* 11, (2023), 2300400.
- [17] J. Lee, G. Yang, C. Kim, R. Mahajan, S. Lee, S. Park, *Energy Environ. Sci.*, 15, (2022), 2233-2258.
- [18] S. Balasubramaniam, A. Mohanty, S. Balasingam, S. Kim, A. Ramadoss, *Nano-Micro Lett.*, 12, (2020), 85.
- [19] Z. Tang, C. Jia, Z. Wan, Q. Zhou, X. Ye, Y. Zhu, *RSC Adv.*, 6, (2016), 112307.
- [20] S. Patil, N. Chodankar, R. Pujari, Y. Han, D. Lee, *J. Power Sources*, 46, (2020), 6228286.
- [21] H. Sun, X. Chen, H. Chai, Y. Wang, D. Jia, Y. Cao, A. Liu, *Appl. Surf. Sci.*, 469, (2019), 118-124.
- [22] Z. Fahimi, O. Moradlou, A. Sabbah, K. Chen, L. Chen, M. Qorbani, *J. Chem. Eng.*, 436, (2022), 135225.
- [23] G. Yao, N. Zhang, Y. Zhang, T. Zhou, *J. Alloys Compd.*, 892, (2021), 162205.
- [24] H. Wang, H. Zhang, D. Zhang, J. Chen, S. Zhang, S. Zhang, J. Yu, Q. Wu, Q. Li, *Appl. Mater. Interfaces*, 14, (2022), 8106-8114.
- [25] V. Nguyen, F. Sari, J. Ting, *RSC Adv.*, 12, (2022), 29170-29176.
- [26] Y. Teng, Y. Li, D. Yu, Y. Meng, Y. Wu, X. Zhao, X. Liu, *ChemistrySelect*, 4, (2019), 956-962.
- [27] S. Liu, S. Sarwar, H. Zhang, Q. Guo, J. Luo, X. Zhang, *Electrochim. Acta*, 364, (2020), 137320.
- [28] C. Li, D. Ma, Q. Zhu, *Nanomaterials*, 12, (2022), 448.
- [29] W. Zhang, L. Kong, X. Ma, Y. Luo, L. Kang, *J. Power Sources*, 269, (2014), 61-68.
- [30] X. Lv, W. Huang, J. Tang, L. Tang, Q. Shi, *Electrochim. Acta*, 380, (2021), 138248.
- [31] S. Sekhar, B. Ramulu, D. Narsimulu, S. Arbaz, J. Yu, *Small*, 16, (2020), 2003983.
- [32] J. Zhou, B. Liu, L. Zhang, Q. Li, C. Xu, H. Liu, *J. Mater. Chem. A*, 10, (2022), 24896-24904.
- [33] Z. Fahimi and O. Moradlou, *J. Energy Storage*, 50, (2022), 104697.
- [34] R. Mishra, P. Panda, S. Barman, *New J. Chem.*, 45, (2021), 5897-5906.
- [35] H. Hosseini and S. Shahrokhian, *J. Chem. Eng.*, 341, (2018), 10-26.
- [36] P. Devi, M. Srivastava, N. Kim, J. Lee, D. Mishra, *Compos. B.*, 227, (2021), 109384.
- [37] X. Lv, W. Huang, Q. Shi, L. Tang, J. Tang, *J. Mater. Sci.: Mater. Electron.*, 31, (2020), 2388-2397.
- [38] W. Low, C. Siong, C. Chia, S. Lim, P. Khiew, *J. Sci-Adv. Mater. Dev.*, 4, (2019), 515-523.
- [39] A. Maitra, A. Das, S. Karan, S. Paria, R. Bera, B. Khatua, *Ind. Eng. Chem. Res.*, 56, (2017), 2444-2457.
- [40] M. Amiri, S. Davarani, S. Kaverlavani, S. Moosavifard, M. Shamsipurd, *Appl. Surf. Sci.*, 527, (2020), 146855, 1-8.
- [41] X. Lv, W. Huang, Q. Shi, L. Tang, J. Tang, *J. Power Sources*, 492, (2021), 229623, 1-10.
- [42] G. Sharma, P. Gupta, S. Sharma, R. Pala, S. Sivakumar, *Appl. Energy Mater.*, 4, (2021), 4758-4771.
-

CHAPTER-6

Summary and Conclusions

Summary and Conclusions

High-performance energy conversion and ESDs are desperately needed in the current energy-crisis-plagued global environment. More importantly, the need for effective ESDs cannot be emphasized, especially when it comes to maximizing the use of renewable energy sources. The advantages of batteries and SCs, discussed in Chapter 1, have attracted much research interest as energy storage alternatives. Researchers have also turned their attention to SCs because of their unique characteristics, which include high ED, PD, extended cycle durability, quick recharge times, and safe operating features. However, with a limited ED, symmetric SC cells with electrodes of the EDLC kind can provide increased PD and longer cycle life. As compared with batteries, asymmetric SC cells with pseudocapacitive-type electrodes have better ED and PD, but they have problems with cycle durability and ED. Thus, it is suggested that HSC cells with two types of electrodes can be used: one EDLC type and the other pseudocapacitive type. As a result, HSC can provide high power, quick charging and discharging times, an ED that is comparable to batteries, and a long cycle life. Nonetheless, the performance of HSCs relies on the effective functioning of their constituent components, including electrode material, electrolyte, and current collector. Thus, ensuring efficient electrochemical activity within the electrodes is crucial for attaining elevated PD, ED, and prolonged cycle life of HSCs.

Electrode materials and electrolytes play pivotal roles in the performance of SCs by facilitating energy storage through ion diffusion and electrochemical reactions. These electrode materials are categorized into three groups: carbon-based materials in various forms, conducting polymers, and TMOs. TMOs offer higher theoretical capacitance due to their multivalence properties, enabling multi-step faradaic processes, variable crystal structures, and diverse morphologies. However, during continuous charge-discharge cycles (inter/de-intercalation), these materials undergo substantial volume expansion, resulting in diminished Cs, reduced electrical conductivity, and poor capacitance retention. MTMOs have emerged as promising electrode materials for faradaic applications due to their varied oxidation states, facilitating reversible redox reactions. The composite materials, carbon-based materials such as rGO enhanced the electrical conductivity and charge transfer rates of nanostructured MTMOs.

In this context, the current study aims to enhance the electrode performance of CVO by composite with carbon-based materials like rGO, thereby facilitating increased SSA and enhanced conductivity. Typically, present research work relies on synthesis methods of CVO and composite with rGO material. Conventional CBS and SILAR methods were used for the synthesis of CVO. The rGO was synthesized using the chemical method. Furthermore, the CVO/rGO composites were prepared by best-performed pristine CVO from CBS and SILAR methods, and these best-performed pristine CVO material composites with rGO by varying rGO concentrations.

The characterizations of the pristine CVO and CVO/rGO composites involved XRD, FT-IR spectroscopy, Raman spectroscopy, XPS, TGA, FE-SEM with EDS, HR-TEM with EDS and SAED, BET, and BJH techniques. Following this, the electrochemical properties of the pristine CVO and CVO/rGO composite electrodes were examined through CV, GCD, and EIS techniques. Subsequently, the best-performed CVO/rGO composite electrodes were used as the cathode electrodes for the fabrication of the HSDs. The five chapters that make up this work's extensive discussion are summarized and concluded in this chapter.

Chapter-1 discusses an introductory overview, outlining the future energy demands and the role of different ESDs, particularly those utilizing TMO materials. It includes a literature review covering various electrode materials for SCs and highlights recent advancements and research trends in this field. The chapter delves into the potential of SCs to address society's energy needs, explaining their fundamental mechanisms and operational principles. It also discusses the essential criteria for SCs using diverse, active electrode materials and provides an in-depth exploration of TMO and their composite materials. Additionally, it summarizes the literature on CVO and its composite materials, particularly rGO. The chapter concludes by stating the objectives and scope of the thesis.

Chapter-2 explores nanomaterial synthesis methods and their classification, providing a theoretical overview of CBS and SILAR methods along with their advantages and the impact of preparation parameters on nanomaterial preparation. It also covers various characterization techniques used to characterize prepared materials, including structural, morphological, and elemental analyses, such as XRD, FT-IR spectroscopy, Raman spectroscopy, XPS,

TGA, FE-SEM, HR-TEM, and EDS. Additionally, the chapter briefly explains the theoretical background of electrochemical techniques utilized to evaluate the electrochemical SC performance of electrodes, including CV, GCD, and EIS.

Chapter-3 describes the chemical synthesis of CVO and CVO/rGO composite electrodes. This chapter is also divided into two sections, i.e., sections 'A' and 'B'. Section A includes the preparation of C-CV series thin films on SS substrate by varying precursor concentrations ratio (Co:V) using a CBS method. Further, the influence of the Co and V precursor concentrations ratio on the physicochemical properties of C-CV thin films was studied. The structural characterization techniques (such as XRD, FT-IR, and XPS) confirm the formation of hydrous CVO ($\text{CoV}_2\text{O}_6 \cdot 4\text{H}_2\text{O}$). The maximum SSA obtained for the C-CV4 sample is $87.5 \text{ m}^2 \text{ g}^{-1}$. Furthermore, the nanosheets of C-CV are obtained by FE-SEM analysis. Among the all C-CV series electrodes, the C-CV4 electrode shows good electrochemical properties. The obtained maximum C_s (capacity) of 619.5 F g^{-1} (309.7 C g^{-1}) at 1 A g^{-1} current density for the C-CV4 electrode owing to low R_{ct} value. The C-CV4 electrode displays remarkable cycling stability, retaining 90.6% of its initial capacitance even after undergoing 5000 charge-discharge cycles which signifies good el. In this section, the precursor concentrations ratio of Co:V (1:2) was optimized to prepare CVO nanomaterial to achieve maximum C_s .

In Section B, the examination of composite electrodes composed of CVO and rGO, synthesized via a CBS method, is presented. The GO and rGO were prepared using modified Hummer's and chemical reduction methods, respectively. Also, the prepared rGO was confirmed by XRD and Raman characterization techniques, and rGO electrodes were tested for electrochemical performance using CV, GCD, and EIS techniques. The CVO/rGO composite materials were prepared by using the CBS method with different rGO concentrations (0.1, 0.2, 0.3, and 0.4 mg ml^{-1}) and labelled C-CVR series material. Moreover, the C-CVR series electrodes were characterized by structural, morphological, and electrochemical techniques. The CVO/rGO composite series materials were confirmed by XRD, FT-IR, Raman, XPS, and EDS techniques. The compositions of CVO and rGO are calculated from TGA as follows: 98.73% and 1.27% for C-CVR1, 97.54% and 2.46% for C-CVR2, 95.53% and 4.47% for C-CVR3, and 88.48% and 11.52% for C-CVR4. Also, the composite morphology of CVO and rGO was observed using the FE-SEM and HR-TEM

techniques and it reveals the growth of CVO 2D micro-plates over 2D rGO nanosheets. For the C-CVR series electrodes, the electrochemical performance was tested. The C-CV4 electrode material composite with rGO material displayed the highest electrochemical performance compared to the pristine C-CVR0 electrode. The C-CVR3 achieved maximum Cs of 1345.2 F g^{-1} at 1 A g^{-1} . Also, the composite C-CVR3 electrode demonstrated low values of R_s and R_{ct} after the introduction of rGO in the CVO material. These results indicate that the composite electrode of CVO/rGO exhibits superior performance compared to pristine CVO material and the optimal (4.4%) quantity of rGO improved conductivity and facilitated electron transfer pathways in C-CVR3 material, without impeding the activity of the active material.

Chapter-4 focuses on synthesizing CVO and CVO/rGO composite thin films using the SILAR method on SS substrates. The chapter consists of two sections, A and B. In section A, pristine S-CV series thin films were synthesized by optimizing the dipping time. XRD analysis confirmed the formation of $\text{Co}_3\text{V}_2\text{O}_8$ material. The altered growth dynamics observed in the S-CV series thin film electrodes lead to alterations in morphology, SSA, and porous structure, consequently impacting the electrochemical performance of the electrodes. Notably, the optimized S-CV2 thin film electrode exhibited the highest Cs of 793 F g^{-1} at 1 A g^{-1} , attributed to its maximal SSA of $74.3 \text{ m}^2 \text{ g}^{-1}$. Among the S-CV series thin films, the S-CV2 electrode prepared at adsorption and reaction:rinsing (1:1) time demonstrates superior electrochemical capacitive performance.

Section B discusses the investigation of composite electrodes comprising CVO and rGO, synthesized through a SILAR method at optimized conditions discussed in section A. CVO/rGO composite materials were synthesized via the SILAR method with varying rGO concentrations (0.1 , 0.2 , and 0.3 mg ml^{-1}) and denoted as S-CVR series samples. The formation of $\text{Co}_3\text{V}_2\text{O}_8/\text{rGO}$ composite series materials was confirmed using XRD, FT-IR, Raman, XPS, and EDS techniques. The composite morphology of marigold-like particles of CVO over 2D rGO nanosheets was observed in FE-SEM and HR-TEM analysis. The compositions of CVO and rGO are calculated from TGA data as; 90.2% CVO and 9.8% rGO in S-CVR1, 78.8% CVO and 21.2% rGO in S-CVR2, and 58.7% CVO and 41.3% rGO in S-CVR3. The composite material, CVO/rGO (S-CVR2), displayed improved capacitive

performance of 2346.3 F g^{-1} at 1 A g^{-1} in comparison to pristine S-CVR0, attributed to the incorporation of optimum amount rGO.

Chapter-5 focuses on the preparation of the fabrication and assessment of performance in HSDs. This chapter is divided into two sections labelled 'A' and 'B'. Section 'A' outlines the CVO/rGO composite and rGO electrode preparation using the CBS and slurry coating methods, respectively. Also, the characterization and evaluation of supercapacitive performance were carried out. The research delved into evaluating the electrochemical efficiency of a newly developed composite electrode by CBS method, CVO/rGO (C-CVR3), in C-AHSD and C-SHSD setups. In C-AHSD, C-CVR3 functioned as the cathode, while rGO served as an anode counterpart, employing a 1 M KOH electrolyte. The C-AHSD constructed using the CBS method of C-CVR3 and rGO electrode demonstrated impressive performance metrics and achieved a maximum C_s of 124.3 F g^{-1} , accompanied by a SE of 44.2 Wh kg^{-1} at a SP of 1.2 kW kg^{-1} . The C-AHSD exhibited pseudocapacitive characteristics with notable charge storage capabilities and consistent discharge profiles across diverse current densities, resulting in impressive ED and PD. The EIS investigation underscored C-AHSD's favorable electrochemical conductivity. Additionally, C-SHSD, utilizing a PVA-KOH gel electrolyte, demonstrated promising practical utility, displaying stable capacitive behavior and remarkable cycle durability. The C-SHSD exhibited a noteworthy C_s of 92.1 F g^{-1} at 2.6 A g^{-1} , with an SE of 32.7 Wh kg^{-1} at 1.1 kW kg^{-1} SP. The two SHSD devices were serially connected and charged for 30 seconds and then discharged by the LED lamp up to 95 s, as shown in Figure 6.1. Notably, C-SHSD showcased its applicability by effectively powering LED lamps, emphasizing the real-world potential of the technology. The study underscores the significance of nanostructured composite electrodes, particularly C-CVR3, in elevating the electrochemical performance of HSCs.

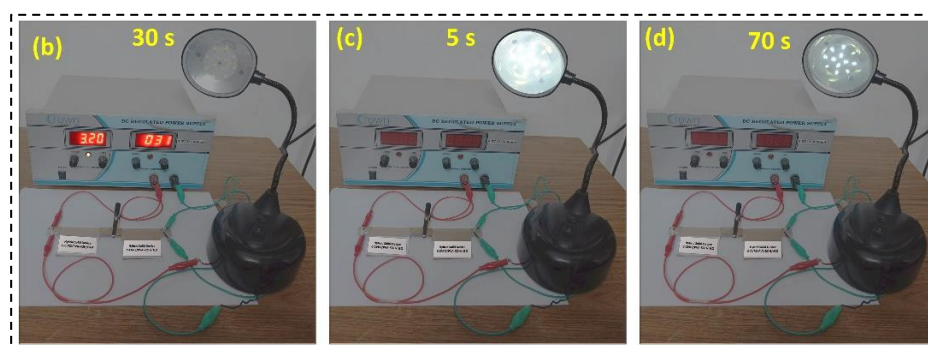


Figure 6.1 (a-c) C-SHSD practical demonstration photographs.

Section 'B' delineates the preparation of the CVO/rGO composite electrode via the SILAR method, their characterization, and the assessment of their supercapacitive performance. The study presented in this section delves into the fabrication and electrochemical evaluation of advanced S-AHSDs and S-SHSDs based on S-CVR2//KOH//rGO and S-CVR2///PVA-KOH//rGO configurations, respectively. The S-AHSD, employing S-CVR2 as the cathode and rGO as the anode electrode, demonstrated exceptional supercapacitive behavior, as evidenced by quasi-rectangular CV curves and non-triangular GCD profiles, indicative of excellent pseudocapacitive performance. Furthermore, the S-AHSD demonstrated a maximum C_s of 150 F g^{-1} at 0.5 A g^{-1} , achieving an SE of 53.3 Wh kg^{-1} at 0.6 kW kg^{-1} SP. Similarly, the S-SHSD, utilizing S-CVR2 as the cathode electrode, showcased remarkable electrochemical performance, characterized by swift redox reaction kinetics and superior cycle stability. The S-SHSD displayed high C_s values at lower current densities, highlighting its pseudocapacitive nature and efficient charge storage. The S-SHSD outperformed C-SHSD by attaining the highest C_s of 132.2 F g^{-1} at 1.5 A g^{-1} current density, with an SE of 47 Wh kg^{-1} at an SP of 1.2 kW kg^{-1} .

Additionally, the SILAR-deposited CVO/rGO-based S-SHSD exhibited an impressive 80.6% capacitive retention over 5000 cycles. Two S-SHSD devices were connected in series and charged for 30 s and they were able to glow LEDs for 120 s discharge time, as illustrated in Figure 6.2. Moreover, practical demonstrations illustrated the S-SHSD's ability to power LED lamps effectively, emphasizing its potential for real-world applications. Overall, this investigation underscores the efficacy of the SILAR-synthesized CVO/rGO composite electrode materials and fabrication techniques in achieving high-performance HSDs with promising energy storage and power delivery capabilities.

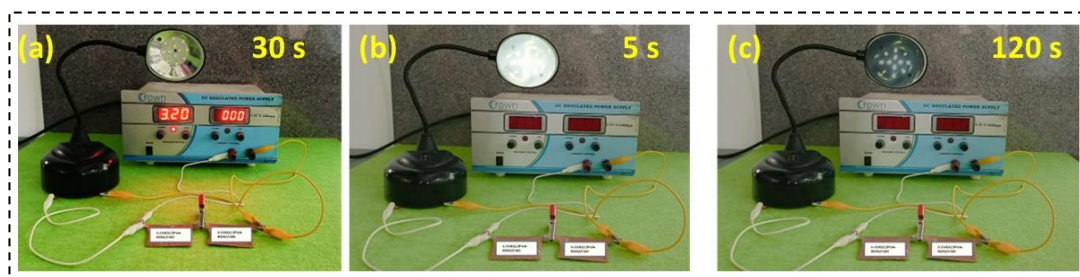


Figure 6.2 (a-c) Photographs of S-SHSDs (S-CVR2//PVA-KOH//rGO) practical demonstration.

The overall conclusion of this chapter is that the S-AHSD and S-SHSD utilizing SILAR-deposited CVO/rGO electrodes exhibit superior supercapacitive characteristics compared to those employing CBS-prepared counterparts. These results imply considerable promise for employing the S-SHSD (S-CVR2//PVA-KOH//rGO) in diverse portable electronic devices, marking substantial progress in energy storage technology.

In **Chapter-6**, passages from all chapters are compiled and summarized, providing a concise overview of each. This work provides a comprehensive perspective of the future energy landscape, emphasizing the crucial role of ESDs, particularly SCs utilizing MTMO materials. By conducting a thorough literature review, recent advancements and research trends are precisely explored, setting the stage for subsequent investigations. The study methodically investigates the synthesis methods, structural characterization, and electrochemical performance evaluation of both pristine CVO and CVO/rGO composite electrodes synthesized using CBS and SILAR methods. The research systematically investigates the impact of rGO concentrations on the physicochemical properties and electrochemical performance of these electrodes.

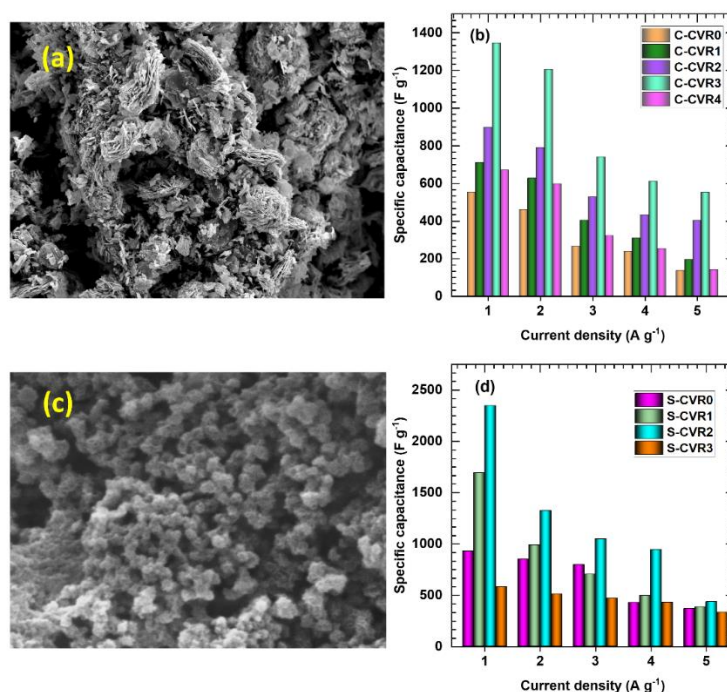


Figure 6.3 (a) FE-SEM image of C-CVR3, (b) bar diagram of Cs vs current density for C-CVR3 electrode, (c) FE-SEM image of S-CVR2, and (d) bar diagram of Cs vs current density for S-CVR2 electrode.

By comparison between CBS and SILAR synthesized CVO/rGO composite electrodes in which SILAR synthesized S-CVR2 marigold-like particle over 2D rGO nanosheets morphology shows maximum performance than CBS prepared C-CVR3 microplate-like structure over 2D rGO nanosheets as depicted in Figure 6.3.

Table 6.1 HSC devices electrochemical performance.

Device Name	Device Type	Cs (F g ⁻¹)	SE (Wh kg ⁻¹)	SP (W kg ⁻¹)	Stability
C-CVR3//rGO	C-AHSD	124.3 at 1.6 A g ⁻¹	44.2	1200	5000 (84.9%)
	C-SHSD	92.1 at 2.6 A g ⁻¹	32.7	1100	5000 (78.3%)
S-CVR2//rGO	S-AHSD	150 at 0.5 A g⁻¹	53.3	600	5000 (85.2%)
	S-SHSD	132.2 at 1.5 A g⁻¹	47	1200	5000 (80.6%)

Moreover, the fabrication and evaluation of performance in HSDs are thoroughly examined. Through methodical experimentation and characterization, the study reveals the superior supercapacitive performance of HSDs employing CVO/rGO composite electrodes synthesized via the SILAR method. Impressively, both S-AHSD and S-SHSD setups demonstrate outstanding Cs, SE, SP, cyclic stability, and practical applicability, outperforming C-AHSD and C-SHSD based on composite electrodes prepared by the CBS method, as elaborated in Table 6.1.

The conclusion of this work underscores the remarkable advancements and potential contributions of nanostructured electrode materials, particularly CVO/rGO composites prepared through the SILAR method with CVO and rGO composition of 78.8% and 21.2%, respectively, towards enhancing the performance of HSDs. Through systematic exploration and analysis across multiple chapters, the study clarifies the synthesis methodologies, structural characterization, and electrochemical evaluation of CVO/rGO composite material, preparing the way for significant progress in energy storage technology.

CHAPTER-7

80_Recommendation

7.1 Recommendations

Drawing from the comprehensive thesis analysis, several recommendations emerge to advance the development and application of HSCs utilizing CVO and CVO/rGO composite electrodes.

- ❖ Further, continuous refinement of synthesis parameters except for CVO and rGO compositions and dip time variation is essential. To improve composite properties like SSA, porosity, and conductivity.
- ❖ Secondly, leveraging advanced characterization techniques offers more profound insights into the structural and electrochemical properties of synthesized materials. So, real-time monitoring through in-situ spectroscopy and operand analysis aids which can aid precise optimization.
- ❖ Additionally, conducting long-term stability studies under realistic conditions is vital for assessing device durability and reliability, informing practical applications.
- ❖ Moreover, integrating HSCs with renewable energy systems and grids is crucial for optimizing overall system performance and efficiency.
- ❖ Prioritizing eco-friendly synthesis methods is paramount, moreover an exploration of alternative electrolytes and electrode materials contributing to sustainability is necessary.
- ❖ Lastly, fostering interdisciplinary collaboration among researchers is required to accelerate innovation in HSC development, driving progress toward viable solutions for global energy challenges.

7.2 Future Findings

Research on CVO combined with rGO materials for SC applications has shown potential, with ongoing studies expected to unveil further enhancements and optimizations.

- ❖ Future investigations may concentrate on refining synthesis methods to improve the electrochemical properties of CVO/rGO composite materials, which may involve exploring novel methods to control the morphology, size, and distribution of CVO nanomaterials on the rGO surface, maximizing the active surface area, and facilitating ion diffusion.

- ❖ Efforts may also be directed towards increasing the Cs and SE by doping CVO with other transition metals or heteroatoms and optimizing the composite's composition.
- ❖ Moreover, to enhance rate capability and cycling stability, nanostructure engineering, conductive additives, or the incorporation of carbonaceous materials other than rGO can be explored.
- ❖ Fabrication techniques such as roll-to-roll printing or inkjet printing can enable the development of flexible and wearable SCs based on CVO/rGO composites, catering to various portable and wearable HSCs.
- ❖ To enhance the performance of CVO, future efforts will focus on making composites with MXene, carbon nitride, and CNTs materials. Integration into hybrid ESDs, combining SCs with other technologies like LIBs, holds promise for improved overall performance, including storing capacity and higher ED. Overall, ongoing research is likely to uncover new insights and innovations, expanding the potential applications of CVO/rGO composites in ESDs.

Publications

Growth Dynamics-Dependent Chemical Approach to Accomplish Nanostructured Cobalt Vanadium Oxide Thin Film Electrodes with Controlled Surface Area for High-Performance Solid-State Hybrid Supercapacitor Devices

Sambhaji S. Kumbhar, Shraddha B. Bhosale, Sachin S. Pujari, Vinod V. Patil, Nitish Kumar, Rahul R. Salunkhe, Chandrakant D. Lokhande, and Umakant M. Patil*

Rational designing of electrode materials having high surface area can accomplish the enhanced charge-storing ability of the electrochemical energy storage devices. Therefore, the surface area of cobalt vanadium oxide (CVO) material is controlled by changing growth dynamics in successive ionic layer adsorption and reaction methods. Structural analysis confirms the formation of hydrous cobalt vanadium oxide nanoparticles ($\text{Co}_3\text{V}_2\text{O}_8 \cdot n\text{H}_2\text{O}$) thin film electrodes, and alteration in the surface area with change in growth dynamics is observed in Brunauer–Emmett–Teller analysis. The CVO1:1 thin film electrode prepared at optimal growth dynamics illustrates high specific capacitance (C_s) (capacity) of 793 F g^{-1} (396.7 C g^{-1}) at 0.5 A g^{-1} , respectively. Moreover, aqueous hybrid supercapacitor devices constructed using CVO1:1 as cathode exhibit high C_s of 133.5 F g^{-1} at 1.1 A g^{-1} , specific energy (SE) of 47.7 Wh kg^{-1} with specific power (SP) of 0.90 kW kg^{-1} . The solid-state hybrid supercapacitor devices also offer high C_s of 102.9 F g^{-1} at 0.3 A g^{-1} , SE of 36.6 Wh kg^{-1} at SP of 0.30 kW kg^{-1} . In the SILAR approach, the dipping time plays a critical role in improving the surface area of the material and, consequently, electrochemical performance, as the current work amply indicates.

of researchers has been focused on new energy storage applications like batteries, supercapacitors, etc. Among available electrochemical energy storage devices (EESDs), aqueous electrochemical energy storage devices (AEESDs) systems are considered a promising alternative to batteries owing to their nontoxic nature, low cost, and superior safety.^[3] Furthermore, in AEESDs, the combination of capacitive and battery features in hybrid supercapacitors (HSCs) are promising AEES systems and offer features such as high energy, power, and stability simultaneously.^[4,5] Moreover, an additional highly anticipated tactic to enhance the energy density of HSCs is to refine the storage capacity of electrodes by controlling the physical (e.g., crystallinity, hydrous nature, conductivity) and morphological (e.g., surface area, porosity, particle size) characteristics of storing materials.


Therefore, in HSCs, several metal hydroxides, oxides, phosphates, and sulfides have been assessed as cathode materials. Based on charge storage mechanisms, most ever-used pseudocapacitive materials can be categorized into intrinsic, intercalation, and extrinsic (battery-type) pseudocapacitive.^[6] Moreover, decreasing the size or crystallinity (nanomaterials) of battery-type materials can illustrate pseudocapacitive activities and are referred to as extrinsic pseudocapacitive

1. Introduction

Energy storage devices (ESDs) are an essential component for the daily operation of nearly all technological necessities, such as electric vehicles, mobile phones, and laptops. Hence, ESDs with extensive cycle life, high energy, and power density, with cost-effectiveness, are in high demand.^[1,2] Therefore, the attention

S. S. Kumbhar, S. B. Bhosale, S. S. Pujari, V. V. Patil, C. D. Lokhande, U. M. Patil
Centre for Interdisciplinary Research
D. Y. Patil Education Society
Kasaba Bawada, Kolhapur 416006, India
E-mail: umakant.physics84@gmail.com

S. S. Pujari
Department of Physics
Yashwantrao Chavan Warana Mahavidyalaya
Warananagar, Kolhapur 416113, India

 The ORCID identification number(s) for the author(s) of this article can be found under <https://doi.org/10.1002/ente.202300400>.

V. V. Patil
School of Chemical Sciences
Punyashlok Ahilyadevi Holkar Solapur University
Solapur 413255, India

N. Kumar, R. R. Salunkhe
Department of Physics
Indian Institute of Technology Jammu
Jagti, Jammu, J & K 181221, India

U. M. Patil
Department of Materials Science and Engineering
Yonsei University
Seodaemun-gu, Seoul 03722, Korea

DOI: 10.1002/ente.202300400

PAPER

Chemical synthesis of binder-free nanosheet-like cobalt vanadium oxide thin film electrodes for hybrid supercapacitor devices†

Cite this: DOI: 10.1039/d4se00932k

Sambhaji S. Kumbhar,^a Shraddha B. Bhosale,^a Sumita S. Patil,^a Akshay Ransing,^b Vinayak G. Parale,^b Chandrakant D. Lokhande,^a Hyung-Ho Park^b and Umakant M. Patil^{*ab}

To enhance the performance of energy storage devices, electrode materials must be designed with a strategic alteration of morphology and electroactive sites, utilizing synergy in bimetallic oxides. Therefore, the present study comprehensively demonstrates that variations in cobalt and vanadate precursor concentrations during chemical bath deposition (CBD) of cobalt vanadium oxide (C-CV) electrode materials significantly impact their physicochemical (structural, morphological and surface area) and electrochemical properties. An increase in vanadium content in the C-CV electrodes induces a notable morphological transformation, from nanoflakes to nanosheets with altered size and surface area. With a nanosheet-like morphology and a surface area of 87.5 m² g⁻¹, the binder-free C-CV4 electrode synthesized with an optimal precursor composition of cobalt and vanadium (1 : 2) exhibits an outstanding specific capacitance (C_s) of 845.3 F g⁻¹ (a specific capacity of 422.6 C g⁻¹) at 1 A g⁻¹. Moreover, an aqueous hybrid supercapacitor device (AHSD) and a solid-state hybrid flexible supercapacitor device (SH-FSD) fabricated employing C-CV4 (cathode) and reduced graphene oxide (rGO) (anode) exhibit noteworthy C_s values of 115 F g⁻¹ and 105.2 F g⁻¹, respectively. Furthermore, the AHSD attains a specific energy (SE) of 40.9 W h kg⁻¹ at a specific power (SP) of 1.8 kW kg⁻¹, while the SH-FSD demonstrates an SE of 37.4 W h kg⁻¹ at a SP of 0.86 kW kg⁻¹. To prepare large-scale binder-free cobalt vanadium oxide with tunable morphology as the cathode material in hybrid energy storage devices, a feasible CBD method is adequate, as demonstrated by the electrochemical performance of hybrid supercapacitor devices.

Received 12th July 2024
Accepted 9th October 2024
DOI: 10.1039/d4se00932k
rsc.li/sustainable-energy

1. Introduction

Over the past few decades, the demand for applications in consumer electronics, medicine, clean energy, and environmental sectors has increased, making wearable and flexible energy storage systems increasingly significant. Although flexible energy storage systems have numerous advantages, their commercialization faces new challenges.^{1–4} Finding highly efficient energy storage devices for storing and dispensing large amounts of specific energy (SE) is one of the significant challenges.⁵ Therefore, flexible hybrid supercapacitors have been developed to achieve higher energy density, faster kinetics, longer cycle life, and enhanced safety with reduced costs.^{6–8} The primary goal of flexible hybrid supercapacitors is to develop

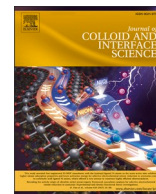
electrode materials with higher energy densities, similar to batteries, while maintaining high power densities and long cycling lifetimes.^{9,10} Consequently, a variety of materials with various morphologies and structures have been investigated as electrodes; nevertheless, transition metal hydroxides and oxides (TMHs/TMOs) are the most remarkable materials for flexible hybrid supercapacitors owing to their high theoretical capacitance with notable energy density.^{1,6} Although significant progress has been made in developing TMOs and TMHs for flexible hybrid supercapacitor electrodes, problems persist when relying solely on a single electrode material with limitations stemming from lower capacitance, limited energy density, and compromised rate capability owing to poor conductivity.⁶ Therefore, modifying intrinsic features by rationally designing structural and morphological features through cation synergy in binary compounds becomes crucial to overcoming the restrictions associated with pristine TMO materials.

Vanadium oxides (V_xO_y) have been extensively researched over the last few decades as potential host materials for electrolyte cations, enabling multi-electron transfer reactions in energy storage applications.¹¹ Moreover, V_xO_y demonstrates a wide

^aCentre for Interdisciplinary Research, D. Y. Patil Education Society, Kasaba Bawada, Kolhapur-416006, India. E-mail: umakant.physics84@gmail.com

^bDepartment of Materials Science and Engineering, Yonsei University, 50 Yonsei-ro, Seodaemun-gu, Seoul-03722, Korea. E-mail: hhpark@yonsei.ac.kr

† Electronic supplementary information (ESI) available. See DOI: <https://doi.org/10.1039/d4se00932k>



Regular Article

Harnessing morphological alteration from microflowers to nanoparticles and cations synergy (Co:Ni) in binder-free cobalt nickel vanadate thin film cathodes synthesized via SILAR method for hybrid supercapacitor devices

Shraddha B. Bhosale^a, Sambhaji S. Kumbhar^a, Sumita S. Patil^a, Akshay Ransing^b,
Vinayak G. Parale^b, Chandrakant D. Lokhande^a, Jayavant L. Gunjekar^a, Hyung-Ho Park^{b,*},
Umakant M. Patil^{a,b,*}

^a Centre for Interdisciplinary Research, D. Y. Patil Education Society, Kasaba Bawada, Kolhapur 416006, India

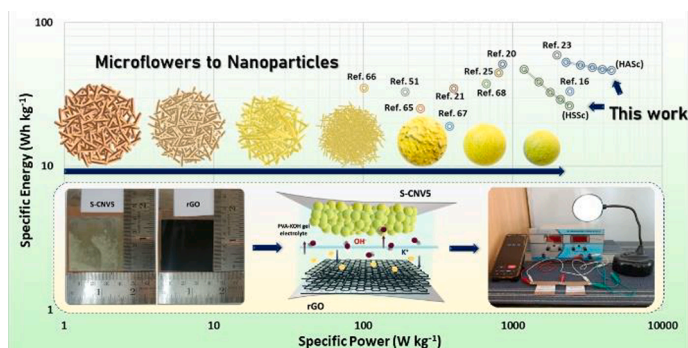
^b Department of Materials Science and Engineering, Yonsei University, 50 Yonsei-ro, Seodaemun-gu, Seoul 03722, Korea



HIGHLIGHTS:

- Novel chemical synthesis of binder-free cobalt nickel vanadate (CNV) by SILAR method.
- Change in cation concentrations in CNV led to morphological alteration: microflower to nanoparticles.
- Maximum specific capacitance (1382 F g⁻¹ at 1 A g⁻¹) is achieved by optimizing the Co:Ni ratio (0.4:0.6) in the CNV electrode.
- Remarkable electrochemical capacitive performance of CNV cathode-based aqueous and solid devices.

GRAPHICAL ABSTRACT



ARTICLE INFO

Keywords:

Cation variation
Hybrid supercapacitor device
Morphology alteration
Nickel cobalt vanadate
SILAR

ABSTRACT

Electrode materials must be rationally designed with morphologies and electroactive sites manipulated through cations' synergy in bimetal compounds in order to maximize the performance of energy storage devices. Therefore, the present study emphasizes binder-free scalable preparation of cobalt nickel vanadate (CNV) thin films by a facile successive ionic layer adsorption and reaction (SILAR) approach with specific cations (Co:Ni) alternation. Increasing the Ni cation content in the CNV notably transforms its microflower structure comprising nanoflakes (252 nm) into nanoparticles (74 nm). An optimized S-CNV5 thin film cathode with Co:Ni molar ratio of ~ 0.4:0.6 and a high specific surface area of 340 m² g⁻¹, provided the excellent specific capacitance (C_{sp}) and capacity (C_{sc}) of 1382 F g⁻¹ and 691 C g⁻¹, respectively at 1 A g⁻¹ current density. A hybrid aqueous supercapacitor (HASC) device with positive and negative electrodes comprising optimized CNV and reduced graphene oxide (rGO), respectively, in a 1 M KOH electrolyte delivered a C_{sp} of 133 F g⁻¹ and a specific energy (SE) of 53 Wh kg⁻¹ at a specific power (SP) of 2261 kW kg⁻¹. Additionally, a fabricated hybrid solid-state supercapacitor (HSSC) device with the same electrodes applying PVA-KOH gel electrolyte displayed a C_{sp} of 119 F g⁻¹, and SE of

* Corresponding authors at: D. Y. Patil Education Society, Kasaba Bawada, Kolhapur 416006, India (U. Patil); Yonsei University, 50 Yonsei-ro, Seodaemun-gu, Seoul 03722, Korea (H-H. Park).

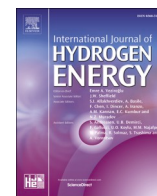
E-mail addresses: hhpark@yonsei.ac.kr (H.-H. Park), umakant.physics84@gmail.com (U.M. Patil).

<https://doi.org/10.1016/j.jcis.2024.04.004>

Received 16 December 2023; Received in revised form 30 March 2024; Accepted 1 April 2024

Available online 2 April 2024

0021-9797/© 2024 Elsevier Inc. All rights reserved.



Impact of Co:Fe cations composition in amorphous and mesoporous cobalt iron phosphate electrocatalysts synthesized by SILAR method on durable electrochemical water splitting

Suraj A. Khalate^a, Sujit A. Kadam^b, Yuan-Ron Ma^b, Sambhaji S. Kumbhar^a, Shraddha B. Bhosale^a, Vinod V. Patil^a, Vinayak G. Parale^d, Sachin B. Kulkarni^c, Chandrakant D. Lokhande^a, Hyung-Ho Park^{d,**}, Umakant M. Patil^{a,d,*}

^a Centre for Interdisciplinary Research (CIR), D. Y. Patil Education Society, Kolhapur, 416 006, India

^b Department of Physics, National Dong Hwa University, Hualien, 97401, Taiwan

^c Department of Physics, Tuljaram Chaturchand College, Baramati, 413 102, India

^d Department of Materials Science and Engineering, Yonsei University, 50 Yonsei-ro, Seodaemun-gu, Seoul, 03722, South Korea

ARTICLE INFO

Handling Editor: Dr J Ortiz

Keywords:

Amorphous thin film electrocatalyst
Cations composition variation
SILAR method
Electrochemical water splitting

ABSTRACT

Efficient and durable electrocatalysts are crucial for energy conversion devices that perform the oxygen evolution reaction (OER) and hydrogen evolution reaction (HER). The structural and morphological characteristics of the electrocatalyst can significantly impact the HER/OER performance. Therefore, it is essential to develop a high-performing electrocatalyst with desired properties using a simple and cost-effective chemical process. So, herein, successive ionic layer adsorption and reaction (SILAR) deposited amorphous, hydrous cobalt iron phosphate (CFP) thin film electrocatalysts are implemented toward electrochemical water splitting. Moreover, in the present work, the molar proportions of cobalt and iron were streamlined to study their synergistic effect on electrochemical HER and OER performance. The electrode of best-performing (CFP-S2) requires the lowest overpotentials of 242 mV for OER and 67.9 mV for HER at a current density of 10 mA/cm², which maintains its activity after 24 h. The alkaline water splitting into a similar electrolytic bath using two electrode systems was demonstrated for 100 h with the lowest overpotential of 1.72 V. The remarkable electrochemical performance and postmortem analysis unambiguously demonstrate that CFP electrodes are a highly promising and robust option for long-duration water-splitting devices, and the facile SILAR method for scalable CFP electrode synthesis indicates enormous potential for commercial applications.

1. Introduction

Hydrogen is a prospective energy source that is profitable to grab the market in the renewable energy sector [1,2]. A primary source of renewable energy has been suggested: hydrogen and has been termed ‘transitioning to a hydrogen society’ [3–5]. Various methods are used to produce hydrogen from different sources, such as reforming steam of natural gas, coal gasification, oxidation of methane, carbon/hydrocarbon assisted water electrolysis, radiolysis, thermolysis, photocatalytic water splitting, fermentative hydrogen production, photobiological water splitting, biocatalysts electrolysis, enzymatic hydrogen generation, etc. [6–8]. Among them, the most practical and

cost-efficient method of producing water splitting is electrochemical for generating oxygen and hydrogen [1,2]. Two half-reactions, specifically the hydrogen evolution reaction (HER) and the oxygen evolution reaction (OER), form the electrochemical process of splitting water, and it requires 1.23 V a theoretical potential to initiate water splitting [9,10]. To split water, excess energy or overpotential is necessary to overcome the barrier of activation energy caused by kinetic effects. Therefore, researchers have been making significant efforts to develop excellent catalysts to decrease the overpotential of water splitting. However, thermodynamics does not favor the direct dissociation of water into hydrogen and oxygen under normal pressure and temperature. Even though the HER process is much more promising in an acidic electrolytic


* Corresponding author. Centre for Interdisciplinary Research (CIR), D. Y. Patil Education Society, Kolhapur, 416 006, India.

** Corresponding author. Department of Materials Science and Engineering, Yonsei University, 50 Yonsei-ro, Seodaemun-gu, Seoul, 03722, South Korea.

E-mail addresses: hypark@yonsei.ac.kr (H.-H. Park), umakant.physics84@gmail.com (U.M. Patil).



Chemical synthesis of manganese ferrite thin films for energy storage application

R. P. Bhosale¹, S. S. Kumbhar², P. P. Bagwade², H. D. Shelke³ , C. D. Lokhande², and V. S. Jamadade^{1,*}

¹ Department of Physics, D. P. Bhosale College, Koregaon, Satara 415516, India

² Centre for Interdisciplinary Research, D. Y. Patil Education Society, Kolhapur 416 006, India

³ Department of Physics, Savitribai Phule Pune University, Pune 411007, India

Received: 16 March 2023

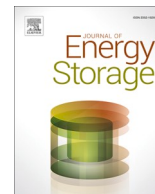
Accepted: 27 November 2023

© The Author(s), under exclusive licence to Springer Science+Business Media, LLC, part of Springer Nature, 2023

ABSTRACT

For the first time, simple chemical bath deposition method was used for the deposition of manganese ferrite (MnFe_2O_4) thin films on stainless steel substrate. The X-ray diffraction study showed cubic spinel crystal structure of MnFe_2O_4 . The surface morphological, structural and elemental studies were carried out using Fourier transform infrared spectroscopy, scanning electron microscopy, Brunauer–Emmett–Teller and energy dispersive X-ray analysis techniques. Scanning electron microscopic study revealed morphology with randomly distributed cubic nanostructured particles. The films exhibited specific surface area of $55.03 \text{ m}^2 \text{ g}^{-1}$ with an average pore size of 1.22 nm. The structural and elemental studies confirmed the formation of MnFe_2O_4 . The electrochemical properties of MnFe_2O_4 films in 1 M KOH electrolyte displayed maximum specific capacitance (C_s) of 687.94 F g^{-1} at a scan rate of 5 mV s^{-1} and exhibited long cyclic stability of 83.2% after 3000 cycles indicating MnFe_2O_4 as a storage electrode. Thus the nanocrystalline particles of cubic spinel ferrite not only increase the number of active sites available for the diffusion of OH^- ions but also decrease the distance that OH^- ions need to travel. These findings demonstrate the potential of the MnFe_2O_4 nanoparticles synthesized in this study as favorable options for pseudocapacitors and other electrochemical applications.

Address correspondence to E-mail: vinayakjamadade@gmail.com



Research Papers

Morphology modulation of MnFe_2O_4 thin film electrode for enhanced performance of hybrid supercapacitor

Rushiraj P. Bhosale^a, Sambhaji S. Kumbhar^b, Shraddha B. Bhosale^b, Rahul R. Salunkhe^c, Vinita A. Kadam^d, Sagar P. Pardhi^e, Sandeep S. Gholap^f, Chandrakant D. Lokhande^{b,*}, Vinayak S. Jamadade^{a,*}

^a Department of Physics, D.P. Bhosale College, Koregaon, Satara 415516, India

^b Centre for Interdisciplinary Research, D. Y. Patil Education Society, Kolhapur 416 006, India

^c Department of Physics, Indian Institute of Technology Jammu Jagti, Jammu, J & K 181221, India

^d Department of Physics, Yashwantrao Chavan Institute of Science Satara (Autonomous), Karmaveer Bhaurao Patil University, Satara 415001, India

^e Department of Physics, Karmaveer Bhaurao Patil College, Urur Islampur 415409, India

^f Agency for Science, Technology and Research (A-STAR), Singapore 138634, Singapore

ARTICLE INFO

Keywords:

Electrodeposition

Hybrid supercapacitor

Manganese ferrite

Morphology modulation

Thin film

ABSTRACT

The preparation of binder-free manganese ferrite electrodes has garnered significant interest in hybrid energy storage devices. This interest stems from their notable electrochemical activity, which is primarily attributed to morphological modulation. Therefore, this study outlines an uncomplicated and scalable synthetic method utilizing electrodeposition (ED) to synthesize manganese ferrite electrodes. These electrodes were synthesized with varying deposition time. By structural analysis, the MnFe_2O_4 phase of synthesized thin films is confirmed. With an increase in the deposition time, the modulation in the morphology of manganese ferrite thin films is evident, progressing from nanoflakes to nanorods. The most favorable deposition time for the manganese ferrite electrode, featuring a worm-like morphology, achieved the highest specific capacitance of 227 F g^{-1} at a current density of 2 A g^{-1} . Additionally, the hybrid solid-state supercapacitor device (HSSD) demonstrated a maximum specific capacitance of 70.1 F g^{-1} with specific energy (SE) of 35.1 Wh kg^{-1} at a specific power (SP) of 3.1 kW kg^{-1} , while retaining 81.1 % of its capacitive performance over 5000 cycles. This research introduces a scalable method for preparing manganese ferrite electrodes without binders, which can serve as cathode in hybrid energy storage devices suitable for real-world applications.

1. Introduction

Global energy consumption is increasing exponentially as a result of the rising population and fast industrialization. As a result, energy has been given top priority in addressing the needs of our modern civilization [1]. Fossil fuels currently serve as the primary source of energy and provide the diverse spectrum of energy needs in various industries. Unfortunately, the availability of fossil fuels is steadily decreasing, and our planet is constantly in danger as a result of the massive environmental degradation these sources produce. According to some studies, by the middle of the century, the world's energy needs would have doubled, and by 2100, they would have tripled [2]. In addition, the widespread use of electronic gadgets, such as wearable technology, digital cameras, laptops, and mobile phones, as well as hybrid electric

cars, has prompted the development of transportable forms of energy. In the report, Bosch's (2007–2022 current state of affairs and expenditure prospects of supercapacitor market in China), the worldwide market of supercapacitors has extended US dollars up to $\$16 \times 10^9$ in 2015, and evaluators look for the market of the supercapacitor to outrun in 2020 up to $\$92.3 \times 10^9$, with a 39 % multiple yearly growth rates. From this view, the progress of the supercapacitor market in the whole world is rising [3]. The development of extremely effective energy conversion as well as storage technologies has been a continuous endeavor in this context. Due to their high energy/power densities, prolonged lives, and quick charging-discharging capabilities, energy storage technologies including supercapacitors, fuel cells, and rechargeable batteries are regarded as viable options for meeting a variety of energy demands [4].

Supercapacitors, also known as ultra-capacitors, are among the most

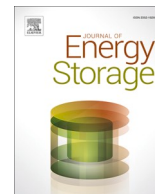
* Corresponding authors.

E-mail addresses: l.chandrakant@yahoo.com (C.D. Lokhande), vinayakjamadade@gmail.com (V.S. Jamadade).

<https://doi.org/10.1016/j.est.2024.111146>

Received 18 November 2023; Received in revised form 14 February 2024; Accepted 28 February 2024

2352-152X/© 2024 Elsevier Ltd. All rights reserved.



Research papers

Development of binder-free, amorphous nickel vanadate cathodes by SILAR method for hybrid supercapacitors: Exploiting surface area by monitoring growth rate

Shraddha B. Bhosale^a, Sambhaji S. Kumbhar^a, Sachin S. Pujari^a, Vinod V. Patil^{a,b}, Nitish Kumar^c, Rahul R. Salunkhe^c, Chandrakant D. Lokhande^a, Jayavant L. Gunjekar^a, Umakant M. Patil^{a,d,*}

^a Centre for Interdisciplinary Research, D. Y. Patil Education Society, Kasaba Bawada, Kolhapur 416006, India

^b School of Chemical Sciences, Purnyashlok Ahilyadevi Holkar Solapur University, Solapur 413255, India

^c Department of Physics, Indian Institute of Technology Jammu, Jagti, Jammu, J & K 181221, India

^d Department of Materials Science and Engineering, Yonsei University, 50 Yonsei-ro, Seodaemun-gu, Seoul 03722, Republic of Korea



ARTICLE INFO

Keywords:

Growth rate variation

Nickel vanadate

SILAR

Surface area

Supercapacitor

Thin film

ABSTRACT

Developing self-supported electrode material in the absence of electro-inert binders considering the effortless transfer of charges and manipulating physicochemical properties of electrodes in energy storage devices is essential. Hence, the present attempt emphasizes the facile synthetic strategy of successive ionic layer adsorption and reaction (SILAR) for controlled nickel vanadate (NV) growth over the conducting plate. In SILAR synthesis, the growth rate is monitored by rinsing and adsorption/reaction time variation to tune the surface area, mesoporous structure, and surface morphology of NV thin films. As a result, the formation of mesoporous, amorphous, hydrous nanoparticles of NV over the stainless-steel substrate is affirmed by structural analysis. Furthermore, alteration in specific surface area with variation in growth rate is observed in BET analysis. As a result, the optimal NV(1:2) thin film electrode exhibited the highest specific capacity (capacitance) of 355 C g^{-1} (710 F g^{-1}) at 1 A g^{-1} current density. Moreover, the fabricated aqueous hybrid supercapacitor device (NV (1:2)/rGO) delivered 109 F g^{-1} specific capacitance at 1.3 A g^{-1} current density, and the device exhibited a maximum specific energy (SE) of 44 Wh kg^{-1} at a particular specific power (SP) of 1.14 kW kg^{-1} . Furthermore, the solid-state hybrid supercapacitor (NV(1:2)/PVA-KOH/rGO) device conferred a specific capacitance of 89 F g^{-1} at 0.5 A g^{-1} current density and an SE of 36 Wh kg^{-1} at 0.482 kW kg^{-1} SP. This research paved an avenue to the binder-free, scalable synthesis of NV electrodes and employed them as a cathode in practical applications of hybrid energy storage devices.

1. Introduction

Increasing concern over the depletion of fossil fuels turned the attention of this generation toward environmentally friendly energy generation and conversion systems. On the other hand, the fluctuations, intermittency, and less continuity of conventional energy generation have urged researchers toward sources of electrical energy devices (EEDs) [1,2]. Hence, efforts toward a highly efficient, sustainable, low-cost, and environmentally friendly energy storage system are still in progress. Among the various energy storage systems, electrochemical energy storage devices (EESDs), such as supercapacitors, batteries, fuel

cells, etc., are highly desirable and environmentally friendly [3,4]. Among the consortium of clean energy storage systems, 'supercapacitors' are the most common alternative to batteries in many applications and have been extensively studied for many decades because of their high specific power (SP), rapid discharge-recharge rate, and exceptional cyclic stability. But less specific energy (SE) sometimes limits the practical use of supercapacitors compared to battery systems. Hence, it is necessary to contribute more significant potential for developing high-energy supercapacitors without sacrificing the SP. Efforts toward enhancing the SE of supercapacitors by fabricating a hybrid device that emphasizes cathode materials superiority, exhibits high

* Corresponding author at: Centre for Interdisciplinary Research, D. Y. Patil Education Society, Kasaba Bawada, Kolhapur 416006, India.

E-mail address: umakant.physics84@gmail.com (U.M. Patil).

<https://doi.org/10.1016/j.est.2023.108417>

Received 6 April 2023; Received in revised form 27 June 2023; Accepted 16 July 2023

2352-152X/© 2023 Elsevier Ltd. All rights reserved.

Research Article

SILAR Synthesized Binder-Free, Hydrous Cobalt Phosphate Thin Film Electrocatalysts for OER Application: Annealing Effect on the Electrocatalytic Activity

Vinod V. Patil ^{1,2}, Sachin S. Pujari ^{1,3}, Shraddha B. Bhosale ¹,
Sambhaji S. Kumbhar ¹, Vinayak G. Parale ⁴, Chandrakant D. Lokhande ¹,
Jayavant L. Gunjekar ¹, Mukund G. Mali ², Dattakumar S. Mhamane ^{2,5},
Hyung-Ho Park ⁴ and Umakant M. Patil ^{1,4}

¹Centre for Interdisciplinary Research, D. Y. Patil Education Society (Deemed to be University), Kolhapur 416006, India

²School of Chemical Sciences, Punyashlok Ahilyadevi Holkar Solapur University, Solapur 413255, India

³Department of Physics, Yashwantrao Chavan Warana Mahavidyalaya, Warananagar, Kolhapur-416113, India

⁴Department of Materials Science and Engineering, Yonsei University, 50 Yonsei-ro, Seodaemun-gu, Seoul 03722, Republic of Korea

⁵Department of Chemistry, Sangameshwar College (Autonomous), Solapur 413001, India

Correspondence should be addressed to Dattakumar S. Mhamane; dkumar.mhamane@gmail.com,
Hyung-Ho Park; hhpark@yonsei.ac.kr, and Umakant M. Patil; umakant.physics84@gmail.com

Received 7 July 2023; Revised 14 October 2023; Accepted 18 October 2023; Published 14 November 2023

Academic Editor: Kisan Chhetri

Copyright © 2023 Vinod V. Patil et al. This is an open access article distributed under the Creative Commons Attribution License, which permits unrestricted use, distribution, and reproduction in any medium, provided the original work is properly cited.

Highly efficient and robust electrocatalysts intended for the oxygen evolution reaction (OER) are essential for energy conversion devices; the structural and morphological fractions of the electrocatalyst can also greatly influence the OER performance. Therefore, developing a high-performing electrocatalyst with desired properties is crucial through a simple and cost-effective chemical process. So, the binder-free, hydrous cobalt phosphate ($\text{Co}_3(\text{PO}_4)_2 \cdot n\text{H}_2\text{O}$) thin film electrocatalysts are prepared via the successive ionic layer adsorption and reaction (SILAR) method onto stainless steel (SS) substrates at ambient temperature. Additionally, the impact of annealing on the OER efficiency of thin film electrodes made of hydrous cobalt phosphate was observed by subjecting the electrocatalysts to different temperatures (200°C and 400°C). The SILAR synthesized hydrous $\text{Co}_3(\text{PO}_4)_2 \cdot n\text{H}_2\text{O}$ with the short-range ordered agglomerated particles transformed into discrete nanoparticles with an annealing temperature. The as-prepared hydrous cobalt phosphate (CP) demonstrated outstanding OER performance with the least overpotential (η) of 265 mV at 10 mA cm^{-2} current density and the lowest Tafel slope of 37 mV dec^{-1} , and the overpotential (η_{10}) increased upon the annealing of catalysts (CP 200 and CP 400). Moreover, the as-prepared electrocatalyst demonstrated overall water splitting at the lowest potential of 1.56 V ($@10\text{ mA cm}^{-2}$) in the alkaline electrolysis system (CP//Pt). The present study reveals that the electrocatalytic performance of the as-prepared cobalt phosphate thin film catalyst is significantly associated with the hydrous content present in catalysts and demonstrates the practical applicability of SILAR-synthesized binder-free cobalt phosphate thin film electrocatalysts.


1. Introduction

The potential of hydrogen gas (H_2) as a green and sustainable energy source is widely recognized within the industry, with an anticipated significant contribution to the expanding renewable energy sector [1, 2]. Among various hydrogen production

processes, electrochemical water splitting ($2\text{H}_2\text{O} \rightarrow 2\text{H}_2 + \text{O}_2$) is one of the attractive paths to produce hydrogen (H_2); however, electrochemical water splitting at a large scale is significantly hindered by the sluggish oxygen evolution reaction (OER) at the anode [3, 4]. Within the OER, multiple surface-adsorbed intermediates result from four proton-coupled



Dielectric behavior and phase transition of $\text{La}_2\text{Mo}_2\text{O}_9$ films synthesized by spray pyrolysis technique

Govinda A. Kadam¹, Sagar A. Patil², Bajarang B. Patil³, Sarita S. Kumbhar⁴, Sambhaji S. Kumbhar², Suraj B. Madake⁴, Laxman D. Kadam⁴, Yuan-Ron Ma⁵, Sujit A. Kadam^{5,*} , and Rajesh K. Nimat^{1,*}

¹ Department of Physics, Balasaheb Desai College, Patan, Maharashtra 415206, India

² Centre for Interdisciplinary Research, D. Y. Patil Education Society, Kasaba Bawada, Kolhapur, Maharashtra 416006, India

³ PG Department of Physics, Balwant College, Vita, Maharashtra 415311, India

⁴ Department of Physics, Shivaji University, Kolhapur, Maharashtra 416004, India

⁵ Department of Physics, National Dong Hwa University, Hualien 97401, Taiwan

Received: 11 November 2022

Accepted: 27 December 2022

Published online:

4 February 2023

© The Author(s), under exclusive licence to Springer Science+Business Media, LLC, part of Springer Nature 2023

ABSTRACT

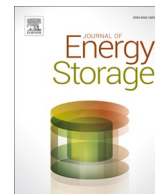
The novel fast oxide ion-conducting material $\text{La}_2\text{Mo}_2\text{O}_9$ (LAMOX) thin films were synthesized by using the cost-effective chemical spray pyrolysis technique. Thermal Gravimetric and differential thermal analysis show the phase transition of $\text{La}_2\text{Mo}_2\text{O}_9$ from α -monoclinic to β -cubic phase at 546.5 °C. Rietveld refinement confirms the stabilization of the β -cubic phase for $\text{La}_2\text{Mo}_2\text{O}_9$ thin films at high temperature. The porous morphology was observed after the annealing and the XPS study revealed elements La, Mo and O observed on the surface of thin films. The temperature and frequency-dependent dielectric constant were studied using an LCR-Q meter in the frequency range of 20 Hz–300 kHz. As the frequency increases, the dielectric constant and dielectric loss decreases for all $\text{La}_2\text{Mo}_2\text{O}_9$ thin films. The dielectric constant, dielectric loss and AC conductivity varied with increasing temperature, shows two relaxation peaks indicating the presence of oxide ion vacancies for ion conduction. The complex impedance shows the Cole–Cole plot for the LAMOX thin films.

1 Introduction

A fuel cell is an electrochemical device that converts chemical energy directly into electrical energy with the water as a by-product [1, 2]. The oxide ion-conducting materials are the interesting materials because of its application mainly in fields like oxygen sensors, oxygen pumps, oxygen separation

membranes and solid oxide fuel cells [3–8]. In 2000, Lacorre [5] discovered the new fast oxide ion-conducting material and illustrated that the lanthanum molybdenum oxide ($\text{La}_2\text{Mo}_2\text{O}_9$) possesses greater ion conduction ability at 800 °C than the conventional oxide ion conductor Yttria Stabilized Zirconia (YSZ). The phase transition of $\text{La}_2\text{Mo}_2\text{O}_9$ takes place from low oxide ion conducting α -monoclinic to high oxide

Address correspondence to E-mail: ksujit17@gmail.com; rajeshknimat@gmail.com



Research Papers

Hydrothermally synthesized nickel copper phosphate thin film cathodes for high-performance hybrid supercapacitor devices

Sachin S. Pujari^a, Sujit A. Kadam^b, Yuan-Ron Ma^b, Satish B. Jadhav^a, Sambhaji S. Kumbhar^a, Shraddha B. Bhosale^a, Jayavant L. Gunjakar^a, Chandrakant D. Lokhande^a, Umakant M. Patil^{a,*}

^a Centre for Interdisciplinary Research, D. Y. Patil Education Society, Kasaba Bawada, Kolhapur 416 006, India

^b Department of Physics, National Dong Hwa University, Hualien 97401, Taiwan



ARTICLE INFO

Keywords:

Concentration variation

Microplates

Microrods

Nickel copper phosphate

Hydrothermal method

Hybrid energy storage devices

Thin film electrode

ABSTRACT

Transition metal phosphate (TMP) based materials are developing as advanced type electrode materials for hybrid supercapacitors (SCs) due to their unprecedented conductivity, and rich redox activity. Attracted by these fabulous physicochemical characteristics of metal phosphates, binder-free nickel copper (Ni-Cu) phosphate thin films directly grown on stainless steel (SS) substrate by hydrothermal method. The morphological alteration from microplates like nickel phosphate to microrods like copper phosphate is detected with increasing copper content in Ni-Cu phosphate thin films. The optimal 1:1 ratio of nickel and copper in Ni-Cu phosphate ($\text{Ni}_{1.62}\text{Cu}_{1.35}(\text{PO}_4)_2 \cdot \text{H}_2\text{O}$) thin film illustrates high specific capacitance (C_s) (capacity (C_c)) of 711 F g^{-1} (355.5 C g^{-1}) at 1.5 A g^{-1} . More significantly, a hybrid aqueous SC (HASC) and all-solid-state SC (HASSC) electrochemical energy storage devices (ESDs) have been fabricated. The HASC device showed superior C_s (85 F g^{-1} at 0.8 A g^{-1}) with specific energy (SE) of 30 Wh kg^{-1} at 1.27 kW kg^{-1} specific power (SP). Additionally, HASSC device offers a higher C_s (52 F g^{-1} at 0.6 A g^{-1}) with 18.53 Wh kg^{-1} SE at 1.64 kW kg^{-1} SP. Also, both HASC and HASSC devices exhibit excellent long-term durability of 84.81 and 80.83 %, respectively, after 5000 GCD cycles. Moreover, HASSC device brightens a panel of 201 red light-emitting diodes (LEDs) illustrating its commercial practicability to next-generation hybrid energy storage devices.

1. Introduction

High-performance electrochemical energy storage devices (ESDs) (e. g., supercapacitors (SCs) and batteries) are acquiring increasing focus from researchers in the industrial field as well as fundamental scientific research [1]. The SC as steady and reversible ESDs has become the most favourable commercial device [2]. Unlike batteries, SCs possess high specific power (SP) and long cycle lifespan that make them promising candidates where (a) peak power demands and (b) maintenance-free ESDs are necessary [3]. A unique scheme to improve the specific energy (SE) of a SC is the usage of electrolytes with a wide working voltage window and a high specific capacitance (C_s) electrode (since $E = 0.5 \text{ CV}^2$) [1,4]. Remarkably, hybrid SC can offer both high SE and excellent SP, ideally suitable for many emerging applications such as smart grids, portable electronics, and electric vehicles [5]. The electrochemical behaviours of hybrid devices depends characteristics of the electrode materials (porosity, surface area and conductivity) and sensitively on

the structures, particularly with the negative electrode materials (carbon based materials) [6,7]. Hence, the design and construction of novel advanced electrode materials along with unique functionalities and structural properties are critical to attaining breakthroughs in the improvement of high-performance hybrid devices [8].

Till today, the various types of cathode materials have been examined for SCs including conducting polymers (polypyrrole, polyaniline, etc.) and transition metal oxides/sulfides/hydroxide. Out of these electrode materials, currently, TMPs have been fascinating enormous attention for several applications including energy conversion, sensors, magnetic devices, and ESDs owing to their metalloid characteristics [9]. Especially, TMPs with the qualities of outstanding redox activity, high conductivity, environmental compatibility, earth abundance, sustainability is more advantageous for ESDs and have been recognized as competitive alternates for conventional metal oxide and hydroxide along with conducting polymers-based electrodes [10]. Basically, PO_4^{3-} polyhedral anions along with a zeolite structure are much more

* Corresponding author.

E-mail address: umakant.physics84@gmail.com (U.M. Patil).

<https://doi.org/10.1016/j.est.2022.105037>

Received 3 March 2022; Received in revised form 18 May 2022; Accepted 1 June 2022

2352-152X/© 2022 Elsevier Ltd. All rights reserved.



Cite this: DOI: 10.1039/d2se00978a

A binder-free facile synthetic approach for amorphous, hydrous nickel copper phosphate thin film electrode preparation and its application as a highly stable cathode for hybrid asymmetric supercapacitors†

Sachin S. Pujari,^a Sujit A. Kadam,^b Yuan-Ron Ma,^b Satish B. Jadhav,^a Sambhaji S. Kumbhar,^a Shraddha B. Bhosale,^a Vinod V. Patil,^{ac} Jayavant L. Gunjekar,^b Chandrakant D. Lokhande^a and Umakant M. Patil^{b,*a}

Currently, amorphous, hydrous compounds are receiving much attention as electrodes in hybrid supercapacitors (S.C.s) as they offer extraordinary electrochemical efficiency because of disorder in their structure and an excellent electrochemical interface. In this study, a simple, cost-effective and binder-free synthetic SILAR method is used for preparing amorphous, hydrous nickel copper phosphate (NCP-S) thin film on a stainless steel substrate (S.S.). The amorphous, hydrous NCP-S thin films exhibit mesoporous, clustered spherical particle-like morphology. The optimal ratio (1 : 1) of nickel and copper in the NCP-S ($\text{Ni}_{1.56}\text{Cu}_{1.44}(\text{PO}_4)_2 \cdot \text{H}_2\text{O}$) material gives a high specific capacitance (C_s) (capacity) of 750 F g^{-1} (412.50 C g^{-1}) at 1.0 A g^{-1} . More significantly, hybrid asymmetric aqueous S.C. (HAASC) and hybrid all-solid-state asymmetric S.C. (HASASC) electrochemical energy storage devices (ESDs) have been fabricated using NCP-S as a cathode and rGO as an anode. The HAASC device showed a superior C_s (95.62 F g^{-1} at 3.0 A g^{-1}) with specific energy (S.E.) of 34 W h kg^{-1} at 2.40 kW kg^{-1} specific power (S.P.). Additionally, the HASASC device offers higher C_s (37.62 F g^{-1} at 0.7 A g^{-1}) with $13.51 \text{ W h kg}^{-1}$ S.E. at 0.55 kW kg^{-1} S.P. Also, both devices exhibit excellent long-term durability (94.11 and 93.81%, respectively, after 5000 GCD cycles). The amorphous, hydrous structures clearly indicate excellent accessibility of ions and stability of electrodes, which is favourable for the hybrid S.C.s. These remarkable supercapacitive results promise the application of amorphous NCP-S as a cathode in commercialized hybrid energy storage systems.

Received 17th July 2022
Accepted 10th November 2022

DOI: 10.1039/d2se00978a

rsc.li/sustainable-energy

1. Introduction

Supercapacitors (S.C.s) have attracted extensive attention among all energy storage devices (ESDs) due to their unique properties, which include long cycling durability, high-power capability, ease of operation and wide working temperature

range. Owing to such excellent properties, they are found to be more favourable ESDs for modern electronic applications in energy regeneration and hybrid electric vehicles, weight leveling, and aerospace industries.^{1–3} Nevertheless, the surface-controlled electrochemical reactions of S.C.s restrict the charge transfer process near and on the electrode surface,

^aCentre for Interdisciplinary Research, D. Y. Patil Education Society, (Deemed to be University), Kasaba Bawada, Kolhapur-416 006, M.S., India. E-mail: Umakant.physics84@gmail.com

^bDepartment of Physics, National Dong Hwa University, Hualien-97401, Taiwan

^cSchool of Chemical Sciences, Punyashlok Ahilyadevi Holkar Solapur University, Solapur 413255, India

† Electronic supplementary information (ESI) available: Formulae for calculation, mass deposition graph, pore size distribution curves of the NCP-S series samples, EDS spectra of the NCP-S series samples, the CV graphs of NCP-S1, NCP-S2, NCP-S4 and NCP-S5 electrodes, pseudocapacitive (surface current) and battery type (bulk current) current density contribution graph at various scan rates for NCP-S1, NCP-S2, NCP-S4 and NCP-S5 electrodes, the GCD curves of NCP-S1, NCP-S2, NCP-S4 and NCP-S5 electrodes, the specific

capacitance of the NCP-S series electrodes at various current densities, XPS study of the NCP-S3 sample before and after stability testing, the structural and electrochemical study of the rGO electrode, the CV and GCD curves of the HAASC device in different potential windows, schematic of HASASC device fabrication, the CV and GCD curves of the HASASC device in different potential windows, compositions of nickel and copper precursors, experimental and observed nickel and copper atomic ratios in NCP-S series thin films, comparison of various amorphous nickel copper phosphate/pyrophosphate based electrodes, EIS fitted circuit parameters of the NCP-S series electrodes, and comparison of electrochemical performance for HAASC and HASASC devices with previous metal phosphate based devices. See DOI: <https://doi.org/10.1039/d2se00978a>

Hydrous and Amorphous Cobalt Phosphate Thin-Film Electrodes Synthesized by the SILAR Method for High-Performing Flexible Hybrid Energy Storage Devices

Vinod V. Patil, Sachin S. Pujari, Shraddha B. Bhosale, Sambhaji S. Kumbhar, Vinayak G. Parale, Jayavant L. Gunjekar, Hyung-Ho Park, Chandrakant D. Lokhande, Mukund G. Mali, Dattakumar S. Mhamane,* and Umakant M. Patil*



Cite This: <https://doi.org/10.1021/acs.energyfuels.2c02202>



Read Online

ACCESS |



Metrics & More

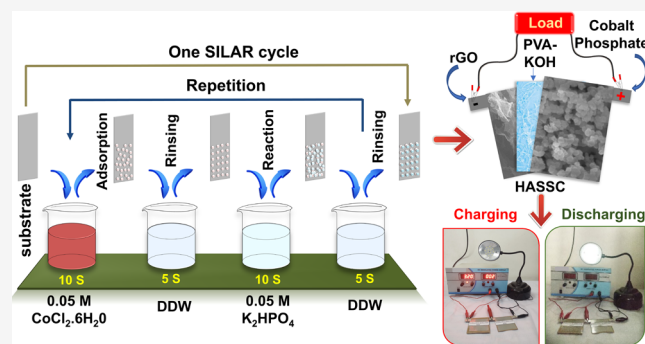


Article Recommendations



Supporting Information

ABSTRACT: Recently, excellent electrochemical performance and good conductivity of transition metal phosphates (TMPs) have been obtained, assuring their potential as a cathode in hybrid supercapacitors. Also, amorphous, hydrous materials are supposed to be exemplary active materials for high-performing supercapacitors because of their unique porous structure, structural flexibility, and rich defects. Therefore, the present investigation describes a simple synthesis method for hydrous and amorphous cobalt phosphate thin-film preparation by the simple successive ionic layer adsorption and reaction (SILAR) method on flexible stainless steel (SS) substrate for supercapacitor application. The structural and morphological analyses reveal mesoporous, agglomerated nanoparticle-like, hydrous, and amorphous cobalt phosphate over the SS substrate. The mesoporous nanoparticles of cobalt phosphate material possess the uppermost specific capacitance of 1147 F g^{-1} and 630.7 C g^{-1} specific capacity at a 1 mA cm^{-2} current density. To demonstrate practical relevance, hybrid supercapacitor devices were assembled with cobalt phosphate and rGO (reduced graphene oxide) as cathode and anode electrodes, respectively. Furthermore, the assembled hybrid aqueous supercapacitor device (S-CP4//KOH//rGO) delivers 44.8 Wh kg^{-1} specific energy (SE) at a specific power (SP) of 4.8 kW kg^{-1} with 126 F g^{-1} specific capacitance. The accumulated all-solid-state hybrid supercapacitor device (S-CP4//PVA-KOH//rGO) achieved the uppermost 77 F g^{-1} specific capacitance and SE of 27.37 Wh kg^{-1} at SP of 1.5 kW kg^{-1} with an outstanding 94% capacitive retention over 5000 cycles. Such remarkable supercapacitive performance results demonstrate that the SILAR method is an easy synthesis process for the binder-free preparation of cathode based on hydrous, amorphous cobalt phosphate thin films for hybrid supercapacitor devices.



1. INTRODUCTION

There has been a recent surge in energy demand for escalating electronic appliances and limitations of existing energy storage systems as the traditional energy storage system does not meet the development trend, which instantly demands efficient and clean energy.^{1–3} Therefore, supercapacitor devices are in high demand and are considered an upcoming generation of energy storage devices based on benefits such as excellent energy storage capability and long cycle life.^{4–6} Nevertheless, their low specific energy confines supercapacitor application in devices that require high energy.^{7,8} Therefore, to improve specific energy and power, hybrid asymmetric capacitor devices have been developed, which consist of two dissimilar electrodes: one as an energy source (cathode), where battery-type or pseudocapacitive material is used, and another as a power source (anode), which consists of capacitor-type or electro-

chemical double-layer capacitor (EDLC) electrode materials.^{9–12}

In general, existing pseudocapacitive materials are categorized into intrinsic, intercalation, and extrinsic types, and they exhibit higher specific energy than EDLC materials. Interestingly, battery-type materials can exhibit pseudocapacitive behavior upon changing their crystallite size or morphology (nanocrystalline) and are referred to as extrinsic pseudocapacitive materials.^{13–16} Therefore, recent research interest has been growing in developing and miniaturizing battery-type

Received: July 1, 2022

Revised: September 18, 2022

Fabian I. Ezema
Chandrakant D. Lokhande
Abhishek C. Lokhande *Editors*

Chemically Deposited Metal Chalcogenide-based Carbon Composites for Versatile Applications



Springer

1D, 2D, and 3D Structured Metal Chalcogenides for Supercapacitor Application



S. S. Kumbhar, S. J. Marje, V. V. Patil, S. B. Bhosale, S. S. Pujari, J. L. Gunjekar, C. D. Lokhande, and U. M. Patil

Abbreviations

1D	One dimensional
2D	Two dimensional
3D	Three dimensional
AB	Acetylene black
CBD	Chemical bath deposition
CC	Carbon cloth
CV	Cyclic voltammetry
EDLC	Electric double-layer capacitor
EIS	Electrochemical impedance spectroscopy
FESEM	Field emission scanning electron microscopy
GCD	Galvanostatic charge-discharge
GO	Graphene oxide
NG	N-doped graphene
NMC	Nitrogen-doped mesoporous carbon
NWs	Nanowires
PANI	Polyaniline
Pt	Platinum
rGO	Reduced graphene oxide
TEM	Transmission electron microscopy

S. S. Kumbhar · S. J. Marje · V. V. Patil · S. B. Bhosale · S. S. Pujari · J. L. Gunjekar
C. D. Lokhande · U. M. Patil (✉)
Centre for Interdisciplinary Research, D. Y. Patil Education Society, Kolhapur, India

Patents



INTELLECTUAL
PROPERTY INDIA
PATENTS | DESIGNS | TRADE MARKS
GEOGRAPHICAL INDICATIONS



सत्यमेव जयते

क्रम सं/SL No :022129010



पेटेंट कार्यालय, भारत सरकार

The Patent Office, Government Of India

पेटेंट प्रमाण पत्र

Patent Certificate

(पेटेंट नियमावली का नियम 74)

(Rule 74 of The Patents Rules)

पेटेंट सं. / Patent No.

459219

आवेदन सं. / Application No.

202221020670

फाइल करने की तारीख / Date of Filing

06/04/2022

पेटेंटी / Patentee

D.Y. PATIL EDUCATION SOCIETY (DEEMED TO BE UNIVERSITY), KASABA BAWADA, KOLHAPUR

आविष्कारकों का नाम / Name of Inventor(s)

1.DR.UMAKANT MAHADEV PATIL 2.MR.SAMBHAJI SHIVAJI KUMBHAR 3.MS.SHRADDHA BANDOPANT BHOSALE 4.MR.VINOD VASANT PATIL 5.PROF.CHANDRAKANT DNYANDEV LOKHANDE 6.DR.PRASHANT RAVASAHEB DESHMUKH

प्रमाणित किया जाता है कि पेटेंटी को, उपरोक्त आवेदन में यथाप्रकटित **CHEMICAL METHOD FOR GROWING A COBALT VANADIUM OXIDE THIN FILM ON SOLID SUBSTRATE** नामक आविष्कार के लिए, पेटेंट अधिनियम, 1970 के उपबंधों के अनुसार आज तारीख अप्रैल 2022 के छठे दिन से बीस वर्ष की अवधि के लिए पेटेंट अनुदत्त किया गया है।

It is hereby certified that a patent has been granted to the patentee for an invention entitled **CHEMICAL METHOD FOR GROWING A COBALT VANADIUM OXIDE THIN FILM ON SOLID SUBSTRATE** as disclosed in the above mentioned application for the term of 20 years from the 6th day of April 2022 in accordance with the provisions of the Patents Act, 1970.



अनुदान की तारीख : 16/10/2023
Date of Grant :

पेटेंट नियंत्रक
Controller of Patents

टिप्पणी - इस पेटेंट के नवीकरण के लिए फीस, यदि इसे बनाए रखा जाना है, अप्रैल 2024 के छठे दिन को और उसके पश्चात प्रत्येक वर्ष में उसी दिन देय होगी।

Note - The fees for renewal of this patent, if it is to be maintained, will fall / has fallen due on 6th day of April 2024 and on the same day in every year thereafter.



सत्यमेव जयते



पेटेंट कार्यालय, भारत सरकार

The Patent Office, Government Of India

पेटेंट प्रमाण पत्र

Patent Certificate

(पेटेंट नियमावली का नियम 74)

(Rule 74 of The Patents Rules)

पेटेंट सं. / Patent No.

529322

आवेदन सं. / Application No.

202221020648

फाइल करने की तारीख / Date of Filing

06/04/2022

पेटेंटी / Patentee

D.Y. PATIL EDUCATION SOCIETY (DEEMED TO BE UNIVERSITY), KASABA BAWADA, KOLHAPUR

आविष्कारकों का नाम / Name of Inventor(s)

1.DR.UMAKANT MAHADEV PATIL 2.MR.SAMBHAJI SHIVAJI KUMBHAR 3.MS.SHRADDHA BANDOPANT BHOSALE 4.MR.VINOD VASANT PATIL 5.PROF.CHANDRAKANT DNYANDEV LOKHANDE 6.DR.RAHUL RAGHUNATH SALUNKHE

प्रमाणित किया जाता है कि पेटेंटी को, उपरोक्त आवेदन में यथाप्रकरित **COBALT VANADIUM OXIDE, PREPARATION METHOD FOR THE SAME, AND SUPERCAPACITOR COMPARISING THE SAME** नामक आविष्कार के लिए, पेटेंट अधिनियम, 1970 के उपबंधों के अनुसार आज तारीख अप्रैल 2022 के छठे दिन से बीस वर्ष की अवधि के लिए पेटेंट अनुदत्त किया गया है।

It is hereby certified that a patent has been granted to the patentee for an invention entitled **COBALT VANADIUM OXIDE, PREPARATION METHOD FOR THE SAME, AND SUPERCAPACITOR COMPARISING THE SAME** as disclosed in the above mentioned application for the term of 20 years from the 6th day of April 2022 in accordance with the provisions of the Patents Act, 1970.



इकात की दंडित

अनुदान की तारीख : 20/03/2024

Date of Grant : 20/03/2024

टिप्पणी - इस पेटेंट के नवीकरण के लिए फीस, यदि इसे बनाए रखा जाना है, अप्रैल 2024 के छठे दिन को और उसके पश्चात प्रत्येक वर्ष में उसी दिन देय होगी।

Note. - The fees for renewal of this patent, if it is to be maintained, will fall / has fallen due on 6th day of April 2024 and on the same day in every year thereafter.

पेटेंट नियंत्रक

Controller of Patents


INTELLECTUAL PROPERTY INDIA
 PATENTS | DESIGNS | TRADE MARKS
 GEOGRAPHICAL INDICATIONS

[illegible]



INTELLECTUAL
PROPERTY INDIA

PATENTS | DESIGNS | TRADE MARKS
GEOGRAPHICAL INDICATIONS



सत्यमेव जयते

क्रमांक : 022124439
SL No :



भारत सरकार
GOVERNMENT OF INDIA

पेटेंट कार्यालय
THE PATENT OFFICE

पेटेंट प्रमाणपत्र
PATENT CERTIFICATE
(Rule 74 of The Patents Rules)

पेटेंट सं. / Patent No. : 432303
आवेदन सं. / Application No. : 202221020644
फाइल करने की तारीख / Date of Filing : 06/04/2022
पेटेंटी / Patentee : D.Y. PATIL EDUCATION SOCIETY (DEEMED TO BE UNIVERSITY), KASABA BAWADA, KOLHAPUR
आविष्कारक (जहां लागू हो) / Inventor(s) : 1.DR.UMAKANT MAHADEV PATIL 2.MR.VINOD VASANT PATIL 3.MR.SAMBHAJI SHIVAJI KUMBHAR 4.MS.SHRADDHA BANDOPANT BHOSALE 5.PROF.CHANDRAKANT DNYANDEV LOKHANDE

प्रमाणित किया जाता है कि पेटेंटी को, उपरोक्त आवेदन में यथाप्रकटित NICKEL COBALT PHOSPHATE THIN-FILM ELECTRODES : CHEMICAL METHOD FOR PREPARATION OF THE SAME APPLICATION FOR SUPERCAPACITOR AND ELECTROCATALYSIS USING THE SAME. नामक आविष्कार के लिए, पेटेंट अधिनियम, 1970 के उपबंधों के अनुसार आज तारीख अप्रैल 2022 के छठे दिन से बीस वर्ष की अवधि के लिए पेटेंट अनुदत्त किया गया है।

It is hereby certified that a patent has been granted to the patentee for an invention entitled NICKEL COBALT PHOSPHATE THIN-FILM ELECTRODES : CHEMICAL METHOD FOR PREPARATION OF THE SAME APPLICATION FOR SUPERCAPACITOR AND ELECTROCATALYSIS USING THE SAME. as disclosed in the above mentioned application for the term of 20 years from the 6th day of April 2022 in accordance with the provisions of the Patents Act, 1970.



अनुदान की तारीख : 19/05/2023
Date of Grant :

पेटेंट नियंत्रक
Controller of Patent

टिप्पणी - इस पेटेंट के नवीकरण के लिए फीस, यदि इसे बनाए रखा जाना है, अप्रैल 2024 के छठे दिन को और उसके पश्चात प्रत्येक वर्ष में उसी दिन देय होगी।

Note. - The fees for renewal of this patent, if it is to be maintained will fall / has fallen due on 6th day of April 2024 and on the same day in every year thereafter.



INTELLECTUAL
PROPERTY INDIA

PATENTS | DESIGNS | TRADE MARKS
GEOGRAPHICAL INDICATIONS



सत्यमेव जयते

भारत सरकार
GOVERNMENT OF INDIA

पेटेंट कार्यालय
THE PATENT OFFICE

पेटेंट प्रमाणपत्र
PATENT CERTIFICATE
(Rule 74 of The Patents Rules)

क्रमांक : 022121485
SL No :



पेटेंट सं. / Patent No. : 415578
आवेदन सं. / Application No. : 202221005137
फाइल करने की तारीख / Date of Filing : 31/01/2022
पेटेंटी / Patentee : DR.VINAYAK SHIVAJIRAO JAMADADE
आविष्कारक (जहां लागू हो) / Inventor(s) :
1.DR.VINAYAK SHIVAJIRAO JAMADADE
2.MR.RUSHIRAJ PRATAPRAO BHOSALE 3.DR.SHIVAJI
BHAURAO UBALE 4.MR.SAMBHAJI SHIVAJI KUMBHAR
5.PROF.CHANDRAKANT DNYANDEV LOKHANDE

प्रमाणित किया जाता है कि पेटेंटी को, उपरोक्त आवेदन में यथाप्रकटित A CHEMICAL SYNTHESIS PROCESS OF MANAGANESE FERRITE THIN FILMS ON CONDUCTING SUBSTRATES FOR ENERGY STORAGE" नामक आविष्कार के लिए, पेटेंट अधिनियम, 1970 के उपबंधों के अनुसार आज तारीख जनवरी 2022 के इक्कीसवें दिन से बीस वर्ष की अवधि के लिए पेटेंट अनुदत्त किया गया है।

It is hereby certified that a patent has been granted to the patentee for an invention entitled A CHEMICAL SYNTHESIS PROCESS OF MANAGANESE FERRITE THIN FILMS ON CONDUCTING SUBSTRATES FOR ENERGY STORAGE" as disclosed in the above mentioned application for the term of 20 years from the 31st day of January 2022 in accordance with the provisions of the Patents Act,1970.



अनुदान की तारीख : 27/12/2022
Date of Grant :

पेटेंट नियंत्रक
Controller of Patent

टिप्पणी - इस पेटेंट के नवीकरण के लिए फीस, यदि इसे बनाए रखा जाना है, जनवरी 2024 के इक्कीसवें दिन को और उसके पश्चात प्रत्येक वर्ष में उसी दिन देय होगी।

Note. - The fees for renewal of this patent, if it is to be maintained will fall / has fallen due on 31st day of January 2024 and on the same day in every year thereafter.

Conferences, Workshops, Seminar



D. Y. PATIL EDUCATION SOCIETY
(Deemed to be University), KOLHAPUR
NAAC 'A' Grade in 3rd Cycle

Certificate

This is to certify that **Mr. /Ms. Kumbhar Sambhaji Shivaji** of Centre for Interdisciplinary Research, DYPS, Kolhapur has delivered invited ~~talk~~/ chaired the session/ presented oral/ presented poster/ participated in the **International Conference on Nanotechnology Addressing the Convergence of Materials Science, Biotechnology and Medical Science (IC-NACMBM-2024)** held at the Centre for Interdisciplinary Research, D. Y. Patil Education Society (Deemed to be University), Kolhapur, Maharashtra, India during 12th to 14th February 2024. His/ Her contribution to the conference is highly appreciated.

Dr. Jayavant L. Gunjekar

Convener

Prof. Meghnad G. Joshi

Convener

Prof. Chandrakant D. Lokhande

Chairman

International Conference

on

“Advanced Materials Synthesis, Characterization and Applications - 2023”

(AMSCA - 2023)

DEPARTMENT OF
PHYSICS



CERTIFICATE OF PARTICIPATION

This is to certify that,

Mr. Sambhaji Kumbhar, D. Y. Patil Education Society, Kolhapur has presented

Poster on the topic **High-Performance Solid-State Hybrid Supercapacitors Based on Cobalt Vanadium**

Oxide Nanoparticles Electrode by Chemical Method in the International Conference on AMSCA - 2023

held at the **Department of Physics, Savitribai Phule Pune University, Pune, Maharashtra,**

INDIA during 21st to 24th November, 2023.

Convener
AMSCA - 2023

Co-Convener
AMSCA - 2023

Head
Department of Physics,
SPPU, Pune



Agricultural Development Trust's

Shardabai Pawar Mahila Arts, Commerce & Science College,
Shardananagar, Malegaon Bk., Tal-Baramati, Dist. - Pune, 413115




National Conference


on


Recent Trends in Functional Materials and Their Applications (RTFMA - 2024)

Certificate

Presented to Dr./Mr./Mrs./Miss. Kumbhar Sambhaji Shivaji from -----
D.Y. Patil Education Society, Kolhapur has actively participated
and presented Oral / Poster in SERB sponsored National conference organized by Department of
Physics on 13th - 14th March 2024.


Dr. V. R. Shinde & Mrs. S. J. Shinde
Organising Secretary


Dr. T. P. Gujar
Coordinator & Head


Prof. Dr. S. V. Mahamuni
Convener & Principal





SHIVAJI UNIVERSITY, KOLHAPUR



SOPHISTICATED ANALYTICAL INSTRUMENT FACILITY (SAIF) – COMMON FACILITY CENTRE (CFC)

WORKSHOP & HANDS-ON TRAINING ON XRD ORGANISED BY SAIF-CFC UNDER STRIDE PROGRAMME

Certificate of Participation

This is certify that Mr. Kumbhar Sambhaji Shivaji has successfully participated in the workshop & hands-on training on XRD organised by SAIF (CFC), Shivaji University, Kolhapur held during 11-12 Nov, 2021 under the STRIDE (Scheme for Trans-disciplinary Research for India's Developing Economy) programme.

Prof. R. G. Sonkawade
Co-ordinator : SAIF, Head (i/c) : CFC
Shivaji University, Kolhapur.
Chairman



SANJAY GHODAWAT UNIVERSITY Kolhapur

Empowering Lives Globally !

(Approved by UGC & Govt. of Maharashtra)

Certificate

This is to certify that

Prof. / Dr. / Mr. / Ms. Sambhaji Shivaji Kumbhar, Ph.D. Scholar

of D. Y. Education Society, Kolhapur has participated in National Seminar on

“Emerging Nano Materials for Renewable Energy”

held on Monday, 26th December, 2022 and organized by Sanjay Ghodawat University, Kolhapur.

Dr. Sambhaji M. Pawar
Convener

Dr. Pallavi D. Bhangre
Convener

Dr. Sarita P. Patil
Co-ordinator

Prof. Dr. Arun S. Patil
Vice-Chancellor



Department of Science and Technology, Govt. of India Supported
Synergistic Training program Utilizing the scientific and Technological Infrastructure
STUTI-2022

ONE WEEK TRAINING PROGRAM

Hands-on Training on Sophisticated Instruments for Materials Science

September 14-20, 2022

CERTIFICATE

This is to certify that Prof./Dr./Mr./Ms. *Sambhaji Shivaji Kumbhar*.....
from *D.Y. Patil Education Society, Kothapur* participated / delivered an Invited Lecture / given
Hands-on-Training on.....*X*.....*X*.....
in the DST-STUTI funded One Week Hands-on Training on Sophisticated Instruments for Materials Science
organized by Bundelkhand University, Jhansi in association with Banasthali Vidyapith, Rajasthan
during September 14-20, 2022



Dr Anupam Vyas
Co-Convener

Dr Lavkush Dwivedi
Co-Convener

Dr Parvej Ahmad Alvi
PMU Coordinator

Dr Sanjeev Kumar Shrivastava
Convener